



**HAL**  
open science

# Hydrogenated nanodiamond as radiosensitizer : chemical and physical investigations of the involved mechanisms

Magdalena Kurzyp

► **To cite this version:**

Magdalena Kurzyp. Hydrogenated nanodiamond as radiosensitizer : chemical and physical investigations of the involved mechanisms. Other. Université Paris Saclay (COmUE), 2017. English. NNT : 2017SACLN060 . tel-01744183

**HAL Id: tel-01744183**

**<https://theses.hal.science/tel-01744183>**

Submitted on 27 Mar 2018

**HAL** is a multi-disciplinary open access archive for the deposit and dissemination of scientific research documents, whether they are published or not. The documents may come from teaching and research institutions in France or abroad, or from public or private research centers.

L'archive ouverte pluridisciplinaire **HAL**, est destinée au dépôt et à la diffusion de documents scientifiques de niveau recherche, publiés ou non, émanant des établissements d'enseignement et de recherche français ou étrangers, des laboratoires publics ou privés.

# Hydrogenated nanodiamond as radiosensitizer: chemical and physical investigations of the involved mechanisms

Thèse de doctorat de l'Université Paris-Saclay préparée à l'École Normale Supérieure de Cachan (École Normale Supérieure Paris-Saclay)

École doctorale n°575:  
Electrical, Optical, Bio-physics and Engineering (EOBE)  
Spécialité de doctorat: Physique

Thèse présentée et soutenue à Saclay, le 20 décembre 2017, par

**Magdalena Kurzyp**

## Composition du Jury :

Anke KRUEGER Professeure, Université de Wurtzbourg, Allemagne	Rapporteur
Jean-François HOICHEPIED Maître de Recherche, MINES ParisTech	Rapporteur
Jean-Louis MARIGNIER Chargé de Recherche, Université Paris-Saclay, LCP	Examineur
Johan ALAUZUN Maître de Conférences, Institut Charles Gerhardt Montpellier	Examineur
Michel MERMOUX Directeur de Recherche, Université Grenoble Alpes, CNRS	Président
Jean-Charles ARNAULT Directeur de Recherche, CEA-LIST	Directeur de thèse
Hugues A. GIRARD Ingénieur-Chercheur, CEA-LIST	Encadrant
Cécile SICARD-ROSELLI Maître de Conférences, Université Paris-Saclay, LCP	Invitée

---

*To my family, co-workers and friends without whom none of my success would be possible.  
Thank you for all your support along the way.*

# Résumé

Les nanodiamants (NDs) sont des candidats pertinents envisagés pour plusieurs domaines d'applications : les composites à base de polymères, les lubrifiants, les capteurs basés sur la luminescence des centres colorés, la catalyse et les applications en biologie. En plus de leur petite taille (5 nm) [1], les nanodiamants de détonation possèdent des propriétés intéressantes pour la nanomédecine avec des applications potentielles pour la thérapie (délivrance de médicaments en utilisant la chimie de greffage du carbone [2]) ou le diagnostic (centres photoluminescents NV [3]).

Parmi les applications en biologie, il a été démontré très récemment que le nanodiamant pouvait agir comme une nanoparticule active avec un effet thérapeutique ajustable. En effet, T. Petit et ses collègues du Laboratoire Capteurs Diamant (CEA-DRT-LIST) ont mis en évidence une activité radiosensibilisante des nanodiamants hydrogénés (H-NDs) en collaboration avec des biologistes du laboratoire de Cancérologie Expérimentale (CEA-DSV-iR2CM) [4]. L'étude *in vitro* a montré que les H-NDs pouvaient générer des radicaux libres à l'intérieur de cellules cancéreuses radiorésistantes exposées à une irradiation gamma. L'effet principal conduit à la mise en sénescence de ces cellules qui correspond à un état de vieillissement avec un arrêt de la prolifération cellulaire [5]. Avec cette propriété de surface, les nanodiamants hydrogénés sont donc des agents radiosensibilisants potentiels pour le traitement de tumeurs afin d'augmenter l'effet des traitements de radiothérapie. L'utilisation de nanoparticules à faible Z par une telle application contraste avec les approches actuellement utilisées qui reposent sur des matériaux métalliques à fort Z. L'effet radiosensibilisant des nanodiamants a donné lieu à un brevet international [6].

Bien que les effets biologiques aient été étudiés en détail, les mécanismes physiques et chimiques permettant d'expliquer l'origine de cet effet radiosensibilisant des H-NDs restent très peu compris. Il a été supposé que la production d'espèces radicalaires de l'oxygène (ROS) était liée aux propriétés électroniques spécifiques des H-NDs et à leur capacité à émettre des électrons sous irradiation. Cette interprétation est liée aux propriétés de la surface du diamant massif hydrogéné qui possède une affinité électronique négative (NEA). Ceci correspond à une structure électronique particulière pour laquelle le minimum de la bande de conduction est situé au-dessus du niveau du vide. Par conséquent, l'émission électronique peut être induite par une illumination correspondant à la largeur de la bande interdite. Cette bande interdite est de 5.5 eV pour le diamant, ce qui correspond à une énergie minimale dans le domaine de l'ultraviolet (~ 225 nm). Les électrons transférés de la bande de valence à la bande de conduction peuvent ensuite facilement diffuser vers la surface sans barrière énergétique. L'exposition à l'air de la surface de diamant hydrogénée conduit à l'apparition d'une conductivité de surface de type p (SC) [7].

En 2014, A. Bolker et al ont mesuré l'affinité électronique de nanodiamants hydrogénés par voie plasma en combinant la spectroscopie STS (Scanning Tunnelling Spectroscopy) et la microscopie KFM (Kelvin Force Microscopy). Ils ont montré que des NDs de tailles allant de 4 à 20 nm possèdent une affinité électronique négative [8]. Ces études rejoignent celles

effectuées par le groupe de R. Hamers (UW-Madison USA) qui a démontré la possibilité d'utiliser des films de diamant hydrogénés comme des sources solides d'électrons solvatés dans des liquides sous illumination UV [9]. Cette propriété ouvre la voie à des réductions catalytiques comme celle de  $N_2$  en  $NH_3$  ou de  $CO_2$  en  $CO$ . Une propriété comparable a été mise en évidence pour des surfaces de diamant aminées (de terminaison  $-NH_2$ ) [10]. Très récemment (juin 2017), le même groupe a aussi mis en évidence ces propriétés photocatalytiques induites sous UV pour des particules de diamant hydrogénées de 125 nm [11]. En revanche, l'effet n'a pas été observé pour des NDs de détonation de 5 nm. Ceci pourrait être expliqué par la densité élevée de défauts cristallins présents dans ces NDs ou l'oxydation de la surface par les espèces radicalaires générées sous UV.

L'interrogation principale porte sur la question suivante : l'effet radiosensibilisant observé sous irradiation gamma par T. Petit et ses collègues est-il lié à la production d'électrons solvatés comme ceci est décrit pour le diamant massif ?

La détection d'une activité des H-NDs de détonation dans l'eau est intimement liée à la radiolyse de l'eau. Pour la radiothérapie traditionnelle, l'interaction de la radiation ionisante avec les molécules d'eau conduit à la formation de ROS dans le milieu biologique. Cet effet observé pour les H-NDs pourrait être associé à une interaction spécifique ayant lieu à l'interface diamant / eau pendant l'irradiation. Parmi les espèces réactives de l'oxygène, l'espèce la plus active conduisant à des dommages biologiques importants correspond aux radicaux hydroxyles ( $HO^\bullet$ ). La présence de  $HO^\bullet$  est accompagnée principalement de celles d'électrons solvatés ( $e_{aq}$ ), d'anions superoxydes ( $O_2^{\bullet-}$ ) et du peroxyde d'hydrogène ( $H_2O_2$ ).

Il est donc essentiel de mettre au point des techniques permettant la détection des radicaux  $HO^\bullet$  et leur quantification. Un protocole de référence a été mis au point par C. Sicard-Roselli et E. Brun de l'Université Paris-Saclay conduisant à la capture de radicaux  $HO^\bullet$  par la molécule de coumarine en présence de nanoparticules d'or [12]. Cette interaction conduit à la formation de la 7-hydroxycoumarine possédant des propriétés de fluorescence qui est proportionnelle à la concentration de  $HO^\bullet$  ayant réagi. La réalisation de ce protocole dans une atmosphère différente permet de détecter et de quantifier les électrons solvatés produits sous irradiation.

**L'objectif principal de ce travail de thèse est d'étudier les mécanismes physiques et chimiques expliquant l'effet radiosensibilisant des H-NDs de détonation.** Pour cela, des suspensions colloïdales de NDs dans l'eau seront préparées et irradiées. La sonde coumarine permettra d'étudier la photo-activité de ces NDs en incluant :

- La quantification des radicaux  $HO^\bullet$  et la production d'électrons
- L'effet de la chimie de surface (oxygène, hydrogène et terminée  $sp^2$ )
- L'effet de l'énergie d'activation (rayons X: 17.5 keV et gamma: 1.17 MeV)
- L'effet de la source de NDs de détonation

Avant d'étudier cette activité sous irradiation, la première étape est de préparer des NDs de différentes chimies de surface.

Le **Chapitre 2** présente les méthodes physiques permettant de modifier la chimie de surface de NDs de détonation provenant de plusieurs sources commerciales. Le recuit thermique sous air conduit à une oxydation de la surface, les traitements par plasma micro-onde d'hydrogène et le recuit sous hydrogène favorisent la formation de liaisons C-H à la surface, le recuit sous vide génère des reconstructions de type  $sp^2$  à la surface. Chacun de ces traitements a été optimisé.

Les propriétés de ces NDs modifiés ont été comparées à celles des NDs initiaux en combinant plusieurs méthodes d'analyse pour caractériser :

1. **La qualité de la structure cristalline** par la microscopie électronique en transmission (TEM) et la spectroscopie Raman

*L'étude en TEM montre tout d'abord la polydispersité des nanodiamants de détonation fournis par la société PlasmaChem (entre 3nm et 10 nm). Le cœur diamant a été identifié par TEM en mesurant des distances inter-réticulaires qui correspondent à celle des plans (111) du diamant.*

*Pour les NDs oxydés, les clichés TEM révèlent une surface dépourvue de carbone amorphe ou de carbone graphitique. Au contraire, une couche de carbone désordonné a été observée à la périphérie des NDs hydrogénés quelle que soit la méthode d'hydrogénation utilisée.*

*Enfin, pour les NDs recuites sous vide à 750 °C, cette couche périphérique est plus organisée avec des domaines de carbone  $sp^2$ .*

*La spectroscopie Raman confirme la présence du diamant quelle que soit la modification de surface effectuée. Le pic du diamant est élargi pour les NDs hydrogénés.*

2. **La composition chimique** par la spectroscopie Infrarouge (FTIR) et la spectroscopie Raman qui constitue une méthode complémentaire moins sensible à la chimie de surface

*Le FTIR confirme l'efficacité du recuit sous air pour éliminer les groupes  $CH_x$  et favoriser la formation de liaisons  $C=O$ . Les deux méthodes d'hydrogénation conduisent à une très forte réduction des liaisons  $C=O$ . La forme des structures liées aux vibrations des liaisons  $CH_x$  diffère selon la méthode d'hydrogénation. Pour le recuit sous vide, le FTIR ne révèle pas de changement majeur pour des températures de recuit inférieures à 850 °C.*

3. **La concentration d'impuretés** métalliques et non métalliques par ICP-MS (Inductively-coupled Plasma Mass Spectroscopy).

*Pour les NDs de détonation (PlasmaChem) utilisées dans cette thèse, l'analyse par ICP-MS montre que la quantité d'impuretés est 5 fois plus faible comparée à une autre source de NDs.*

*Pour la majeure partie des modifications de surface appliquées à ces NDs, une réduction très significative de la concentration d'impuretés est constatée : - 67 % après l'hydrogénation thermique, - 34 % après l'hydrogénation plasma et - 25 % après le recuit sous vide. En revanche, une contamination plus élevée a été mesurée pour les NDs recuits sous air.*

Les expériences étant réalisées dans l'eau, le **Chapitre 3** concerne les propriétés colloïdales des NDs en milieu aqueux en fonction de leur chimie de surface. L'objectif est de déterminer

les paramètres qui gouvernent la stabilité colloïdale. Tout d'abord, le protocole de préparation des suspensions a été optimisé en ajustant les différents paramètres impliqués. Ensuite, une étude comparative a été menée se focalisant sur les interactions des molécules d'eau avec la surface des NDs. La stabilité colloïdale à court terme (< 24 h) et à long terme (50 – 60 jours) a été étudiée par chacune des chimies de surface en utilisant la même source de NDs de détonation.

*Les NDs oxydés sont extrêmement stables en suspension. Après 40 jours, malgré une diminution significative, le potentiel zeta reste égal à - 40 mV.*

*Les suspensions de NDs hydrogénés préparées par les deux méthodes (plasma, recuit) présentent des propriétés colloïdales proches pour des suspensions fraîches avec un potentiel zeta positif. Une légère réoxydation de la surface hydrogénée a été observée au FTIR qui favorise l'hydrophilicité des H-NDs. Ces suspensions présentent néanmoins une moins bonne stabilité colloïdale après plusieurs dizaines de jours. Les NDs hydrogénés par plasma sont les moins stables par rapport à ceux préparés par recuit. Une agrégation importante des H-NDs est constatée avec la formation de bulles à la surface des suspensions. Le rôle joué par des nanobulles dans le colloïde est discuté.*

*Pour les NDs recuits sous vide, les suspensions aqueuses préparées juste après le recuit ont des propriétés colloïdales très similaires avec un potentiel zeta positif. En revanche, leur vieillissement est très différent. En effet, les NDs recuits à des températures supérieures à 750 °C s'agrègent très rapidement tandis que les NDs préparés à 750 °C pendant une heure conservent une bonne stabilité colloïdale avec un potentiel zeta de 45 - 50 mV. Le lien entre la stabilité colloïdale et la chimie de surface des NDs est discuté en détail.*

Le **Chapitre 4** fait la synthèse des comportements des NDs modifiés en suspension dans l'eau sous irradiation. La production de radicaux HO• a été mesurée sous rayons X et rayons gamma pour les différentes chimies de surface (oxydée, hydrogénée et terminée sp<sup>2</sup>). Cette détection a été réalisée avec la coumarine (Cou) qui est sensible à la présence de radicaux HO•. En parallèle, les électrons solvatés produits seront sondés en utilisant le même protocole sous une atmosphère de N<sub>2</sub>O/O<sub>2</sub>.

*Les NDs oxydés par recuit sous air en suspension dans l'eau n'induisent pas de surproduction de radicaux HO• par rapport à ceux produits par la radiolyse de l'eau lorsqu'ils sont irradiés sous rayons X ou rayons gamma quelle que soit la concentration.*

*Au contraire, les NDs hydrogénés conduisent à une surproduction de radicaux HO• de + 40 % et + 50 % pour les NDs traités par plasma et par recuit sous hydrogène, respectivement. Cette propriété a été observée pour trois sources différentes de NDs de détonation. Ceci démontre que le phénomène ne dépend pas de la source de NDs. Lorsque les suspensions sont irradiées par des rayons gamma, la surproduction est plus élevée (+ 60 %). Cette production de radicaux HO• a été étudiée en fonction du temps. Les NDs recuites sous hydrogène ont une meilleure stabilité puisqu'une surproduction de radicaux HO• de + 40 % est conservée après 64 jours tandis que celle induite par les NDs hydrogénés par plasma est très fortement réduite à moins de 10 %. Le lien entre la surproduction de radicaux HO• et la stabilité colloïdale est discuté en*

détail. Des électrons solvatés produits sous irradiation ont été détectés pour les H-NDs. La surproduction est de + 80 % et + 100 % sous rayons X et rayons gamma.

De façon surprenante, les NDs recuits sous vide à 750 °C conduisent aussi à une surproduction de radicaux HO• par rapport à la radiolyse de l'eau. Ceci est observé également pour des NDs recuites à 850 °C. Cependant, le comportement diffère en fonction de la concentration des NDs. Pour atteindre une surproduction de + 50 %, il faut utiliser une concentration trois fois plus importante de NDs recuites à 850 °C.

Pour toutes les chimies de surface exceptée la surface oxydée sous air, une saturation de la production de radicaux HO• est observée pour des concentrations en NDs supérieures à 20 µg.mL<sup>-1</sup>. Les expériences réalisées permettent d'exclure un effet de « quenching » de la fluorescence. Cette saturation est plutôt liée à une recombinaison des radicaux HO• produits à forte concentration de NDs et/ou à une interaction de ces radicaux avec la surface des NDs conduisant à des modifications de leur chimie de surface.

L'origine du mécanisme conduisant à cette surproduction de radicaux HO• et d'électrons solvatés sous irradiation (rayons X ou gamma) pour les H-NDs et les NDs recuites sous vide est ensuite discutée. Le rôle joué par la structure des molécules d'eau autour de ces NDs est en particulier envisagé.

## Références

- [1] A. S. Barnard, *Analyst*, 2009, **134**, 1751–64.
- [2] E. K. Chow, X.-Q. Zhang, M. Chen, R. Lam, E. Robinson, H. Huang, D. Schaffer, E. Osawa, A. Goga and D. Ho, *Sci. Transl. Med.*, 2011, **3**, 73ra21.
- [3] R. Schirhagl, K. Chang, M. Loretz and C. L. Degen, *Annu. Rev. Phys. Chem*, 2014, **65**, 83-105.
- [4] T. Petit, J.-C. Arnault, H. A. Girard, M. Sennour, T.-Y. Kang, C.-L. Cheng, P. Bergonzo, T. Koitaya, J. Yoshinobu, M. Kawai, A. M. Lear, L. L. Kesmodel, S. L. Tait and M. C. Hersam, *Nanoscale*, 2012, **4**, 6792.
- [5] R. Grall, H. Girard, L. Saad, T. Petit, C. Gesset, M. Combis-Schlumberger, V. Paget, J. Delic, J.-C. Arnault and S. Chevillard, *Biomaterials*, 2015, **61**, 290–298.
- [6] WO 2014009930 A1, *International Pat.*, 2013.
- [7] X. Gao, L. Liu, D. Qi, S. Chen, A. T. S. Wee, T. Ouyang, K. P. Loh, X. Yu and H. O. Moser, *J. Phys. Chem. C*, 2008, **112**, 2487–2491.
- [8] A. Bolker, C. Saguy and R. Kalish, *Nanotechnology*, 2014, **25**, 385702.
- [9] D. Zhu, L. Zhang, R. E. Ruther and R. J. Hamers, *Nat. Mater.*, 2013, **12**, 836–841.
- [10] D. Zhu, J. A. Bandy, S. Li and R. J. Hamers, *Surf. Sci.*, 2016, **650**, 295–301.
- [11] L. Zhang and R. J. Hamers, *Diam. Relat. Mater.*, 2017, **78**, 24–30.
- [12] C. Sicard-Roselli, E. Brun, M. Gilles, G. Baldacchino, C. Kelsey, H. Mcquaid, C. Polin, N. Wardlow and F. Currell, *Small*, 2014, **10**, 3338–3346.



# List of Abbreviations

**7-OH Cou** : 7-hydroxycoumarin chemical compound, also called umbelliferone

**a-C** : Amorphous carbon

**AFM** : Atomic Force Microscopy

**AgNP(s)** : Silver nanoparticle(s)

**Al<sub>2</sub>O<sub>3</sub>** : Aluminum(III) oxide chemical compound, also called alumina or alumina crucible

**Ar** : Argon gas

**ATR-FTIR** : Attenuated Total Reflectance Fourier Transform Infrared Spectroscopy

**AuNP(s)** : Gold nanoparticle(s) also abbreviated as **GNP(s)**

**BET** : Brunauer-Emmett-Teller method of the specific surface area (**SSA**) analysis with gas

**CNT(s)** : Carbon Nanotube(s)

**CO** : Carbon oxide gas

**CO<sub>2</sub>** : Carbon dioxide gas

**Cou** : Coumarin chemical compound

**DLS** : Dynamic Light Scattering

**DMSO** : Dimethyl sulfoxide

**DSC** : Differential Scanning Calorimetry

**e<sub>aq</sub>** : Solvated or hydrated electron (electron entrapped by the water structure)

**EPS** : Electron Paramagnetic Resonance

**FLR** : Fullerene-like reconstruction

**FTIR** : Fourier Transform Infrared Spectroscopy

**H<sup>•</sup>** : Hydrogen atom

**H<sub>2</sub>O<sup>2</sup>** : Hydrogen peroxide

**HB** : Hydrogen bond

**H-ND** : Hydrogenated nanodiamond

**HO<sup>•</sup>** : Hydroxyl radical

**HV** : High Vacuum conditions (pressure Torr)

**ICP-MS** : Inductively Coupled Plasma Mass Spectrometry

**IICI** : Incoherent Interfacial Coulombic Interactions

**KFM** : Kelvin Force Microscopy

**KPM** : Kelvin Probe Microscopy

**MPCVD** : Microwave Plasma Chemical Vapor Deposition or plasma hydrogenation technique

**NAA** : Neutron Activation Analysis

**NaCl** : Sodium Chloride chemical compound, commonly named as salt

**ND(s)** : Nanodiamond(s)

**NH** : Secondary amide

**NH<sub>2</sub>** : Amidogen or amide chemical group

**NP(s)** : Nanoparticle(s)

**O<sub>2</sub><sup>-</sup>** : Superoxide anion

**OLC** : Onion-like carbon

**Ox-ND** : Air annealed or air oxidized nanodiamond

**PCA** : Photon Correlation Spectroscopy

**poly-ND** : polyfunctional nanodiamond

**PRF** : Pulse Repetition Frequency

**ROS** : Reactive Oxygen Species

**RS** : Raman Spectroscopy

**SAUD** : Salt-assisted Ultrasonic Deaggregation

**SAXS** : Small Angle X-ray Scattering

**SC** : Surface conductivity

**SDND** : Single-digit nanodiamond or single / one primary sized nanodiamond particle

**SF<sub>6</sub>** : Sulfur hexafluoride gas

**Si** : Silicon (wafer)

**sp<sup>2</sup>-ND** : Vacuum annealed nanodiamond or surface-graphitised nanodiamond

**SPT** : Single Particle Tracking

**SSA** : Specific surface area

**STS** : Scanning Tunnelling Spectroscopy

**TEM** : Transmission Electron Microscopy

**UDD** : Ultra-dispersed detonation diamond powder

**UV** : Ultra-violet wavelength

**ZP** : Zeta Potential



---

# Table of Contents

<b>Résumé.....</b>	<b>iii</b>
<b>List of Abbreviations .....</b>	<b>ix</b>
<b>General introduction .....</b>	<b>7</b>
<b>Bibliography .....</b>	<b>11</b>
<b>Characterization of nanodiamonds .....</b>	<b>13</b>
<b>2.1 Introduction.....</b>	<b>15</b>
<b>2.2 Surface modifications of detonation nanodiamonds .....</b>	<b>15</b>
2.2.1 Materials .....	16
2.2.2 Thermal annealing under air.....	16
2.2.3 Microwave plasma hydrogenation .....	17
2.2.4 Thermal annealing under hydrogen .....	18
2.2.5 Vacuum annealing.....	19
2.2.6 Summary .....	20
<b>2.3 Fourier Transform Infrared Spectroscopy .....</b>	<b>21</b>
2.3.1 As-received detonation nanodiamonds.....	21
2.3.2 Air annealed nanodiamonds.....	23
2.3.3 Plasma hydrogenated nanodiamonds .....	25
2.3.4 Hydrogen annealed nanodiamonds.....	27
2.3.5 Vacuum annealed nanodiamonds .....	28
2.3.6 Summary .....	30
<b>2.4 Raman Spectroscopy .....</b>	<b>30</b>
2.4.1 Surface-modified nanodiamonds.....	30
2.4.2 Summary .....	32
<b>2.5 Inductively Coupled Plasma Mass Spectrometry .....</b>	<b>32</b>
2.5.1 As-received nanodiamonds .....	33
2.5.2 Surface modified nanodiamonds .....	34
2.5.3 Summary .....	36
<b>2.6 Transmission Electron Microscopy .....</b>	<b>37</b>
2.6.1 As-received nanodiamonds .....	37
2.6.2 Air annealed nanodiamonds .....	39

---

2.6.3 Plasma hydrogenated nanodiamonds .....	39
2.6.4 Hydrogen annealed nanodiamonds.....	40
2.6.5 Vacuum annealed nanodiamonds .....	41
2.6.6 Summary .....	42
<b>Bibliography .....</b>	<b>43</b>
<b>Colloidal properties of nanodiamonds .....</b>	<b>49</b>
<b>3.1 Introduction.....</b>	<b>52</b>
<b>3.2 Bibliography review .....</b>	<b>53</b>
3.2.1 Colloidal properties of nanodiamonds .....	53
3.2.2 Deaggregation strategies for nanodiamond hydrosol preparation.....	56
3.2.3 Colloidal stability of nanodiamonds versus their surface chemistry .....	56
3.2.4 Interaction of nanodiamonds with solvents .....	60
3.2.5 Summary .....	62
<b>3.3 Nanodiamond hydrosol preparation .....</b>	<b>63</b>
3.3.1 Preparation of colloids: general concept of sonication and centrifugation .....	64
3.3.2 Suspended-solid concentration measurement.....	66
3.3.3 Characterization of colloids: Dynamic Light Scattering .....	70
3.3.4 Representation of the dynamic light scattering results.....	73
3.3.5 Calibration of the DLS equipment.....	77
3.3.6 Optimization of the NDs colloid preparation.....	80
<b>3.4 Colloidal behavior of NDs with different surface chemistries .....</b>	<b>86</b>
3.4.1 Colloidal properties of air annealed nanodiamonds .....	86
3.4.2 Colloidal properties of plasma hydrogenated nanodiamonds .....	88
3.4.3 Colloidal properties of hydrogen annealed nanodiamonds .....	91
3.4.4 Properties of vacuum annealed nanodiamonds.....	93
3.4.5 Summary .....	94
<b>3.5 Stabilisation and aging effect.....</b>	<b>95</b>
3.5.1 Stability over 24 h .....	95
3.5.2 Stability over 50 days .....	100
<b>3.6 FTIR study .....</b>	<b>107</b>
3.6.1 Surface-modified nanodiamond powder.....	107
3.6.2 Surface-modified nanodiamond pellet.....	108
3.6.3 Surface-modified nanodiamond suspension .....	109
3.6.4 Summary .....	110

---

<b>3.7 Discussion about the colloidal properties of nanodiamonds according to their surface chemistries</b> .....	<b>111</b>
3.7.1 Air annealed nanodiamonds.....	111
3.7.2 Hydrogenated nanodiamonds .....	111
3.7.3 Vacuum annealed nanodiamonds .....	113
3.7.4 General discussion on the colloidal behavior of cationic nanodiamonds .....	114
<b>Bibliography</b> .....	<b>116</b>
<b>Irradiation of nanodiamonds</b> .....	<b>123</b>
<b>4.1 Introduction</b> .....	<b>125</b>
<b>4.2 Bibliography review</b> .....	<b>125</b>
4.2.1 Water radiolysis .....	126
4.2.2 Fluorescence probes for HO <sup>•</sup> detection.....	126
4.2.3 Emission of electrons from detonation nanodiamond particles .....	128
4.2.4 Radiosensitization with nanoparticles .....	130
<b>4.3 Establishment of the irradiation protocol</b> .....	<b>132</b>
4.3.1 Properties of coumarin .....	132
4.3.2 Properties of 7-hydroxycoumarin .....	133
4.3.3 Fluorescence properties of nanodiamonds alone .....	136
4.3.4 Colloidal stability of nanodiamonds in coumarin / 7-hydroxycoumarin .....	137
4.3.5 Fluorescence properties of 7-hydroxycoumarin in the presence of nanodiamonds ....	138
4.3.6 Summary .....	142
<b>4.4 Measurements of HO<sup>•</sup> radicals</b> .....	<b>142</b>
4.4.1 Air annealed nanodiamonds.....	143
4.4.2 Plasma hydrogenated nanodiamonds .....	145
4.4.3 Hydrogen annealed nanodiamonds.....	148
4.4.4 Vacuum annealed nanodiamonds .....	150
4.4.5 Summary .....	151
4.4.6 Aging effect vs. measurements of HO <sup>•</sup> radicals .....	152
<b>4.5 Gamma irradiation</b> .....	<b>157</b>
<b>4.6 Detection and quantification of solvated electrons via HO<sup>•</sup> and N<sub>2</sub>O / O<sub>2</sub></b> .....	<b>158</b>
4.6.1 Principle of the method .....	158
4.6.2 X-rays irradiation.....	158
4.6.3 Gamma irradiation.....	160
4.6.4 Summary .....	162
<b>4.7 Discussion about the behavior of nanodiamonds under irradiation</b> .....	<b>163</b>

---

4.7.1 Discussion on the origin of the phenomenon.....	164
<b>Bibliography .....</b>	<b>171</b>
<b>General conclusions and perspectives.....</b>	<b>177</b>
Perspectives .....	179
Bibliography .....	181
<b>Scientific communication .....</b>	<b>183</b>
Publications.....	183
Oral Presentations .....	183
Posters .....	183
<b>Appendix .....</b>	<b>185</b>
A.1 PlasmaChem GmbH commercial nanodiamonds powder: quality data sheet .....	186
A.2 Submicron latex beads as a spherical nanoparticles standard for DLS .....	187
A.3 Effect of centrifugal force and speed .....	188
A.4 Colloidal properties of as-received PlasmaChem nanodiamonds .....	188
A.5 Stability over 50 days .....	189
A.6 Fourier Transform Infrared Spectroscopy.....	189





# Chapter 1

## General introduction

Nanodiamonds (NDs) are pertinent candidates for different fields of applications: polymer composites, lubricants, sensors, catalysts, and bioapplications. More specifically, detonation NDs with a primary diameter of 5 nm have suitable assets for nanomedicine applications including their small size<sup>1</sup>. NDs are carbon-based materials possessing a wide range of properties with high potential for therapy (delivery via carbon surface chemistry<sup>2</sup>) or diagnosis (stable luminescent Nitrogen-Vacancy – NV centers<sup>3</sup>).

Among these well-identified bioapplications of nanodiamonds, it was recently shown that NDs can also act as active nanoparticles, with a therapeutic effect which can be triggered. Indeed, T. Petit and his colleagues from the Diamond Sensors Laboratory (CEA-DRT-LIST) have demonstrated a radiosensitizing activity of hydrogen-terminated NDs (H-NDs) in collaboration with biologists from the Experimental Cancerology Laboratory (CEA-DSV-iR2CM). The *in vitro* investigation has demonstrated that H-NDs can generate free radicals into radioresistant cancer cell lines when exposed to gamma irradiation leading these cells to a senescence state, i. e. an irreversible aging state with stopping of their proliferation<sup>4</sup>. Considering this surface-property, H-NDs could potentially act as radiosensitizing agents to treat resistant tumors by enhancing the effect of radiotherapy treatment. The use of carbon nanoparticles for such application is in contrast with the common radiosensitizing strategies where mostly high-Z (e.g. metals) nanoparticles are currently used. This rare idea to use non-metallic H-NDs for generating free radicals for therapeutic purposes under radiation also resulted in an international patent in the radiology field<sup>5</sup>.

While the *in vitro* biological effects of H-ND radiosensitization have been investigated in details, the physical and chemical mechanisms behind the effect remains not well understood. It was suggested that the unusual activity toward the production of reactive oxygen species (ROS) in cells was linked to specific electronic properties and irradiation-induced ability to emit electrons from the surface of H-NDs. In other words, important modifications of the electronic band structure may take place when the surface of detonation NDs is terminated with hydrogen, in particular, after exposure to a microwave hydrogen plasma.

The traditional interpretation found its source in the origin of detonation NDs belonging to the diamond-based family of nanomaterials. All the features observed for detonation NDs were then linked to properties of the bulk diamond which when terminated with hydrogen

possess unique electronic assets such as a negative electron affinity (NEA). The NEA term corresponds to a particular electronic structure where the position of the vacuum level lies below the conduction band minimum. As a consequence of such band configuration, the emission of electrons can be induced with a bandgap or even sub-bandgap illumination ( $E_{\text{gap}} = 5.5 \text{ eV}$ ) with minimum energy corresponding to the UV range ( $\sim 225 \text{ nm}$ ). Electrons excited from the valence band into conduction band can then easily diffuse to the surface without a physical barrier. Moreover, the air exposure of H-terminated diamond can confer it a *p*-type surface conductivity (SC)<sup>6</sup>.

The connection with diamond properties was made explaining that origin of the ROS production and the radiosensitization should be also assigned to the NEA phenomena occurring for H-NDs. Later in 2014, the same hypothesis was experimentally confirmed for the first time by the work of A. Bolker et al<sup>7</sup>. Using a combination of Scanning Tunnelling Spectroscopy (STS) and Kelvin Force Microscopy (KFM), the researchers probed electron affinity of isolated detonation NDs previously exposed to microwave hydrogen plasma for 20 min. It was demonstrated that NDs of different primary size down to 4 nm exhibit NEA due to band bending explicitly observed in the presence of hydrogen on the surface.

All these studies on H-NDs related to the ROS production, radiosensitizing effect, SC and NEA property were also in line with the work of R. Hamers' group from UW-Madison, USA. The particular interest of Hamers' group in physical and chemical properties of surface and interfaces resulted in several studies dealing with electron ejection from diamond materials. The pioneering work in that topic showed that photo-illuminated under UV diamond with H-terminations can act as a solid-state source of electrons in liquids<sup>8</sup>. The paradigm of diamond's photoactivity observed in water was attributed to specific surface terminations leading to NEA property and production of solvated electrons under illumination<sup>9</sup>. The importance of H-diamond as a solid source of solvated electrons resides in the possibility to have access to highly-energetic electrons<sup>10</sup>. This is due to the position of the conduction band which lies above the conduction band of other semiconductors. This unique property of H-terminated surface may drive chemically and biologically important catalytic reductions (e.g. reduction of  $\text{N}_2$  to  $\text{NH}_3$  or  $\text{CO}_2$  into CO) which are non-accessible by other materials.

Research activities were also driven toward other surface functionalities, including amino-terminated ( $\text{NH}_2$ ) diamond surface<sup>11</sup>. The experiments involved UV-activation of amino-modified diamond followed by emission of electrons into vacuum and water. The results revealed that protonated amide create stable NEA and are equally active as H-diamond under illumination. The studies expanded toward photoemission measured in a gaseous atmosphere (e.g. argon – Ar, air and sulfur hexafluoride -  $\text{SF}_6$ ) instead of water. Up to this point, the NEA and electron emission effect from the H- and the amino-terminated surface of diamond was confirmed in 2016.

The most recent findings (2017), published by the same research group, demonstrated similar UV-induced photocatalytic reduction properties of non-defective H-terminated diamond

particles (125 nm) instead of planar structures<sup>12</sup>. However, the same effect was not demonstrated for smaller detonation H-NDs (diameter ~5 nm) which are more suitable for any possible bioapplications due to their ultra-small size. Lack of surface-activity of detonation H-NDs was attributed to their low-crystallographic quality, the presence of structural defects and the fast surface-oxidation induced by reactive oxygen species under UV-range.

The particularity of the studies conducted by T. Petit and co-workers relies on the activation of the H-ND surface with high energy gamma rays ( $E = 660$  keV), whereas experiments performed by R. Hamers et al. involved illumination of H-diamond (bulk and nano) with UV ( $E > 5.5$  eV). Low absorption of carbon in gamma rays compare to UV may strongly limit the phenomenon of spontaneous oxidation seen for detonation NDs under UV. But, at the same time and for the same reason, electron emission is naturally expected much lower in the MeV range compared to UV.

Thus, an important question is raised: is the effect of radiosensitization under  $\gamma$  rays observed by T. Petit and co-workers somehow linked to the production of solvated electrons as described on hydrogenated bulk materials? The current state-of-art did not consider utilization of X-rays (keV) or Gamma-rays (MeV), conventionally used for radiotherapy treatment, to prove the same effect on NDs as seen for H-terminated planar diamond and natural diamond particles of larger size.

Detection of H-terminated activity of detonation NDs in aqueous media is closely linked to water radiolysis mechanism. In traditional radiotherapy, the interaction of ionizing radiation with water molecules leads to the production of ROS in bio-media. The effect previously observed on H-NDs should also be associated with specific interaction taking place on diamond/water interface under irradiation<sup>13</sup>. Referring back to water radiolysis phenomenon, the major and most invasive ROS species responsible for biological damage to cells due to oxidative destruction are hydroxyl radicals ( $\text{HO}^\bullet$ ). Presence of  $\text{HO}^\bullet$  is accompanied by the production of solvated electrons ( $e_{\text{aq}}$ ), superoxide anions ( $\text{O}_2^{\bullet-}$ ) along with hydrogen/oxygen atoms ( $\text{H}^\bullet/\text{O}^\bullet$ ), and hydrogen peroxide ( $\text{H}_2\text{O}_2$ ).

The importance of  $\text{HO}^\bullet$  in photochemical damage or cellular dysfunctions resulted in many studies dealing with their effective detection and quantification<sup>14,15</sup>. A reference protocol was previously developed by C. Sicard-Roselli and E. Brun from Paris Sud University which allows scavenging  $\text{HO}^\bullet$  radical via coumarin (Cou) molecule in the presence of nanoparticles (e.g. gold - Au)<sup>16</sup>. As a consequence, the probe is converted into 7-hydroxycoumarin with fluorescence properties proportional to  $\text{HO}^\bullet$  concentration. Apart from  $\text{HO}^\bullet$  radical, the same method can be used for detection of solvated electrons under a specific atmosphere (e.g.  $\text{N}_2\text{O}/\text{O}_2$ ).

Thus, following the previous work of T. Petit et al. and the current state-of-art, **the aim of this Ph.D. work is to investigate the physical and chemical effect behind the radiosensitization of detonation H-NDs in aqueous media**. Coumarin probe will be used to study photoactivity of NDs including:

- quantification of HO<sup>•</sup> and electron production
- effect of the surface chemistry (oxygen, hydrogen and sp<sup>2</sup>-terminated)
- effect of the activation energy (X-ray: 17.5 keV and gamma: 1.17 MeV)
- effect of the source of detonation NDs

However, before undertaking any experiments related to photochemical activity of H-NDs, the focus will be on production of modified NDs toward homogeneous surface chemistry.

**Chapter 2** will deal with physical methods used to obtain various surface terminations of commercially produced detonation NDs. Thermal annealing under air, plasma and thermal hydrogenation, and annealing under vacuum will be performed under optimized and controlled conditions.

Following the physical surface activation, properties of such modified NDs with respect to native material will be probed and characterized by various complementary techniques allowing to assess:

4. The quality of crystallographic structure via Transmission Electron Microscopy (TEM) and Raman Spectroscopy
5. The chemical composition via Fourier Transform Infrared Spectroscopy (FTIR)
6. The level of metallic and non-metallic impurities probed by Inductively Coupled Plasma Mass Spectroscopy (ICP-MS).

Hence the experiments with NDs will be conducted in water, **Chapter 3** will investigate the colloidal properties of NDs with respect to their surface chemistry to determine which parameters are governing the colloidal stability. Optimization of the hydrosol preparation parameters and characterization protocol allowed to conduct a comparative study focusing on the specific interaction of water molecules with the surface of NDs. Short-term (< 24 h) and long-term (50 – 90 days) colloidal stability of such stabilizer-free ND suspensions will be investigated.

**Chapter 4** will present results related to the behavior of modified NDs under irradiation. The production of HO<sup>•</sup> radicals will be measured under X-rays and Gamma-rays with respect to their surface chemistry (oxidized, hydrogenated and sp<sup>2</sup>-C terminated). The detection of HO<sup>•</sup> radicals will be realized in the presence of the chemical probe – Cou sensitive to the presence of HO<sup>•</sup> radicals. In parallel, solvated electrons will be probed by the mean of a gaseous mixture – N<sub>2</sub>O/O<sub>2</sub> acting as electron scavengers.

## Bibliography

1. Barnard, A. S. Diamond standard in diagnostics: nanodiamond biolabels make their mark. *Analyst* **134**, 1751–64 (2009).
2. Chow, E. K. *et al.* Nanodiamond therapeutic delivery agents mediate enhanced chemoresistant tumor treatment. *Sci. Transl. Med.* **3**, 73ra21 (2011).
3. Schirhagl, R., Chang, K., Loretz, M. & Degen, C. L. Nitrogen-Vacancy Centers in Diamond: Nanoscale Sensors for Physics and Biology. *Annu. Rev. Phys. Chem* **65**, 83–105 (2014).
4. Grall, R. *et al.* Impairing the radioresistance of cancer cells by hydrogenated nanodiamonds. *Biomaterials* **61**, 290–298 (2015).
5. Petit, T. *et al.* Use of nanodiamonds for generating free radicals for therapeutic purposes under radiation. WO/2014/009930 *International Patent* (2013).
6. Gao, X. *et al.* Water-induced negative electron affinity on diamond (100). *J. Phys. Chem. C* **112**, 2487–2491 (2008).
7. Bolker, A., Saguy, C. & Kalish, R. Transfer doping of single isolated nanodiamonds, studied by scanning probe microscopy techniques. *Nanotechnology* **25**, 385702 (2014).
8. Zhu, D., Zhang, L., Ruther, R. E. & Hamers, R. J. Photo-illuminated diamond as a solid-state source of solvated electrons in water for nitrogen reduction. *Nat. Mater.* **12**, (2013).
9. Hamers, R. J. & Bandy, J. Atmospheric-pressure photoelectron emission from H-terminated and amino-terminated diamond; Atmospheric-pressure photoelectron emission from H-terminated and amino-terminated diamond. *Phys. Status Solidi A* **213**, 2069–2074 (2016).
10. Zhang, L., Zhu, D., Nathanson, G. M. & Hamers, R. J. Selective photoelectrochemical reduction of aqueous CO<sub>2</sub> to CO by solvated electrons. *Angew. Chemie - Int. Ed.* 9746–9750 (2014).
11. Zhu, D., Bandy, J. A., Li, S. & Hamers, R. J. Amino-terminated diamond surfaces: Photoelectron emission and photocatalytic properties. *Surf. Sci.* **650**, 295–301 (2016).
12. Zhang, L. & Hamers, R. J. Photocatalytic reduction of CO<sub>2</sub> to CO by diamond nanoparticles. *Diam. Relat. Mater.* **78**, 24–30 (2017).
13. Le Caër, S. Water Radiolysis: Influence of Oxide Surfaces on H<sub>2</sub> Production under Ionizing Radiation. *Water* **3**, 235–253 (2011).
14. Gomes, A., Fernandes, E. & Lima, J. L. Fluorescence probes used for detection of reactive oxygen species. *J. Biochem. Biophys. Methods* **65**, 45–80 (2005).
15. Newton, G. L. & Milligan, J. R. Fluorescence detection of hydroxyl radicals. *Radiat. Phys. Chem.* **75**, 473–478 (2006).
16. Sicard-Roselli, C. *et al.* A New Mechanism for Hydroxyl Radical Production in Irradiated Nanoparticle Solutions. *Small* **10**, 3338–3346 (2014).



# Chapter 2

## Characterization of nanodiamonds

### Summary

---

<b>2.1 Introduction</b> .....	<b>15</b>
<b>2.2 Surface modifications of detonation nanodiamonds</b> .....	<b>15</b>
2.2.1 Materials .....	16
2.2.2 Thermal annealing under air.....	16
2.2.3 Microwave plasma hydrogenation .....	17
2.2.4 Thermal annealing under hydrogen .....	18
2.2.5 Vacuum annealing.....	19
2.2.6 Summary .....	20
<b>2.3 Fourier Transform Infrared Spectroscopy</b> .....	<b>21</b>
2.3.1 As-received detonation nanodiamonds.....	21
2.3.1.1 Effect of sample drying .....	22
2.3.2 Air annealed nanodiamonds.....	23
2.3.3 Plasma hydrogenated nanodiamonds .....	25
2.3.4 Hydrogen annealed nanodiamonds.....	27
2.3.5 Vacuum annealed nanodiamonds .....	28
2.3.6 Summary .....	30
<b>2.4 Raman Spectroscopy</b> .....	<b>30</b>
2.4.1 Surface-modified nanodiamonds.....	30
2.4.2 Summary .....	32
<b>2.5 Inductively Coupled Plasma Mass Spectrometry</b> .....	<b>32</b>
2.5.1 As-received nanodiamonds .....	33
2.5.2 Surface modified nanodiamonds.....	34
2.5.3 Summary .....	36
<b>2.6 Transmission Electron Microscopy</b> .....	<b>37</b>
2.6.1 As-received nanodiamonds .....	37
2.6.2 Air annealed nanodiamonds.....	39

---

2.6.3 Plasma hydrogenated nanodiamonds .....	39
2.6.4 Hydrogen annealed nanodiamonds.....	40
2.6.5 Vacuum annealed nanodiamonds .....	41
2.6.6 Summary .....	42
<b>Bibliography .....</b>	<b>43</b>

---

## 2.1 Introduction

The following chapter provides information about various types of modifications used to change the physicochemical composition of NDs under well-controlled and reproducible conditions. The detailed description of the apparatus used for thermal annealing under air, plasma and hydrogen annealing, and vacuum annealing of detonation NDs is presented and discussed. The parameters applied were carefully chosen based on literature available in the diamond field including long-term expertise and experimental experience shared among researchers from the Diamond Sensors Laboratory.

Secondly, the physicochemical properties and purity of as-received and surface-modified NDs with respect to different sources of detonation NDs are discussed. Complementary techniques will be used to probe the core and the surface of NDs while assuring optimized experimental parameters. Bearing in mind the nanometric size of NDs, a probability of inducing critical, structural damage through characterization is higher as compared to larger scale materials and needs to be eliminated. To avoid such effects, softer Transmission Electron Microscopy (TEM) and Raman Spectroscopy conditions will be applied. Finally, the interaction between detonation NDs and their external environment (e.g. water, air atmosphere) are probed with respect to their surface chemistry.

Inductively Coupled Plasma Mass Spectrometry (ICP-MS) will be used to estimate the contamination of samples, Raman Spectroscopy, and Transmission Electron Microscopy (TEM) will probe structural properties and hybridization of carbon. Surface chemistry of NDs will be analyzed via Fourier Transform Infrared Spectroscopy (FTIR).

## 2.2 Surface modifications of detonation nanodiamonds

The inhomogeneous surface chemistry of as-received detonation NDs limits their possible bioapplications e.g. as nanocarriers<sup>1</sup>, radiosensitizers<sup>2</sup> or imaging agents<sup>3</sup>. As-received NDs are mostly covered by amorphous carbon, graphite shells<sup>4</sup>, and various oxygen-containing groups such as ethers, ketones, hydroxyls, and carboxylic acids<sup>5</sup>. Their initial surface chemistry is highly dependent on the purification steps which differ from one source to another. The different reactivity of surface functional groups limits the possibility of direct functionalization due to uncontrolled surface chemistry. The homogenization of the surface terminations helps to overcome these limitations while opening doors toward functionalization of NDs under more controlled conditions which may also limit their toxicity<sup>6,7</sup>. Different pathways have been explored by the scientists to better understand and control the complex chemistry of the raw NDs<sup>8</sup>. Herein, the physical surface modifications via plasma and annealing conditions used during this Ph.D. work are presented.

### 2.2.1 Materials

PlasmaChem GmbH company was chosen as the main supplier of the detonation NDs. Germany-based brand provides extra-pure NDs (grade G-02, purity > 99 %) and low ash content (< 0.1 %). According to the quality certificate given by the producer, the NDs have an average size between 4 – 6 nm with a specific surface area (SSA) > 350 m<sup>2</sup>.g<sup>-1</sup>, as measured by BET, and density: ca. 3.18 g.cm<sup>-3</sup>. (Appendix, section A.1)

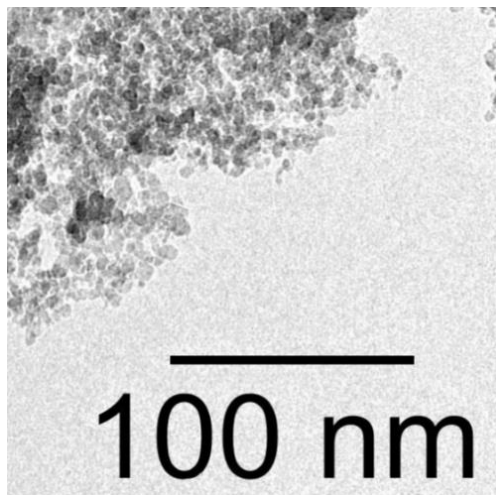


**Figure 2.1** – TEM micrograph of PlasmaChem detonation NDs. (source: PlasmaChem GmbH)

The second type of detonation NDs was kindly provided by Olga Shenderova from Adamas Nanotechnologies (USA). Particles (RuD150) had an average diameter of ~5 nm and were oxidized because of post-synthesis purifications. These NDs were not commercially available.

The last type of uncommercial source of NDs was given by Eiji Osawa from Nanocarbon Research Institute Co. in Japan. The typical primary size of NDs was within 3 - 6 nm range with well-defined diamond core and amorphous shell<sup>9</sup>. The same source of detonation NDs was previously used by the former Ph.D. student from the LCD laboratory - Tristan Petit who also worked on surface modifications of NDs<sup>10</sup>.

### 2.2.2 Thermal annealing under air

Annealing of NDs under controlled temperature in the air atmosphere was performed. Such treatment reduces the influence of the outer shell by removing amorphous and sp<sup>2</sup> carbon from the surface while promoting the formation of COOH groups among other oxygen-related functions<sup>11,12,13,14</sup>.

Technically, NDs provided by PlasmaChem and Adamas Nanotechnologies (100 - 150 mg) were manually milled with mortar and pestle prior to the oxidative treatment. NDs were then placed in a long alumina crucible (Al<sub>2</sub>O<sub>3</sub>, maximum working temperature = 1200 °C). Tubular furnace Carbolite Gero, equipped with silicon carbide heating elements, was used. Thermal annealing of NDs was carried out for 1 h 30 min by introducing and removing the crucible

when the oven is set at 550 °C. The temperature and duration of the treatment were carefully chosen after several tests, as the treatment has to be strong enough to oxidize the surface without etching completely the material<sup>11,15</sup>. We also paid attention to parameters like the amount of NDs in the crucible and the thickness of the NDs layer. At the end of the process, the crucible containing NDs was removed from the oven and left to cool down. Typically, introducing 150 mg of NDs in the oven, we collected 30 mg at the end of the process. Modified NDs were then transferred into a glass vial, tightly closed and stored in an ambient temperature. The dry powder was used for further experiments.



**Figure 2.2** – Picture of Carbolite Gero tube furnace used for thermal annealing of NDs under air atmosphere.

The air oxidized NDs will be used as a reference type of material for colloidal properties and irradiation experiments presented in Chapter 3 and 4, respectively.

### 2.2.3 Microwave plasma hydrogenation

The homogenization of the NDs surface with hydrogen termination using a microwave plasma has been studied for a long time in the laboratory, with the first published work in 2010<sup>8</sup>. This approach is based on a home-made chemical vapor deposition (MPCVD) set-up<sup>4,10</sup>. Such a treatment reduces all oxygenated surface terminations while promoting the creation of C-H groups at the NDs surface, as confirmed by the FTIR study (section 2.3). NDs provided by PlasmaChem, Adamas Nanotechnologies and Nanocarbon Research Institute Co., were hydrogenated using the same method.

Manually milled NDs powder (40 - 50 mg) was placed in a quartz tube and transferred into the microwave waveguide cavity connected to a microwave generator working at 2.45 GHz produced by Sairem (model: GMP G3, 2 kW) industry. The quartz tube (HSQ300) used is transparent to microwaves and resistant to very high temperatures without degradation. After closing the tube, pumping of the system was carried out for 1 h (down to  $1 \times 10^{-2}$  mbar). High-quality hydrogen gas (6.0, purity  $\geq 99.9999\%$ ), with a flow of 10 sccm, was then injected into the tube. The pressure measured by the automatic controller was stabilized at 12 mbar and the microwave alimentation was turned on. The microwave power of 250 W was applied

to decompose the H<sub>2</sub> gas into highly-reactive atomic hydrogen under plasma conditions. When the plasma conditions were stable (no changes in visual appearance, temperature, density or electric field), hydrogenation of NDs was continued for 20 min followed by 10 min of exposure to hydrogen flow. Post-plasma hydrogen treatment helps to saturate the dangling bonds at the surface of NDs with hydrogen while reducing the possible recombination with oxygen after exposure to air. After the MPCVD treatment, the quartz tube was removed from the microwave cavity and modified NDs were placed in a glass vial, closed and stored in ambient conditions. The same conditions were applied to all types of detonation NDs presented in the manuscript.

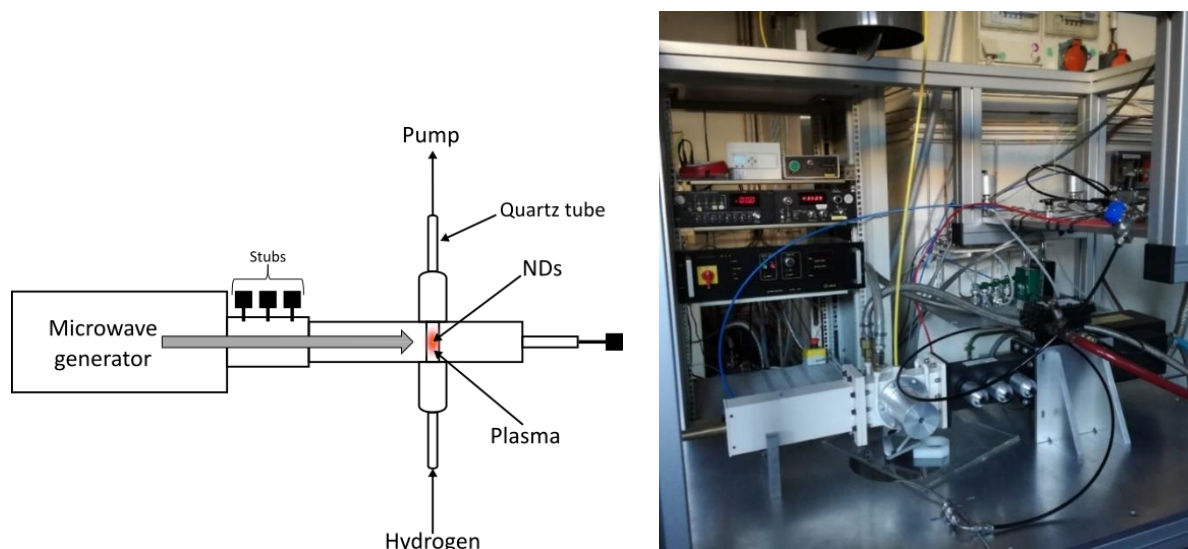


**Figure 2.3** – Scheme (left) and picture (right) of the MPCVD experimental set-up used for plasma hydrogenation of detonation NDs.

### 2.2.4 Thermal annealing under hydrogen

The thermal annealing under hydrogen constitutes an alternative to MPCVD to reduce oxygen groups present at NDs surface<sup>16,17,18</sup>. This technique is also used by colleagues from the Tritium Labelling Laboratory (CEA Saclay), who aim to label NDs with hydrogen isotopes like deuterium and tritium<sup>19</sup>. While hydrogen annealing is usually performed under flow conditions, they developed an alternative approach to realize the same treatment in a closed system for safety reasons. Hydrogen annealed NDs used in this manuscript were thus provided by Emilie Nehlig from the Tritium Labelling Laboratory. Here is a short description of the system:

Detonation NDs supplied by PlasmaChem and Adamas Technologies were manually milled and used for the thermal hydrogenation. 30 - 35 mg of dry NDs powder were treated each time and placed in a quartz flask. The vacuum was achieved for 3 h of dynamic pumping ( $1 \times 10^{-5}$  mbar) and then loaded with H<sub>2</sub> gas (200 - 250 mbar) (Figure 2.5 - left). Annealing was performed for 1 h at 550 – 560 °C. During the treatment, the system is connected to a cold trap to condense the vapors. After hydrogenation, the quartz flask was closed, and the tubular oven was removed. The NDs were placed in a glass vial and stored at an ambient temperature.

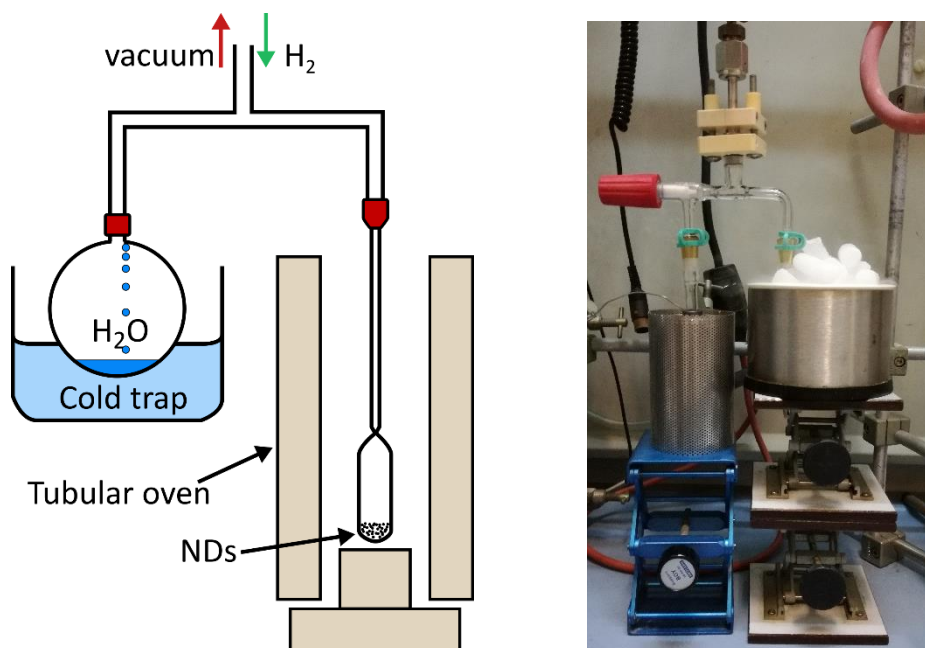


**Figure 2.4** – Scheme (left) and picture (right) of the experimental set-up used for thermal hydrogenation of detonation NDs.

### 2.2.5 Vacuum annealing

The last type of modification was performed via annealing under secondary vacuum aiming to induce  $sp^2$  reconstruction on the surface of detonation NDs. PlasmaChem NDs (140 – 150 mg) were manually milled and placed in a small alumina crucible. The crucible was covered and transferred into a furnace equipped with a turbomolecular vacuum pump used for vacuum annealing ( $< 10^{-8}$  mbar) of a diamond. The vacuum chamber heats up due to a heating element (brand: Ceramisis) in size of 2 inches made of graphite covered with a ceramic. The heating element temperature is measured by a thermocouple (range of  $-200$  °C to  $+1350$  °C) whereas the sample's temperature is measured indirectly by an infrared pyrometer (brand: Impac, model: IGA 140) which operates between  $250$  °C to  $1350$  °C.

The crucible with NDs was placed on the heating plate next to the piece of silicon which allows the pyrometer to measure the temperature. The NDs were treated via annealing under vacuum ( $1.0 \times 10^{-6}$  mbar) at various temperatures and time conditions: 1 h /  $750$  °C, 2 h /  $750$  °C, 1 h /  $850$  °C and 2 h /  $850$  °C. Similar studies were previously performed in LCD laboratory by T. Petit and co-workers (2011) investigating early stages of surface graphitization of detonation NDs. Such conditions assure decomposition of oxygen-containing groups and  $CH_x$  groups which decompose at  $300 - 900$  °C and  $700 - 1150$  °C, respectively<sup>20</sup>.

After vacuum annealing, the chamber was brought back to ambient pressure, the NDs sample was cooled down and the crucible was transported into the fume cupboard. The dry powder was placed in a glass vial and stored at ambient temperature.

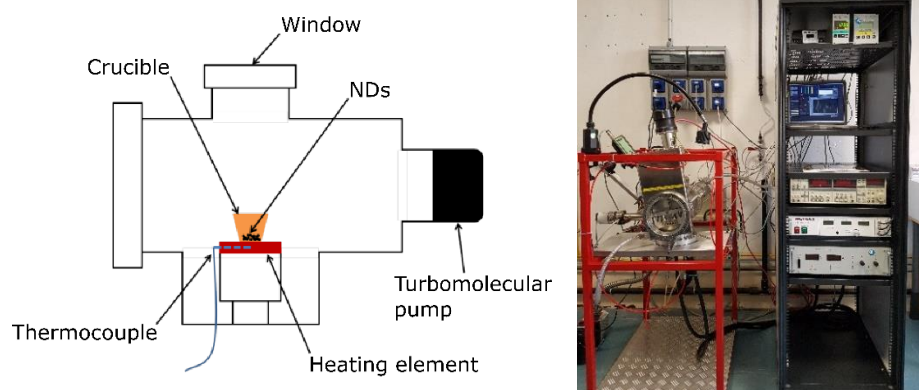


**Figure 2.5** – Scheme (left) of the chamber and picture (right) of the experimental set-up used for thermal annealing of detonation NDs under secondary vacuum.

### 2.2.6 Summary

Three sources of detonation NDs were modified toward surface chemical homogenization: PlasmaChem GmbH (commercial), Adamas Nanotechnologies and Nanocarbon Research Institute Co. (non-commercial). Air annealing, plasma and thermal hydrogenations, and vacuum annealing treatment were applied using specific conditions listed in the table below.

Surface modification	Mass (mg)	Time (min)	Temperature (°C)	Power (W)	Pressure (mbar)	H <sub>2</sub> flow/pressure
Air annealing	~150 mg introduced 30 mg collected	90	550	n/a	n/a	n/a
Plasma hydrogenation	40 - 50	20	estimated 800 <sup>1</sup>	250	12	10 sccm
Thermal hydrogenation	30 - 35	60	550 - 560	n/a	200-250	static
Vacuum annealing	140 - 150	60	750	n/a	$1 \times 10^{-6}$	n/a
		120	750			
		60	850			
		120	850			

**Table 2.1** – Summary of treatment conditions used for surface modifications of detonation NDs (various sources).

<sup>1</sup> Fiber-optic temperature measurement

## 2.3 Fourier Transform Infrared Spectroscopy

Fourier Transform Infrared Spectroscopy (FTIR) provides information about the surface chemistry of the investigated NDs. Their diamond core is transparent to infrared but their rich external chemistry ensures sensitivity to various functional groups (mostly oxygen and hydrogen related), exalted by their high surface area ( $> 350 \text{ m}^2\cdot\text{g}^{-1}$ ). With our chosen experimental approach (transmission through KBr pellet), FTIR technique will only be used qualitatively. However, the technique itself is simple, fast and accurate, thereby allowing monitoring of changes in surface chemical compositions after several different chemical and physical modifications.

The FTIR spectra were measured in transmission mode using a ThermoNicolet 8700 spectrometer. KBr pellets ( $\sim 150 \text{ mg}$ ) were prepared with ca. 2 wt.% of NDs, dried or not within the spectrometer by the  $\text{N}_2$  flow (for technical details see Appendix, section A.6).

### 2.3.1 As-received detonation nanodiamonds

Three sources of detonation NDs were characterized via FTIR spectroscopy at room temperature, such as PlasmaChem, Adamas Nanotechnologies, and NanoCarbon Research Institute.

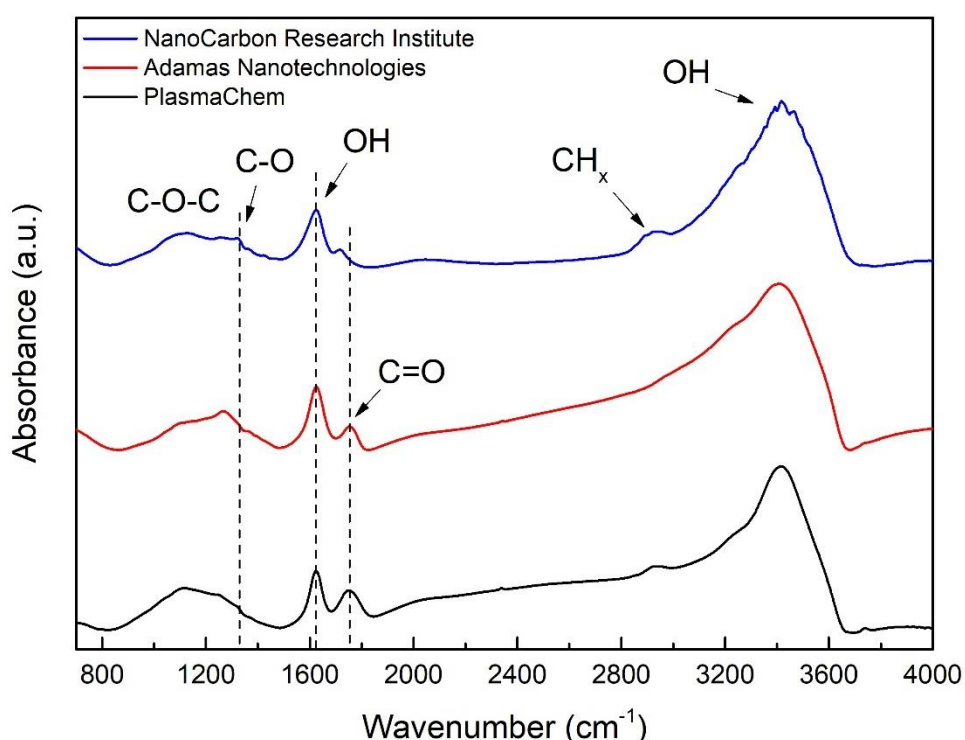


**Figure 2.6** – Absorbance spectra of native PlasmaChem (black), Adamas Nanotechnologies (red), and NanoCarbon Research Institute (blue) NDs taken immediately after pellet preparation, without any drying. Spectra were background-corrected.

To begin with, as the samples were not dried, the signature of adsorbed water on the NDs or in the KBr is clearly visible on all samples with the two contributions of OH stretching and bending modes at  $1635\text{ cm}^{-1}$  and around  $3400\text{ cm}^{-1}$ , respectively. The effect of drying will be presented in the next paragraph.

Apart from water-related bands, some differences between various sources can be observed. Concerning the fingerprint area between  $800$  and  $1400\text{ cm}^{-1}$ , which correspond to the superposition of structural defects and diverse contributions including C-O related groups like ethers (around  $1100\text{ cm}^{-1}$ ) or alcohols ( $1200 - 1300\text{ cm}^{-1}$ ), the NDs provided by Adamas differ slightly compared to the two other sources.

More important is the area above  $1635\text{ cm}^{-1}$  with the contributions related to C=O stretching modes, associated with ketones, carboxylic acids or anhydrides functionalities. Downshifted to  $1720\text{ cm}^{-1}$  and of weak intensity for particles provided by NanoCarbon Research Institute, this band is clearly visible and of the same intensity at  $1750\text{ cm}^{-1}$  for particles provided by PlasmaChem and Adamas Nanotechnologies.

The region between  $2800 - 3000\text{ cm}^{-1}$  with multiple-bands appears for PlasmaChem and NanoCarbon Res. Inst. but seems not to be present for Adamas particles. These bands come from C-H<sub>x</sub> stretching modes<sup>21,22</sup> of C-H<sub>2</sub> and C-H<sub>3</sub> and can be attributed to alkyl functionalities at the surface of the NDs, or surface contamination with amorphous carbon. Note that the presence of water in the sample and the related OH stretching modes around  $3400\text{ cm}^{-1}$  partially hides this part of the spectrum.

To sum up, all sources of detonation NDs have oxygen-containing groups on the surface, in different proportion, which can be seen either in the fingerprint area or around  $1750\text{ cm}^{-1}$ . In addition to that, the PlasmaChem and NanoCarbon Research Institute exhibit C-H<sub>x</sub> features which are not observed for ND particles from Adamas Nanotechnologies.

### 2.3.1.1 Effect of sample drying

FTIR spectra of NDs often have a high content of water which is quickly adsorbed on the surface when particles are exposed to air atmosphere<sup>23,24</sup>. The high content of adsorbed water on the surface can easily disturb or mask the signal coming from other surface functional groups not related to H<sub>2</sub>O. Even though the affinity toward water molecules of NDs is high, adsorbed water layer can be progressively reduced via drying procedure which leads to its desorption. A very simple method of drying of the FTIR samples is to keep them at room temperature under a flow of an inert dry gas (e.g. nitrogen<sup>25</sup>) for a few days. If water is not completely desorbed by this mean, a spectrum is still ameliorated. Note that a more effective method will be to expose the KBr pellet *in-situ* at elevated temperature (above  $25^\circ\text{C}$  up to  $80^\circ\text{C}$ ) and under vacuum<sup>4</sup>. However, using this technique, some modification of the surface chemistry is suspected and for this reason, abandoned.

To show the effect of a simple drying on FTIR spectrum, as-received PlasmaChem sample, which was presented in the previous paragraph, was left under nitrogen flow for 48 h at room

temperature. The resulting spectrum is plotted together with the one obtained prior to the drying step.

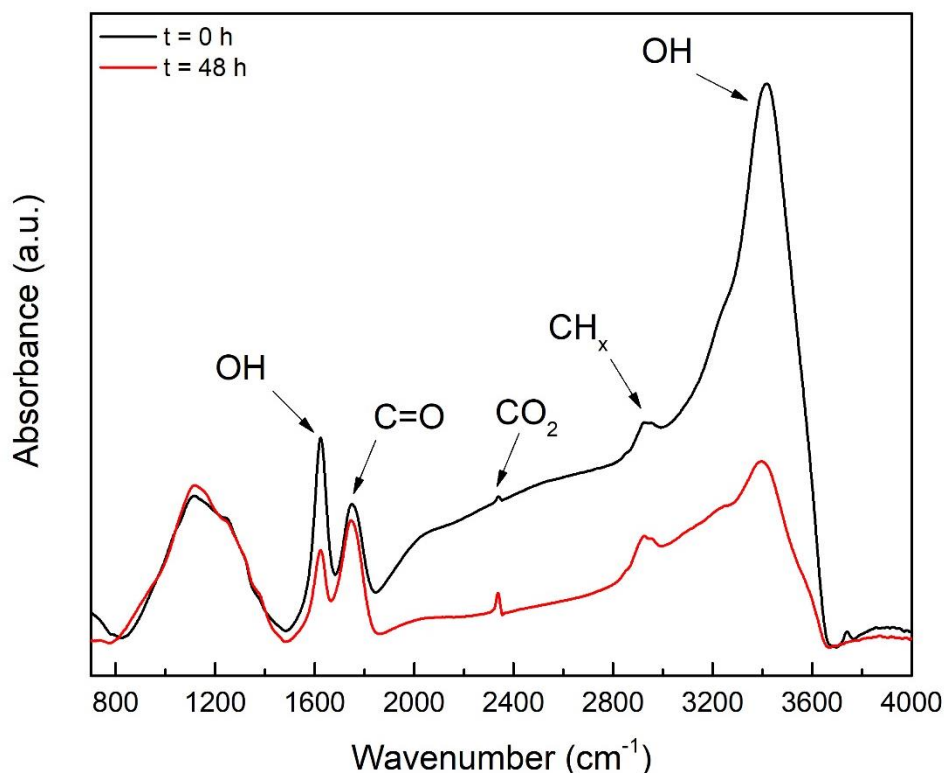


**Figure 2.7** – Absorbance FTIR spectra of native PlasmaChem NDs taken immediately after pellet preparation (black) followed by drying under nitrogen flow (red). Normalization of the fingerprint area has been applied. Spectra were also background-corrected.

It can be noticed that after 48 h there has been a reduction in the signal related to the O-H stretch at  $3400\text{ cm}^{-1}$  and the  $\text{H}_2\text{O}$  bending mode at  $1630\text{ cm}^{-1}$ . As a consequence, features around  $1730 - 1750\text{ cm}^{-1}$  (C=O stretching) and  $2800 - 3000\text{ cm}^{-1}$  (C- $\text{H}_x$  vibrations) are more pronounced. The drying does not affect the fingerprint area (single bonds around  $900 - 1500\text{ cm}^{-1}$ ) which are specific for each type of NDs (the peak around  $2230\text{ cm}^{-1}$  is due to the vibration of  $\text{CO}_2$ )<sup>26</sup>.

For the following experiments, all samples were dried for at least 24 h under nitrogen flow at room temperature.

### 2.3.2 Air annealed nanodiamonds

The first modification of detonation NDs involved air annealing, performed on PlasmaChem and Adamas Nanotech. The pellets were left for drying inside FTIR spectrometer for 24 h under nitrogen flow.

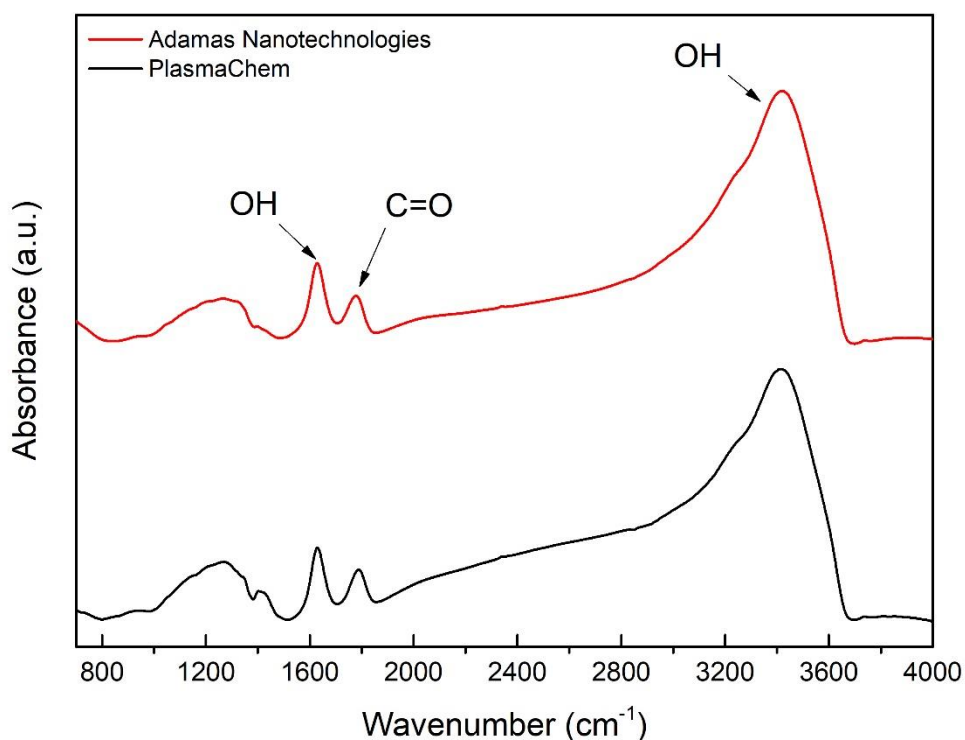


**Figure 2.8** – Absorbance FTIR spectra of air annealed PlasmaChem (black) and Adamas Nanotechnologies (red) detonation NDs. Spectra were background-corrected.

At the first glance, it can be seen that the spectrum of the NDs produced by Adamas Nanotechnologies did not evolve strongly after oxidative treatment (Figure 2.8). The native particles already possess a high content of C=O groups (1730 - 1750  $\text{cm}^{-1}$ ), as shown in the first part of the FTIR characterization. The same features as described for the native sample, are still present on the surface of NDs, only the fingerprint area evolves slightly. In terms of PlasmaChem NDs, the suppression of the C-H<sub>x</sub> vibrations region (2800 - 3000  $\text{cm}^{-1}$ ) is observed after thermal oxidation.

After further drying of PlasmaChem particles (Figure 2.9), the C=O stretching band (peak around 1730 - 1750  $\text{cm}^{-1}$ ) is enhanced as compared to the water signature (OH bending at 1630  $\text{cm}^{-1}$ ). Notably, some weak C-H vibrations (2800 - 3000  $\text{cm}^{-1}$ ) can now be observed, but much less intense than for native PlasmaChem NDs. The O-H stretching bands at 3400  $\text{cm}^{-1}$  and 1630  $\text{cm}^{-1}$  are present due to the use of an incomplete drying method. However, the O-H stretch at 3400  $\text{cm}^{-1}$  could also come from the COOH content. The multiple-vibration in the fingerprint region 900 - 1500  $\text{cm}^{-1}$  are observed whereas the peak at 1100  $\text{cm}^{-1}$  can be related to single oxygen bond (C-O) present in CH<sub>2</sub>OH groups.

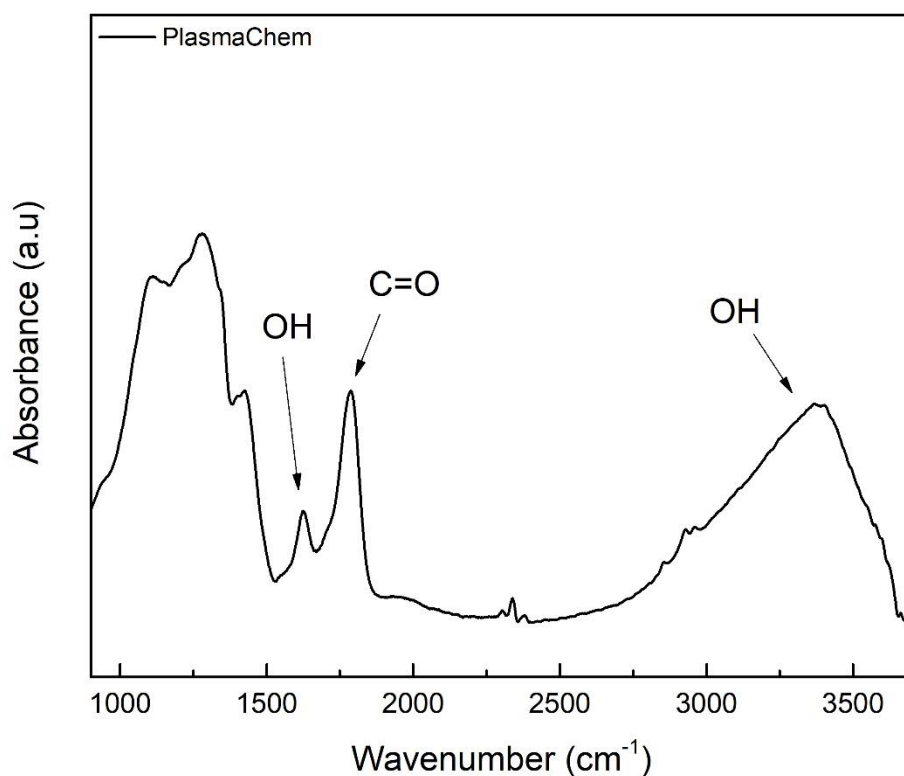


**Figure 2.9** – Absorbance FTIR spectrum of dried (48 h) air annealed PlasmaChem NDs. Spectrum was background-corrected.

To sum up, air annealing of NDs reduces the C-H<sub>x</sub> content originally present on the native NDs. Normalized to the fingerprint area, the amount of C=O does not seem to significantly increase. Thermal annealing does not modify the broad absorbance in the region 900 - 1500 cm<sup>-1</sup> associated with the fingerprint (wavenumber < 1500 cm<sup>-1</sup> representing bending vibrations characteristic for the NDs). O-H groups are detected on the surface coming either from adsorbed water and hydroxylic groups (C-OH).

### 2.3.3 Plasma hydrogenated nanodiamonds

Plasma treatment of NDs was carried out for 20 min under hydrogen flow of 10 sccm and microwave generator power of 250 W (at 2.45 GHz). The detonation NDs provided by PlasmaChem, Adamas Nanotechnologies, and NanoCarbon Research Institute were modified under the same hydrogenation conditions. KBr pellets were prepared immediately after the modification and dried under nitrogen flow prior the FTIR analysis.

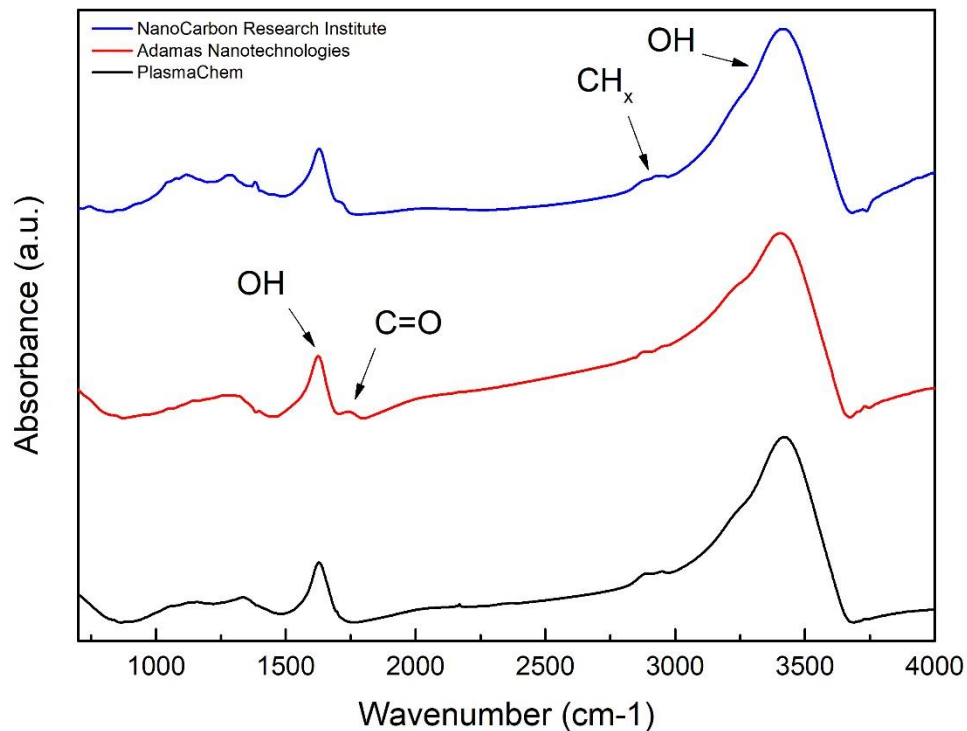


**Figure 2.10** – Absorbance FTIR spectra of plasma hydrogenated: PlasmaChem (black), Adamas Nanotechnologies (red), and NanoCarbon Research Institute (blue) detonation NDs. Spectra were taken after drying for 24 h under nitrogen flow, and background-corrected.

At first glance, a few differences between detonation NDs are clearly noticeable (Figure 2.10). The C=O content ( $1730 - 1750 \text{ cm}^{-1}$ ) is reduced for all samples. However, the Adamas samples still have the highest remaining amount of C=O groups present on the surface. The C-H<sub>x</sub> features are observed for all samples, but they are partially masked by the water adsorbed on the surface, which is still present after 24 h of drying.

The PlasmaChem sample was left for further drying under nitrogen flow (Figure 2.11). Indeed, the high content of adsorbed water may partially mask the effect of plasma modification where the hydrogenation is mainly evidenced by the loss of C=O groups ( $1750 \text{ cm}^{-1}$ ) and exaltation of C-H<sub>x</sub> stretching bands ( $2800 - 3000 \text{ cm}^{-1}$ )<sup>22</sup>. Further drying enhances the presence of C-H<sub>x</sub> groups and progressively reduces the O-H bands ( $3300$  and  $1050 \text{ cm}^{-1}$ ). However, the conditions used were not sufficient to completely remove the water content. These bands may also be related to the presence of hydroxylic groups on the surface<sup>27</sup>.

Looking at the spectrum of plasma H-NDs (PlasmaChem), two other features can be observed (Figure 2.11). Firstly, the OH band at  $1630 \text{ cm}^{-1}$  has a small shoulder around  $1718 \text{ cm}^{-1}$  which have been previously observed on polyfunctional NDs and H-NDs<sup>28</sup>. This band has been attributed to remaining carbonyl or lactone groups<sup>21,29</sup>. The second thing worth noticing is the shape of the C-H<sub>x</sub> band. Two local maxima are seen:  $2879 \text{ cm}^{-1}$  and  $2931 \text{ cm}^{-1}$  which have already been observed on other plasma H-NDs<sup>8</sup>. Notably, the feature at  $2931 \text{ cm}^{-1}$  is more

distinctive than the one at  $2879\text{ cm}^{-1}$  which is also in agreement with the previous study focused on plasma hydrogenation mechanism<sup>4</sup>.

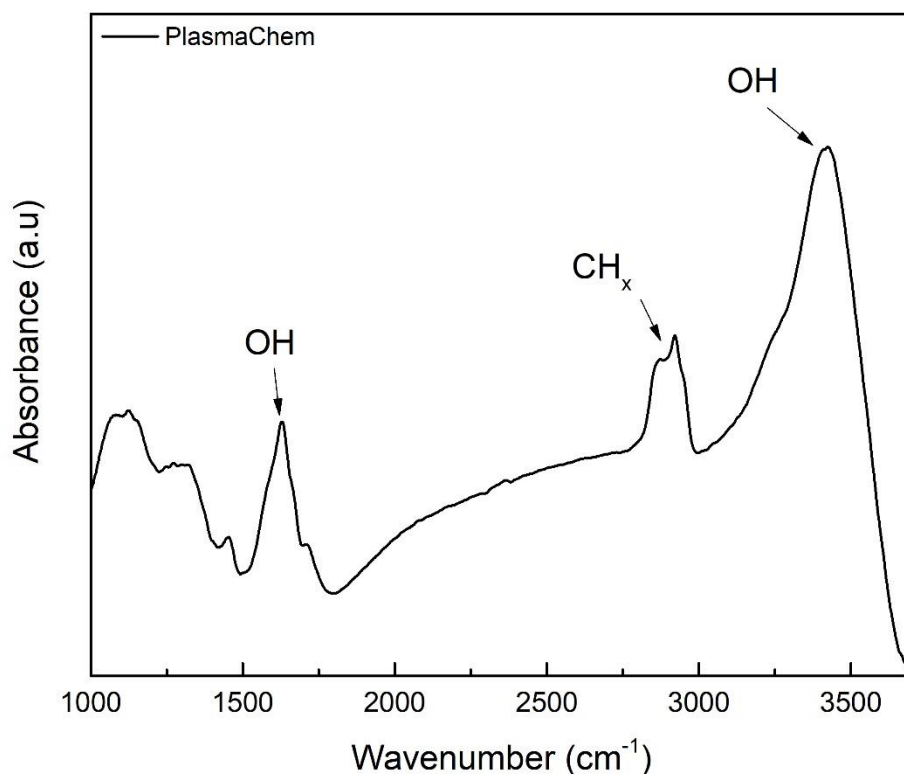


**Figure 2.11** – Absorbance FTIR spectrum of dried (72 h) plasma hydrogenated PlasmaChem NDs. The main bands of interest (oxygen and hydrogen related) are indicated on the spectrum.

In conclusion, plasma hydrogenation reduces the C=O content, whatever the initial source of detonation NDs. The same conditions of MPCVD treatment seem to be insufficient in terms of strongly oxidized Adamas particles (small amount of C=O around  $1730 - 1750\text{ cm}^{-1}$  is still present). The drying procedure reduces the adsorbed water content whereas the plasma treatment exalts the C-H<sub>x</sub> stretching bands. The C-H<sub>x</sub> band after plasma treatment has a unique shape with two local maxima.

#### 2.3.4 Hydrogen annealed nanodiamonds

The as-received PlasmaChem and Adamas Nanotechnologies NDs underwent another hydrogenation treatment via thermal annealing under hydrogen (1 h,  $550\text{ °C}$ ). The ND powder was mixed with KBr and left to dry for 48 hrs prior to the FTIR acquisition.

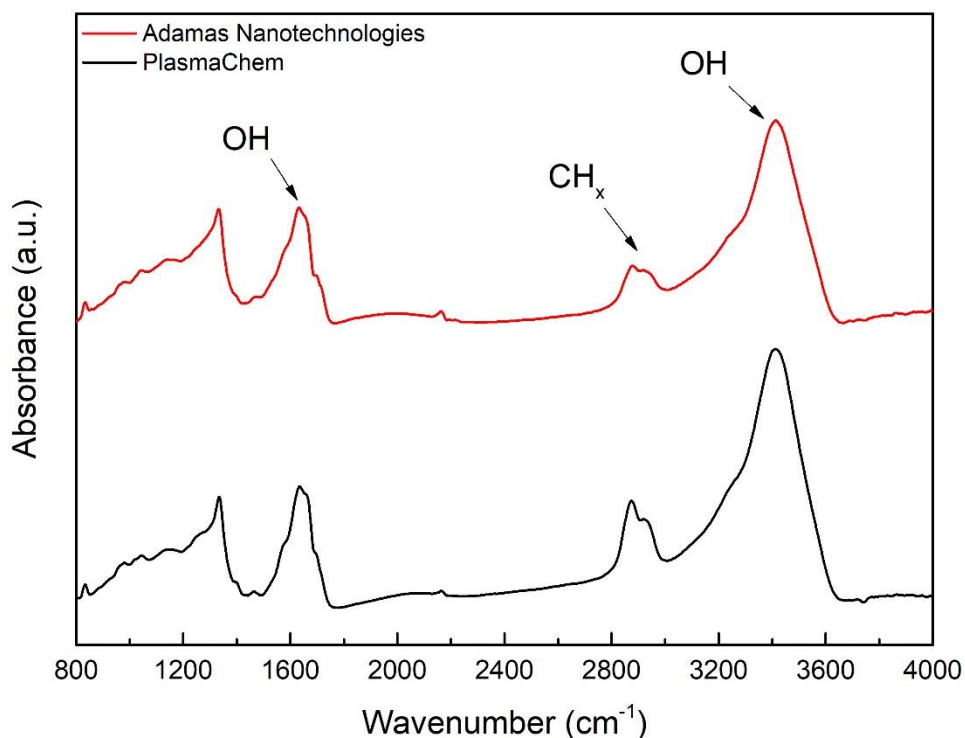


**Figure 2.12** – Absorbance FTIR spectra of hydrogen annealed PlasmaChem (black) and Adamas Technologies (red) NDs. Samples were dried for 48 h under nitrogen flow and spectra were recorded at room temperature.

The main confirmation of successful modification is the almost complete reduction of C=O groups ( $1730 - 1750 \text{ cm}^{-1}$ ) and the enhancement of C-H<sub>x</sub> (C-H, C-H<sub>2</sub>, C-H<sub>3</sub>) bands ( $2800 - 3000 \text{ cm}^{-1}$ )<sup>18</sup> (Figure 2.12). Moreover, the C-H<sub>x</sub> bands exhibit two distinctive peaks: around  $2879 \text{ cm}^{-1}$  and  $2925 \text{ cm}^{-1}$ , which have also been observed on plasma H-NDs<sup>8</sup>. They have previously been associated with C(111) and C(100) surfaces, respectively. However, the shifted positions ( $2870 \text{ cm}^{-1}$  and  $2940 \text{ cm}^{-1}$ ) may also come from size domain effect and polydispersity of detonation NDs<sup>22</sup>. Another interesting observation can be made by looking at the shape of the peak in the region between  $1500 - 1750 \text{ cm}^{-1}$  with 4 local maxima:  $1579 \text{ cm}^{-1}$ ,  $1630 \text{ cm}^{-1}$ ,  $1660 \text{ cm}^{-1}$ , and  $1695 \text{ cm}^{-1}$ . The latter can be attributed to remaining carbonyl or lactone groups<sup>21,29</sup>, as previously seen for plasma treated samples. The peak located at  $1630 \text{ cm}^{-1}$  is attributed to the OH bending modes of water, while the feature around  $1580 \text{ cm}^{-1}$  may be associated with some C=C bonds<sup>30</sup>.

In conclusion, the thermal hydrogenation of detonation NDs results in the reduction of oxygen content (C=O peak) and the modification/increase of C-H<sub>x</sub> bands. However, no obvious differences in chemical composition of PlasmaChem and Adamas particles can be seen.

### 2.3.5 Vacuum annealed nanodiamonds

The last surface treatment involves a thermal annealing of PlasmaChem NDs under vacuum. Various annealing conditions were applied, such as 1 h /  $750 \text{ }^\circ\text{C}$ , 2 h /  $750 \text{ }^\circ\text{C}$ , 1 h /  $850 \text{ }^\circ\text{C}$  and

2 h / 850 °C. Immediately after modification, the dry powder was mixed with KBr (2 wt.%) and left for drying prior the FTIR analysis.

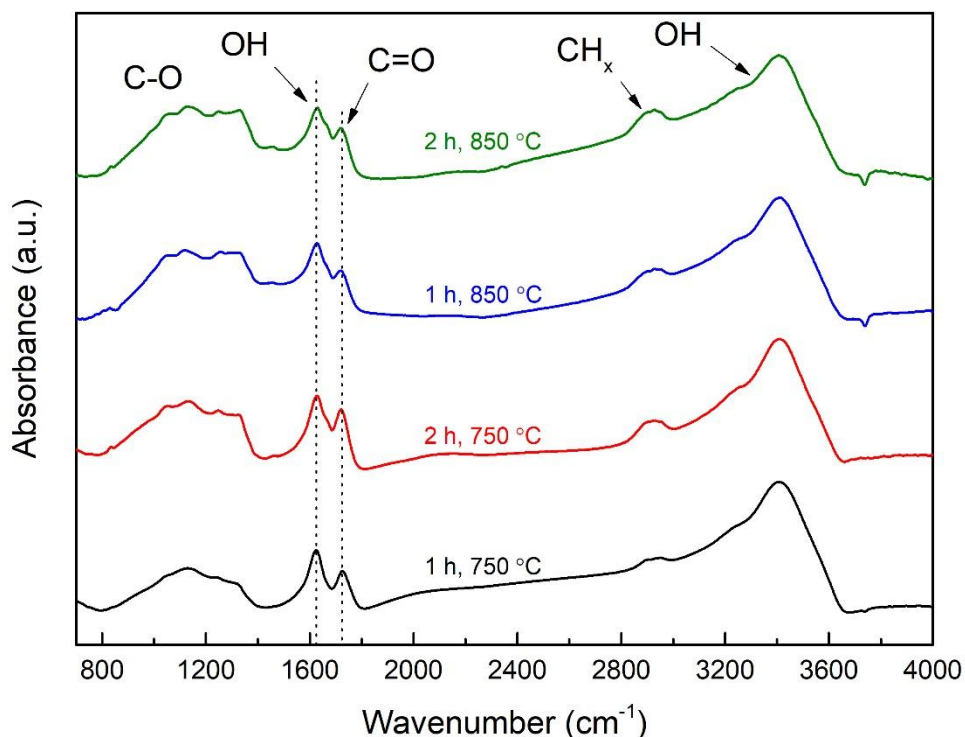


**Figure 2.13** – Absorbance FTIR spectra of vacuum annealed PlasmaChem NDs for 1 h at 750 °C (black), 2 h at 750 °C (red), 1 h at 850 °C (blue), and 2 h at 850 °C (green). Samples were dried for 48 h under nitrogen flow. Spectra were background-corrected and normalized to the fingerprint area.

Looking at the FTIR spectra obtained, the chemical surface chemistry on NDs treated under vacuum remains similar for all samples (Figure 2.13). The features previously described on the native PlasmaChem NDs are still observed with C-O contributions between 800 and 1300  $\text{cm}^{-1}$ , C-H<sub>x</sub> features between 2800 - 3000  $\text{cm}^{-1}$ , and C=O signature around 1730  $\text{cm}^{-1}$ . Nevertheless, small modifications can be detected by looking at the intensity of the C=O related peak (normalized to the fingerprint), with a slight decrease according to the strength of the treatment. Smooth exaltation of the C-H related bands is also noticeable after treatment in the harshest conditions.

In the literature, it is well-established that graphitization of detonation NDs' resulting in OLC structure takes place only when the temperature of thermal annealing under vacuum exceeds 1000 °C<sup>31</sup>. In our case, the temperature remains below 900 °C at which surface graphitic reconstructions have been reported to affect only the outer shell<sup>32</sup> while preserving the diamond core. Moreover, the highest temperature used (850 °C) was also insufficient to completely desorb the C=O groups, which can be easily seen from the FTIR spectrum, thereby supporting the previous statement. The FTIR method is not sufficient to give an answer about exact surface graphitic reconstruction occurring during each annealing condition.

### 2.3.6 Summary

- Native detonation NDs have similar surface chemistry
- Sample drying under nitrogen flow reduces the water adsorbed on the surface of NDs
- Air annealing reduces the C-H<sub>x</sub> groups and slightly increases the surface coverage with C=O, as seen for PlasmaChem and Adamas NDs
- Hydrogenation reduces significantly the C=O content. However, some small amount can still be detected when hydrogenation is performed at the same conditions on different sources of detonation NDs
- The shape of C-H<sub>x</sub> bands is different for plasma and thermally hydrogenated samples
- Vacuum annealing below a temperature of 850 °C does not drastically change the surface chemistry of native PlasmaChem NDs
- The findings presented in this part of the chapter are consistent with previously published works on thermally Ox-NDs, plasma and thermally H-NDs as well the vacuum annealed NDs<sup>17,33,13,4</sup>.

## 2.4 Raman Spectroscopy

The Raman Spectroscopy is a complementary technique to FTIR providing information about the carbon phase composition ( $sp^2$ - $sp^3$  content), the crystalline structure, and the homogeneity of carbon-materials<sup>34</sup>, e.g. nanodiamonds<sup>35</sup>. Surface modifications of NDs toward homogenization change the composition of the surface functional groups and can lead to soft-shell reconstructions (change in the  $sp^2$ - $sp^3$  ratio)<sup>9</sup>. The experimental conditions used for Raman analysis, which minimalizes any possible laser-induced effects (e.g. local sample heating and modification/damage due to high power density) of NDs, have been shown to be essential when monitoring the surface treatment of detonation NDs<sup>9</sup>. However, this technique is not fully sensitive to surface-functional groups of NDs and exact interpretation of Raman peaks is not always straightforward after modifications<sup>34</sup>.

### 2.4.1 Surface-modified nanodiamonds

Raman spectra of as-received, air annealed (1 h 30 min, 550 °C), plasma hydrogenated (250 W, 12 mbar, 20 min) and hydrogen annealed (1 h, 550 °C) PlasmaChem (ultra-pure, grade G-02) NDs were recorded at room temperature. Ultra-violet (UV) laser excitation (325 nm, HeCd laser) with low power density (< 200  $\mu$ W) was employed to avoid heating of NDs. Raman analysis was done by Michel Mermoux at LEPMI (Grenoble).

The main features on Raman spectra are located at 1328  $cm^{-1}$ , 1640  $cm^{-1}$  and 1750  $cm^{-1}$  (Figure 2.14). The first band (1328  $cm^{-1}$ ) is associated with the first order diamond Raman peak (C-C bonds in a tetrahedral structure of the diamond lattice)<sup>36</sup>. However, for detonation NDs, which exhibit size smaller than 10 nm, this diamond Raman peak is relatively weak, broad and downshifted compared to the pure diamond structure. Broadening and

downshifting of the peak position can be a consequence of nanometric particles' size and/or defected lattice structure. This has been previously explained by a phonon confinement effect<sup>9</sup>. Weak diamond peak intensity in NDs is attributed to the interaction of the diamond core ( $sp^3$ -C) with the soft-shell (e.g.  $sp^2$ -C, a-C)<sup>35</sup> present on the surface of NDs.

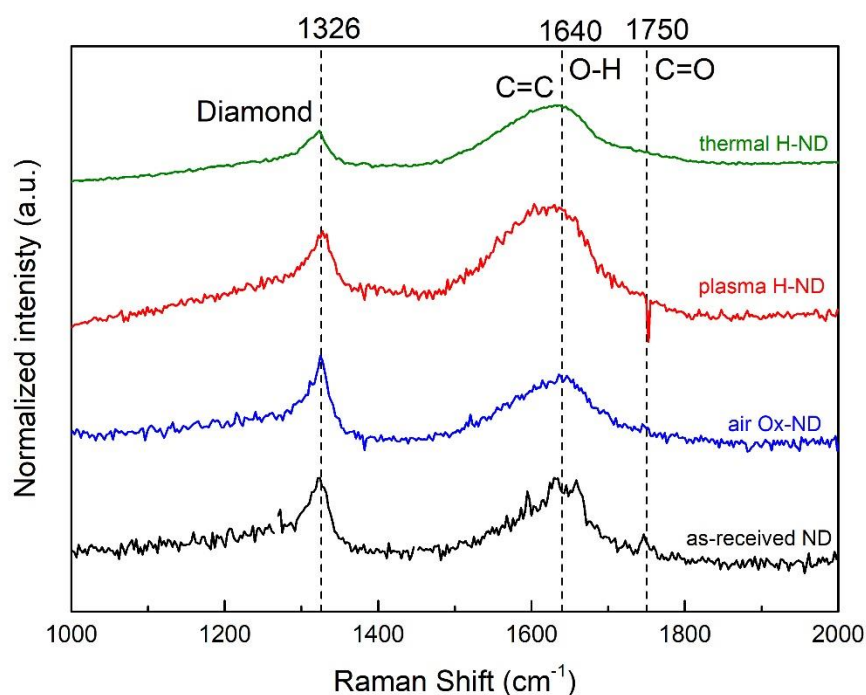


**Figure 2.14** – Raman spectra of PlasmaChem as-received (black), air annealed (blue), plasma (red) and thermally (green) hydrogenated NDs. Raman intensity was normalized on intensity with the main features (dashed lines) indicated. Measurements were performed at room temperature.

Features around  $1640\text{ cm}^{-1}$  correspond to G band as an analogy to  $sp^2$ -containing C-based materials (Figure 2.14). However, the band is very broad in all samples. In previous Raman study on detonation NDs, the G band has been demonstrated to represent a superposition of 3 peaks:  $sp^2$ -C band ( $1600\text{ cm}^{-1}$ ), O-H bending vibrations ( $1660\text{ cm}^{-1}$ ) and C=O stretching vibrations ( $1750\text{ cm}^{-1}$ )<sup>37,38,9</sup>. The position and the width of the G band seen on H-NDs (plasma and thermal) are much larger compared to as-received and Ox-NDs. Moreover, the band maximum is downshifted, especially for H-NDs, which can be associated with changes in the structure or surface chemical composition (partial surface graphitization induced either by the laser beam or hydrogen plasma treatment)<sup>9,34</sup>. The C=O vibrations can only be observed on as-received and air annealed NDs, whereas the band vanishes after plasma and thermal hydrogenation due to the reduction of oxygen-containing groups. The detection of C=O groups by Raman can be achieved if the content of oxygen-containing groups is between 12 – 14 % of the total surface atoms<sup>9</sup>. The reduction of C=O is also in agreement with the FTIR spectra of H-NDs (plasma, thermal). Unfortunately, Raman spectra of vacuum annealed NDs were not obtained due to time constraints. The Raman study performed is in agreement with the literature<sup>9,39,34,37</sup>.

In conclusion, we find that whatever the treatment, the diamond peak at  $1328\text{ cm}^{-1}$  remain unchanged which confirms that the core of the particle is not affected. This statement is important, as in this study we aim to probe only the effect of surface modification and not of the entire particle. On the other hand, the broadening and the downshift of the G band confirm that plasma or thermal annealing induces a strong modification of the surface, with some carbon reconstruction expected into  $\text{sp}^2$  hybridization. The presence of  $\text{sp}^2\text{-C}$  was evidenced by the TEM study of surface-modified NDs (section 2.6).

### 2.4.2 Summary

- Raman can be used to characterize effects of surface treatment on detonation NDs
- Spectra of as-received, air annealed, and hydrogenated NDs (plasma, thermal) have similar features and are similar in shape
- The first order diamond peak is still present after surface-modifications
- Peak broadening of the G band is observed after both hydrogenation methods
- Pure D band of  $\text{sp}^2\text{-C}$  is not observed on any sample characterized
- Surface functional groups such as C=O, O-H, and C=C are present on all samples
- The C=O band ( $1750\text{ cm}^{-1}$ ) is only observed on as-received and air annealed NDs.

## 2.5 Inductively Coupled Plasma Mass Spectrometry

The detonation synthesis produces soot containing NDs surrounded by a soft shell of non-diamond carbon ( $\text{sp}^2\text{-C}$ , a-C)<sup>40</sup> saturated with functional groups<sup>35</sup> and non-carbon impurities (metal and non-metal elements)<sup>41,42</sup>. These impurities mostly come from the production method and depend on the nature of detonation explosives, the material from the walls of the production chamber, and the detonator<sup>42</sup>. Metals (Si, Al, Fe, Ti, Cr, etc.) and non-metal elements (B, P, S, etc.) contents in detonation NDs may come up to 8 wt.%<sup>42</sup>. Amount and type of impurities can be partially reduced by post-productive purification steps which aim to isolate and clean the NDs from the synthetic detonation soot<sup>43</sup>. Methods of purification vary between the vendors but mostly involve wet chemistry (acid treatment: a dichromate-sulfuric acid mixture or superficial nitric acid)<sup>5</sup> and/or oxidative treatment (with gaseous ozone<sup>44</sup> or heating in air atmosphere) which may also introduce an additional contamination<sup>13</sup>. Information about the purity of detonation NDs is often neglected by the vendors and is rarely found in commercial quality certificates. However, the impurity content can be accurately measured by various analytical methods. Among many techniques (e.g. Neutron Activation Analysis – NAA) high-resolution Inductively Coupled Plasma Mass Spectrometry (ICP-MS) was chosen as it provides a fast and an excellent ion detection sensitivity (range from  $10^{-5}$  down to  $< 10^{-11}$  wt.% depending on elements). The technique detects up to 71 elements in low concentration water suspension ( $0.05 - 0.10\text{ mg.ml}^{-1}$ )<sup>42</sup>. Taking into account that impurities are mostly located in the outer shell<sup>45</sup>, a high concentration of metal / non-metal elements can be the main source of contamination and could even confer toxicity to NDs. Impurities

can reduce the NDs quality while affecting the final product of various surface modifications toward homogeneous surface chemistry<sup>46,47</sup>.

### 2.5.1 As-received nanodiamonds

ICP-MS analysis was performed on native detonation NDs purchased from PlasmaChem GmbH (Germany). As a comparison, non-commercial detonation NDs kindly provided by Olga Shenderova were also used. The NPs were suspended in water prior to the experiment and analyzed toward 19 elements (Al, Mn, Fe, Ni, Cu, Zn, Ag, In, Pb, Pd, Sn, Sb, Hf, B, Ti, Zr, Mo, Ta, W).

Element	PlasmaChem GmbH, grade G-02 ( $\mu\text{g}\cdot\text{g}^{-1}$ )	Adamas Nanotechnologies, RuD150 ( $\mu\text{g}\cdot\text{g}^{-1}$ )
Al	50.4	363.4
Mn	3.6	33.1
Fe	34.6	2324.5
Ni	2.3	104.8
Cu	5.6	472.8
Zn	368.7	50.6
Ag	1.0	no data
In	0.1	no data
Pb	0.8	4.3
Pd	no data	no data
Sn	11.7	no data
Sb	0.3	no data
Hf	no data	no data
B	243.1	318.1
Ti	25.8	48.5
Zr	1.0	1.2
Mo	1.3	1.8
Ta	no data	no data
W	7.0	1.7
<b>Total</b>	<b>744</b>	<b>3725</b>

**Table 2.2** – Comparison of major elemental impurities in native NDs from PlasmaChem GmbH (grade G-02) and non-commercial NDs from Adamas Nanotechnologies (RuD150). The total sum excludes elements with a missing value (no data).

At first glance (Table 2.2), differences in impurity levels can be observed between the two analyzed sources of detonation NDs. PlasmaChem NDs has an ultra-pure grade (G-02) with a purity > 99 % according to the data quality certificate (Appendix, section A.1). The total content of minor elements is ca. 5-times lower compared to RuD150 NDs which are not commercialized by the Adamas company.

Varying the source of NDs reveals how impurities, and especially metallic content, can change. For instance, the total content of the main metallic elements such as Al, Mn, Fe, Ni, Cu is ca. 34 times higher in RuD than in PlasmaChem G02. Such metal elements may come from the detonation synthesis as a sub-product of the explosive method done inside the metal chamber. In contrast, the content of zinc (Zn) is ca. 7-fold higher in PlasmaChem, and the main source of Zn is the detonator/initiator (other types: Mg, Fe, Cu, Al, Pb, Hg, As) used to catalyze the carbon detonation reaction during the synthesis process<sup>48</sup>.

A relatively low content of Ag, In, Pb, Sb, Zr, Mo ( $< 2 \mu\text{g}\cdot\text{g}^{-1}$ ) is observed for both PlasmaChem and RuD150 NDs (except Ag, In, Sb where no data are provided). The amount of tungsten (W) is ca. 4-times higher in PlasmaChem and the main source of this material is the construction material of the detonation chamber<sup>45</sup>. Lastly, ca. 1.3-fold higher content of boron (B) was detected in RuD150. Boron impurity can come from inhibitors used during the isolation and purification step but also from the laboratory glassware used for storage.

## 2.5.2 Surface modified nanodiamonds

Physical and chemical surface modifications of detonation NDs aim to homogenize the surface termination while reducing the amount of non-diamond carbon and impurities. Native PlasmaChem, described in the previous part, were modified by means of thermal and plasma treatments. Thermal annealing under air (1 h, 550 °C), plasma (250 W, 12 mbar, 20 min) and thermal (1 h, 550 °C) hydrogenations and vacuum annealing (1 h, 750 °C) were performed on manually milled NDs powder. With similar conditions as for the native particles, the ICP-MS analysis was repeated for the modified NDs.

Element	As-received ( $\mu\text{g}\cdot\text{g}^{-1}$ )	Air annealed ( $\mu\text{g}\cdot\text{g}^{-1}$ )	Plasma H <sub>2</sub> ( $\mu\text{g}\cdot\text{g}^{-1}$ )	Thermal H <sub>2</sub> ( $\mu\text{g}\cdot\text{g}^{-1}$ )	Vacuum annealed ( $\mu\text{g}\cdot\text{g}^{-1}$ )
Al	50.4	471.18	47.89	87.06	16
Mn	3.6	18.77	1.75	2.99	0.55
Fe	34.6	448.77	26.25	48.25	29.42
Ni	2.3	29.8	1.68	3.47	1.59
Cu	5.6	17.07	1.56	2.33	1.21
Zn	368.7	6.67	4.79	no data	5.21
Ag	1.0	8.29	0.06	0.56	0.26
In	0.1	no data	no data	no data	no data
Pb	0.8	no data	no data	no data	no data
Pd	no data	0.17	0.12	0.03	0.05
Sn	11.7	129.19	11.44	21.88	2.45
Sb	0.3	3.54	0.24	0.52	0.37
Hf	no data	0.13	0.52	0.01	0.02
B	243.1	1608.79	141.02	298.7	119.37
Ti	25.8	no data	no data	no data	no data
Zr	1.0	6.95	0.61	1.2	1.82
Mo	1.3	12.78	2.37	2.26	0.99
Ta	no data	0.09	0.03	0.04	0.04

W	7.0	66.12	4.89	10.68	4.8
<b>Total</b>	<b>731</b>	<b>2828</b>	<b>245</b>	<b>487</b>	<b>184</b>

**Table 2.3** – Comparison of major elemental impurities after various surface-modifications of detonation NDs (PlasmaChem GmbH, grade G-02). The total sum excludes elements with a missing value (no data) apart from Zn contamination.

Looking at Table 2.3, it can be seen that the impurity content depends on the type of surface treatment applied. To better highlight the effect of surface modifications, the total amount of impurities is normalized with respect to the reference amount of incombustible impurities detected in PlasmaChem ( $731 \mu\text{g.g}^{-1}$ ). The total values presented in the table are generally lower than the reference one, showing a reduction of metal / non-metal content. The lowest impurity level is observed for vacuum annealed ( $184 \mu\text{g.g}^{-1}$ ) and plasma hydrogenated NDs ( $245 \mu\text{g.g}^{-1}$ ), which corresponds to a reduction of impurities by  $\sim 75\%$  and  $\sim 67\%$ , respectively. The thermal hydrogenation also reduces the total amount of impurities by  $\sim 34\%$ . We notice that the true value for thermally hydrogenated NDs is higher, since the Zn contamination has been neglected. However, comparing the sources of ND and their impurity level before and after surface modification, it is expected to be less than  $10 \mu\text{g.g}^{-1}$ , which corresponds to a maximum increase of  $1\%$  in the true value of total contamination. On the contrary, air annealing introduces large amounts of Al (coming from alumina crucible used for the thermal treatment) and B (storage glassware) which results in a  $\sim 287\%$  of the increase.

On the whole, the amount of major elemental impurities present after surface treatment can be put in order according to the total contamination mass reduction:

Air annealing > thermal  $\text{H}_2$  > plasma  $\text{H}_2$  > Vacuum annealing

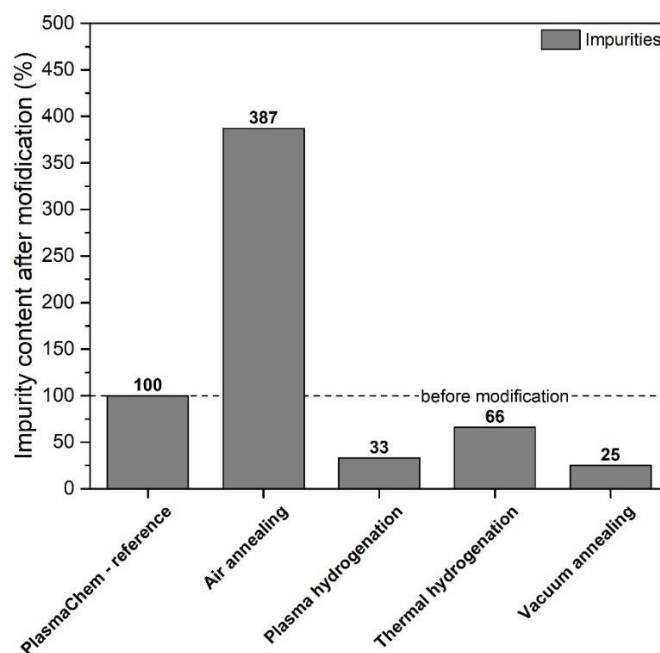


**Figure 2.15** – Normalized impurity content after different surface modifications of PlasmaChem NDs with respect to the reference sample (raw powder) provided by the German diamond industry.

To conclude, it has been shown that surface-modifications such as plasma and thermal treatments (except air annealing) significantly reduce the impurity content whereas air annealing raises the contamination level. However, the presence of aggregates may limit the possible reduction efficiency due to metals and other elements being trapped within tight NDs' agglomerations<sup>42</sup>.

### 2.5.3 Summary

- Ultra-pure PlasmaChem NDs have 5 times lower impurity content than the non-commercial particles kindly provided by Olga Shenderova. It appears that the main source of NDs contamination comes from the detonation synthesis, namely from the construction material of the chamber (e.g. Fe, Ni, W), the detonator material (e.g. Cu, Pb, Al, Zn) used to initiate the explosion or the oxidative residues applied in isolation and the purification steps (e.g. Mn, Ag, B)<sup>45</sup>.
- Surface modifications of NDs (PlasmaChem) reduce significantly the elemental composition of the soft-shells depending on the treatment conditions. The impurity level is the lowest after vacuum annealing at 750 °C (~25 %), plasma H<sub>2</sub> (~33 %) and thermal H<sub>2</sub> (~66 %). The air annealing oxidative treatment surprisingly raises the total impurity level by 287 % affected mostly by the presence of a high content of Al, Fe, Sn, B, and W.

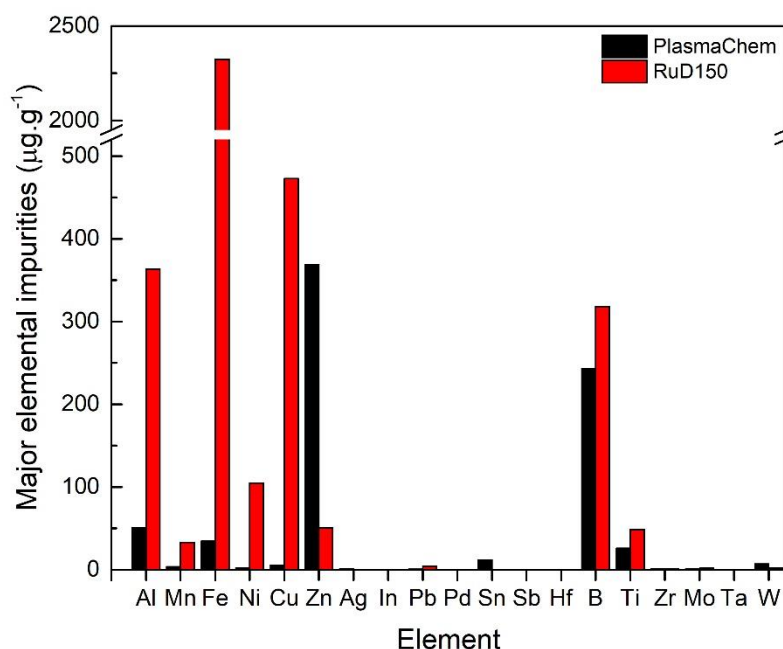


**Table 2.16** – Elemental impurities in native NDs from PlasmaChem GmbH - black (ultra-pure, grade G-02) and non-commercial RuD150 form Adamas Nanotechnologies - red.

## 2.6 Transmission Electron Microscopy

The transmission electron microscopy (TEM) technique allows probing of the crystallographic structure of detonation NDs showing information about their size distribution and their morphology. According to high-resolution micrographs, ordered  $sp^3$ -C, non-diamond structures (e.g. a-C,  $sp^2$ -C), and other structural defects can be identified<sup>49,50</sup>.

TEM images were obtained in collaboration with M. Sennour from Mines Paris Tech (Centre des Matériaux) using a JEM-2010 instrument equipped with a gun field-emission microscope (TECNAI F20 ST) operating at 200 kV and possessing a lattice resolution of 1.4 Å. The TEM studies focused on the PlasmaChem detonation NDs (ultra-pure, grade G-02) which were mainly used in this Ph.D. work. Both native and surface-modified NDs were dispersed in ultra-pure water (18.2 MΩ) and deposited on a copper mesh grid (type: S167-3 Holey Carbon Film300) at a concentration of 0.1 mg.ml<sup>-1</sup> by simple dipping for a few minutes.

In this part, a qualitative comparison of TEM micrographs is provided between the different NDs before and after surface modifications, e.g. air annealing, hydrogen plasma treatment, annealing under hydrogen, and vacuum annealing. The deposition of NDs on the copper grid induced agglomeration of the NDs and the images were acquired on isolated NDs. The size measurements were performed using ImageJ free-access software.

### 2.6.1 As-received nanodiamonds

The as-received detonation NDs provided by PlasmaChem were characterized prior to any surface-modification. The TEM micrographs of native NDs are presented below.

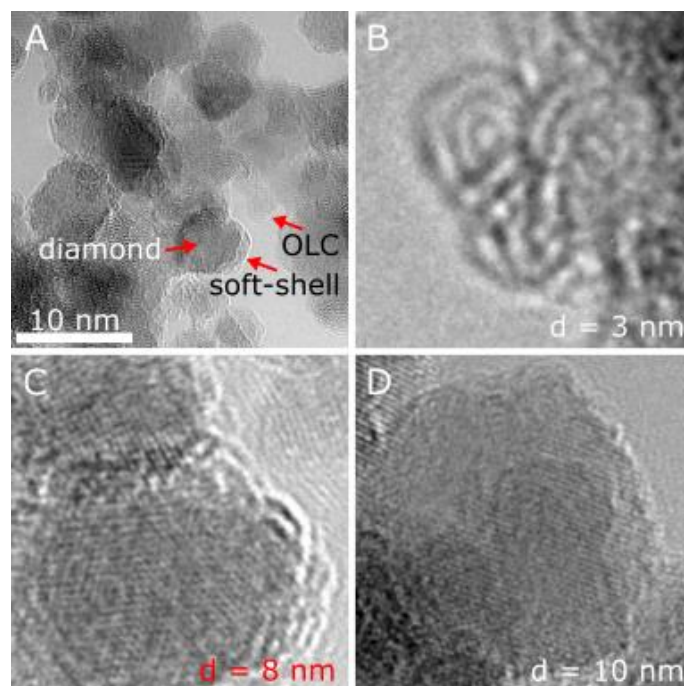


**Figure 2.17** – HRTEM images of as-received PlasmaChem NDs for different sizes. The top-left micrograph shows a crystallographic structure of NDs (A) whereas other images represent particles according to the size (B, C, and D).

The as-received product contains quasi-spherical NDs of different sizes (Figure 2.17). The diameters ( $d$ ) of the particles were measured and revealed sizes spanning from 3 nm up to 10 nm. This range of size indicates a polydispersity of the native material which suggest that the size population given by the producer may lack precision.. The smallest particles ( $d \sim 3$  nm) exhibit a clear onion-like carbon (OLC) (image B) structure with a ring-like organization of carbon atoms. At the same time, the larger NDs have a well-defined diamond core surrounded by a soft-shell made of non-diamond carbon (image A). Disordered carbon structures (e.g. a-C) can be also observed.

Sp<sup>2</sup>-C patches are seen on NDs with a diameter of 8 nm (C) and the thickness of the shell is higher compared to larger particles (D). The biggest NDs measure up to 10 nm and have the purest diamond structure observed so far with a very thin layer of structural defects present on the outer shell. Notably, fraction of amorphous C is also visible among NDs.

In conclusion, the as-received NDs are polydisperse in size and sp<sup>2</sup>-shell fraction varies depending on the initial size of NDs. The smallest particles (3 nm) exhibit a clear OLC structure whereas larger particles have a well-defined diamond core with disordered carbon present only at the surface. The polydispersity of NDs suggests that their reactivity toward surface modifications may be different depending on the primary size of the particles.

### 2.6.2 Air annealed nanodiamonds

The PlasmaChem NDs were air annealed at 550 °C for 1 h 30 min. The TEM micrographs were taken from NDs dispersed in suspension and then deposited by a dipping method on the copper grids.

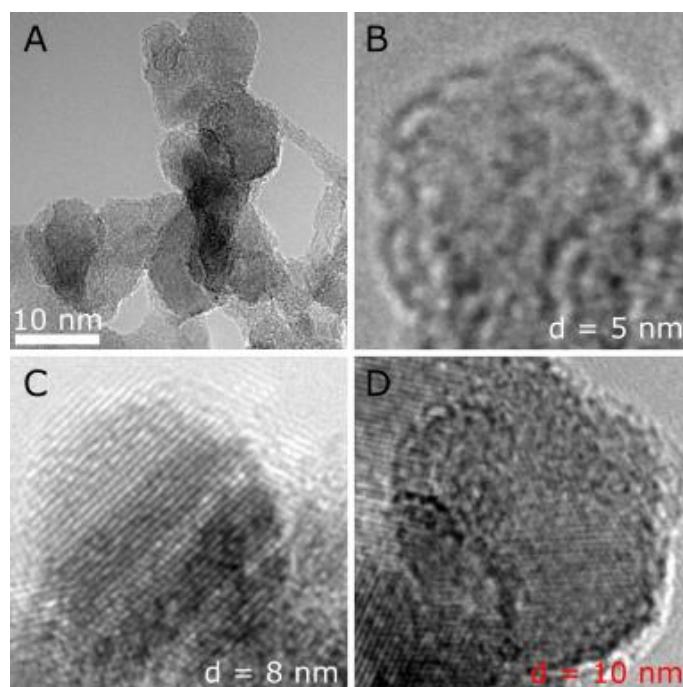


**Figure 2.18** – HRTEM images of air annealed PlasmaChem NDs.

Compared to as-received NDs, the crystallographic structure of air annealed NDs appears to be clean of  $sp^2$  and OLC carbon at the surface (Figure 2.18). This observation is related to the etching of NDs which occurs during the annealing under air<sup>13,35</sup>. Moreover, the level of aggregation after oxidative treatment is reduced as compared to the native NDs. Some small fraction of a-C can still be observed. However, a pure diamond structure seems to dominate. The larger NDs (8 nm – C, and 11 nm - D) appear as clean diamond particles with only very thin patches of non-diamond structures seen at the bigger NDs. Contrary to as-received particles, OLC of 3 nm are not observed anymore after air annealing whereas the smallest NDs have mostly a diameter of 5 nm. Such small particles have been most probably etched away during the annealing.

### 2.6.3 Plasma hydrogenated nanodiamonds

Microwave plasma treatment was carried out on manually-milled PlasmaChem NDs (250 W, 20 min, 12 mbar). The TEM micrographs of post-modified particles are presented below, still from NDs dispersed in water suspension.

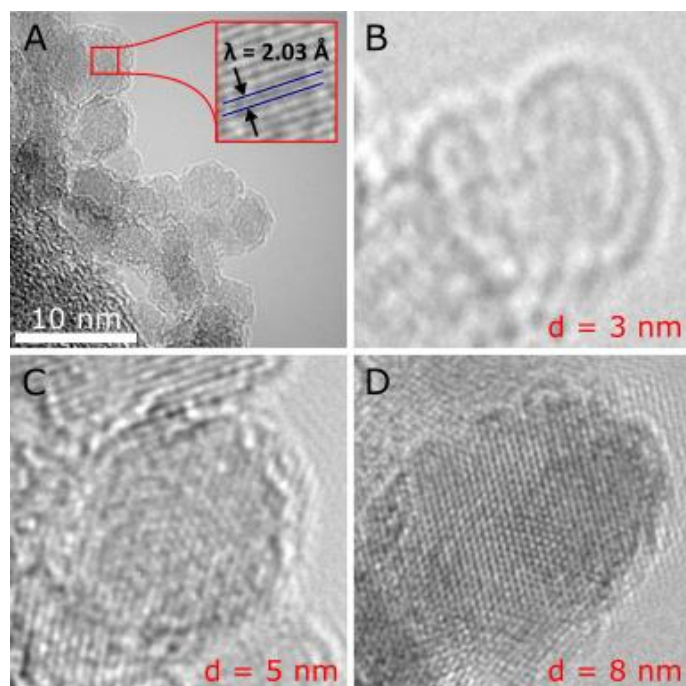


**Figure 2.19** – HRTEM images of plasma hydrogenated NDs.

According to the TEM images (Figure 2.19), the size distribution of plasma H-NDs ranges from 3 to 8 nm. The distance between crystallographic planes which was measured in the core of the NDs well corresponds to the diamond (111) one (2.03 Å). The smallest particles exhibit an OLC structure while the bigger NDs are surrounded by  $sp^2$  and/or amorphous carbon shells.

#### 2.6.4 Hydrogen annealed nanodiamonds

The PlasmaChem NDs thermally annealed under hydrogen (1 h, 550 °C) were also imaged by TEM as shown below:

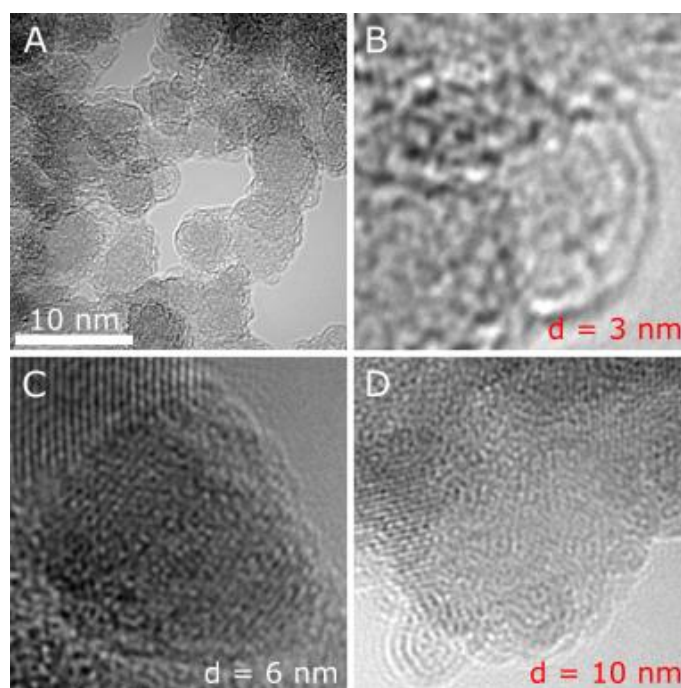


**Figure 2.20** – HRTEM images of hydrogen annealed NDs.

The size distribution of hydrogen annealed H-NDs ranges from 3 to 10 nm (Figure 2.20). TEM observations are very similar to plasma H-NDs with the presence of small OLC particles and bigger NDs surrounded by  $sp^2$ -C and/or a-C shells.

### 2.6.5 Vacuum annealed nanodiamonds

The TEM images were taken of vacuum annealed particles at 750 °C for 1 h (source: PlasmaChem). The NDs represent the lowest conditions of vacuum annealing tested.

The NDs treated under vacuum have a higher degree of aggregation compared to air oxidized NDs (Figure 2.21, image A). The smallest particles (B - 3 nm), which appear as OLC on the native material, are still present after the vacuum treatment without significant modification. Larger NDs (C - 6 nm and D - 9 nm) are surrounded by a soft-shell layer. The pure diamond core is still observed for the largest NDs whereas the 6 nm NDs have higher level of disorders on the outer shell with a cloud-like appearance. The diamond core is less visible due to the thicker layer of soft-shell being present on the surface. Moreover, the  $sp^2$ -C patches are clearly observed. Vacuum annealing affects the crystallographic structure of NDs, however, the effect is size-dependent.

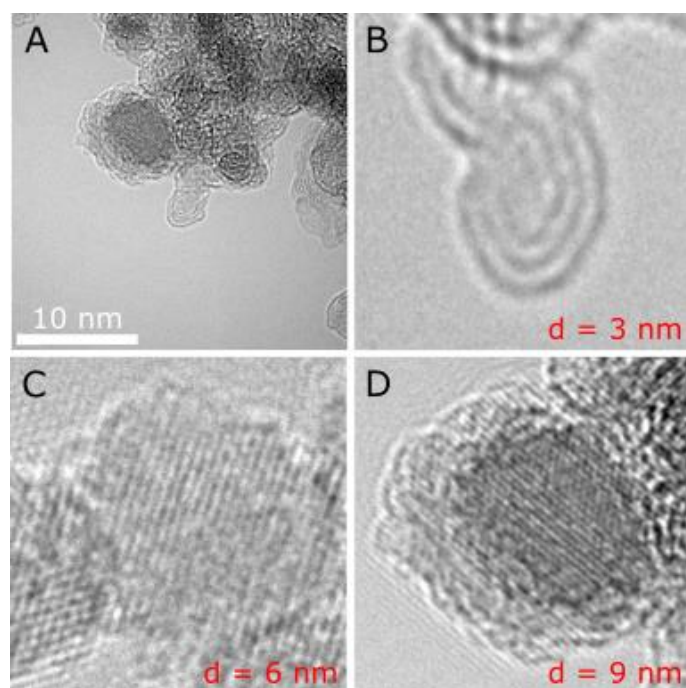


**Figure 2.21** – HRTEM images of vacuum annealed NDs.

### 2.6.6 Summary

- Native NDs from PlasmaChem are highly polydisperse (3 - 10 nm)
- Oxidative treatment cleans the NDs surface from non-diamond species and reduces the thickness of the soft-shell layer
- Plasma and thermally hydrogenated NDs exhibit a very similar structure. Small OLC (3 nm) and larger NDs surrounded by  $sp^2$  / a-C shell are observed
- Vacuum annealing of NDs increases the level of disorganization of carbon structures on the surface for the comparable size of NDs.

## Bibliography

1. Alhaddad, A. *et al.* Nanodiamond as a vector for siRNA delivery to Ewing sarcoma cells. *Small* **7**, 3087–3095 (2011).
2. Grall, R. *et al.* Impairing the radioresistance of cancer cells by hydrogenated nanodiamonds. *Biomaterials* **61**, 290–298 (2015).
3. Slegerova, J. *et al.* Nanodiamonds as Intracellular Probes for Imaging in Biology and Medicine. In: Prokop, A., Iwasaki, Y. & Harada, A. (eds.) *Intracellular Delivery II*, vol. 7. Netherlands, Dordrecht, 363–401 (*Springer*, 2014).
4. Girard, H. A. *et al.* Surface properties of hydrogenated nanodiamonds: a chemical investigation. *Phys. Chem. Chem. Phys.* **13**, 11517–11523 (2011).
5. Krüger, A. *et al.* Surface functionalisation of detonation diamond suitable for biological applications. *J. Mater. Chem.* **16**, 2322–2328 (2006).
6. Prasad, G. L. Biomedical Applications of Nanoparticles. In: Webster, T. J. (ed.) *Safety of Nanoparticles*, 89–109 (*Springer*, 2009).
7. Moche, H. *et al.* Carboxylated nanodiamonds can be used as negative reference in *in vitro* nanogenotoxicity studies. *J. Appl. Toxicol.* **37**, 954–961 (2017).
8. Girard, H. A. *et al.* Hydrogenation of nanodiamonds using MPCVD: A new route toward organic functionalization. *Diam. Relat. Mater.* **19**, 1117–1123 (2010).
9. Mermoux, M., Crisci, A., Petit, T., Girard, H. A. & Arnault, J.-C. Surface Modifications of Detonation Nanodiamonds Probed by Multiwavelength Raman Spectroscopy. *J. Phys. Chem. C* **118**, 23415–23425 (2014).
10. Arnault, J.-C. *et al.* Surface chemical modifications and surface reactivity of nanodiamonds hydrogenated by CVD plasma. *Phys. Chem. Chem. Phys.* **13**, 11481–11487 (2011).
11. Osswald, S., Havel, M., Mochalin, V., Yushin, G. & Gogotsi, Y. Increase of nanodiamond crystal size by selective oxidation. *Diam. Relat. Mater.* **17**, 1122–1126 (2008).
12. Shenderova, O. *et al.* Modification of detonation nanodiamonds by heat treatment in air. *Diam. Relat. Mater.* **15**, 1799–1803 (2006).
13. Gaebel, T., Bradac, C., Chen, J., Hemmer, P. & Rabeau, J. R. Size-reduction of nanodiamonds via air oxidation. *Diam. Relat. Mater.* **21**, 28–32 (2012).
14. Wolcott, A. *et al.* Surface structure of aerobically oxidized diamond nanocrystals. *J. Phys. Chem. C* **118**, 26695–26702 (2014).
15. Pichot, V. *et al.* An efficient purification method for detonation nanodiamonds. *Diam. Relat. Mater.* **17**, 13–22 (2008).
16. Korolkov, V. V., Kulakova, I. I., Tarasevich, B. N. & Lisichkin, G. V. Dual reaction capacity of hydrogenated nanodiamond. *Diam. Relat. Mater.* **16**, 2129–2132 (2007).

17. Williams, O. A. *et al.* Size-dependent reactivity of diamond nanoparticles. *ACS Nano* **4**, 4824–4830 (2010).
18. Ahmed, A.-I., Mandal, S., Gines, L., Williams, O. A. & Cheng, C.-L. Low temperature catalytic reactivity of nanodiamond in molecular hydrogen. *Carbon* **110**, 438–442 (2016).
19. Girard, H. A. *et al.* Tritium labelling of detonation nanodiamonds. *Chem. Commun.* **50**, 2916–2918 (2014).
20. Butenko, Y. V. *et al.* The Thermal Stability of Nanodiamond Surface Groups and Onset of Nanodiamond Graphitization. *Fullerenes, Nanotub. Carbon Nanostructures* **14**, 557–564 (2006).
21. Jiang, T., Xu, K. & Ji, S. FTIR studies on the spectral changes of the surface functional groups of ultradispersed diamond powder synthesized by explosive detonation after treatment in hydrogen, nitrogen, methane and air at different temperatures. *J. Chem. Soc. Faraday Trans.* **92**, 3401–3406 (1996).
22. Chenga, C.-L., Chen, C.-F., Shaio, W.-C., Tsai, D.-S. & Chen, K.-H. The CH stretching features on diamonds of different origins. *Diam. Relat. Mater.* **14**, 1455–1462 (2005).
23. Ji, S., Jiang, T., Xu, K. & Li, S. FTIR study of the adsorption of water on ultradispersed diamond powder surface. *Appl. Surf. Sci.* **133**, 231–238 (1998).
24. Arnault, J. C. & Girard, H. A. Hydrogenated nanodiamonds: Synthesis and surface properties. *Curr. Opin. Solid State Mater. Sci.* **21**, 10–16 (2016).
25. Kurzyp, M. *et al.* Hydroxyl Radicals Production Induced by Plasma Hydrogenated Nanodiamonds under X-ray Irradiation. *Chem. Commun.* **53**, 1237–1240 (2017).
26. Zou, Q., Wang, M. Z. & Li, Y. G. Analysis of the nanodiamond particle fabricated by detonation. *J. Exp. Nanosci.* **5**, 319–328 (2010).
27. Shenderova, O. *et al.* Hydroxylated Detonation Nanodiamond: FTIR, XPS, and NMR Studies. *J. Phys. Chem. C* **115**, 19005–19011 (2011).
28. Petit, T. *et al.* Unusual Water Hydrogen Bond Network around Hydrogenated Nanodiamonds. *J. Phys. Chem. C* **121**, 5185–5194 (2017).
29. Mathkar, A. *et al.* Controlled, Stepwise Reduction and Band Gap Manipulation of Graphene Oxide. *J. Phys. Chem. Lett.* **3**, 986–991 (2012).
30. Osswald, S., Yushin, G., Mochalin, V., Kucheyev, S. O. & Gogotsi, Y. Control of sp<sup>2</sup>/sp<sup>3</sup> carbon ratio and surface chemistry of nanodiamond powders by selective oxidation in air. *J. Am. Chem. Soc.* **128**, 11635–11642 (2006).
31. Kuznetsov, V. L., Chuvilin, A. L., Butenko, Y. V., Mal'kov, I. Y. & Titov, V. M. Onion-like carbon from ultra-disperse diamond. *Chem. Phys. Lett.* **222**, 343–348 (1994).
32. Petit, T., Arnault, J.-C., Girard, H. A., Sennour, M. & Bergonzo, P. Early stages of surface graphitization on nanodiamond probed by x-ray photoelectron spectroscopy. *Phys. Rev. B* **84**, 233407 (2011).

33. Petit, T. *et al.* Oxygen hole doping of nanodiamond. *Nanoscale* **4**, 6792–6799 (2012).
34. Ferrari, A. C. & Robertson, J. Raman spectroscopy of amorphous, nanostructured, diamond-like carbon, and nanodiamond. *Philos. Trans. A. Math. Phys. Eng. Sci.* **362**, 2477–512 (2004).
35. Mochalin, V. N., Shenderova, O., Ho, D. & Gogotsi, Y. The properties and applications of nanodiamonds. *Nat. Nanotechnol.* **7**, 11–23 (2012).
36. Hodkiewicz, J. Characterizing Carbon Materials with Raman Spectroscopy. *Thermo Fisher Scientific*, Madison, WI, USA (2010).
37. Cebik, J. *et al.* Raman spectroscopy study of the nanodiamond-to-carbon onion transformation. *Nanotechnology* **24**, 205703 (2013).
38. Zou, Q., Wang, M. Z., Li, Y. G. & Lu, B. High-resolution transmission-electron microscope characterization of onionlike carbon transformed from nanodiamond. *J. Vac. Sci. Technol. B, Nanotechnol. Microelectron. Mater. Process. Meas. Phenom.* **28**, 935–939 (2010).
39. Mochalin, V., Osswald, S. & Gogotsi, Y. Contribution of Functional Groups to the Raman Spectrum of Nanodiamond Powders. *Chem. Mater.* **21**, 273–279 (2009).
40. Krüger, A. *et al.* Unusually tight aggregation in detonation nanodiamond: Identification and disintegration. *Carbon* **43**, 1722–1730 (2005).
41. Mitev, D., Dimitrova, R., Spassova, M., Minchev, C. & Stavrev, S. Surface peculiarities of detonation nanodiamonds in dependence of fabrication and purification methods. *Diam. Relat. Mater.* **16**, 776–780 (2007).
42. Mitev, D. P., Townsend, A. T., Paull, B. & Nesterenko, P. N. Direct sector field ICP-MS determination of metal impurities in detonation nanodiamond. *Carbon* **60**, 326–334 (2013).
43. Dolmatov, V. Y. Detonation synthesis ultradispersed diamonds: properties and applications. *Russ. Chem. Rev.* **70**, 607–626 (2001).
44. Arnault, J.-C. *et al.* Surface graphitization of ozone-treated detonation nanodiamonds. *Phys. Status Solidi A* **211**, 2739–2743 (2014).
45. Nesterenko, P. N., Mitev, D. & Paull, B. Elemental analysis of nanodiamonds by inductively coupled plasma hyphenated methods. In: Arnault, J.-C. (ed.) *Nanodiamonds. Advanced Material Analysis, Properties and Applications*, 109–130 (*Elsevier*, 2017).
46. Perchyonok, V. T., Souza, J., Zhang, S., Moodley, D. & Grobler, S. Bio-Active Nano-Diamond Designer Materials and Dentures : From Design to Application. *Dentistry* **5**, 5–11 (2015).
47. Krueger, A. & Lang, D. Functionality is Key: Recent Progress in the Surface Modification of Nanodiamond. *Adv. Funct. Mater.* **22**, 890–906 (2012).
48. Non-primary explosive detonator. Retrieved from: <http://russianpatents.com/patent/207/2071590.html> (Accessed: 10<sup>th</sup> October 2017)

49. Turner, S. *et al.* Determination of Size, Morphology, and Nitrogen Impurity Location in Treated Detonation Nanodiamond by Transmission Electron Microscopy. *Adv. Funct. Mater.* **19**, 2116–2124 (2009).
50. Arnault, J. C. Surface Modifications of Nanodiamonds and Current Issues for Their Biomedical Applications. In: Nianjun, Y. (ed.) *Novel Aspects of Diamond*, 85–122 (*Springer*, 2014).





# Chapter 3

## Colloidal properties of nanodiamonds

### Summary

---

<b>3.1 Introduction</b> .....	<b>52</b>
<b>3.2 Bibliography review</b> .....	<b>53</b>
3.2.1 Colloidal properties of nanodiamonds .....	53
3.2.2 Deaggregation strategies for nanodiamond hydrosol preparation.....	56
3.2.3 Colloidal stability of nanodiamonds versus their surface chemistry .....	56
3.2.4 Interaction of nanodiamonds with solvents .....	60
3.2.5 Summary .....	62
<b>3.3 Nanodiamond hydrosol preparation</b> .....	<b>63</b>
3.3.1 Preparation of colloids: general concept of sonication and centrifugation .....	64
3.3.1.1 Sonication.....	64
3.3.1.2 Centrifugation .....	64
3.3.1.3 Parameters influencing the quality of the suspension .....	65
3.3.2 Suspended-solid concentration measurement.....	66
3.3.2.1 First method – weight scale balance.....	66
3.3.2.2 Second method – microbalance .....	68
3.3.3 Characterization of colloids: Dynamic Light Scattering .....	70
3.3.3.1 Hydrodynamic size distribution measurement.....	70
3.3.3.2 Zeta Potential measurement .....	72
3.3.4 Representation of the dynamic light scattering results.....	73
3.3.4.1 Size distribution by Intensity.....	73
3.3.4.2 Size distribution by Number .....	74
3.3.4.3 Zeta Potential.....	76
3.3.5 Calibration of the DLS equipment.....	77
3.3.5.1 Measuring cuvette .....	77
3.3.5.2 Effect of sample concentration.....	78
3.3.5.3 Summary .....	80

---

3.3.6 Optimization of the NDs colloid preparation.....	80
3.3.6.1 Effect of sonication time .....	80
3.3.6.2 Effect of centrifugation time.....	81
3.3.6.3 Effect of centrifugal force and speed.....	83
3.3.6.4 Effect of sample temperature on DLS measurements.....	83
3.3.6.5 Summary .....	85
<b>3.4 Colloidal behavior of NDs with different surface chemistries .....</b>	<b>86</b>
3.4.1 Colloidal properties of air annealed nanodiamonds .....	86
3.4.2 Colloidal properties of plasma hydrogenated nanodiamonds .....	88
3.4.3 Colloidal properties of hydrogen annealed nanodiamonds .....	91
3.4.4 Properties of vacuum annealed nanodiamonds.....	93
3.4.5 Summary .....	94
<b>3.5 Stabilisation and aging effect.....</b>	<b>95</b>
3.5.1 Stability over 24 h .....	95
3.5.1.1 Air annealed nanodiamonds .....	96
3.5.1.2 Plasma hydrogenated nanodiamonds .....	96
3.5.1.3 Hydrogen annealed nanodiamonds.....	98
3.5.1.4 Vacuum annealed nanodiamonds .....	98
3.5.1.5 Summary .....	100
3.5.2 Stability over 50 days.....	100
3.5.2.1 Concentration effect .....	100
3.5.2.2 Air annealed nanodiamonds .....	102
3.5.2.3 Hydrogenated nanodiamonds .....	103
3.5.2.4 Vacuum annealed nanodiamonds .....	104
3.5.2.5 Summary .....	106
<b>3.6 FTIR study.....</b>	<b>107</b>
3.6.1 Surface-modified nanodiamond powder.....	107
3.6.2 Surface-modified nanodiamond pellet.....	108
3.6.3 Surface-modified nanodiamond suspension .....	109
3.6.4 Summary .....	110
<b>3.7 Discussion about the colloidal properties of nanodiamonds according to their surface chemistries.....</b>	<b>111</b>
3.7.1 Air annealed nanodiamonds.....	111
3.7.2 Hydrogenated nanodiamonds .....	111
3.7.3 Vacuum annealed nanodiamonds .....	113
3.7.4 General discussion on the colloidal behavior of cationic nanodiamonds .....	114

---

**Bibliography ..... 116**

## 3.1 Introduction

Chapter 3 presents colloidal properties of nanodiamonds (NDs). As surface-modified NDs will be investigated in the next chapter in terms of reactive oxygen species (ROS) production in water, hence it requires studying their colloidal properties and stability in aqueous suspension. The aim of this chapter is thus, to investigate the behavior of the surface-modified ND powders, prepared and characterized in the previous chapter, after dispersion in ultra-pure water.. The studies involves characterization of the NDs colloids immediately after hydrosol preparation, but also over time.

Surface-modified NDs come in a form of a tightly aggregated powder which can be put into suspension using sonication and centrifugation methods. The sonication helps break the ND aggregates via ultrasound power and the centrifugation creates a centrifugal body force which separates the NDs according to their size. The details regarding the experimental protocol are given in the first technical part of this chapter.

In the following part of the chapter, NDs' colloidal properties such as hydrodynamic diameter and surface charge are studied using the Dynamic Light Scattering (DLS) technique. To begin with, a commercial NDs suspension has been used as a model of well-dispersed particles to optimize the characterization protocol, such as the concentration measurement methods as well as DLS parameters (e.g. NDs' concentration, type of the measuring cuvette). The practical presentation of the results and the way to analyze the data are shown and discussed.

Key parameters affecting sonication and centrifugation steps are identified and tested using plasma hydrogenated NDs (H-NDs) as an example of the surface-modified NDs. The hydrodynamic diameter and Zeta Potential (ZP) of water-dispersed H-NDs are presented and compared for various sonication and centrifugation conditions leading to final hydrosol preparation conditions.

After applying the same preparation protocol, colloidal properties of air oxidized, hydrogenated (via plasma or thermal annealing) and vacuum annealed NDs freshly suspended in water are presented. Relations between their specific surface chemistry and behavior in water are shown and discussed according to the literature. Monitoring of the colloidal stability after 24 h and 50 days in water suspension are studied revealing differences between their short and long-term colloidal properties.

Finally, Fourier Transform Infrared Spectroscopy (FTIR) characterization of modified NDs suspended in water compared to the 'dried' ones will be presented. The relation between surface chemistry of NDs and specific interaction with water molecules is discussed.

## 3.2 Bibliography review

### 3.2.1 Colloidal properties of nanodiamonds

The as-received NDs comes in a form of aggregated powder made of a pure diamond core and an outer shell, so-called 'soft-shell', containing metallic impurities and non-diamond carbons (e.g. amorphous carbon, graphite-like carbon). These NDs have limited ability toward water dispersion<sup>1</sup>, however, the outer shell of NDs is highly reactive allowing modify the surface structure whereas the diamond core is considered to be chemically inert and stable<sup>2</sup>.

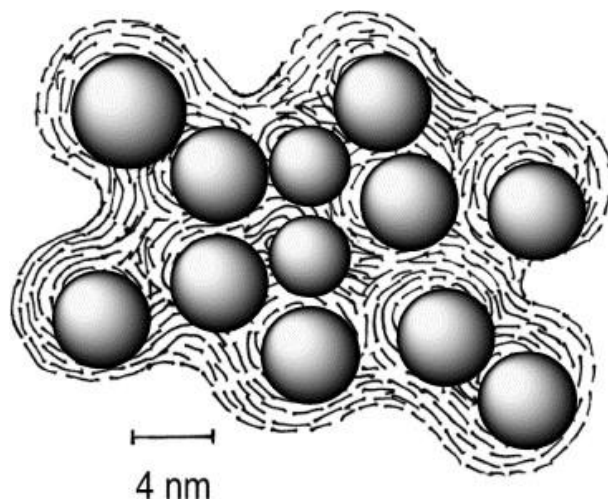


**Figure 3.1** – A model of core aggregates, which resembles the well-known grape-shaped 'aggregate structure' of the hardest type of black carbon<sup>1</sup>.

In the literature, several factors are claimed to be responsible for the aggregation of NDs:

- Attractive forces such as interfacial interactions (Incoherent Interfacial Coulombic Interactions - IICIs)<sup>3</sup>
- Presence of a soft-shell surrounding the diamond core made of graphitic carbon structures ( $sp^2$ -C) and / or amorphous carbon (a-C)<sup>4</sup>
- Surface terminations responsible for hydrophobic / hydrophilic solid-solvent interactions<sup>5</sup>.

The majority of the work aims to produce stable colloidal solutions made of single-digit NDs (in case of detonation NDs with primary diameter of 5 nm)<sup>1,6,7</sup>. However, raw NDs powder usually present multiple and rather uncontrolled functions on their surface such as ethers, hydroxyls, carboxylic groups and ketones, amorphous carbon, alkyl functions, etc<sup>8</sup>. Several studies performed directly on commercial raw NDs suspended in water has led to rather versatile, non-coherent conclusions and a lack of possibility to compare results making the study source-dependent. The reason behind that comes from the polyfunctional surface chemistry of the as-received NDs affecting affinity toward liquid molecules (hydrophobic or hydrophilic nature). The type of such interactions is a key factor responsible for the colloidal properties and stability of the NDs suspension<sup>9</sup>. For this reason, an important work in the

literature is focused on the improvement of the colloidal properties of NDs, playing on their surface chemistry, suspension protocol and type of a solvent<sup>1,6,7</sup>.

For instance, behavior and size-reduction of commercial NDs (New Technologies, Co., Chelyabinsk, Russian Federation, size = 4 nm) after purification and a solvent dispersion have been studied in 2010 by O. Shenderova and co-workers. The authors showed the influence of the liquid medium as well as the sonication and centrifugation steps on the hydrodynamic diameter measured via photon correlation spectroscopy (PCS) equipped with Beckman–Coulter N5 submicron particle size analyzer<sup>10</sup>.

Solvent	Size of polydisperse NDs (nm)	NDs size in supernatant (nm)	wt.% of NDs in supernatant
H <sub>2</sub> O	183	25	0.25
DMSO	170	30	0.50
Methanol	185	40	0.05
Ethanol	210	45	0.10

**Table 3.1** - Comparison of the particle sizes of detonation NDs (Chelyabinsk, Russia) in different solvents (water – H<sub>2</sub>O, dimethyl sulfoxide – DMSO, methanol, and ethanol) as well as size and yield in a supernatant after centrifugation of 1 wt.% ND at the same conditions<sup>10</sup>.

The authors concluded that aggregation decreases with increased sonication or milling time and can be even further reduced via centrifugation. Another factor affecting the final size distribution is the dispersing solvent. However, the authors do not provide any specific details regarding sonication and centrifugation parameters whereas full deaggregation is not presented (Table 3.1)<sup>11</sup>.

Similar experiments have been performed on the surface-modified NDs in 2009 by N. Gibson et al., showing significant reduction of the NDs size after physical (atmospheric plasma in oxygen or nitrogen gas) or chemical (NaCl) treatment. More importantly, such a surface-modified NDs showed better colloidal stability after dispersion in water compared to the native NDs for the hydrodynamic diameter < 100 nm. The authors also used centrifugation to fraction the NDs suspension whereas the persistence toward aggregation / sedimentation has been attributed to the presence of surface functionalities, mostly oxygen and hydrogen groups<sup>12</sup>.

Another study conducted by I. Larionova et al. in 2006 investigated properties of fractions according to the centrifugal force. The smallest fraction measured with average size of 30 nm corresponds to the NDs yield of 20 wt.%<sup>13</sup>. which is comparable to the previous results presented by O. Shenderova et al<sup>14</sup>. Similar results were also obtained in 2017 showing that the combination of sonication and centrifugation procedure led to the hydrodynamic diameter of 36 nm depended on the surface chemistry of NDs<sup>15,16</sup>.

In 2014, A. Shakun et al., published work presenting aggregation of NDs caused by the presence of the soft-shell around the as-received NDs (Figure 3.2). Surface functionalisation may significantly reduce the aggregation state of NDs but a chemical interaction between the surface functionalities may also induce the formation of larger agglomerates via bridging<sup>4</sup>.

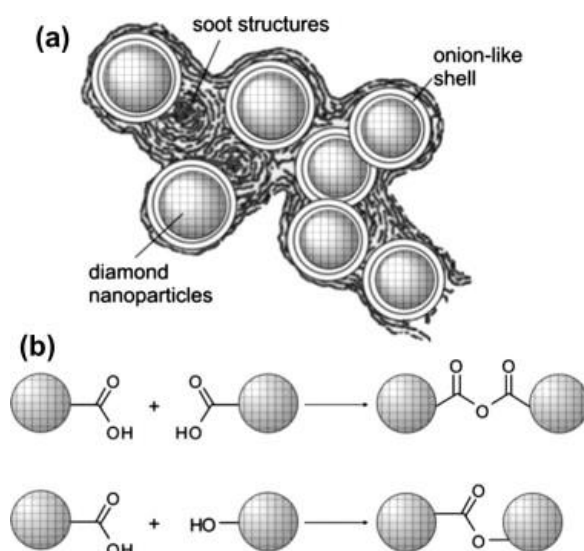


**Figure 3.2** – Soft-shell aggregation (a) and chemical bond between the surface-functional groups (b)<sup>1</sup>.

Most recently, A. T. Dideikin and co-workers (2017) reported on the influence of the  $sp^3$ - $sp^2$  rehybridization of the carbon atoms on the detonation ND facets (Figure 3.3). Multiple techniques (TEM, AFM, XPS, Raman, XRD, and DLS) led to a complete model explaining the reason behind the agglomeration and possible deagglomeration method toward individual NDs. According to the authors, the contacting surface between the aggregates is very small including hypothesis that only soft-shell ( $sp^2$ -C fraction with metallic impurities) present on the surface is responsible for the aggregation state. The  $sp^3$  –  $sp^2$  transformation can be progressively initiated via annealing under high-vacuum (abv. HV,  $\sim 10^{-10}$  Torr) at a controlled temperature (min. temperature required is 450 °C) leading to an increase of the  $sp^2$  fraction present in the corners while weakening the hardness of its primarily aggregates<sup>17</sup>.

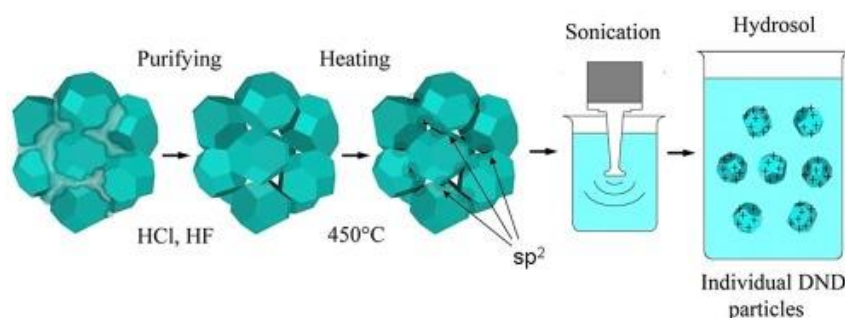


**Figure 3.3** – Model of single-digit NDs hydrosol preparation proposed by A.T. Dideikin<sup>17</sup>.

Aggregation of the detonation NDs dispersed in a liquid medium seems to be a rather complex problem. Commercial NDs suspension with diameter of the particles at less than 50 nm is considered to be resistant to agglomeration / sedimentation for at least one year<sup>14</sup>. However, NDs' colloidal stability is mostly determined by the surface chemistry rather than the size of NDs. Chemical composition of the surface is the key factor affecting behavior of the NDs in contact with solvents<sup>12</sup>. In the literature, no specific data is given in terms of possible hydrodynamic size evolution over time concluding that high ZP and relatively small size (< 100

nm) of NDs in suspension guarantee good colloidal stability<sup>12</sup>. Change in suspension's pH may also improve colloidal stability as reported by S. Kashyap et al., in 2014<sup>18</sup>.

### 3.2.2 Deaggregation strategies for nanodiamond hydrosol preparation

The preparation of the NDs hydrosol mostly involves the utilization of the ultrasonic sound to break aggregated NDs leading to significantly smaller hydrodynamic diameter and better dispersion in a liquid medium (e.g. water, ethanol). Sonication by a sonotrode immersed inside the suspension with supplying power of 400 W and frequency of 24 kHz over a specific time ranging from minutes up to hours is a standard method used for NDs hydrosol preparation<sup>19</sup>.

An alternative way to disperse NDs involves combination of mechanical ball milling with ceramic microbeads ( $ZrO_2$  or  $SiO_2$ ) and ultrasound sonication. The mechanical milling allows weakening the strength of the NDs aggregates allowing the ultrasound to be more effective and reducing the production time. The main disadvantage of this method is the contamination of the final NDs suspension with traces of the bead material and higher  $sp^2$ -C content<sup>6,19</sup>. However, the dispersion with only ultrasound seems to be effective even without the milling step leading to 85 wt.% of the NDs present in a liquid medium<sup>19</sup>.

The most novel techniques substitute the ceramic microbeads with water-soluble salt or sugar crystals to avoid possible contamination. In 2010, A. Pentecost et al., studied salt or sugar-assisted milling (Salt-Assisted Ultrasonic Deaggregation - SAUD) technique which is an efficient, an inexpensive and contamination-free method compared to the mechanical milling with metallic beads<sup>20,21</sup>.

The size-reduction effect can be also obtained by combining sonication and centrifugation techniques allowing to fractionate the NDs according to their size and molecular weight<sup>22,13</sup>. Centrifugation step with ultra-high rotation speed (5000 to 15000 rpm) may lead to significant reduction of the hydrodynamic size but also removal of high mass fraction resulting in low concentration of NDs<sup>23</sup>. Optimization in the degree of sonication and centrifugation may be needed to meet the application-dependent requirements regarding the NDs' size and the NDs' hydrosol concentration.

### 3.2.3 Colloidal stability of nanodiamonds versus their surface chemistry

The colloidal stability of the NDs hydrosol is an asset allowing to expand the number of possible applications. The detonation NDs undergo purification steps (e.g. acid treatments) leading to non-homogeneous surface chemistry<sup>24</sup>. The as-received NDs powder when dispersed in water usually exhibit low colloidal stability with tendency to aggregate / agglomerate (medium size up to hundreds of nanometers) and flocculation after several months<sup>3</sup>. Surface modifications of NDs toward homogenous surface chemistry (e.g. oxidation, hydrogenation and hydroxylation) have been shown to be effective in the control of colloidal

properties and the stability of the NDs hydrosols<sup>25,26,27</sup>. ND particles in contact with an aqueous environment create a specific surface charge on the solid-liquid interface which can be indirectly assessed via a Zeta Potential (ZP) measurement (electrophoretic mobility of the particles in the applied field)<sup>28</sup>.

Until now, the surface of the bulk diamond exposed to water has been used as a model of interfacial solid-liquid interactions<sup>29</sup>. Oxygen-terminated diamond surface is known to be hydrophilic. On the other hand hydrogenated ones are considered to be hydrophobic with a negative ZP at neutral or basic pH<sup>30,31</sup>. At the nanoscale, interactions with water molecules and detonation NDs are different compared to the bulk diamond due to the specific water structure created around the surface, which has been recently probed and explained by T. Petit and co-workers (2017)<sup>9</sup>. Hydrogen microwave plasma<sup>32</sup> or thermal annealing under hydrogen<sup>33</sup> at temperature range of 400 - 500 °C results in hydrogen-terminated NDs surface with a positive Zeta Potential (> 40 mV) measured in water<sup>34</sup>. In contrast, the air annealing at temperature < 600 °C leads to surface terminations with oxygen-containing groups (mostly carboxylic groups - COOH) exhibiting a negative ZP at neutral pH<sup>16</sup>.

The negative ZP has been associated with de-protonation of the surface carboxylic groups in water. Such a mechanism has been reported by many groups and is widely accepted in the diamond community<sup>35</sup>. The scheme below (Figure 3.4) illustrates the de-protonation mechanism of the carboxylated NDs surface:

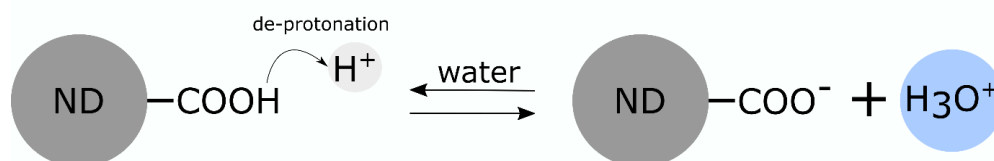


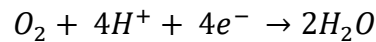
**Figure 3.4** – Schematic representation of the de-protonation of oxidized NDs surface resulting in negative surface charge. De-protonation of carboxylic groups in water is reversible.

The positive ZP of hydrogen terminated NDs is more controversial and has triggered many studies investigating the origin behind it. As a consequence, several models explaining phenomenon of positive surface charge of H-NDs have been proposed but none of them received wide acceptance so far.

The conductivity of the bulk diamond surface covered with bounded hydrogen was first studied in 1989 by M. Landstrass and K. V. Ravi<sup>36</sup>. At first, the source of such peculiar behavior of diamond after air exposure was unexpected and surely unclear since the diamond layer was undoped. These observations resulted in further investigations where the accumulation of the positive charge carriers (holes) were probed near the diamond surface noticeable exclusively in the presence of hydrogen terminations. One possible explanation, given 10 years after by R. S. Gi et al., claimed that electrons are transferred into the water layer adsorbed on the diamond surface.

A more thorough study was done in 2007 by Chakrapani et al., who proposed redox couple mechanism as a source of the positive surface charge of H-terminated diamond surfaces<sup>30</sup>. The experimental part included monitoring of oxygen level and pH changes after addition of

natural diamond particles (size range: 0.5 – 1.0  $\mu\text{m}$ ) into water. Results have shown a systematic charge exchange between the surface and water redox couple leading to either formation or consumption of  $\text{O}_2$  via the following mechanism:



According to the authors, charge exchanges result in the formation of a water layer around the diamond surface with specific contact angles typical for the hydrophobic materials. Such a charge transfer mechanism has been considered to enhance and stabilize electrostatic adhesion of water around the hydrophobic surface. Chakrapani and co-workers also speculated that similar behavior can be expected when the hydrogenated diamond surface is exposed to humid air. However, similar  $\text{O}_2$  reduction in an aqueous environment may also take place in the presence of metallic impurities present in the diamond lattice. The same statement related to unusual surface conductivity of diamond and nanocrystalline diamond powder induced by the hydrogen coverage has been also reported by others in 2000<sup>37</sup>. Photoelectron yield spectroscopy study verified the existence of the superficial conductive layer (SCL) on the diamond-water interface with lower electron emission threshold due to a property called negative electron affinity (NEA) induced by hydrogenation. The NEA is commonly associated with the specific electronic structure of hydrogenated diamond surfaces where the vacuum level ( $E_{\text{vac}}$ ) is located below the minimum of the conduction band ( $E_c$ ). As a consequence, an eased electron extraction may take place due to external stimulation<sup>38,39</sup>.

A similar study performed in 2013 by T. Petit et al., has shown that a surface-transfer doping mechanism is also observed on detonation NDs (5 nm) hydrogenated by microwave plasma<sup>40</sup>. The dispersion of NDs in water resulted in a positive charge (holes) accumulation on the diamond-water interface leading to changes in the electronic structure with the apparition of a band bending. It has been suggested that the position of the Fermi Level can change according to the accumulated holes controlled by the hydrosol's pH. Authors demonstrated via a HCl titration that the highly positive ZP (> 40 mV) is only observed for  $\text{pH} < 9$  whereas an increase in the basicity leads to a decrease of the ZP down to 0 mV (isoelectric point - IEP). At  $\text{pH} \sim 12$ , no electronic band bending occurs due to the water-surface equilibrium resulting in rapid agglomeration of the H-NDs (Figure 3.5).

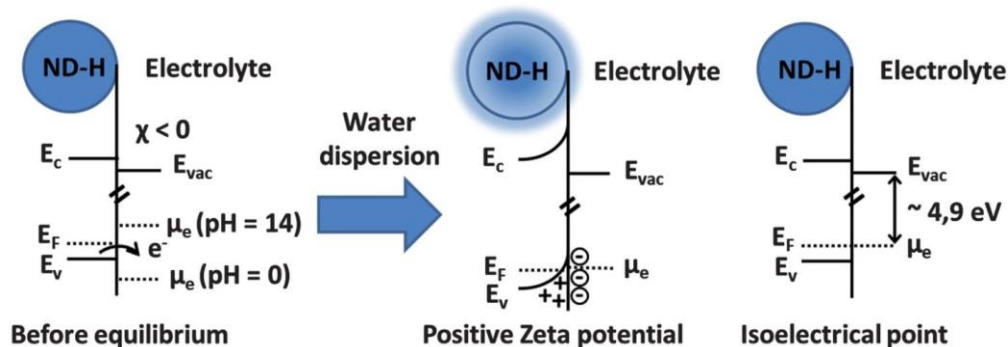


**Figure 3.5** – Surface transfer doping mechanism of plasma H-NDs before and after water dispersion. The electron density in and around the H-NDs is illustrated in blue color. Positive ZP results in band bending and charge accumulation on the surface-water interface<sup>40</sup>.

The combination of DLS, XPS, and SEM studies have also shown that carboxylated NDs, which do not exhibit any surface conductivity in water, does not possess any surface-transfer doping activity (no charge accumulation observed).

The origin of the positive surface charge of vacuum annealed detonation NDs resulted in even more speculations than H-NDs. Petit and co-workers associated it with oxygen hole doping mechanism probed via XPS and FTIR. The chemisorption of  $O_2$  molecules may result in the formation of endoperoxide groups which can be easily protonated explaining the pH-dependent evolution of the ZP<sup>41</sup>. A similar hypothesis of endoperoxide formation has been postulated in 2003 by G. Dukovic et al. for carbon nanotubes<sup>42</sup>. Briefly, the graphitic structures present on the surface are made of basal planes which can adsorb  $O_2$  molecules creating endoperoxide groups. The instability of endoperoxides for  $pH < 7$  results in protonation and transformation of such chemical compounds into hydroperoxide carbocation ( $C-O_2H^+$ ) and the formation of delocalized holes located on  $\pi$ -conjugated planes. The positive ZP should be associated with the behavior of other graphite-like nanocarbons (onion-like carbons – OLCs, fullerene-like reconstructions – FLRs or carbon nanotubes – CNTs) considering that increasing the number of graphitic layers may screen any surface charge of the NDs<sup>43</sup>.

The most recent model published by L. Gines et al. in 2017 stated that the positive surface charge seen on vacuum annealed or hydrogenated NDs comes from the graphitic layers present on the outer shell of NDs<sup>44</sup>. Authors performed Transmission Electron Microscopy (TEM) and Raman study on 50 nm high-pressure high-temperature (HPHT) diamond powder. The results showed that the positive charge is only exhibited in the presence of  $sp^2$ -C structure on the surface whereas clean,  $sp^2$ -free hydrogen annealed NDs have a negative ZP similar to the bulk hydrogenated diamond surface. The positive charge is created when the basal graphitic planes are protonated with  $H_3O^+$  and  $H^+$  ions leaving oxygen-free Lewis sites (filled molecular orbitals with a pair of electrons not involved in chemical bonding) promoting the suppression of acidic functional groups (see below).

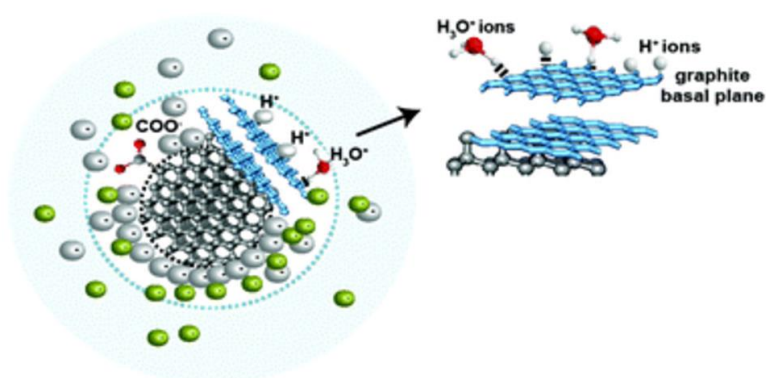


**Figure 3.6** – Model of the positive surface charge of the HPHT NDs created in contact with water ions. Blue color indicates graphitic planes at the surface<sup>44</sup>.

However, a similar study has not been done on the detonation NDs. The HPHT diamond particles have been chosen for their well-defined crystallographic structure and bigger size.

The non-diamond content was removed from the HPHT surface via air annealing. In contrast to, the detonation NDs come with a high content of  $sp^2$ -C present on the outer shell difficult to eliminate by any method. In addition to that, it has been evidenced by XPS, Raman, and XAS that vacuum annealing at 450 °C may already graphitize the surface of detonation NDs due to the presence of metallic impurities in the soft-shell and the high reactivity of 5 nm particles<sup>17</sup>. The same origin of the positive ZP has been also suggested by N. Gibson and co-workers in 2009<sup>12</sup>.

### 3.2.4 Interaction of nanodiamonds with solvents

The interfacial solid-liquid interactions of NDs have attracted research interest. The reactivity of the liquid-dispersed NDs and their possible future applications, e.g. in medicine or other bio-related fields, strongly depends on such interactions. Surface properties of nanometric particles, particularly different compared to larger in size NDs due to their high surface-to-volume ratio, are the key determining factors affecting the reactivity with surrounding molecules (e.g. water, ethanol, buffers).

In 1998, Ji, S. et al. noticed that Ultra-dispersed Detonation Diamond powder (UDD) easily adsorbs atmospheric water<sup>45</sup>. The FTIR study showed an OH stretching vibration spectral band appearing shortly after air exposure. Moreover, the amount of adsorbed water has been controlled in the presence of various gases (air, hydrogen, or nitrogen).

The study of water adsorption on UDD surfaces triggered more experiments and resulted in the proposal of several models for interfacial interactions. In 2007, Korobov et al. suggested the creation of the nanophase water around the detonation ND surface (diameter ca. 5 nm) using the Differential Scanning Calorimetry (DSC) technique. However, the authors did not take into account the initial surface chemistry of the tested NDs<sup>46</sup>.

More recently, Petit et al. in 2015 showed that the organisation of water molecules around the water-dispersed detonation NDs is associated with the initial surface chemistry<sup>47</sup>. Transmission soft X-ray Absorption Spectroscopy (XAS) evidenced a long-range ordering of water molecules with a particular structure on the first solvation shell. The differences in such a water structure have been observed in the presence of NDs with either positive or negative ZP. In particular, oxygen-terminated surfaces with negative ZP break the hydrogen bonds (HB) of water (surface wetting related to the hydrophilic surface properties) whereas the positive ones maintain HB of the interfacial water (surface repulsion due to hydrophobic properties).

Such results are also complementary to the study conducted by Stehlik et al. who investigated water content present on thermally oxidized (Ox-NDs) and hydrogenated (H-NDs) nanodiamond surfaces<sup>48</sup>. The combination of the thermal analysis, the Fourier Transform Infrared Spectroscopy (FTIR), and the Kelvin Probe Microscopy (KPM) techniques revealed that Ox-NDs with negative ZP adsorb less water than the positively charged H-NDs' surface.

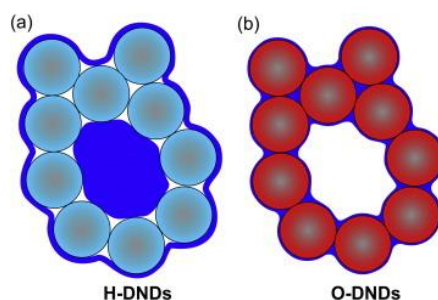


**Figure 3.7** – Model of interfacial interaction between hydrogenated (a) oxidized (b) detonation NDs and water molecules. Blue color indicates water content<sup>48</sup>.

Stehlik, S. et al. have concluded that water content is directly related to the configuration of the water molecules present in proximity of the NDs surface resulting either in a strong (Ox-NDs) or weak (H-NDs) interfacial electrostatic absorption (Figure 3.7)<sup>48</sup>.

The development of a versatile physical and chemical modification technique resulted in a more extensive study of interfacial water interaction between different types of surface-terminated NDs. Similar to the previous study, the specific surface chemistry responsible for the charge of the water-dispersed NDs has been considered as the main factor responsible for the interaction with water molecules on the water-nanodiamond interface.

The most recent study of Petit et al. has compared the HB network of water molecules created around hydroxylated (-OH), hydrogenated (-H), carboxylated (-COOH) and polyfunctional (non-homogenous) NDs surfaces<sup>9</sup>. The FTIR, XAS, and Raman analyzes performed *in situ* in aqueous environments have shown different water structures around positively charged H-NDs surface compared to other surface chemistries. Particularly, no evidence of the HB creation has been presented. However, the long-range interruption of the water network around the H-NDs surfaces has been observed. The authors explained it as being due to the hydrophobic nature of the H-NDs as well as the electron accumulation at the nanodiamond–water interface<sup>9</sup>. The model recently proposed by Petit and co-workers is shown below.

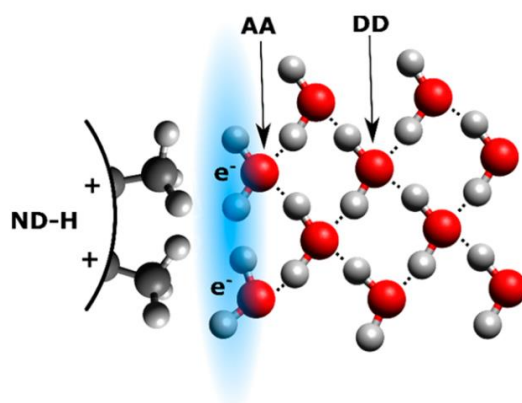


**Figure 3.8** – Model of hydrogen bonding between positively charged H-NDs surface and water molecules in double HB acceptor (AA) and donor (DD) configuration. Blue color indicates interfacial accumulation of electrons with weak HBs marked with dotted lines<sup>9</sup>.

The authors have concluded that the accumulation of electrons on the interface allows to disperse the H-NDs in water as well as stabilize the ND-water structure (Figure 3.8). Until now, no more evidence of another possible HB structure has been presented. More surprisingly, the same behavior as for H-NDs has not been observed on another positively charged poly-functional NDs surface. This has been explained by the presence of OH groups on the NDs surface forming strong HB with water molecules. A remaining question is whether the same electron accumulation mechanism and the lack of HB can be also expected on positively charged NDs with homogenous surface chemistry, e.g. vacuum annealed NDs. Assuming the positive answer, water-dispersion and illumination-induced electron emission properties should be possible.

Finally, in 2016, G. A. Inel and co-workers studied *in situ* interactions between the oxidised NDs after dispersion in another polar solvent such as ethanol by means of Attenuated Total Reflectance Fourier Transform Infrared Spectroscopy (ATR-FTIR). Spectral results showed a specific orientation and an ordering of ethanol molecules around the NDs surface, 60 min after dispersion. The creation of several layers of ethanol and the possibility of the creation of HB via hydrophilic -OH ethanol bond have been suggested by the authors. The model of single-layer arrangement of ethanol adsorbents proposed is presented below<sup>5</sup>.

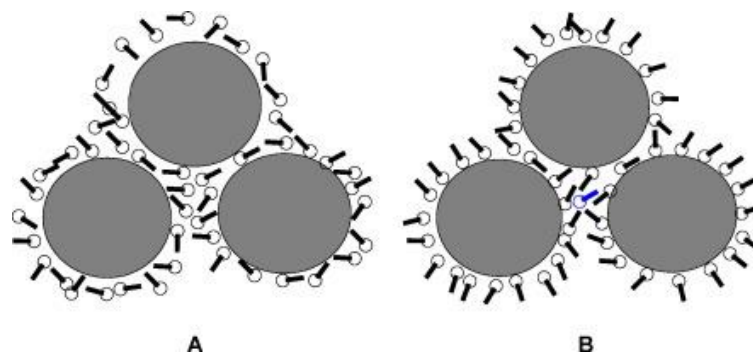


**Figure 3.9** – Model of interaction between air oxidised NDs and ethanol proposed by G. A. Inel *et al.*, in 2016. Hydrophilic -OH groups are indicated by open circles; black sticks represent hydrophobic -C<sub>2</sub>H<sub>5</sub> groups<sup>5</sup>.

### 3.2.5 Summary

- Mechanical milling or ultrasound sonication reduce the hydrodynamic size of the NDs aggregates whereas the centrifugation allows to progressively fractionate the sample according to the size and the molar weight. Only a combination of different treatments leads to well-dispersed NDs hydrosol
- Surface modifications improve deaggregation, water-dispersivity, and colloidal stability of NDs
- Size of NDs in the colloid depends on hydrosol preparation parameters (sonication, milling, and centrifugation)
- Surface-modified NDs exhibit either positive or negative ZP in water depending on the surface termination

- Hydrogenated surface results in the electron accumulation and a specific water structure in the NDs-water interface with no clear evidence of the HB
- Reorganisation of solvent molecules around the NDs surface has been evidenced to be dependent on their surface chemistry.

### 3.3 Nanodiamond hydrosol preparation

Independent of the source and the initial surface chemistry, NDs come in a form of strongly aggregated powder. As this Ph.D. work relies almost exclusively on NDs suspensions, we decided to discuss in detail the general concept and the main factors affecting each step of the preparation protocol of NDs suspension. Even if some experimental points will appear rather obvious, we noticed all along the work that simple details can drastically affect the properties of the colloidal suspension including results of any further experiments. For instance, the way to measure the concentration which is finally poorly described in the literature while essential for any comparative work, the effect of the initial concentration and volume before sonication, the way we can perform the DLS analysis, etc. For these reasons, here will be thoroughly detailed the experimental part of the work done during the Ph.D.

The preparation of a well-dispersed and stable NDs hydrosol requires following a specific protocol based on 4 steps presented below on Figure 3.10.

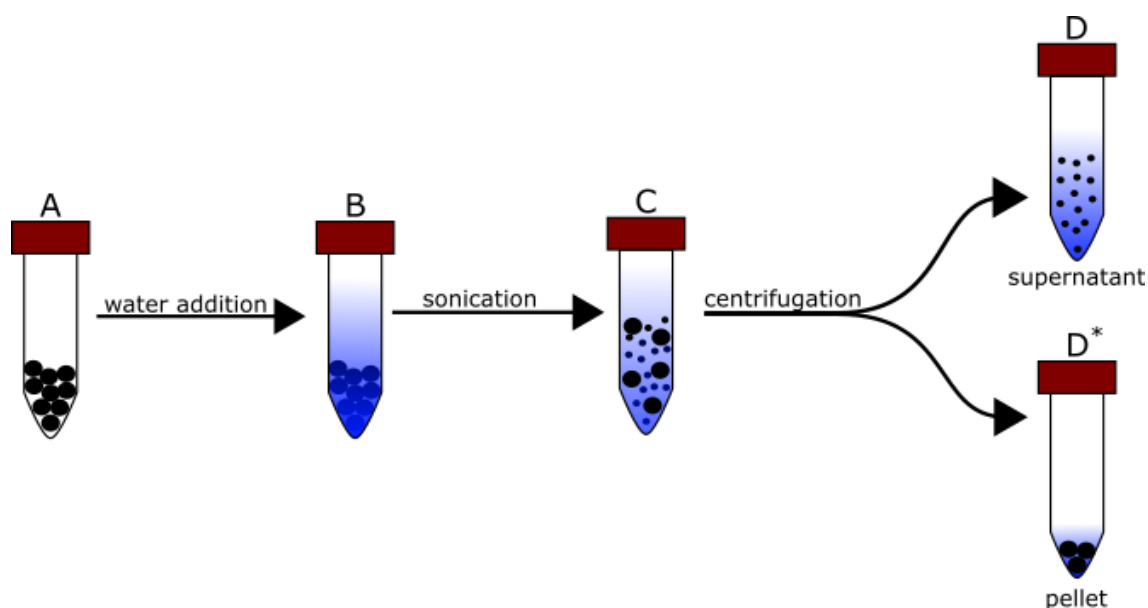


**Figure 3.10** – Schematic illustration of the preparation protocol of nanodiamonds aqueous suspension. Nanodiamonds powder (A) is dispersed in ultra-pure water (B), sonicated (C) and centrifuged (C) followed by supernatant separation (D). Aggregated NDs remaining in the pellet (D\*) can be either nano-waste disposed or re-suspended by repeating the protocol steps.

Briefly, NDs are placed in a falcon followed by the addition of ultra-pure water (steps A and B). Water-mixed NDs are then sonicated for a certain duration of time (step C) to break the agglomerated aggregates followed by a size-separation by a centrifugation method (step D). As a consequence, smaller and well-dispersed NDs remain in water suspension in a form of a

supernatant (D) whereas the larger one forms a pellet made of agglomerated NDs (D\*). Only the supernatant is kept and used for further experiments.

The quality of the NDs water suspension, in terms of colloidal properties, concentration or stability over time, are dependent on the specific parameters used during the sample preparation protocol.

### 3.3.1 Preparation of colloids: general concept of sonication and centrifugation

#### 3.3.1.1 Sonication

In the first step, water-dispersed NDs are sonicated using an ultrasonic power of 400 W generated by an ultrasonic processor (Hielsher UP400S). The sonication power is transferred into the suspension via a sonotrode (H3 type) made of titanium with a tip diameter of 3 mm submerged properly inside the NDs suspension. In order to have comparable results, we decided at the beginning of the work to use an initial concentration always ranging between 4.5 mg.ml<sup>-1</sup> and 5.5 mg.ml<sup>-1</sup>. In the same way, we always used a glass vial (max. volume = 12 ml) filled with 4 ml of suspension during the sonication step, an amplitude set at 80 % (max. sonication power amplitude is 400 W) and a short pulse of 0.5 cycle per second. Effect of the duration of the sonication will be discussed later in the chapter.

#### 3.3.1.2 Centrifugation

As large aggregates remain after sonication, further fractionation of the NDs is required via a centrifugation step. The centrifugation is an effective laboratory and industrial method allowing to increase the rate of sedimentation of larger nanoparticles by exploiting the centrifugal force obtained by rotation. Particles' size and density influence the rate of separation in NDs suspension since it is governed by a force balance between the before mentioned centrifugal force and the drag on the particle. For spherically shaped nanoparticles, this drag is simply given as the Stokes drag (Equation 3.1). For particles of similar density, the particles of larger size sediment quadratically faster as compared to the smaller particles:

$$v = \frac{d^2(\rho - \rho_m) \times g}{18 \mu}$$

#### **Equation 3.1**

Where  $v$  is the sedimentation rate (cm.s<sup>-1</sup>) or velocity of a sphere,  $d$  is the diameter of the NP sphere (cm),  $\rho$  and  $\rho_m$  are the particle and medium densities (g.cm<sup>-3</sup>), respectively,  $\mu$  is the medium's dynamic viscosity (g.cm<sup>-1</sup>.s<sup>-1</sup>) and  $g$  represents the acceleration due to gravity (980.7 cm.s<sup>-2</sup>). The radial force during the fast-spinning of the rotor can be expressed as a relative centrifugal force (RCF) or shortly the ' $g$  force'. The ' $g$ ' value relates to the speed of

rotation (Q) defined as revolutions per minute (rpm) but also depends on the distance (r, in cm) from the sample to the rotation axis (which may vary between different rotor types).

$$RCF = 11.8 \times r \times \left(\frac{Q}{1000}\right)^2$$

### **Equation 3.2**

Note that the centrifugation system automatically calculates the RCF value for the selected type of the rotor according to the adjustable speed of the spinning rotation.

In this work, we studied the effect of the duration as well as the effect of the relative centrifugal force, which will be presented later in the chapter. All other parameters were remained constant, as the volume of suspension centrifuged, the vessel used, and the initial concentration of NDs.

#### **3.3.1.3 Parameters influencing the quality of the suspension**

When preparing the colloidal suspension by successive sonication and centrifugation steps the following parameters should be considered:

(i) Sonication step

- **initial volume of the sample (ml)**
- **initial sample concentration (mg.ml<sup>-1</sup>)**
- **sonication time (min)**
- sonotrode frequency (kHz)
- sonotrode power amplitude (%) and pulse repetition frequency (number of cycles per second)

(ii) Centrifugation step

- **centrifugation time (min)**
- rotation speed (rpm) as a factor responsible for the centrifugal force (RCF)
- **final concentration (mg.ml<sup>-1</sup>) of the NDs suspension**

The main factors such as sonication and centrifugation times, initial and final concentrations have been selected as key parameters responsible for the NDs' colloidal properties including the sample quality in general. However, before the actual effect of sonication and centrifugation parameters is investigated, the method to measure a concentration of NDs in water needs to be established. The concentration measurement is a key parameter allowing to compare the colloidal properties of different NDs suspensions.

### 3.3.2 Suspended-solid concentration measurement

The centrifugation step results in a partial loss of mass of NDs due to a separation of the supernatant and the pellet. Consequently, the concentration of the supernatant is lower compared with the initial sample. The problem of accurate suspended-solid concentrations related to the NDs has been encountered by many<sup>49</sup>. Up-to-date, spectroscopy techniques such as spectrophotometry and thermal lens spectrometry, have been widely studied. Both techniques have detection limits from 60 ng.ml<sup>-1</sup> up to 2 µg.ml<sup>-1</sup>, depending on the NDs type but are not drawback-free<sup>50</sup>. The high complexity of the experimental set-up and the calibration procedure are required whereas the results are affected by the presence of a background and a convective noise<sup>51</sup>. These techniques are also quite sensitive to the level of agglomerates present in the suspension, which is difficult to control precisely especially when playing with the surface chemistry. Furthermore, the NDs suspension preparation protocol in a routine way requires simplicity. In the next section, two alternative and simple methods for the concentration estimation are presented and discussed.

#### 3.3.2.1 First method – weight scale balance

Presumably, the simplest way to estimate the concentration of NDs is to measure the mass of the dry powder before and after making the suspension using an analytical weight scale (brand: Mettler Toledo, model: Quantos QB1). To start with, the mass of the dry NDs ( $m_0$ ) placed inside a falcon, of known weight, is measured (Figure 3.11 – A). Hereafter, the NDs suspension is sonicated and centrifuged, followed by the supernatant separation step (Figure 3.11 – B, C, and C\*).

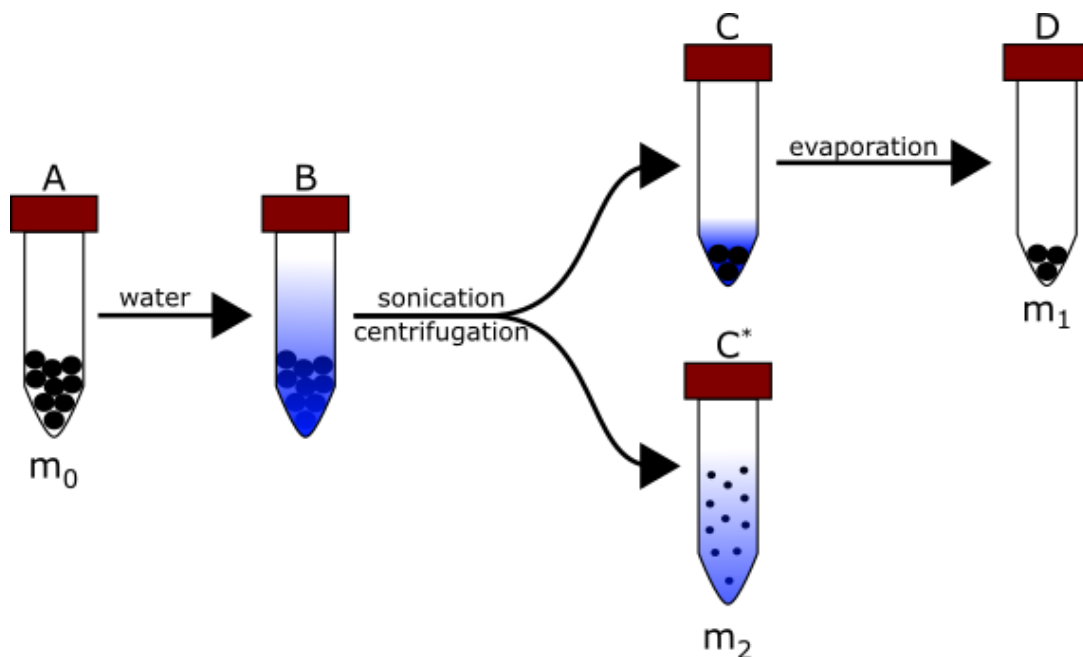


**Figure 3.11** – Schematic illustration of the first method of concentration estimation.

The remaining water suspension containing non-suspended NDs is left for drying overnight. The total mass of the dry pellet and the falcon ( $m_1$ ) is measured once again (Figure 3.11 - D) and subtracted from the initial mass of the dry powder ( $m_0$ ). Assuming a conservation of the ND mass, the difference between  $m_0$  and  $m_1$  will give the mass of NDs present in the supernatant.

$$m_2 = m_0 - m_1$$

### Equation 3.3

Finally, the mass concentration ( $C_m$ ) of the NDs suspension is equal to the mass difference ( $m_2$ ) divided by the volume ( $V$ ) of the supernatant separated using the high precision micropipette with adjustable volume (Biosigma HP<sub>PETTE</sub>, volume range: 100 - 1000  $\mu$ l):

$$C_m = \frac{m_0 - m_1}{V}$$

### Equation 3.4

The error of such concentration estimation can be calculated as:

$$\partial_{C_m} = C_m * \left( \frac{\partial V}{V} + \frac{\partial m_0 + \partial m_1}{m_0 - m_1} \right)$$

### Equation 3.5

Where the volume error is the square-sum of the random error ( $\partial V_{random} = 0.6 \% = 0.006$ ) and the systematic error ( $\partial V_{systematic} = 0.2 \% = 0.002$ ) according to the micropipette producer.

The main limitation of this technique is related to having two measurements of the mass; the initial mass ( $m_0$ ) of the NDs powder and the final mass ( $m_1$ ) of the pellet. Errors are thus doubled due to the subtraction involved in the calculation of the final mass. In turn, both the final mass and the error are comparable causing a large relative error. In addition to that, NDs are highly electrostatic and as they are placed inside the falcon, it causes loss of mass thus adding an additional error to this technique. Addition of water requires the falcon to be reopened after mass  $m_0$  measurement resulting in an supplementary loss of NDs. During the measurement of the final mass  $m_1$ , the high hydrophilicity of the NDs causes also mass variation. This happens even when performing a long drying (e.g. 24 h) procedure. Despite careful sample handling during these experiments, this method exhibited a very low reproducibility. That the uncertainties are coupled to the unstable measurement procedure, rather than the sample preparation, is corroborated through the observation that the initial suspensions had similar colors indicating similar NDs environments. As an example, Table 3.2 reports final concentrations measured for suspensions prepared with the same protocol and which appeared visually very similar.

$m_0$ (mg)	$m_1$ (mg)	$V$ (ml)	$C_m$ (mg.ml <sup>-1</sup> )
23.860 ± 0.005	20.345 ± 0.005	4.0 ± 0.8 %	0.879 ± 0.008
22.255 ± 0.005	17.055 ± 0.005	4.0 ± 0.8 %	1.300 ± 0.011
21.040 ± 0.005	9.285 ± 0.005	4.0 ± 0.8 %	2.939 ± 0.021

**Table 3.2** – Mass measurements of plasma H-NDs dry powder and resulting final concentration obtained using the analytical weighing scale. The same conditions for the colloidal suspension preparation were applied.

This method was rapidly abandoned in the preparation protocol. A better approach would be a direct measurement of the NDs mass ( $m_2$ ) present in the supernatant, since this would remove the largest contributions to the uncertainty. The new strategy is dependent on having access to a more precise microbalance.

### 3.3.2.2 Second method – microbalance

This method aims to measure directly the mass of the NDs dispersed in the supernatant using a microbalance (Mettler Toledo, XS microbalance) and a silicon (Si) wafer. Both microbalance and Si wafers are stored in a clean room with humidity control to avoid additional water adsorption on the Si pieces during the experiment. Firstly, the mass of a small piece of Si wafer is measured ( $m_0$ ) followed by deposition of two droplets (10 µL each) of the NDs suspension using a regularly calibrated micropipette (Rainin Classic Pipette, PR-10) with microliter precision (Figure 3.12 – A and B). After evaporation of water, the NDs are firmly attached to the Si surface allowing to measure their mass as a difference between the initial mass of the Si wafer and after the drying step (Figure 3.12 - C).

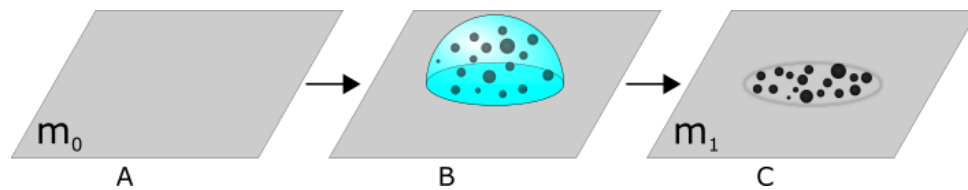


**Figure 3.12** – Sketch of the NDs concentration measurement method using silicon wafer.

The final concentration is a function of the mass difference and the deposited volume ( $V$ ) of the droplet. Note that all mass measurements are repeated three times by removing and redepositing the sample on the balance each time.

$$C_m = \frac{m_1 - m_0}{V}$$

#### Equation 3.6

This method was first tested using commercial NDs suspension (Adamas Nanotechnologies, ND-H2O-5P, 5 nm, 1 wt.% slurry in DI water) where the concentration of NDs is already given by the producer. As-received and diluted NDs suspensions have been used for the experiment. For a start, three Si wafers were used to check the initial concentration of the NDs suspension (10 mg.ml<sup>-1</sup>). Two drops of 10 µl of NDs were deposited with a micropipette

on each piece of Si wafer and let for drying over 5 h in ambient conditions in a clean room in order to avoid any possible contamination. Note that the minimum drying time has been verified, and after 3 h, no difference is seen on the final mass measurement. Then, the commercial NDs suspension was diluted by a factor of 10 (100  $\mu\text{l}$  of suspension plus 900  $\mu\text{l}$  of ultra-pure water) using the same micropipette and tested in the same way as the previous sample. Results are shown in Table 3.3.

Silicon wafer measurement	Expected concentration (mg.ml <sup>-1</sup> )	Measured concentration (mg.ml <sup>-1</sup> )	Expected concentration (mg.ml <sup>-1</sup> )	Measured concentration (mg.ml <sup>-1</sup> )
1	10	10.9 $\pm$ 0.6	1	1.2 $\pm$ 0.2
2	10	10.9 $\pm$ 0.6	1	1.2 $\pm$ 0.2
3	10	11.1 $\pm$ 0.6	1	1.2 $\pm$ 0.2

**Table 3.3** – Microbalance concentration measurements using Si wafer method for the commercial detonation NDs suspension produced by Adamas Nanotechnology.

It has been shown that this method works well for both high and low concentrations of commercial NDs and the results stay within the range  $\pm 10\%$ . Since the method used by the manufacturer to measure the NDs concentration in solution remains unknown, we can surely see that the method is accurate and reproducible. The dilution of the initial sample introduces an additional error. However, the dilution factor as a function of the averaged final concentration before and after dilution is equal to 9.2. In fact, the NDs suspension prepared in the laboratory has a final concentration included between 1 - 3 mg.ml<sup>-1</sup> which does not require any dilution step. In addition to that, a very small volume (microliters) of the liquid is used for the microbalance test making this method even more effective.

The error of the microbalance measurement presented in Table 3.3 is a combination of two independent errors related to the microbalance mass measurement and the micropipette volume of the sample. Mass measurement error is the sum of a random microbalance mass reading error ( $\partial m_{0,1} = 0.001$  mg) and the microscale reading precision ( $\partial_{scale} = 0.0005$  mg) given as:

$$\partial_m = \sqrt{\left(\frac{\partial m_0 + \partial m_1}{m_0 - m_1}\right)^2 + \left(\frac{\partial_{scale}}{m_0 - m_1}\right)^2}$$

#### Equation 3.7

Volume measurement error, given by micropipette quality certificate, is a sum of random error ( $\partial V_{random} = 1.9\% = 0.019$ ) and the systematic error ( $\partial V_{systematic} = 3.8\% = 0.038$ ) where the latter varies depending on the measured sample volume and the producer:

$$\partial_v = \sqrt{\left(\frac{\partial V_{random}}{V}\right)^2 + \left(\frac{\partial V_{systematic}}{V}\right)^2}$$

#### Equation 3.8

The final error value can be expressed as:

$$\partial_{C_m} = error \times C_m = (\partial_v + \partial_m) \times C_m$$

### Equation 3.9

In conclusion, the microbalance method has been selected as a ‘gold standard’ for the experimental protocol due to its simplicity, high reproducibility, and efficiency using a small sample volume. The time required to dry the microliter droplet deposited on the Si wafer is lower compared to complete the water evaporation of the larger volume (ml) from the pellet which makes it also very time-effective. Moreover, all along the Ph.D. work, this technique was regularly checked using commercial suspensions to ensure its validity.

In the next part, the characterization technique of NDs colloidal suspension is presented and discussed.

### 3.3.3 Characterization of colloids: Dynamic Light Scattering

Several methods such as Dynamic Light Scattering (DLS), Single Particle Tracking (SPT), Small Angle X-ray Scattering (SAXS) or microscope-based techniques, e.g. Atomic Force Microscopy (AFM), Transmission Electron Microscopy (TEM) and optical microscopy, are commonly used to characterize the dimensions of the nanoparticles. Each technique can assess a certain size range and could be applied to either powder or colloid. The narrow size distribution (3 - 10 nm) of the primary NDs produced by detonation and the high polydispersity of the NDs aggregates in colloidal suspension significantly limits the choice of the characterization techniques. Consequently, the DLS is mainly employed allowing to detect and characterize NDs as small as 1 nm up to 1  $\mu\text{m}$  depending on the producer and character of the sample.

#### 3.3.3.1 Hydrodynamic size distribution measurement

The DLS provides information about the size measuring the hydrodynamic diameter ( $d_h$ ) or radius ( $r_h$ ) of the particles dispersed in suspension. For a polydisperse system, the DLS gives access to the size distribution of the objects present in suspension including an additional thin layer of solvated ions surrounding the surface. The measurement itself is possible due to a laser (HeNe) used as a source of light tracking the time-dependent changes in the colloidal suspension induced by the intensity variations of the scattered light (backscattered angle of 173°). According to the Rayleigh theory, measured light intensity is directly proportional to the particle diameter  $I \propto d^6$  including the shell of solvated ions (Figure 3.13).

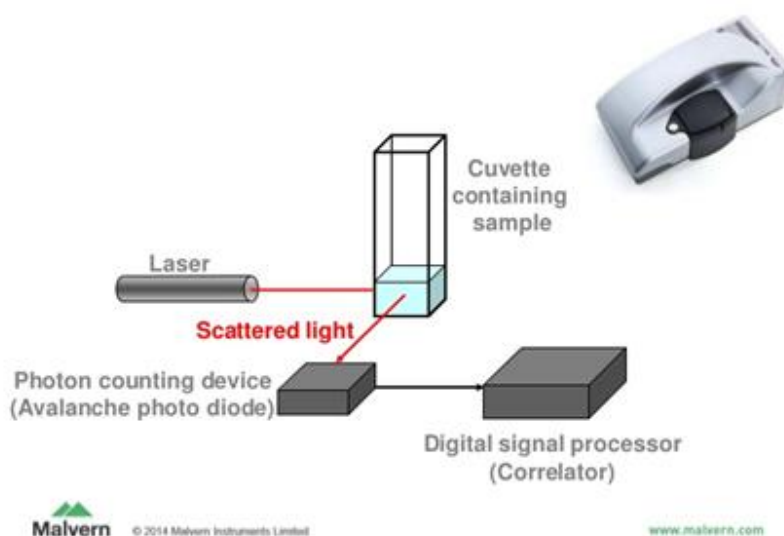


**Figure 3.13** – Principle of Dynamic Light Scattering measurement. (source: Malvern.com)

NPs dispersed in colloidal suspension move with a constant and random motion (so-called Brownian motion). However, this movement is affected by the particle size, the molecular weight (slower movement of the larger and heavier particles), the sample viscosity but also by the temperature (faster movement at higher temperature). Difficulties arise when we attempt to analyze single 5 nm NDs which tend to aggregate creating larger, non-spherical aggregates (Figure 3.14 - B) responsible for the polydisperse nature of the NDs suspension. The DLS uses an approximation of a spherical particle shape and is not detected easily, for instance, during the linear aggregation state (Figure 3.14 - C).

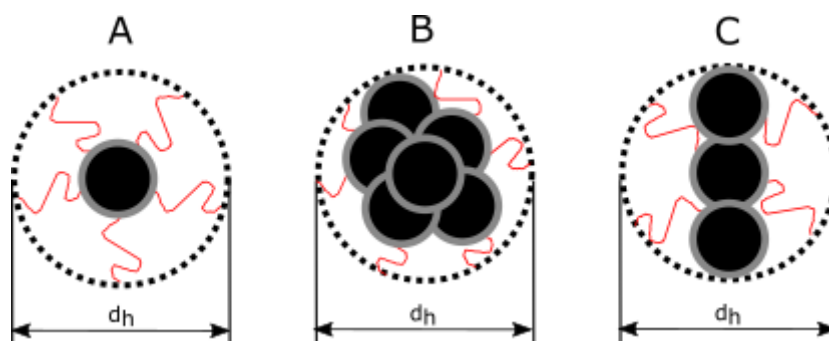


**Figure 3.14** – Hydrodynamic diameter (black, dashed line) representation measured by the DLS. Black solid color represents nanoparticles surrounded by a thin shell of solvated ions (grey contour). Red lines simulate the Brownian motion of the particles.

As a consequence, the value of  $d_h$  given by the DLS may be much higher than the real diameter of NDs making the results only an approximated model.

## 3.3.3.2 Zeta Potential measurement

The DLS instrument can also be used to estimate the surface charge of NDs in a given medium (e.g. water) via Zeta Potential (ZP) measurement. Positive or negative surface charges of NDs dispersed in colloidal suspension attracts oppositely charged solvent ions creating a thin, double-layer around the surface (so called electrical double layer). The first part of the double-layer direct attached to the ND surface is named Stern-layer whereas the second one is called a slipping plane. Consequently, the ZP is defined as an electric potential measured on the boundary of the double-layer (more precisely on the boundary of the slipping plane) and the solvent ions. In the previous paragraph, it has been mentioned that the size distribution measurement is affected by the presence of this double-layer. In addition to that, surrounding surface ions can also travel together with the NDs when the electric field is applied allowing to measure the conductivity of the sample. The magnitude of the ZP is used to predict colloidal behavior and stability of NDs in the solvent. An absolute value of the ZP below 30 mV may suggest aggregation of the NDs via Van Der Waals inter-particle attraction mechanism. In contrast, the highly charged NDs possessing the absolute value of the ZP higher than 30 mV remain stable in colloidal suspension due to repulsive forces. The presence of such forces effectively prevents progressive agglomeration of the NDs leading to their flocculation. The schematic diagram explaining the principle of the ZP measurement is presented below.

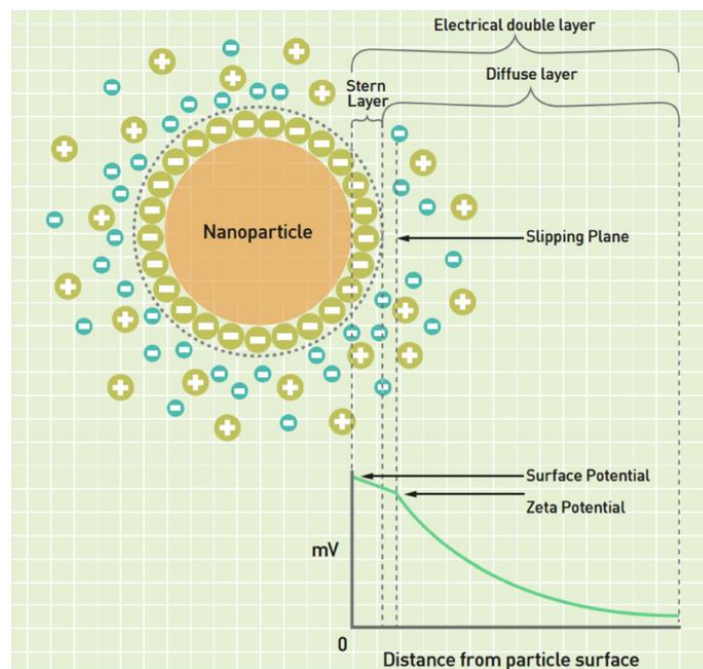


**Figure 3.15** – Principle of Zeta Potential measurement. The precise location of the Stern layer and the slipping plane can be associated with the idea behind the creation of the electrical double-layer of solvated ions around the surface of charged NDs. (source: Malvern.com)

### 3.3.4 Representation of the dynamic light scattering results

DLS technique offers multiple modes to present results. The parameters (e.g. number of measurements, absorption coefficient, refractive coefficient, viscosity, temperature etc.) used during the measurements are determined individually by the user. Herein, the short description of each mode tested for commercial NDs (Adamas Nanotechnologies, ND-H2O-5N, 5 nm, 1 wt.%, ZP = -50 mV) is presented giving its advantages and disadvantages.

#### 3.3.4.1 Size distribution by Intensity

The most direct way to present hydrodynamic diameter distribution is to measure the weighted intensity of the backscattered light. Since the intensity is directly proportional to the diffusion of the objects, it is more sensitive to the presence of aggregates or larger particles. The presence of larger particles dominates the final size distribution while masking the fraction of small NDs. The results obtained show size distribution with mean values being the most representative one. Each NDs characterization is done by measuring three times the same sample at concentration of  $1 \text{ mg.ml}^{-1}$  (Figure 3.16).

The perfect NDs suspension with narrow size distribution should give only one peak with a similar mean value obtained during the three independent measurements, but in reality it is rarely the case.

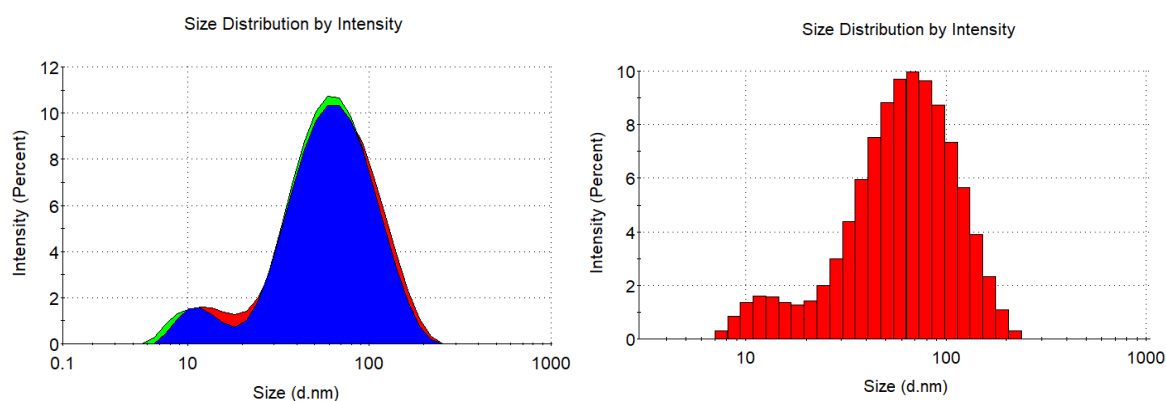


**Figure 3.16** – DLS distribution of the hydrodynamic size given by measured intensity of the backscattered light. The left plot represents three independent and overlapping measurements, peak area of each measurement is colored (1<sup>st</sup>- red, 2<sup>nd</sup> - green, 3<sup>rd</sup> - blue) and the corresponding mean values with standard deviation (peak broadening) are given in Table 3.4. The right plot shows histogram of the 1<sup>st</sup> measurement (red) which will be used to present and discuss properties of surface-modified NDs given by intensity.

The DLS results with intensity peak values and weighted mean intensity of the overall distribution for commercial NDs suspension are presented below.

Measurement	Peak 1 (nm)	Inten. (%)	Peak 2 (nm)	Inten. (%)	Peak 3 (nm)	Inten. (%)	Weighted mean inten. (nm)
1	73 ± 37	92 %	13 ± 3	8 %	0	0	69
2	70 ± 33	93 %	11 ± 3	7 %	0	0	66
3	71 ± 35	93 %	12 ± 3	7 %	0	0	67
Mean peak value	71 ± 2	93 %	12 ± 1	7 %	0	0	67 ± 2

**Table 3.4** – Corresponding peaks values of the DLS size distribution by intensity. Weighted mean intensity is automatically calculated by the DLS based on the contribution of the peaks in measured light scattered intensity in %. The grey field highlights the final value which will be used to present size distribution by intensity as an average value of 3 independent, consecutive measurements.

More sensitive to the presence of aggregates, the intensity size distribution mode can be used to evaluate the aggregation state of the NDs suspension or at least the evolution of their polydispersity. In this work where we aim to look at the stability over the time of the suspension, this parameter will be helpful. The progressive agglomeration and the appearance of some larger agglomerates leads to a higher mean intensity due to immediate broadening of the size distribution peaks. In the case of multiple peaks, the way to analyze and present the data is to calculate the weighted mean intensity value of the 3 peaks obtained during the 3 independent measurements (grey field in the Table 3.4) as it gives the information about the colloidal properties and the stability of the system.

#### 3.3.4.2 Size distribution by Number

Another way to present the DLS results involves the hydrodynamic size distribution given by numbers derived directly from the measured intensity. Size distribution by number show a relative amount of material for a given particle refractive index and absorption. Indeed, these properties are size-dependent and the main drawback of this method comes from the transformation from intensity to volume / number requiring to know the optical properties (e.g. refractive index) of the sample. In addition to that, the transformation is based on Mia theory which describes how particles of different sizes and optical properties scatter light assuming a spherical shape only. The plot (Figure 3.17) presents the size distribution for the same commercial NDs suspension (Adamas Nanotechnologies, concentration = 1 mg.ml<sup>-1</sup>) as in the previous section.

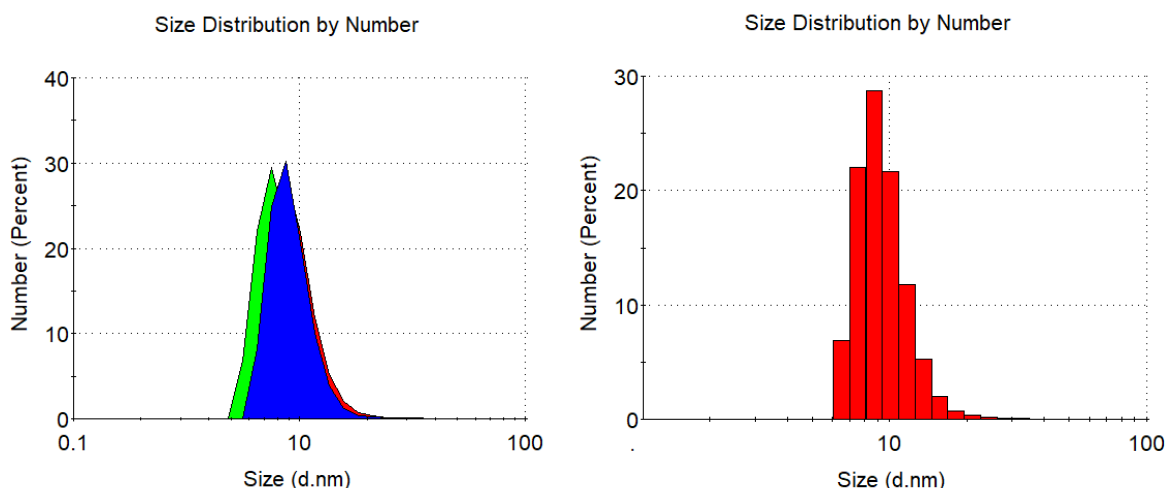


**Figure 3.17** – DLS distribution of hydrodynamic size given by number. The left plot represents three independent and overlapping measurements, peak area of each measurement is colored (1<sup>st</sup> - red, 2<sup>nd</sup> - green, and 3<sup>rd</sup> - blue) and the corresponding mean values with standard deviation (peak broadening) are given in Table 3.5 below. The right plot shows the histogram of the 1<sup>st</sup> measurement (red) which will be used to present and discuss properties of surface-modified NDs given by number.

Measurement	Peak 1 (nm)	Inten. (%)	Peak 2 (nm)	Inten. (%)	Peak 3 (nm)	Inten. (%)	Weighted mean inten. (nm)
1	10 ± 3	100	0	0	0	0	10
2	8 ± 2	100	0	0	0	0	8
3	9 ± 2	100	0	0	0	0	9
Mean peak value	9 ± 1	100	0	0	0	0	9 ± 1

**Table 3.5** – Corresponding peaks values of the DLS size distribution by number. The weighted mean number is automatically calculated by DLS based on % contribution of the peaks. The grey field highlights the final value which will be used to present size distribution by number as an average value of 3 independent, consecutive measurements.

The ND size distribution by number is significantly different compared to the size distribution by intensity with lower mean peak values (Table 3.5). In this mode, we have access to the hydrodynamic size of the majority of the particles in suspension, which is not affected by the presence of larger particles. This mode can be used to assess the properties of NDs in terms of main population.

## 3.3.4.3 Zeta Potential

NDs are charged either positively or negatively depending on their surface chemistry. The sign and the value of the surface charge is directly related to the measurement of the Zeta Potential (ZP). The movement of NDs produces a frequency shift in the applied electric field which is either higher (positive ZP) or lower (negative ZP) compared to the modulator frequency (320 Hz). The example of the ZP measurement performed on commercial NDs (Adamas Nanotechn., ND-H2O-5N, 5 nm, 1 wt.%, ZP = - 50 mV) is detailed below.

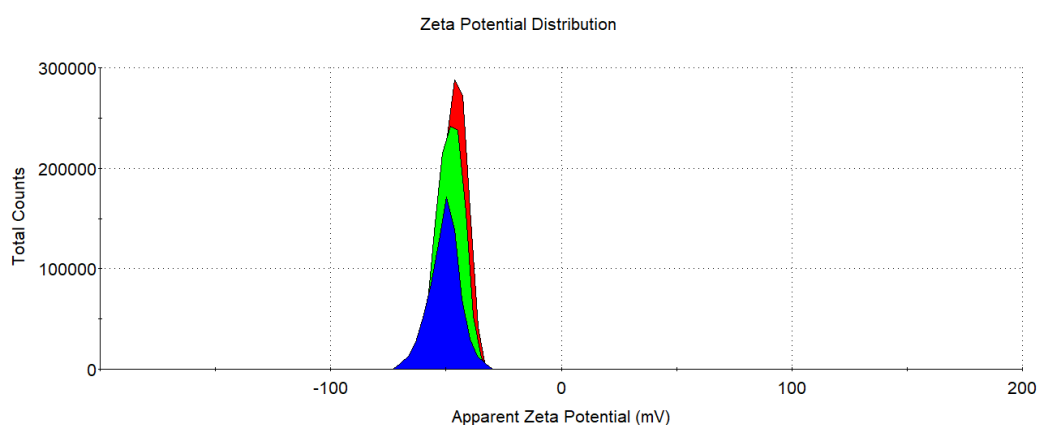


**Figure 3.18** – Zeta Potential distribution of the three independent DLS measurements. Colored peaks represent each DLS measurement (1<sup>st</sup> - red, 2<sup>nd</sup> peak - green, and 3<sup>rd</sup> peak - blue).

The ideal ZP measurement shows one fine peak with the mean value being nearly the same for each of the three measurements performed. The sample instability related either to the non-homogenous surface chemistry or NDs' aggregation gives several peaks with a multiple mean peak value and a DLS measuring error (low data quality). One example of good ZP measurements with only one peak detected during each run is given in Table 3.6.

Measurement	Peak 1 (mV)	Area (%)	Peak 2 (mV)	Area (%)	Peak 3 (mV)	Area (%)	Mean Zeta Potential (mV)
1	- 46 ± 5	100	0	0	0	0	- 46
2	- 48 ± 6	100	0	0	0	0	- 48
3	- 50 ± 7	100	0	0	0	0	- 50
Mean peak value	- 48 ± 2	100	0	0	0	0	- 48 ± 2

**Table 3.6** – Mean peaks values of the Zeta Potential measurement given by DLS for commercial Adamas Nanotechnologies NDs. The final value is in close proximity with the one given by the producer (- 50 mV).

The final ZP value presented in this Ph.D. work is calculated as a mean peak value of the three measurements with a standard deviation between the 3 peaks (the grey field in the Table 3.6). The measurement of the ZP brings information about the surface chemistry (in accordance with the FTIR spectra) and the colloidal stability (repulsion / attraction forces) of the NDs suspension. It is important to note that the ZP value is not equal to exact surface

charge of the NDs. The ZP value only represents the potential difference between the surface of the NDs dispersed in a conducting liquid (e.g. water) and the bulk liquid. As a consequence, the ZP is also solvent-dependent in terms of nature and conductivity. During the Ph.D. work, most of the ZP measurements have been done on the NDs dispersed in ultra-pure water, without addition of salts or stabilizer.

### 3.3.5 Calibration of the DLS equipment

Before establishing a precise characterisation protocol, the reliability of the DLS measurement was tested according to the standardized quality control test. Monodispersed, spherical latex beads with a known hydrodynamic diameter ( $d_h = 200 \pm 6$  nm) are commonly used to test the accuracy and the precision of the DLS equipment. A step-by-step calibration procedure, given by the manufacturer (Malvern company) was completed to check the accuracy of the equipment used in the LCD laboratory. The details regarding the measurements are enclosed in the Appendix (section A.2).

#### 3.3.5.1 Measuring cuvette

Once the DLS equipment is calibrated and fully operational, the measuring cuvette type has to be chosen. Generally, there are two different types. Some cuvettes are designed to measure only the hydrodynamic size distribution of NDs, while others can be used for both the size and the ZP analysis. A comparison of the results obtained using the two different types of cuvettes was performed by measuring the hydrodynamic diameter of the commercial NDs suspension (Adamas Nanotechnologies, ND-H20-5N, 5 nm, ZP = - 45 mV, concentration 0.1 mg.ml<sup>-1</sup>). Table 3.7 summarizes these findings.

Cuvette type	Weighted mean intensity (nm)	Weighted mean number (nm)	Mean Zeta Potential (mV)
Dispensable micro cuvette (ZEN0040)	35 ± 1	19 ± 1	n/a
Dispensable sizing cuvette (DTS0012)	34 ± 1	20 ± 1	n/a
Clear dispensable zeta cell (DTS1070)	36 ± 1	18 ± 1	- 45 ± 2

**Table 3.7** – Results of the hydrodynamic size distribution (weighted mean intensity and number) and Zeta Potential measurements (uncertainty obtained as standard sample deviation,  $n = 3$ ) for 0.1 mg.ml<sup>-1</sup> of commercial NDs water suspension at ambient temperature for three types of measuring cuvettes.

The weighted means (by intensity and number) of the hydrodynamic size measurements are consistent from cuvette to cuvette, as seen by the overlapping estimates when including their standard deviation. It can be concluded, that the measured hydrodynamic diameters are not affected by the type of testing cuvette. However, only the clear dispensable zeta cell

(DTS1070) allows analysis of the ZP of NDs without transferring the suspension into another cuvette. For this reason, the zeta cell was chosen as it decreases the duration of the NDs characterization without compromising the quality. Tested DLS cuvettes are presented below.



**Figure 3.19** – Dynamic light scattering measuring’s cuvettes. (source. Malvern.com)

### 3.3.5.2 Effect of sample concentration

Since the DLS characterization is an intensity-based technique, another factor which may affect the quality and reliability of the measurements is related to the concentration of the NDs dispersed in a liquid. This aspect is very important in this work as some of the DLS characterization will have to be done on ultra-fresh suspension with unknown concentration (estimated), as it will be explained later. Therefore, the effect of NDs concentration is discussed here and a range of acceptable concentration for ‘blind’ measurements will be decided.

Up to now, the commercial NDs suspension (Adamas Nanotechnologies) was diluted down to  $0.1 \text{ mg.ml}^{-1}$  according to the official recommendation given by the DLS producer (Malvern company) for a measured size  $< 100 \text{ nm}$  (grey field, Table 3.8).

Particle size	Min. concentration (recommended)	Max. concentration (recommended)
$< 10 \text{ nm}$	$0.5 \text{ mg.ml}^{-1}$	Only limited by the sample material interaction, aggregation, gelation etc.
10 nm to 100 nm	$0.1 \text{ mg.ml}^{-1}$	5 % of mass
100 nm to $1 \mu\text{m}$	$0.01 \text{ mg.ml}^{-1}$ ( $10^{-3}$ % of mass)	1 % of mass
$> 1 \mu\text{m}$	$0.1 \text{ mg.ml}^{-1}$ ( $10^{-2}$ % of mass)	1 % of mass

**Table 3.8** – Malvern’s recommendations for the DLS measurements. The grey field indicates measured size distribution of the commercial NDs suspension with the corresponding concentration recommended by the producer. (source. Malvern.com)

However, NDs concentration may slightly vary from sample to sample even when using the same protocol, and it can happen that DLS characterization has to be performed before actually knowing the precise concentration of the NDs (microbalance method, section 3.3.2.2). We therefore investigated the effect of the concentration on the DLS measurements with NDs.

DLS characterization was performed for six different concentrations (5.0, 1.0, 0.5, 0.1, 0.05, 0.01 mg.ml<sup>-1</sup>) of commercial NDs (Adamas Nanotechnologies) suspension (Figure 3.20).

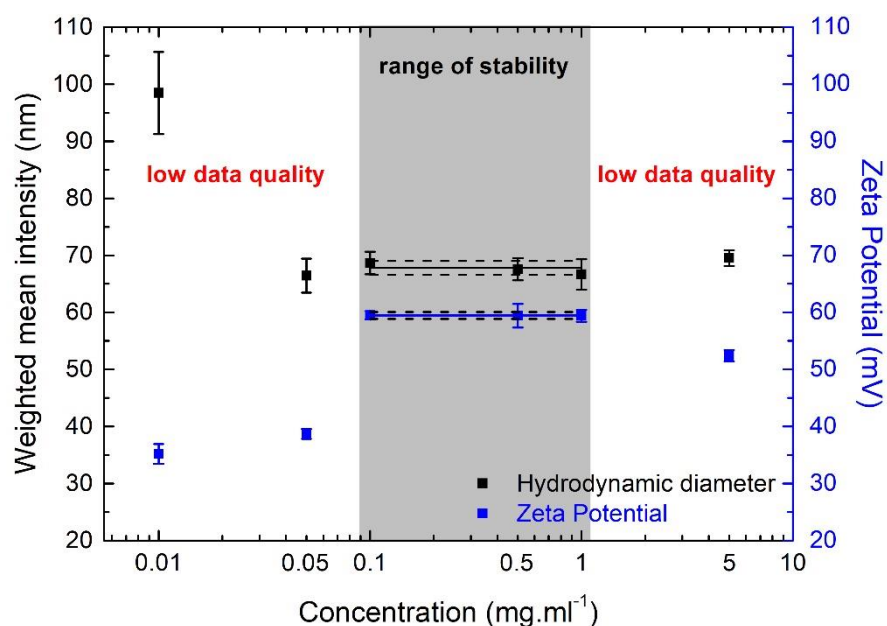


**Figure 3.20** – Weighted average of hydrodynamic diameter (by intensity) and Zeta Potential values obtained for varying concentrations of the commercial NDs. The range of stability is highlighted in grey and the three data points within are used to calculate the stable level as the weighted mean values (diameter - solid black line, ZP - solid blue line) with uncertainty (diameter - dashed black line, ZP - dashed blue line).

The results show the concentration-dependency of the measured hydrodynamic size and the ZP values. The two diluted samples (concentration < 0.1 mg.ml<sup>-1</sup>) leads to an artificial increase of the hydrodynamic diameter due to a low number of NDs detected by the instrument. In contrast, concentration > 1 mg.ml<sup>-1</sup> results in high absorption and multiple scattering effects giving the lower intensity of the measured light and smaller value of the final hydrodynamic diameter. The ZP is also linked to the hydrodynamic size measurement as the number of the NDs affects the particle mobility in water induced by the electric field. When the electric field is applied, presence of a highly concentrated suspension (> 1 mg.ml<sup>-1</sup>) limits the electrophoretic movement of NDs toward oppositely charged electrodes. Consequently, the lower net charged (lower ZP) is detected. In terms of low ND concentration (< 0.1 mg.ml<sup>-1</sup>), the ZP measurement becomes more difficult due to small overall sample conductivity lowering the general ability of the DLS to detect any charged NDs<sup>52</sup>. Based on the results obtained and recommendations given by the Malvern company, the aqueous concentrations included between 0.1 mg.ml<sup>-1</sup> and 0.5 mg.ml<sup>-1</sup> will be used for further experiments with NDs. These values are also in close agreement with the literature where NDs concentrations of 0.2 mg.ml<sup>-1</sup> and 0.3 mg.ml<sup>-1</sup> were prepared for the sample characterization using the DLS technique<sup>53,3</sup>.

### 3.3.5.3 Summary

- (i) Measurements of NDs concentration with microbalance and Si wafers method
- (ii) DLS characterization:
  - Size distribution by intensity for the polydispersity of the suspension and size distribution by number for the hydrodynamic diameter of the main population
  - NDs concentration range for the DLS characterization: 0.1 - 0.5 mg.ml<sup>-1</sup>
  - Zeta cell (DTS1070) as a measuring cuvette.

### 3.3.6 Optimization of the NDs colloid preparation

In the previous part, a general description of the methods used for the preparation of NDs hydrosol (sonication, centrifugation, and concentration measurement) were presented. The method of sample characterization by the DLS technique followed by appropriate analysis of the results was discussed with respect to commercial NDs suspension provided by Adamas Nanotechnologies.

In this part, the actual influence of the selected parameters is discussed as a part of the preparation protocol (sonication and centrifugation time, initial and final concentrations of NDs, etc). The following experiments have been conducted on plasma hydrogenated NDs (250 W, 12 mbar, 10 sccm, 20 min) because the majority of this Ph.D. work focuses on the properties of the H-terminated surface. The key parameters associated with sonication, centrifugation, and sample temperature together with colloidal properties of H-NDs are examined.

#### 3.3.6.1 Effect of sonication time

The sonication step reduces the size of the aggregated NDs dispersed in water suspension. Herein, an influence of the sonication time (20, 60, and 120 min) on the hydrodynamic diameter was tested. The other parameters (amplitude = 80 %, pulse repetition frequency – PRF = 0.5 cycle per second, titanium ultra-sound probe H3, sample volume = 4 ml) were kept constant. The centrifugation time was set to 40 min corresponding to the centrifugation force of 3260 g and the rotation speed of 4500 rpm (rotor 11192). The experiment aimed to establish whether the sonication time affects the final hydrodynamic diameter of the plasma H-NDs (Table 3.9).

Sonication time (min)	Centrifugation time (min)	Weighted mean intensity (nm)	Weighted mean number (nm)
20	40	99 ± 3	36 ± 9
60	40	100 ± 1	24 ± 5
120	40	95 ± 1	40 ± 2

**Table 3.9** – Effect of increasing sonication time on colloidal properties of plasma H-NDs suspension. The DLS characterization (weighted mean intensity and number of three measurements was performed within 1 h after suspension preparation).

At first glance, it can be noticed that the sonication time (grey field in the Table 3.9) has a small influence on the measured hydrodynamic diameter (weighted mean intensity), with the smallest size obtained after 120 min ( $95 \pm 1$  nm) as one could expect. The hydrodynamic diameters after 20 and 60 min are overlapping due to the standard deviation range. The only difference between all samples can be observed when looking at the weighted mean number. The H-NDs sonicated for 60 min have a 12 nm smaller hydrodynamic radius compared to a 20 min treatment (36 nm). Nevertheless, the shortest sonication time results in a higher standard deviation ( $\pm 9$  nm) of the weighted mean number coming from multiple sizes by number peaks detected by the DLS discussed in the section 3.3.4. In consequence, sample sonicated for 20 min has a broader hydrodynamic size distribution compared to the other suspensions. Surprisingly, the longest sonication time (120 min) did not significantly reduce the final hydrodynamic size distribution (weighted mean intensity) whereas the weighted mean number is 16 nm higher compared to the 60 min of sonication. The only advantage of a longer sonication time is that the H-NDs sample possesses a narrower size distribution as suggested by the low value of the standard deviation ( $\pm 2$  nm). In the literature, the real effect of sonication time has not been studied but conditions such as 120 min<sup>54</sup> and 60 min<sup>9</sup> of sonication have already been used by others.

In conclusion, increasing the sonication time does not significantly reduce the final hydrodynamic diameter (weighted mean intensity) of H-NDs. As a compromise between the final hydrodynamic size and the duration of the process, 60 min of sonication was chosen to be applied as a constant parameter in the following experiments including NDs sample preparation protocol.

### 3.3.6.2 Effect of centrifugation time

Previously, a centrifugation step of 40 min (centrifugal force = 3260 g and speed = 4500 rpm) was applied. The centrifugation time is considered to affect the final concentration of the H-NDs suspension by simply reducing the number of water-dispersed particles remaining in the supernatant. Low concentration ( $< 1$  mg.ml<sup>-1</sup>) may limit possible further applications. For instance, NDs concentration  $> 2$  mg.ml<sup>-1</sup> is required to meet the injection volume limit for mouse intravenous injection with a maximum volume of 0.2 ml<sup>55</sup>. Centrifugation times of 20, 40, and 80 min were tested to check the effect on the final concentration and colloidal properties of the H-NDs suspension. All suspensions were prepared at an initial concentration

of around 5 mg.ml<sup>-1</sup> while keeping constant the sample volume of 4 ml and the sonication parameters (time = 60 min, amplitude = 80 %, PRF = 0.5 cycle per second, titanium ultra-sound probe H3). Same sonication conditions ensure a similar level of deaggregation of the H-NDs suspension. Table 3.10 summarizes the findings of the centrifugation experiment.

Initial concentration (mg.ml <sup>-1</sup> )	Sonication time (min)	Centrifugation time (min)	Final concentration (mg.ml <sup>-1</sup> )	Weighted mean intensity (nm)	Weighted mean number (nm)
5.6	60	20	2.5	124 ± 1	48 ± 22
5.2	60	40	2.3	100 ± 1	24 ± 5
5.3	60	80	1.2	84 ± 2	34 ± 2

**Table 3.10** – Relation between centrifugation time and final concentration of the plasma H-NDs suspension. The DLS characterization (weighted mean intensity and number of three measurements) was performed with a sample concentration of 0.1 - 0.2 mg.ml<sup>-1</sup> within 1 h after the sample preparation.

The final concentration of the plasma H-NDs suspension decreases for an increasing centrifugation time highlighted in grey in the table above. Samples centrifuged for 20 and 40 min have a similar final concentration above 2 mg.ml<sup>-1</sup>. However, it has been noticed that a centrifugation time lower than 40 min sometimes makes it difficult to separate the supernatant and the pellet due to a strong, dark color of the suspension as a natural consequence of the higher concentration of NDs. In terms of colloidal properties, 20 min of centrifugation leads to a higher hydrodynamic diameter of 124 ± 1 nm (by weighted mean intensity) compared to the sample centrifuged for 40 min (100 ± 1 nm). A weighted mean number revealed that larger H-NDs are still present in the suspension after 20 min of centrifugation leading to multiple peaks and a higher standard deviation (± 22 nm) between the mean peak values. In contrast, the longest centrifugation time tested (80 min) reduced by ~77 % the initial H-NDs concentration suspension (5.3 mg.ml<sup>-1</sup>) resulting in the final concentration of < 2 mg.ml<sup>-1</sup>. Since the time is twice longer than the middle experimental range (40 min), such a great loss of the H-NDs dispersed in water can be expected to lead to lower hydrodynamic diameter size distribution (weighted mean intensity, 84 ± 2 nm). A weighted mean number of H-NDs centrifuged for 40 and 80 min varies only by 10 nm which can be associated with a small agglomeration induced by sample dilution (a lower number of particles results in lower repulsive forces felt by the H-NDs present in the water suspension)<sup>3</sup>.

In conclusion, centrifugation duration is a factor responsible for the final concentration and colloidal quality of the H-NDs suspension. Time above 40 min leads to significant loss of the material resulting in H-NDs concentration lower than 2 mg.ml<sup>-1</sup> rendering it inappropriate when considering other applications. A final sample concentration > 2 mg.ml<sup>-1</sup> along with good colloidal dispersion requires the NDs preparation protocol to include 60 min of sonication followed by 40 min of centrifugation.

### 3.3.6.3 Effect of centrifugal force and speed

The effect of centrifugation parameters (G-force, rotation speed) on final concentration and colloidal properties of H-NDs suspension is presented. Previously, the decreasing centrifugation time was tested for the constant value of the G-force (3260 g) corresponding to the rotation speed of 4500 rpm. Herein, the centrifugation parameters were reduced down to 2400 g and 3861 rpm to test another possible treatment. The sonication parameters were kept constant (time = 60 min, amplitude = 80 %, pulse repetition frequency – PRF= 0.5 cycle per second, titanium ultra-sound probe type H3, sample volume = 4 ml) (Table 3.11).

Initial concentration (mg.ml <sup>-1</sup> )	Centrifugation			Final concentration (mg.ml <sup>-1</sup> )	Weighted mean intensity (nm)	Weighted mean number (nm)
	time (min)	force (g)	speed (rpm)			
5.8	40	2400	3861	2.2	114 ± 5	32 ± 16
5.2	40	3260	4500	2.3	100 ± 1	24 ± 5

**Table 3.11** – Relation between centrifugal force / speed and final concentration of the plasma H-NDs suspension. The DLS characterization (weighted mean intensity and number of three measurements) was performed with a sample concentration of 0.1 mg.ml<sup>-1</sup> within 1 h after suspension preparation.

The centrifugation conditions affect the colloidal properties of H-NDs suspension while not having a significant impact on the final concentration. The weighted mean intensity is 14 nm higher compared to the maximum centrifugation speed (4500 rpm). The weighted mean number with quite high standard deviation suggest a multiple peak size distribution (32 ± 16 nm) whereas the sample centrifuged at 3260 g has a narrower size distribution profile (24 ± 5) with lower weighted mean intensity (100 ± 1 nm). Centrifugation conditions do not significantly affect the final concentration of H-NDs suspension.

The maximum centrifugation speed was selected due to the narrow size distribution of the H-NDs, as shown both in weighted mean intensity and number. It is important to mention that the preparation protocol should be developed separately for each type of surface-modified NDs due to their hydrophobic / hydrophilic nature. Sonication and centrifugation may lead to some differences between the suspensions depending on the surface termination. Following that, in the Appendix (section A.3), the same experiment was also performed on PlasmaChem air annealed NDs proving the previous statement. However, during this Ph.D. work, the same preparation protocol was applied for each kind of surface terminated NDs due to limited access to the equipment and the amount of powder produced after certain types of modifications.

### 3.3.6.4 Effect of sample temperature on DLS measurements

The preparation protocol includes sonication and centrifugation steps which may result in an increased temperature of the suspension. As DLS characterization may have to be done on

ultra-fresh suspension, this part aims to investigate whether the temperature of the sample affects colloidal properties measured by DLS after the H-NDs suspension preparation. Another outcome of temperature experiment connects changes in the storing (fridge temperature is equal to 4 °C) and the transportation conditions but also possible further applications of H-NDs in e.g. nanomedicine. The temperature of all *in vitro* or *in vivo* manipulations is set for ~37 °C in order to imitate the natural human body environment. Most of the time, ambient laboratory conditions (~25 °C) do not include a possibility of sample destabilization induced by temperature. Preparation and characterization protocol should take into account a possible increase in the sample temperature after sonication and centrifugation step whereas a good colloidal stability of H-NDs not affected by the temperature is an additional asset. The DLS characterization of the plasma H-NDs suspension was performed while decreasing the sample temperature from 40 °C down to 1 °C automatically controlled by the instrument. The data were normalized with respect to the hydrodynamic diameter obtained at ambient temperature (Figure 3.21).

The changes in the hydrodynamic diameter can be seen over the whole tested range. However, the majority of points stay within the standard deviation ( $\pm 10\%$ ) of the nominal value measured at ambient conditions. Hydrodynamic diameter is slightly higher than  $100 \pm 10$  nm only at the maximum temperature of 40 °C and at 10 °C but by no more than 13 %.

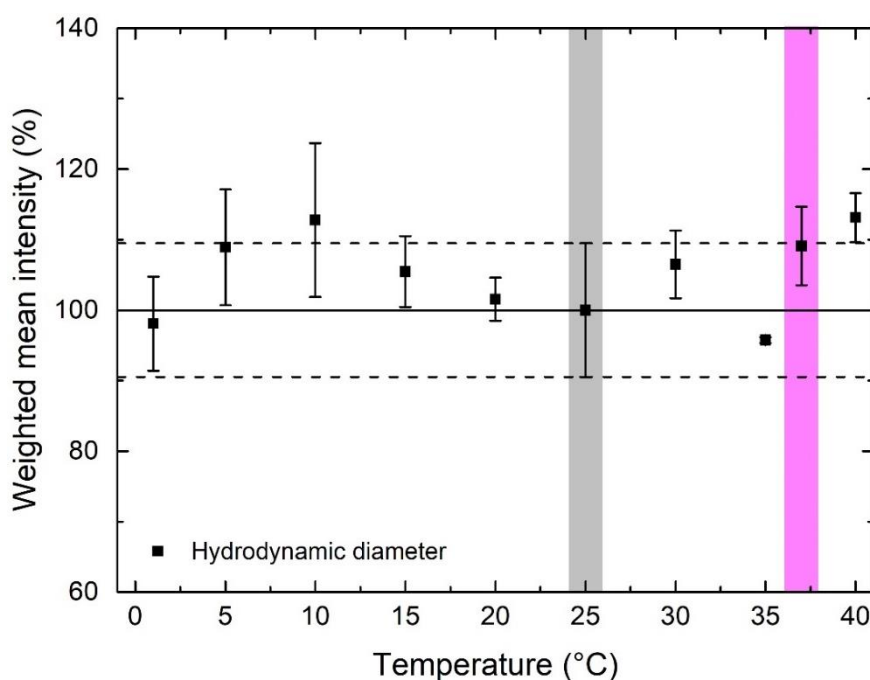


**Figure 3.21** – Temperature stability of  $0.1 \text{ mg.ml}^{-1}$  plasma H-NDs aqueous suspension at various temperatures (1 - 40 °C) with experimental (grey area) and biomedical temperature (pink area) indicated. Hydrodynamic diameter is given as the weighted mean intensity value normalized to results obtained at 25 °C.

In conclusion, the experiments show good colloidal stability in terms of hydrodynamic diameter over the tested temperature range of plasma H-NDs suspension. A sample may be stored either at ambient temperature or in the fridge including possible bioapplications.

## 3.3.6.5 Summary

It has been shown that the combination of the sonication and the centrifugation is required to prepare H-NDs hydrosol. The times of sonication and centrifugation including the centrifugal force have been chosen as a part of the preparation protocol based on satisfying colloidal quality of H-NDs suspension. That includes parameters such as:

- (i) Sonication time = 60 min
- (ii) Centrifugation time = 40 min
- (iii) Centrifugal force = 3260 g and rotation speed = 4500 rpm

Sonication time (min)	Weighted mean intensity (nm)	Weighted mean number (nm)	Centrifugation time (min)	Weighted mean intensity (nm)	Weighted mean number (nm)
60	369 ± 35	66 ± 23	40	100 ± 1	24 ± 5

**Table 3.12** – Colloidal properties of plasma H-NDs sample after applying selected sonication and centrifugation time. The DLS characterization was performed within 10 min after each preparation step. Weighted mean intensity / number shows average of three measurements.

It has been demonstrated that sonication effectively breaks the H-ND aggregates. However, it is not sufficient to obtain clear, well-dispersed suspension (Figure 3.22 - A). The centrifugation removes the non-disaggregated or larger in size NDs while leaving the suspension clear brown with only the water-dispersed H-NDs (Figure 3.22 - B).

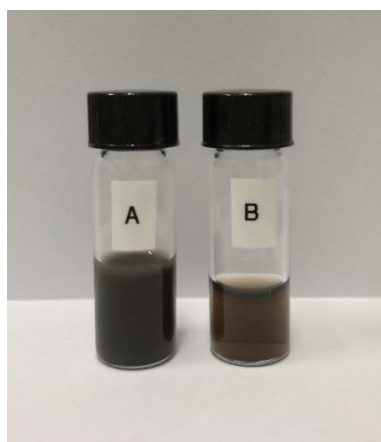


**Figure 3.22** – Picture of the plasma H-NDs suspension after 60 min of sonication (A) followed by 40 min centrifugation (B) taken at the NDs concentrations of 5.6 mg.ml<sup>-1</sup> and 2.3 mg.ml<sup>-1</sup>, respectively. Picture was taken shortly after each preparation step.

The DLS experiment has shown that H-NDs have good colloidal stability up to the temperature of 40 °C proving its suitability for various applications but also different storage and transportation conditions.

### 3.4 Colloidal behavior of NDs with different surface chemistries

Each step of the protocol for preparation and characterisation of colloidal suspensions has been carefully investigated in previous parts. Using the optimized conditions, the colloidal properties of NDs prepared and characterized in Chapter 2 and dispersed in ultra-pure water will be now presented.

The DLS characterization includes measurements performed on freshly-prepared suspensions (< 1 h after centrifugation), after 24 h as well as long-term (50 days). At the end, the FTIR spectra of the surface-modified powders, pellets, and suspensions are presented.

#### 3.4.1 Colloidal properties of air annealed nanodiamonds

As described in the previous chapter, so-called 'oxidised' NDs, were achieved by air annealing of the native powder at a constant temperature of 550 °C for 90 min. Two sources of detonation NDs were treated in the same way: PlasmaChem (Germany) and Adamas Nanotechnologies (USA). Following the air oxidative treatment, the NDs were dispersed in the ultra-pure water (18.2 MΩ) and characterized via DLS technique.

Source of NDs	Weighted mean intensity (nm)	Weighted mean number (nm)	Mean Zeta Potential (mV)
PlasmaChem	103 ± 2	37 ± 17	- 61 ± 1
Adamas Nanotech.	160 ± 3	86 ± 2	- 20 ± 1

**Table 3.13** – Hydrodynamic diameter (average value of weighted mean intensity and number) and ZP of air Ox-NDs dispersed in ultra-pure water. Values in the table represents average of 3 independent measurements. Two sources were measured on the same day after suspension preparation (referred as fresh suspension).

PlasmaChem and Adamas NDs form agglomerated clusters when being dispersed in water (Table 3.13). In case of PlasmaChem, the measured hydrodynamic diameter (by weighted mean intensity and number) is higher than the primary size distribution (3 - 10 nm), as probed by the TEM (Chapter 2, section 6). In terms of Adamas NDs, significantly larger diameters of aggregates are observed as compared to PlasmaChem (+ 57 nm). However, the exact size distribution of the primarily particles remains unknown (no TEM data available). The reason may come from the initial composition of both NDs sources (FTIR and ICP-MS study are presented in Chapter 2, sections 3 and 5, respectively). Surface-modification via thermal oxidation strongly depends on the reactivity of the surface functional groups meaning that air annealing conditions are source-dependent. Size distributions by intensity and number of the air annealed NDs are presented below (Figures 3.23 and 3.24).

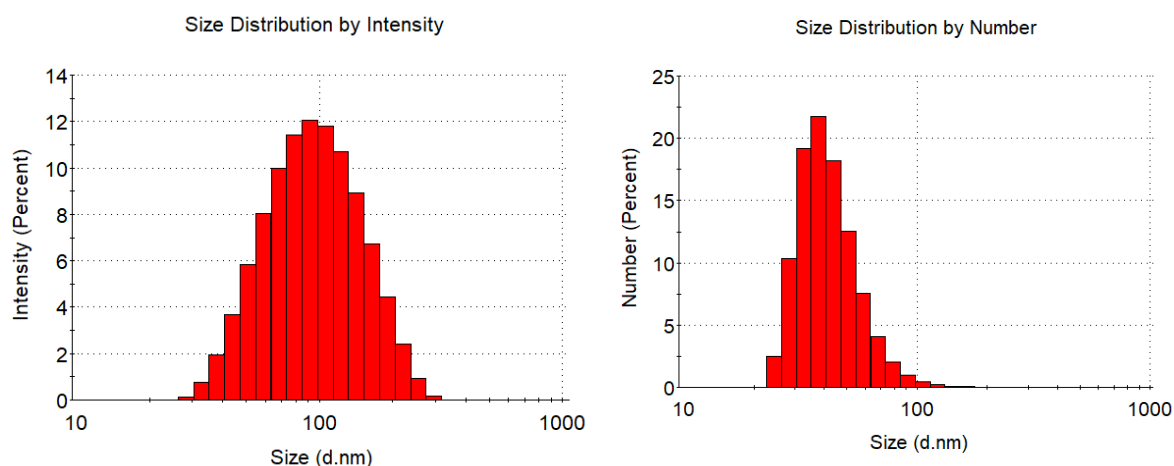


**Figure 3.23** – Size distribution of one DLS measurement given by intensity (left) and number (right) of the air annealed PlasmaChem NDs.

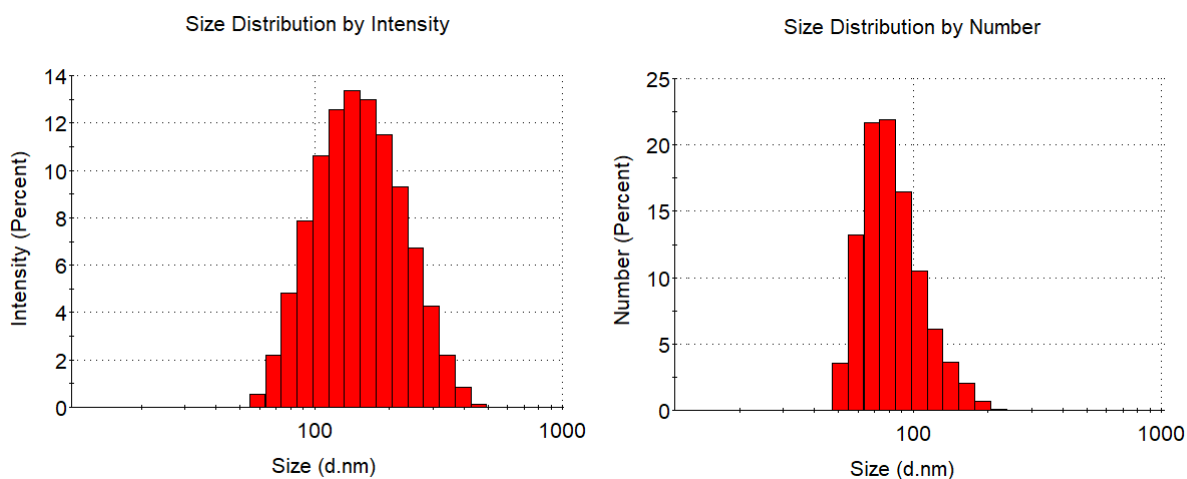


**Figure 3.24** – Size distribution of one DLS measurement given by intensity (left) and number (right) of the air annealed Adamas Nanotechnologies NDs.

In terms of surface charge, Adamas and PlasmaChem NDs both exhibit negative ZP in water after air oxidation. The values shown in the Table 3.13 are in agreement with the literature<sup>48</sup> while the origin of the negative ZP is mostly related to the COOH groups present at the surface (see Chapter 2, section 3), which at pH = 6 (ultra-pure water) tends to be easily deprotonated creating carboxylate form ( $COO^-$ ) on the surface which mainly contribute to the negative surface charge<sup>8,26,56</sup>.

The absolute ZP value of PlasmaChem Ox-NDs remains above 30 mV suggesting a good colloidal stability. In contrast, the Adamas NDs have an absolute ZP value below 30 mV which may lead to rather unstable behavior. This suggest a lower number of carboxylic groups on Adamas Ox-NDs. The colloidal properties of both NDs are different but the FTIR analysis of the modified powders does not show discrepancies in the surface's chemical composition (see Chapter 2, section 3). But, the FTIR does not provide a quantitative analysis of COOH groups.

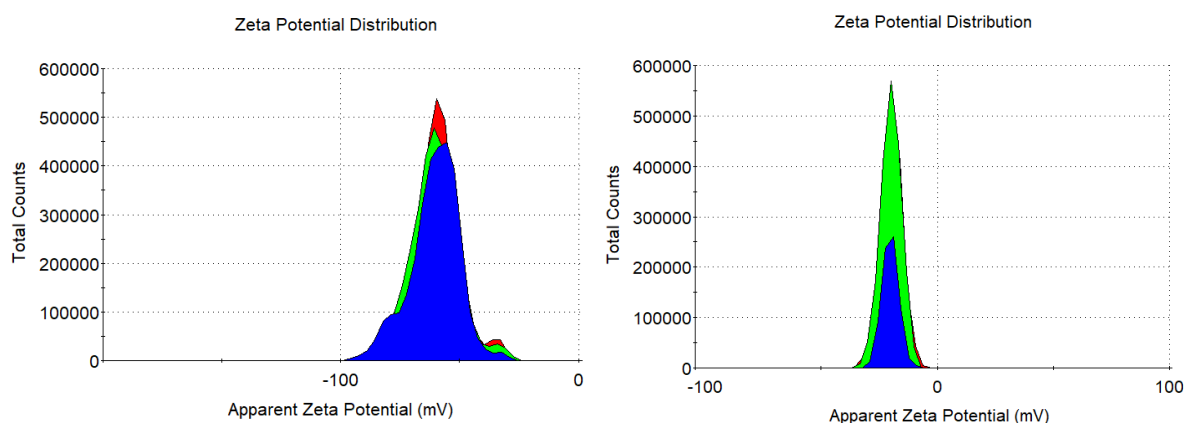


**Figure 3.25** – Zeta Potential distribution of air annealed PlasmaChem (left) and Adamas Nanotech. (right) NDs. The colors represents three independent ZP measurements.

As shown in Figure 3.25, a broadening of the ZP peak has been regularly observed for freshly prepared air Ox-NDs suspension (DLS measurements done less than 1 h after sonication and centrifugation). As it will be shown and discussed in the next parts of this chapter, this broadening disappears when the measurement is repeated after 24 h.

Note that the as-received Adamas NDs exhibited already a negative ZP ( $-40 \pm 3$  mV). Surprisingly, this additional treatment resulted in degradation of the ZP in water, with a less negative ZP ( $-20 \pm 1$  mV) and higher hydrodynamic diameters. In contrast, the as-received PlasmaChem NDs have positive ZP in water (Appendix, section A.4) whereas after air annealing the NDs become negatively charged.

### 3.4.2 Colloidal properties of plasma hydrogenated nanodiamonds

The plasma hydrogenation treatment is a well-known method used to obtain H-terminated diamond films<sup>8</sup>. Since 2010, the LCD team also apply this technique to detonation NDs<sup>57</sup>. Three types of NDs (PlasmaChem, Adamas Nanotechnologies, and NanoCarbon Research Institute from Japan) were hydrogenated using the same conditions (250 W, 12 mbar, 10 sccm, 20 min) and water-dispersed according to the preparation protocol. The colloidal properties of such H-NDs are presented in the Table 3.14.

Source of NDs	Weighted mean intensity (nm)	Weighted mean number (nm)	Mean Zeta Potential (mV)
PlasmaChem	$99 \pm 1$	$45 \pm 2$	$55 \pm 1$
Adamas Nanotech.	$108 \pm 2$	$35 \pm 3$	$54 \pm 3$
NanoCarbon Res. Inst.	$233 \pm 33$	$24 \pm 4$	$51 \pm 2$

**Table 3.14** – Hydrodynamic diameter (weighted mean intensity and number) and zeta potential of microwave plasma H-NDs. Colloidal properties of three different ND sources are compared.

The microwave plasma conditions for hydrogenation produce NDs with hydrodynamic diameter ranging from  $99 \pm 1$  nm (PlasmaChem) up to  $233 \pm 33$  nm (NanoCarbon Research Institute) looking at the values given by the weighted mean intensity. The significantly higher size of NanoCarbon Research Institute NDs reflects the presence of higher polydispersity of the suspension and the presence of aggregates. Looking at the weighted mean number values, PlasmaChem H-NDs exhibit the highest aggregation state ( $45 \pm 2$  nm) compared to the Adamas ( $35 \pm 3$  nm) and the NanoCarbon Research Institute ( $24 \pm 4$  nm) H-NDs (Figures 3.26, 3.27, and 3.28).

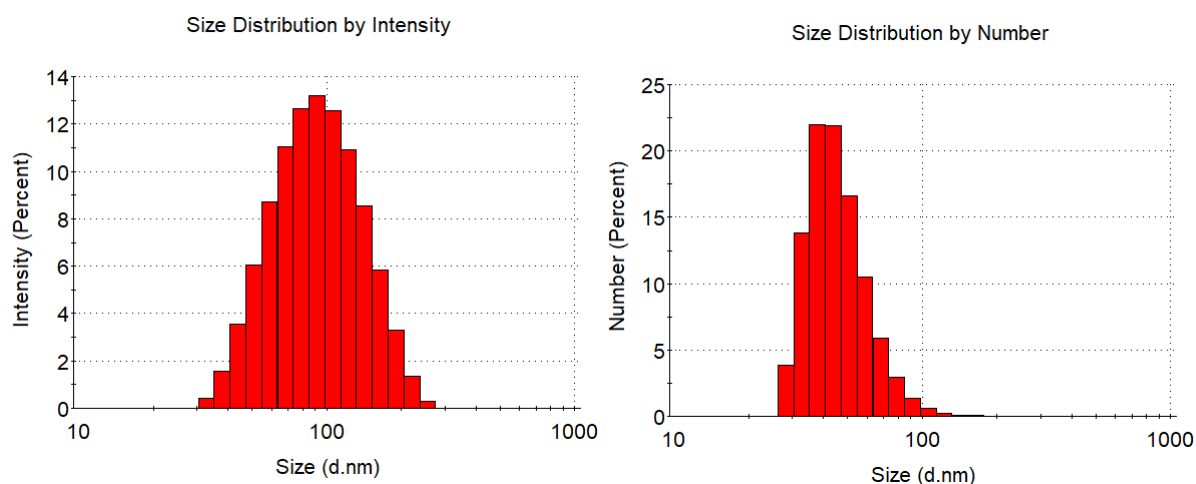


**Figure 3.26** – Size distribution of one DLS measurement given by intensity (left) and number (right) of plasma hydrogenated PlasmaChem NDs.

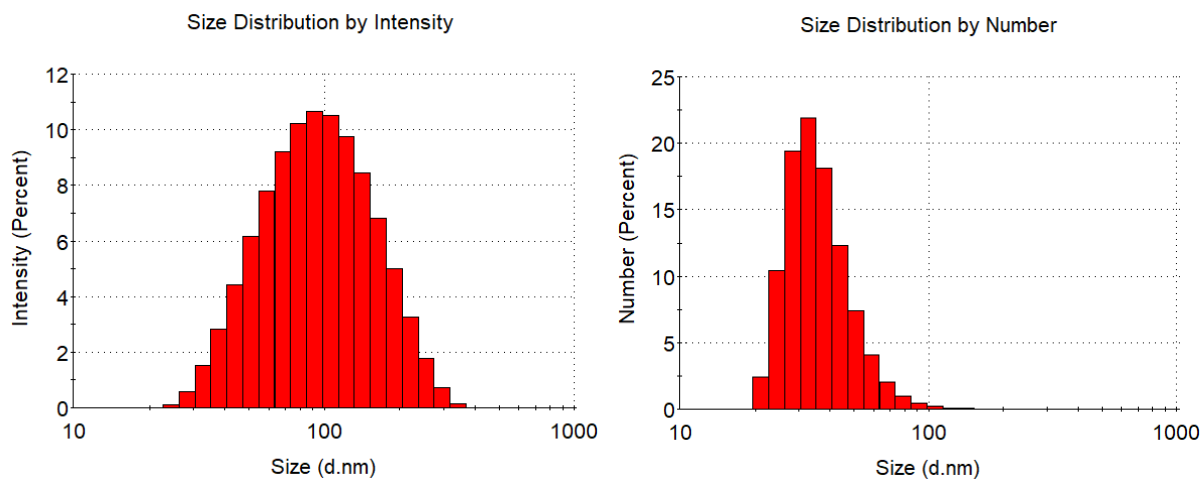


**Figure 3.27** – Size distribution of one DLS measurement given by intensity (left) and number (right) of plasma hydrogenated Adamas Nanotechnologies NDs.

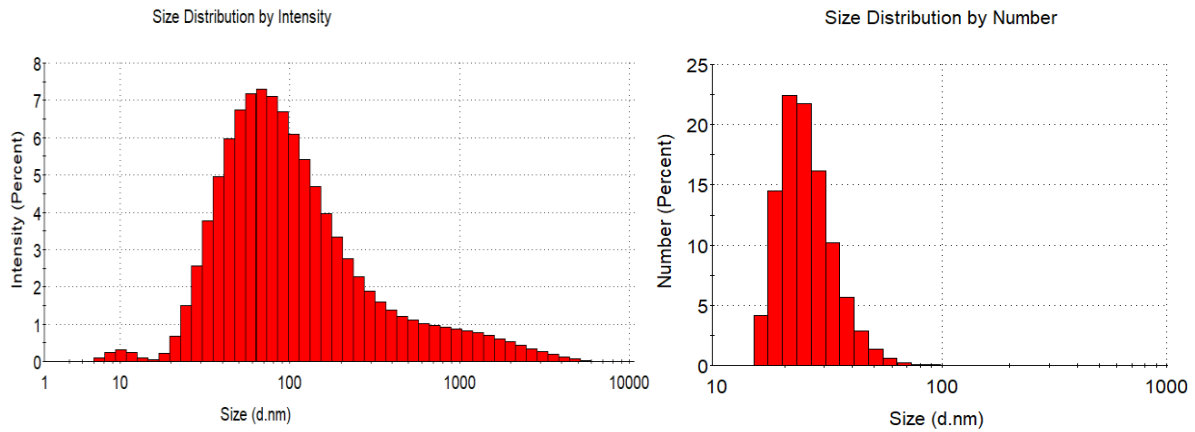


**Figure 3.28** – Size distribution of one DLS measurement given by intensity (left) and number (right) of plasma hydrogenated NanoCarbon Research Institute NDs.

In terms of a surface charge, plasma treatment under hydrogen results in positive ZP of the NDs observed in water suspension with mean values above 50 mV, whatever the source of particles. The ZP measurement of the three sources of H-NDs is presented below (Figures 3.29 and 3.30).

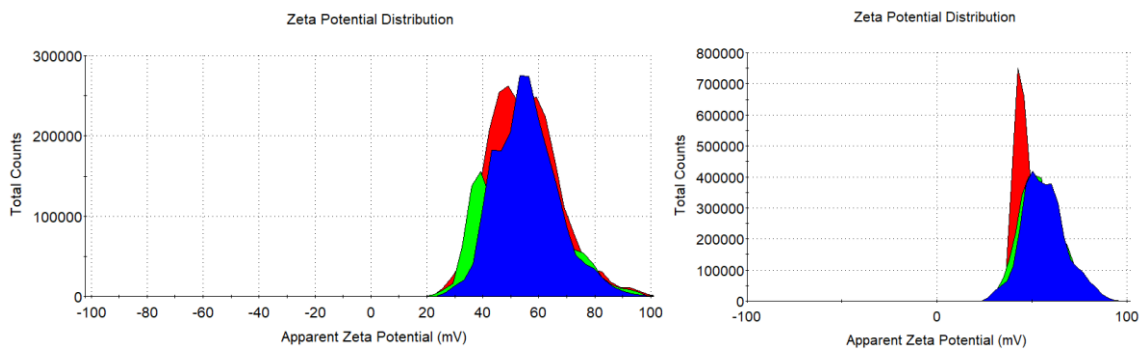


**Figure 3.29** – Zeta Potential distribution of plasma hydrogenated PlasmaChem (left) and Adamas Nanotech. (right) particles. Colors represent three independent and consecutive ZP measurements.

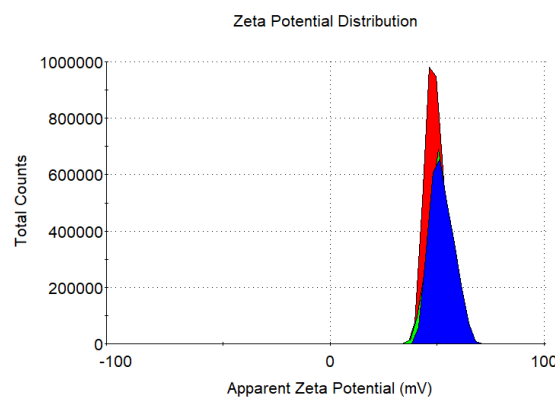


**Figure 3.30** – Zeta Potential distribution of plasma hydrogenated NanoCarbon Research Institute NDs. Colors represent three independent and consecutive ZP measurements.

Freshly-prepared H-NDs also exhibit a ZP peak broadening, linked to certain instability of the suspension. However, since the mean value of the ZP is above 30 mV, a good colloidal stability of prepared suspensions can be expected. The FTIR study (Chapter 2, section 3) of PlasmaChem H-NDs shows removal of the oxygen content (reduction of the C=O peak) from the surface along with formation and stabilization of carbon-hydrogen bonds<sup>58,32,59</sup>. The origin of such positive surface charge has been associated with accumulation of holes near the diamond-water interface (surface-transfer doping mechanism)<sup>40</sup>. The TEM study (Chapter 2, section 6) shows that sp<sup>2</sup>-C is also present on the surface of the plasma-hydrogen treated NDs, which can also participate to the origin of the positive ZP<sup>44,41</sup>.

### 3.4.3 Colloidal properties of hydrogen annealed nanodiamonds

The thermal annealing under hydrogen gas is an alternative to the hydrogen plasma treatment leading to hydrogenated NDs surface<sup>23,60</sup>. The same thermal annealing conditions (1 h, 550 °C) were applied to NDs supplied by PlasmaChem and Adamas company. After modification, the NDs were dispersed in ultra-pure water and characterized according to the adjusted protocol.

Source of NDs	Weighted mean intensity (nm)	Weighted mean number (nm)	Mean Zeta Potential (mV)
PlasmaChem	114 ± 2	43 ± 18	64 ± 2
Adamas Nanotech.	141 ± 4	16 ± 1	72 ± 3

**Table 3.15** – Colloidal properties of hydrogen annealed Adamas and PlasmaChem NDs obtained on the day of suspension preparation. Data represents the average values of three independent and consecutive measurements.

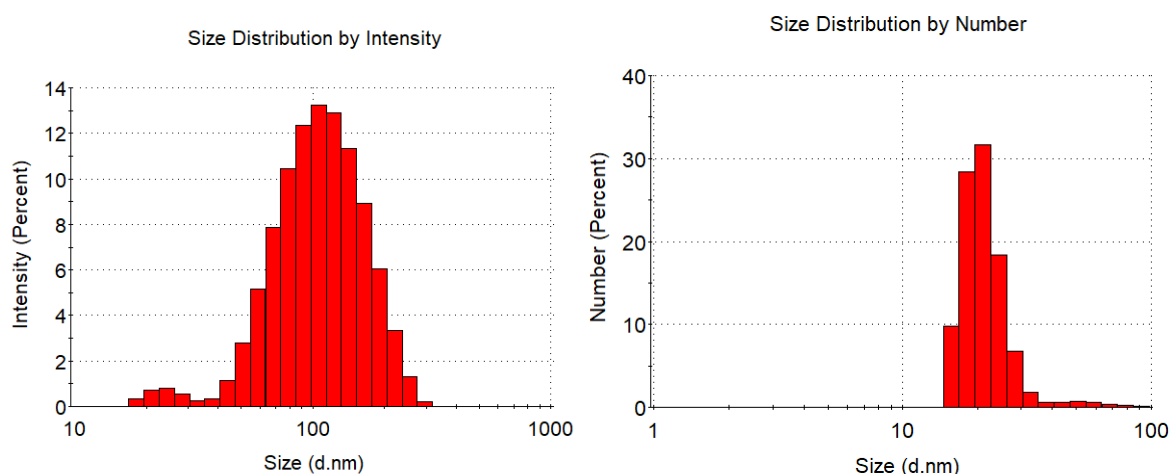


**Figure 3.31** – Size distribution of one DLS measurement given by intensity (left) and number (right) of PlasmaChem NDs modified via thermal annealing under hydrogen.

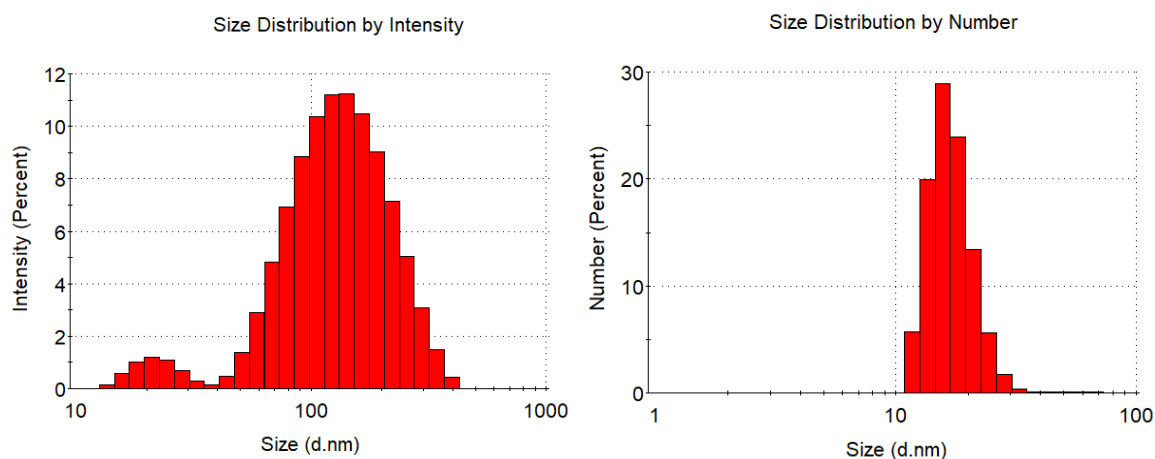


**Figure 3.32** – Size distribution of one DLS measurement given by intensity (left) and number (right) of Adamas Nanotechnologies NDs modified via thermal annealing under hydrogen.

From weighted mean intensity and number values, we can see that hydrogenated Adamas suspension contains a population of smaller aggregates, with hydrodynamic diameters around 16 nm, while hydrogenated PlasmaChem exhibit a population of aggregates around 40 nm. However, in both cases, larger aggregates are present in the suspension, as shown by the intensity size distribution.

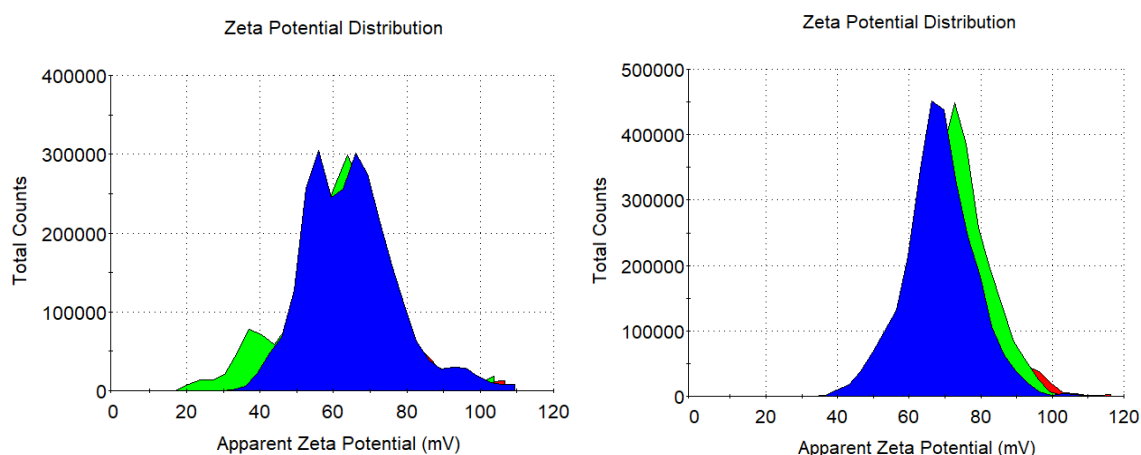


**Figure 3.33** – Zeta Potential distribution of hydrogen annealed NDs: PlasmaChem (left) and Adamas Nanotech. (right). Colors represent three independent and consecutive ZP measurements.

Modifications of the surface via thermal annealing under hydrogen also results in positive surface charge (positive ZP), independently on the source of NDs (Figure 3.33). The same instability of freshly-prepared PlasmaChem H-NDs is observed as previously shown for other surface chemistries. However, mean ZP values are higher than 60 mV (PlasmaChem) and 70 mV (Adamas Nanotech.) with respect to plasma H-NDs (ZP around 50 mV) as seen for the same NDs source. The positive ZP of water-dispersed thermally annealed H-NDs is also in agreement with the literature<sup>23</sup>. As for plasma treatment, the TEM images shows some graphitic reconstructions on the NDs surface (Chapter 2, section 6) whereas the FTIR spectra

clearly indicated the presence of C-H bonds (Chapter 2, section 3) with slightly different shapes compared to plasma H-NDs.

### 3.4.4 Properties of vacuum annealed nanodiamonds

The last surface modification involved thermal annealing under vacuum (to induce surface graphitisation)<sup>41</sup>. PlasmaChem NDs were annealed at temperatures ranging from 750 °C up to 850 °C for various durations (1 h, 2 h). Dry powders were dispersed in water and characterized by DLS within 1 h after suspension preparation.

Vacuum annealing conditions	Weighted mean intensity (nm)	Weighted mean number (nm)	Mean Zeta Potential (mV)
1 h, 750 °C	131 ± 29	35 ± 11	47 ± 1
2 h, 750 °C	110 ± 2	42 ± 7	46 ± 3
1 h, 850 °C	111 ± 1	46 ± 10	47 ± 2
2 h, 850 °C	116 ± 4	45 ± 4	47 ± 2

**Table 3.16** – Colloidal properties of vacuum annealed NDs in water. Data were obtained less than 1 h after suspension preparation and represent an average value of three independent, consecutive DLS measurements.

Vacuum annealed NDs have a hydrodynamic diameter ranging from 110 ± 2 nm (2 h, 750 °C) and up to 131 ± 29 nm (1 h, 750 °C) as revealed by weighted mean intensities. Mean size, weighted by number, ranges from 35 ± 11 (1 h, 750 °C) up to 46 ± 10 (1 h, 850 °C). Vacuum annealed NDs are also positively charged with ZP values between 46 – 47 ± 2 mV<sup>26</sup>.

An example of the DLS size and ZP distribution of the vacuum annealed sample (grey field in the Table 3.16) is presented on Figure 3.34.

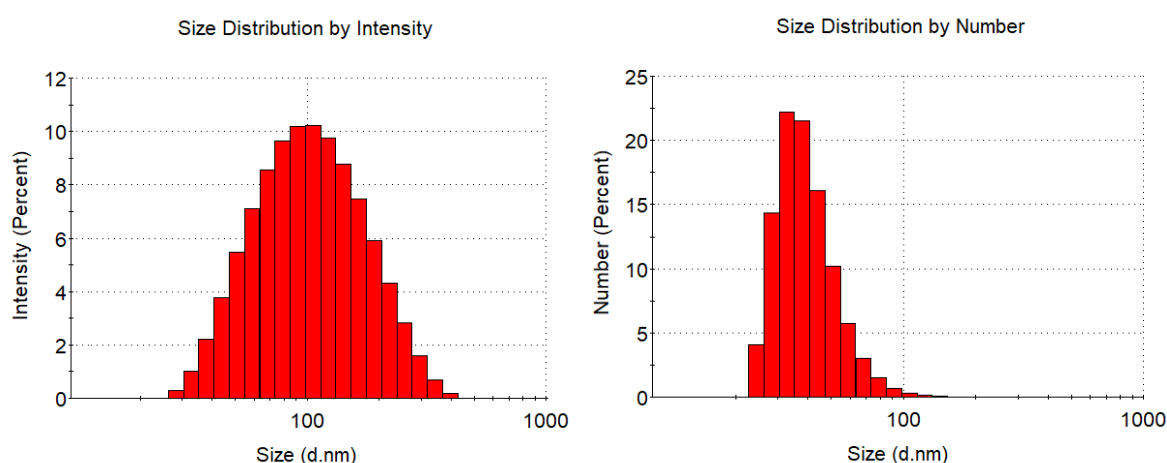


**Figure 3.34** – Size distribution of one DLS measurement given by intensity (left) and number (right) of PlasmaChem NDs modified via vacuum annealing (1 h, 750 °C).

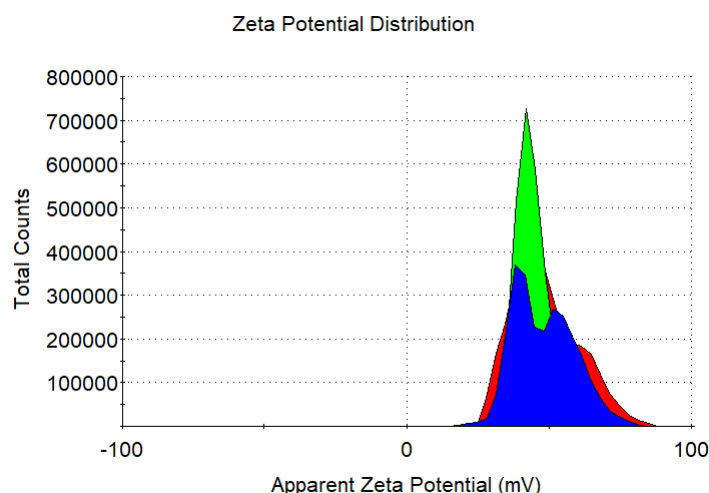


**Figure 3.35** – Zeta Potential distribution of vacuum annealed (1 h, 750 °C) PlasmaChem NDs. Colors represent three independent and consecutive ZP measurements.

Colloidal behaviors of these freshly prepared vacuum annealed NDs are rather similar whatever the conditions. Surprisingly, the hydrodynamic diameters and the polydispersity as evidenced by the intensity and number values are roughly the same whatever the treatment, as well as the ZP values. It is not possible to discuss these results according to the amount of sp<sup>2</sup>-carbon at the surface for the different annealed NDs. Only NDs annealed at 750 °C during 1 h have been characterized by TEM (Chapter 2, section 6).

### 3.4.5 Summary

Surface treatments of detonation NDs like carboxylation, hydrogenation or graphitization result in different colloidal properties of NDs depending on the source of the particles. Since the majority of the Ph.D. work has been done on PlasmaChem NDs, their colloidal properties are summarized below for the different surface chemistries.

Modification type (PlasmaChem, G-02)	Weighted mean intensity (nm)	Weighted mean number (nm)	Mean Zeta Potential (mV)
Air annealing	< 120	< 45	negative
Plasma hydrogenation	< 100	< 45	positive
Hydrogen annealing	< 120	< 45	positive
Vacuum annealing	< 140	< 50	positive

**Table 3.17** – Summary of the main findings regarding colloidal properties of the surface-modified PlasmaChem NDs.

The air oxidation leads to the negative surface charge in water whereas the positive ZP is measured after vacuum annealing, plasma or thermal hydrogen treatments. The hydrodynamic size of freshly-prepared suspension is below 50 nm and exhibits roughly the same polydispersity if we consider the weighted mean intensity values.

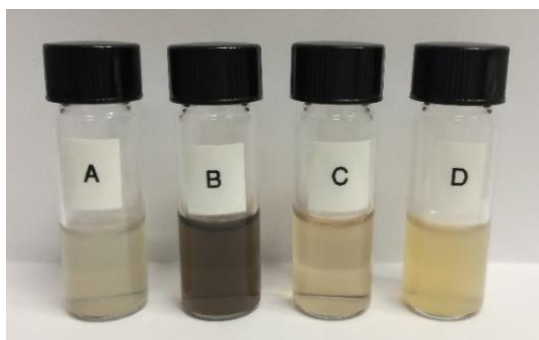


**Figure 3.36** – Picture of air oxidised (A), plasma hydrogenated (B), hydrogenated via thermal annealing (C), and vacuum annealed for 1 h at 750 °C (D) PlasmaChem NDs suspended in water. Pictures were taken of NDs concentrations of 1 mg.ml<sup>-1</sup> one day after sample preparation.

Although the colloidal properties of modified PlasmaChem NDs are similar, the visual appearance of the hydrosols is quite different. In particular, plasma H-NDs suspension has dark brown color (Figure 3.36 - B). This may be related to the presence of the small OLCs (3 nm) evidenced by TEM (Chapter 2, section 6). Annealing under hydrogen or in vacuum results in light brown color (Figure 3.34 - C and D) of the suspensions. Air Ox-NDs suspension is rather opaque with light, yellow-like appearance (Figure 3.34 - A). The brownish color of ND's colloids has already been attributed to the light interaction (Rayleigh scattering) with colloidal particles<sup>6,20</sup>.

### 3.5 Stabilisation and aging effect

The colloidal stability of NDs in water over time is a crucial parameter not often reported in the literature or simply generalized based on the ZP value. The following experiments aim to establish whether the colloidal properties of the surface-modified NDs, presented in the previous paragraph, undergo any changes over short (24 h) and long (50 days) period of time. The monitoring of the hydrodynamic diameter and the ZP of water-dispersed PlasmaChem NDs is performed via DLS measurements.

#### 3.5.1 Stability over 24 h

The colloidal properties of suspensions, ultra-fresh (< 2 h) and after 24 h, are compared for air oxidized, hydrogenated (plasma and thermal methods) and vacuum annealed NDs. Water-dispersed NDs were kept in closed glass vials in ambient conditions and at their initial concentration (usually between 2 and 3 mg.ml<sup>-1</sup>). They were diluted down to 0.1 mg.ml<sup>-1</sup> just prior the DLS characterization.

## 3.5.1.1 Air annealed nanodiamonds

In the first part, the characterization of the ultra-fresh and after 24 h air Ox-NDs suspension is presented.

Air annealing (1 h 30 min, 550 °C)	Weighted mean intensity (nm)	Weighted mean number (nm)	Mean Zeta Potential (mV)
Fresh suspension	103 ± 2	37 ± 17	-60 ± 1
After 24 h	101 ± 1	25 ± 20	-62 ± 1

**Table 3.18** – Colloidal properties of Ox-NDs measured for freshly-prepared (< 2 h) suspension and after 24 h.

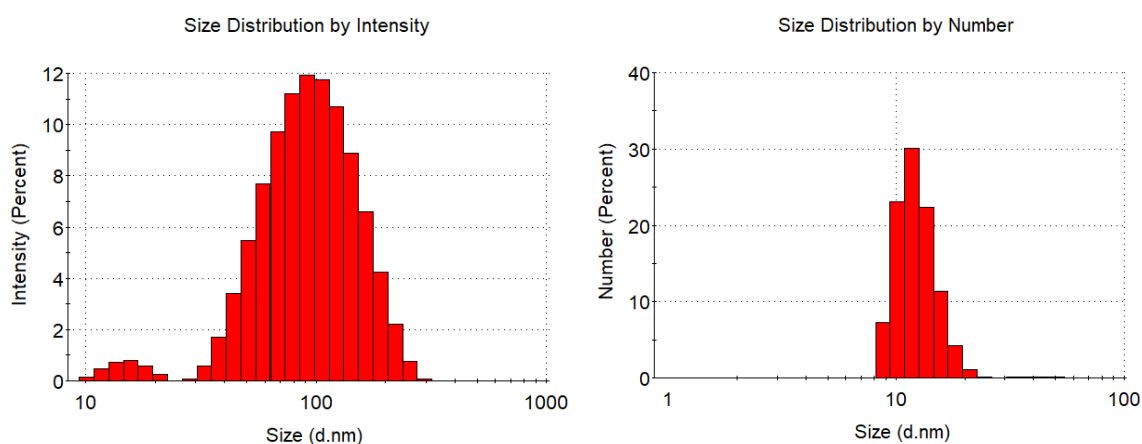


**Figure 3.37** – Size distribution of one DLS measurement by intensity (left) and number (right) of the air annealed PlasmaChem NDs after 24 h.

The hydrodynamic diameter given by weighted mean intensity remains the same whereas weighted mean number shows changes in the suspensions. Specifically, high standard deviation between the values ( $\pm 17 - 20$  nm) were seen for the fresh suspension and resulted in multiple peak size distribution (Table 3.18). After 24 h, the mean value of the hydrodynamic diameter decreases by 12 nm and the standard deviation goes down ( $\pm 3$  nm) possibly due to stabilization effect. More importantly, the ZP does not change and stay highly negative (around -61 mV) not being interrupted by reorganisation of NDs (Table 3.37). Such changes in colloidal properties of Ox-NDs were often observed during the first 24 h after sample preparation in my Ph.D. work.

## 3.5.1.2 Plasma hydrogenated nanodiamonds

Similarly to air Ox-NDs, a comparative characterization of plasma H-NDs suspension on the day of preparation and after 24 h is presented.

Microwave plasma hydrogenation (250 W, 12 mbar, 20 min)	Weighted mean intensity (nm)	Weighted mean number (nm)	Mean Zeta Potential (mV)
Fresh suspension	$95 \pm 1$	$44 \pm 2$	$53 \pm 1$
After 24 h	$108 \pm 1$	$35 \pm 5$	$43 \pm 1$

**Table 3.19** – Colloidal properties of plasma H-NDs measured on freshly-prepared suspension (< 2 h) and after 24 h.

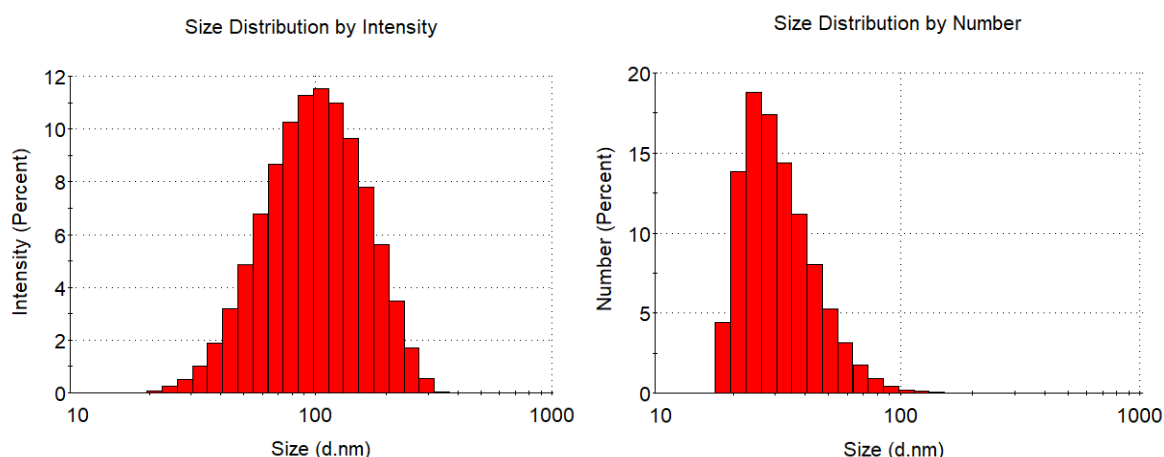


**Figure 3.38** – Size distribution of one DLS measurement by intensity (left) and number (right) of the plasma hydrogenated PlasmaChem NDs after 24 h.

Plasma hydrogenated NDs undergo more significant changes in comparison to air oxidized NDs. An evolution of the hydrodynamic diameter, as seen by weighted mean intensity, shows an increase while number distribution decrease (with higher standard deviation) (Table 3.19). A limited agglomeration effect seems to occur within the first 24 h. This effect goes along with a decrease of the ZP from  $53 \pm 1$  mV down to  $43 \pm 1$  mV, also reflecting that H-NDs evolve after 24 h in water suspension as shown below.

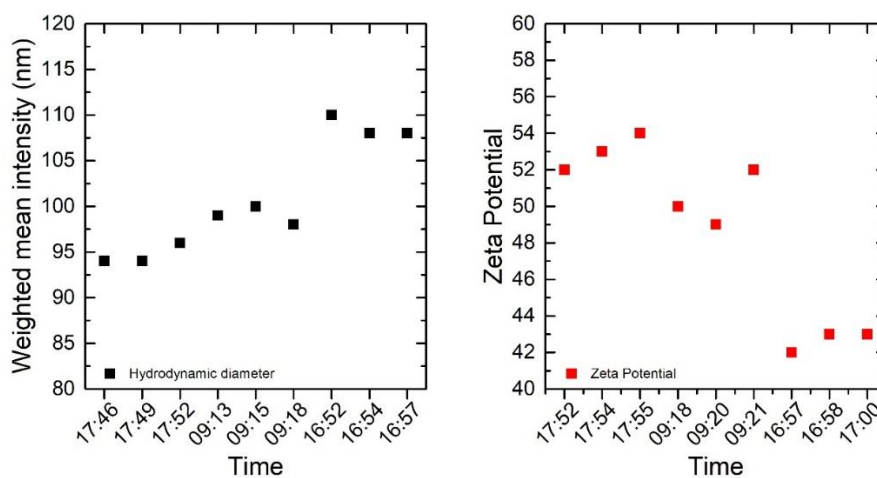


**Figure 3.39** – Evolution of colloidal properties (hydrodynamic diameter - black, ZP - red) of plasma H-NDs measured over first 24 h after preparation. Plot represents single data points of each DLS measurement.

It has to be stressed out that this effect of ‘stabilization’ of the H-NDs suspension after 24 h, reflected by a lower ZP and a limited increase of the hydrodynamic diameter (weighted mean intensity), has been observed on almost every samples produced during this Ph.D. work.

### 3.5.1.3 Hydrogen annealed nanodiamonds

Complementary to plasma H-NDs, the DLS characterization on the day of sample preparation and after 24 h was done for annealed under hydrogen NDs.

Thermal annealing under hydrogen (1 h, 550 °C)	Weighted mean intensity (nm)	Weighted mean number (nm)	Mean Zeta Potential (mV)
Fresh suspension	114 ± 2	43 ± 18	64 ± 2
After 24 h	118 ± 2	39 ± 18	44 ± 2

**Table 3.20** – Colloidal properties of thermally annealed H-NDs measured on freshly-prepared suspension (< 2 h) and after 24 h.

Similarly to plasma H-NDs, thermally annealed H-NDs suspension evolves after 24 h (Table 3.20). While the hydrodynamic size remains nearly the same, the ZP drops down by 20 mV. The standard deviation of the hydrodynamic size (weighted mean number) suggests inhomogeneity in size fraction.

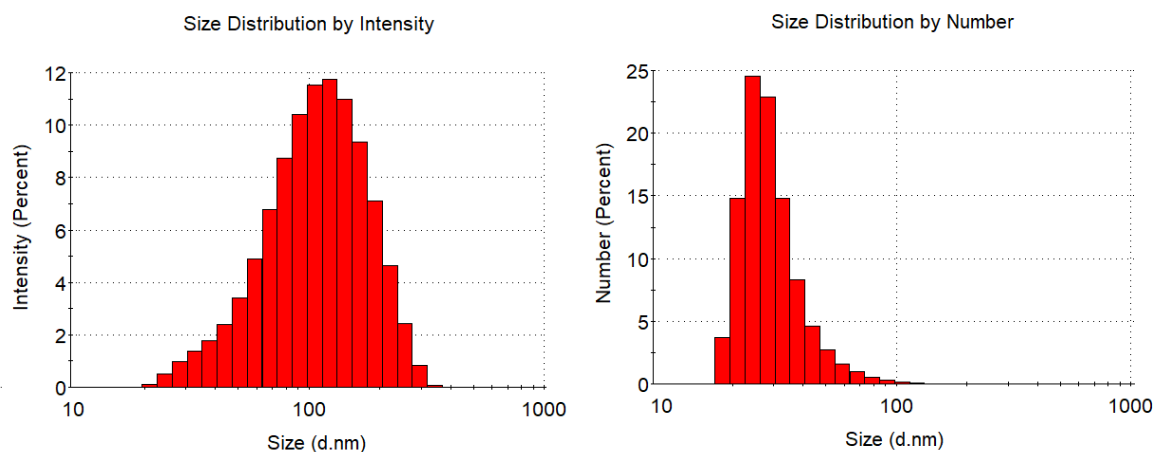


**Figure 3.40** – Size distribution of one DLS measurement by intensity (left) and number (right) of the hydrogen annealed PlasmaChem NDs after 24 h.

### 3.5.1.4 Vacuum annealed nanodiamonds

Lastly, the DLS characterization performed on the same day of sample preparation and after 24 h for vacuum annealed NDs is presented (several time / temperature conditions).

Hydrodynamic diameter given by weighted mean intensity values of vacuum annealed NDs certainly increases after 24 h for almost all tested samples, except for NDs treated for 1 h at 750 °C (Table 3.21). In terms of values given by weighted mean number, samples agglomerate toward larger hydrodynamic diameter (> 60 nm) whereas the lowest value is observed for NDs treated for 1 h at 750 °C ( $54 \pm 4$  nm). Concerning ZP values, no evolution is significant, and we do not observe the same drop of potential as seen for hydrogenated NDs. The presence of graphitic structures has been evidenced by the TEM study for NDs annealed at 750 °C during 1 h (Chapter 2, section 6). Nevertheless, it was not possible to observe NDs annealed under other conditions to confirm an increase in the graphitization level.

Vacuum annealing ( $1 \times 10^{-6}$ mbar)		Weighted mean intensity (nm)	Weighted mean number (nm)	Mean Zeta Potential (mV)
1 h, 750 °C	Fresh suspension	$131 \pm 29$	$35 \pm 11$	$47 \pm 1$
	After 24 h	$138 \pm 30$	$54 \pm 4$	$44 \pm 2$
2 h, 750 °C	Fresh suspension	$110 \pm 2$	$42 \pm 7$	$46 \pm 3$
	After 24 h	$197 \pm 7$	$84 \pm 4$	$42 \pm 1$
1 h, 850 °C	Fresh suspension	$111 \pm 1$	$46 \pm 10$	$47 \pm 2$
	After 24 h	$205 \pm 38$	$70 \pm 38$	$41 \pm 1$
2 h, 850 °C	Fresh suspension	$116 \pm 4$	$45 \pm 4$	$47 \pm 2$
	After 24 h	$155 \pm 7$	$67 \pm 9$	$46 \pm 1$

**Table 3.21** – Colloidal properties of vacuum annealed NDs measured the same day (< 2 h) and after 24 h in ultra-pure water.

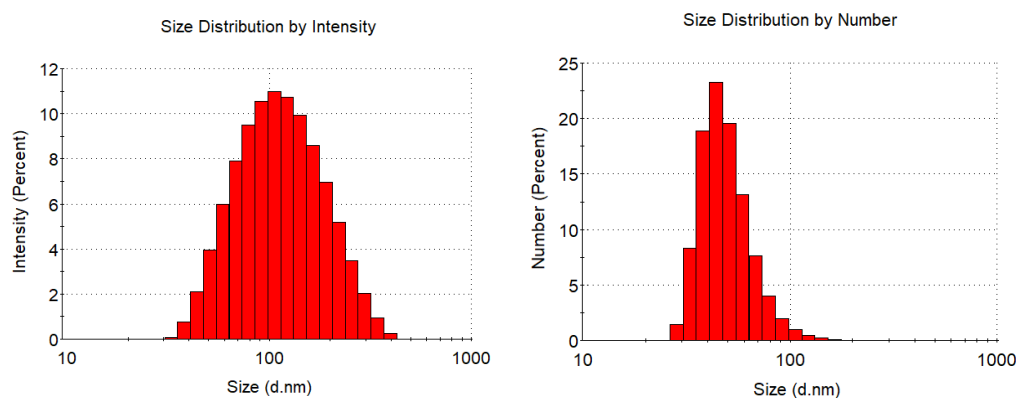


**Figure 3.41** – Size distribution of one DLS measurement by intensity (left) and number (right) of the vacuum annealed (1 h, 750 °C) PlasmaChem NDs after 24 h.

### 3.5.1.5 Summary

The DLS study evidenced the stabilisation and the evolution of colloidal properties of surface-modified NDs after 24 h in water suspension. The most relevant findings are summarized in the Table below.

Surface modification	Hydrodynamic diameter after 24 h (weighted mean intensity)	Zeta Potential after 24 h
Air Ox-NDs	no change	no change
Plasma H-NDs	higher (+ 12 %)	lower (- 19 %)
Thermally H-NDs	higher (+ 3 %)	lower (- 31 %)
Vacuum annealed NDs (1 h, 750 °C)	higher (+ 5 %)	no change
Vacuum annealed NDs (other conditions)	higher (+ 66 %)	no change

**Table 3.22** – Summary of changes in colloidal properties of surface-modified NDs dispersed in ultra-pure water after 24 h.

- The Zeta Potential and the hydrodynamic size of air oxidized NDs do not change
- A slightly higher increase of the hydrodynamic size is observed for plasma H-NDs compared to NDs thermally treated under hydrogen after 24 h in water suspension, while a decrease of their ZP is observed for both, more pronounced for thermally treated
- For vacuum annealed detonation NDs, Zeta Potential (> 30 mV) is not affected by the progressive agglomeration of the NDs while the value itself suggests a good colloidal stability of such NDs, which is rather controversial and not supported by the results.

### 3.5.2 Stability over 50 days

In the previous paragraphs, colloidal properties of freshly-prepared (< 1 h) and after 24 h were presented for surface-modified NDs suspensions. The results suggested that behavior of NDs in aqueous medium can evolve to a certain extent over time. As a logical consequence, the long-term (50 - 90 days) colloidal stability study should be conducted as well.

#### 3.5.2.1 Concentration effect

In the literature, concentration is suggested to have a substantial effect on ND's stability dispersed in a solvent<sup>12,3</sup>. To ensure the best conditions for such long-term experiment, the concentration effect is tested. The protocol for sample preparation, established at the beginning of this chapter, typically leads to NDs concentration of 2 mg.ml<sup>-1</sup>, depending on the surface chemistry. The monitoring of the colloidal properties of plasma (20 min, 12 mbar, 250 W) and thermally annealed (1 h, 550 °C) H-NDs over 50 days was performed to test an influence of ND's concentration as a part of storage conditions. Samples were prepared at the concentration of 2 mg.ml<sup>-1</sup> with part of the sample diluted down to 0.2 mg.ml<sup>-1</sup>. Prior to the

DLS characterization, a suspension at  $2 \text{ mg.ml}^{-1}$  was diluted down to  $0.2 \text{ mg.ml}^{-1}$  whereas the part of the sample kept at  $0.2 \text{ mg.ml}^{-1}$  was only manually mixed and measured directly without any further step. The evolution of the hydrodynamic diameter (weighted mean intensity) and the ZP is presented (Figure 3.45).

The data obtained clearly support that storage concentration of H-NDs affects its colloidal properties. An increase in the hydrodynamic diameter along with a decrease in the ZP is observed for all samples. However, the instability induced by progressive agglomeration occurs faster in terms of diluted samples. Notably, the size of the diluted plasma H-NDs agglomerates is 70 % higher with respect to initial value whereas the size of the annealed H-NDs increases by 80 % after 10 - 11 days. The situation changes after 50 days where the hydrodynamic size of diluted plasma H-NDs goes up c.a. 13-fold while the annealed H-NDs 8-fold time compared to initially measured value (day 0).

Interestingly, H-NDs suspensions (plasma and annealed) stored at a relatively high concentration of  $2 \text{ mg.ml}^{-1}$  also evolve after 50 days but the increase in the hydrodynamic diameter is significantly lower than the diluted samples (190 % of increase for hydrogen plasma and 90 % of increase for the hydrogen annealed particles). The H-NDs produced via annealing method are stable for a longer time. An evolution of the hydrodynamic diameter takes place but an increase in size is less than 10 % after 11 days. In contrary, plasma H-NDs are significantly larger (by 60 %) after 10 days.

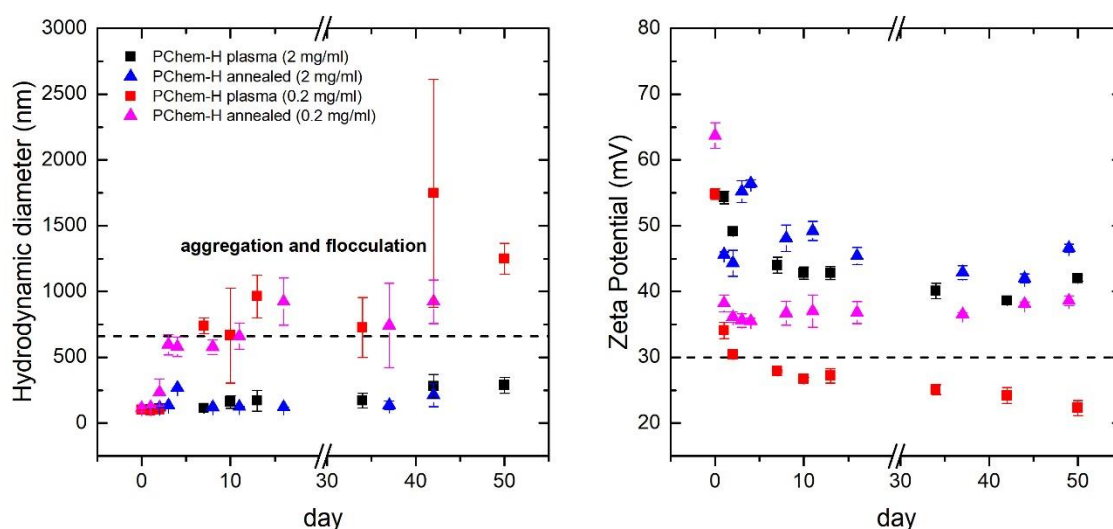


**Figure 3.45** – Evolution of colloidal properties of H-NDs (microwave plasma and annealed under hydrogen). NDs were suspended in water and stored at high ( $2 \text{ mg.ml}^{-1}$ ) and low ( $0.2 \text{ mg.ml}^{-1}$ ) concentration over 50 days. DLS measurements were done at NDs concentration of  $0.2 \text{ mg.ml}^{-1}$  (only samples stored at high concentration were diluted before the experiment). Black dashed line indicates sample's instability threshold (low data quality) induced by flocculation of the particles during the experiment resulting in only an estimated value (high standard deviation).

A similar situation occurs in terms of the Zeta Potential. Majority of NDs are positively charged with an average value around 40 mV, as measured over 50 days (except for diluted plasma H-

NDs sample). Such results are not in agreement with the literature, where  $ZP > 30$  mV is required to maintain highly repulsive forces between the NDs suggesting good colloidal stability of the particles<sup>26</sup>.

Water-dispersed and stabilizer-free NDs need to be prepared and stored at high concentration ( $> 2$  mg.ml<sup>-1</sup>) to reduce agglomeration state of the particles. Further experiments should be preferably performed only on freshly-prepared samples (within 7 days).



**Figure 3.46** – Picture of plasma H-NDs sample taken after several months. Particles progressively agglomerated and precipitated at the bottom of the glass vial resulting in complete liquid - solid phase separation.

### 3.5.2.2 Air annealed nanodiamonds

The air Ox-NDs suspension was prepared and stored at a concentration of 2 mg.ml<sup>-1</sup> at room temperature. Colloidal properties, including hydrodynamic diameter (by weighted mean intensity) and ZP (average value) were measured by DLS for 50 days to monitor time-induced changes in suspension.

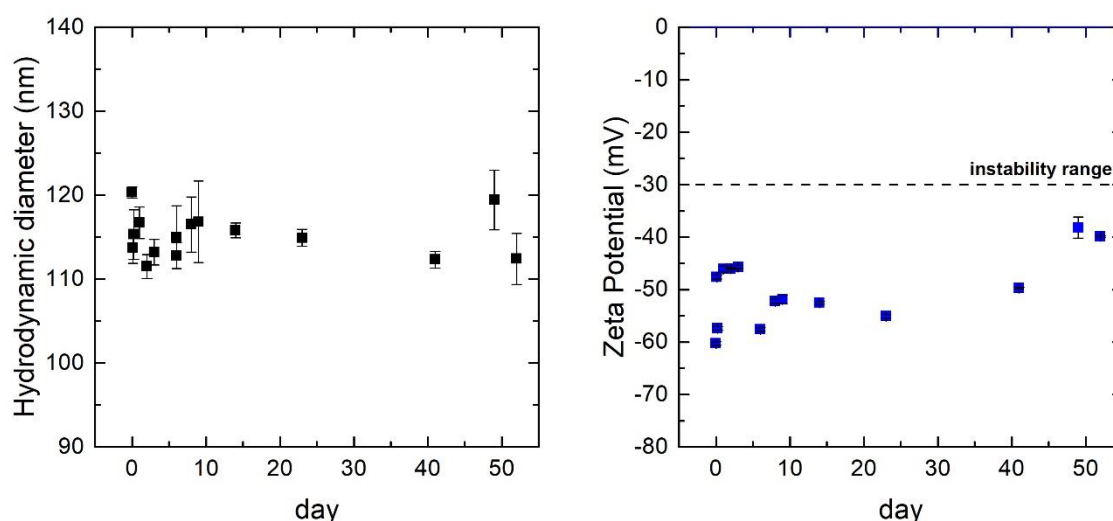


**Figure 3.42** – Colloidal properties of the Ox-NDs measured for 50 days (left – hydrodynamic diameter by weighted mean intensity, right – ZP). Data were collected for sample diluted down to 0.1 mg.ml<sup>-1</sup> immediately before the experiment.

The study of air annealed NDs (1 h 30 min, 550 °C) indicates a very good colloidal stability of NDs suspended in ultra-pure water up to 50 days. Some fluctuations in hydrodynamic diameter (weighted mean intensity, oscillation between 110 - 120 nm) can be observed. However, the general trend does not indicate any progressive agglomeration of NDs. More significant changes are observed on the ZP plot with a decrease in the absolute ZP value from absolute value  $60 \pm 1$  mV down to  $40 \pm 1$  mV. The ZP reflects changes in concentrations of ions on the slipping plane where the ZP is measured. Since the hydrodynamic diameter can be considered as a stable parameter, the ZP shows that ND surface-water interface is a dynamic system. Such lowering of the ZP can be related to many factors, as discussed for data obtained after 24 h (section 3.5.1). In addition to suggested ND's instability and possible surface modification induced by the presence of water molecules, exposure to light and air due to multiple sample manipulation can also have an effect<sup>53</sup>, especially on the dissolved species in water and related pH (but variation is not measurable).

### 3.5.2.3 Hydrogenated nanodiamonds

After Ox-NDs suspension, the colloidal stability of H-NDs (plasma: 250 W, 12 mbar, 20 min and thermally annealed: 1 h at 550 °C) was studied over 50 days. ND suspensions were prepared and stored at room temperature at a concentration of  $\sim 2$  mg.ml<sup>-1</sup>. See Appendix (section A.5) for complementary experiment with hydrogen annealed NDs from Adamas Nanotechnologies.

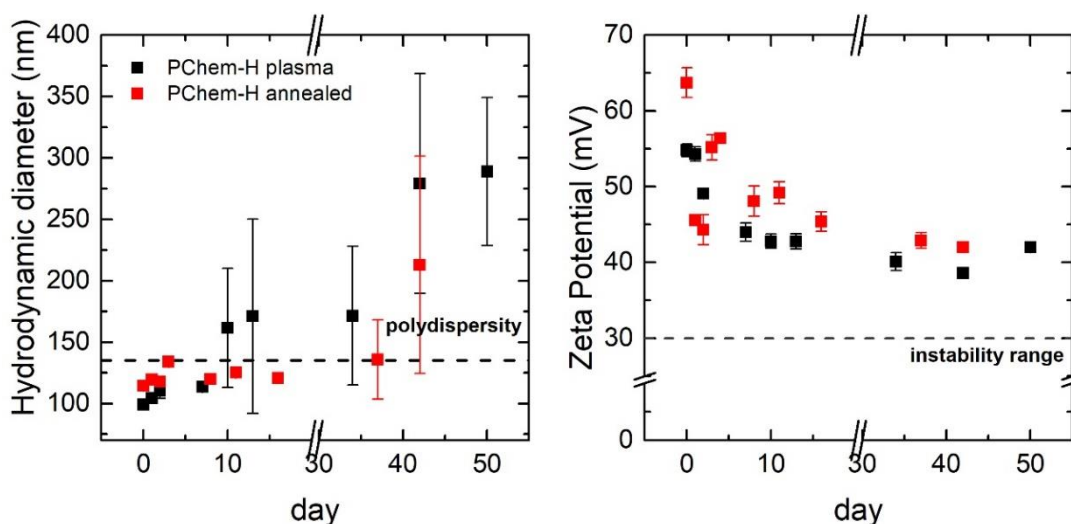


**Figure 3.43** – Colloidal properties (left – hydrodynamic diameter, right – ZP) of H-terminated (red - thermally annealed; black - plasma hydrogenated) NDs monitored over 50 days. Black dashed line indicates instability region in which DLS measurement have low data quality due to agglomeration and flocculation of NDs during the analysis. Note the axis breaks.

The hydrodynamic diameter of microwave plasma and thermally annealed H-NDs evolve after 50 days with similar colloidal properties up to 10 days. After 10 days, plasma H-NDs slowly agglomerate (size increase by factor 2.9) while the thermally annealed NDs are still stable up to 15 days (small increase by 6 %). After 42 days, hydrodynamic diameter of plasma and

thermally annealed H-NDs is c.a. 2.8 and 1.9-fold higher with respect to the initial value, respectively.

In terms of ZP evolution, a similar behavior (decrease over time) of H-NDs is observed as for air Ox-NDs, whatever the method of hydrogenation. Thermally annealed H-NDs with initially high ZP ( $64 \pm 2$  mV) undergo change and possess a lower surface charge ( $42 \pm 1$  mV) after 42 days. The plasma H-NDs exhibit the same decrease from initially being highly positive; a value of  $55 \pm 1$  mV down to  $39 \pm 1$  mV. Overall, the ZP stays above the stability threshold (absolute ZP  $> 30$  mV). After 50 days the visual appearance of H-NDs suspension (plasma, thermal) change. Samples become pale and cloudy with some bubbles occurring on top of the suspension (Figure 3.44). These changes are enhanced over time and are observed as soon as the colloidal properties starts to evolve (progressive agglomeration of NDs can be measured).



**Figure 3.44** – Plasma H-NDs hydrosol with some bubbles (red arrow) present on top of the suspension.

In conclusion, the H-NDs suspensions have limited colloidal stability when stored at a concentration of  $2 \text{ mg.ml}^{-1}$  at room temperature. However, the evolution seems to be quicker for plasma treated sample. The progressive agglomeration of the NDs leads to higher hydrodynamic diameter accompanied by lowering of the ZP, as observed after 50 days. Nanobubbles are formed and stabilized on top of the samples, this may indicate a progressive destabilization of H-NDs. The agglomeration state of H-NDs suspension can be possibly reduced by increasing sample's concentration and air exposure.

#### 3.5.2.4 Vacuum annealed nanodiamonds

The last long-term (up to 90 days) colloidal stability study was done for the vacuum annealed NDs. Four ND samples were treated at various annealing conditions (1 h /  $750^\circ\text{C}$ , 2 h /  $750^\circ\text{C}$ , 1 h /  $850^\circ\text{C}$ , and 2 h /  $850^\circ\text{C}$ ) and dispersed in ultra-pure water. The suspensions were kept at ambient temperature at the initial concentration between  $1.3 - 1.6 \text{ mg.ml}^{-1}$ . Prior the hydrodynamic diameter (weighted mean intensity) and ZP measurement, each sample was diluted down to  $0.1 \text{ mg.ml}^{-1}$ .

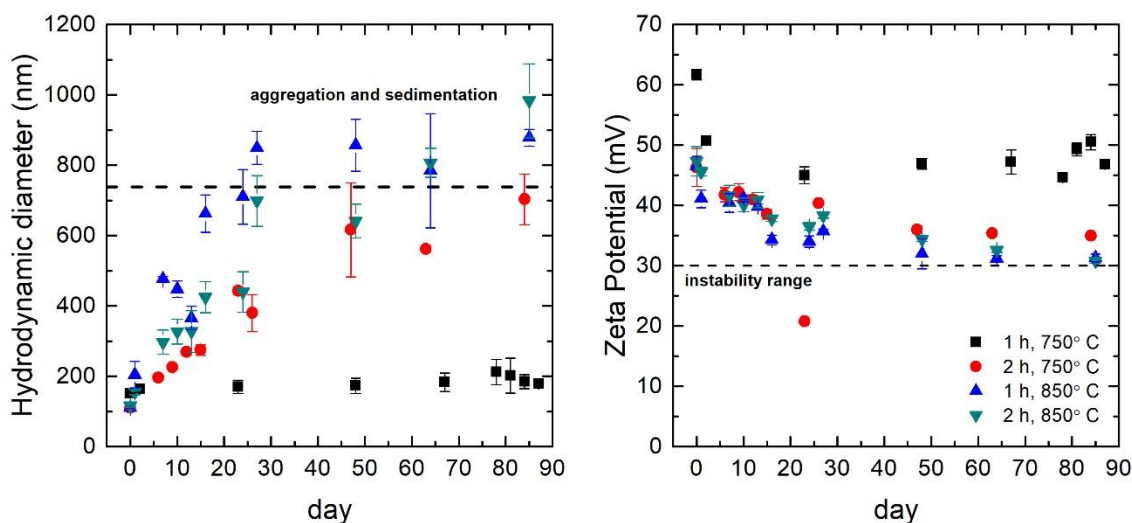


**Figure 3.47** – Evolution of colloidal properties of vacuum annealed NDs dispersed in water and monitored over 90 days. Black dashed line indicates low DLS data quality (left plot) induced by agglomeration of the particles during the analysis as well as ZP instability range (right plot).

At first glance, vacuum annealed NDs have lower long-term colloidal stability compared to the other surface terminations (Figure 3.47). However, an exception from this trend is the NDs vacuum annealed for 1 h at 750 °C, already known to be stable in water<sup>43</sup>.

The hydrodynamic diameter of NDs increases by factor 6.5 (2 h / 750 °C and 1 h / 850 °C) and 8.5 (2 h / 850 °C) after 90 days. The slowest and less significant size evolution is observed for samples vacuum annealed for 1 h and 2 h at 750 °C whereas an exponential increase can be seen for the NDs treated for 1 h and 2 h at 850 °C. Above 800 nm, particles flocculate during the measurement resulting in samples' instability and low DLS data quality (values above 800 nm, presented on the graph, are only illustrative to show the general trend). The ZP remains positive (> 30 mV) and is not screened by the progressive agglomeration of the NDs. However, only NDs annealed at 750 °C / 1 h have the ZP around 50 mV measured after 90 days while the other suspensions have the ZP closer to stability range threshold (30 mV). Similar decrease in the ZP over time is also observed for vacuum annealed NDs as seen for other surface modifications (air annealing, hydrogenation via plasma or thermal annealing).

As for other surface chemistries, an evolution of the hydrodynamic diameter can be also affected by the concentration, which is lower than intended one, when applying the same preparation protocol (< 2 mg.ml<sup>-1</sup>). Hydrophobic nature of the sp<sup>2</sup>-NDs makes the vacuum annealed NDs more resistant toward water-dispersion resulting in lower sample concentration.

Vacuum annealed NDs dispersed in water create brown-colored suspension which agglomerate quicker than H-NDs samples (except the stable NDs 1 h / 750 °C). Complete water-diamond separation occurs within a couple of days which is another proof of NDs' hydrophobicity, requiring the sample to be manually mixed before the DLS characterization. Nanobubbles can be also formed and stabilized on top of the sp<sup>2</sup>-NDs suspension, as

previously observed for the H-NDs. The bubbles occur especially when the particles are often exposed to air atmosphere (vial opened) or extensively mixed due to sample manipulation.

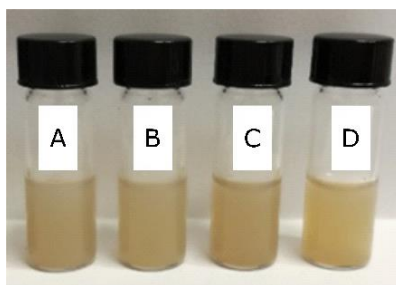


**Figure 3.48** – Pictures of the vacuum annealed ND suspensions (A - 1 h / 750 °C; B - 2 h / 750 °C; C - 1 h / 850 °C; D - 2 h / 850 °C). Samples were freshly-prepared (< 1 h) at concentration of NDs equal to 1 mg.ml<sup>-1</sup>.

To conclude, a progressive increase of vacuum annealing conditions results in higher hydrophobicity and lower colloidal stability of vacuum annealed NDs. Long-term colloidal stability is only observed for the early-stage graphitized particles (1 h / 750 °C). Highly positive Zeta Potential (> 30 mV) is maintained even after 90 days, indicating good colloidal stability of NDs, which are not supported by the hydrodynamic size evolution data.

#### 3.5.2.5 Summary

- Concentration for NDs affects its colloidal stability. Low concentration (0.2 mg.ml<sup>-1</sup>) results in a progressive agglomeration and flocculation of NDs whereas the higher one (2 mg.ml<sup>-1</sup>) limits time-induced changes in colloidal properties of NDs
- Progressive agglomeration of surface-modified NDs is not always reflected by the value of the ZP, as seen for even very large agglomerates (e.g. vacuum treated NDs). However, the decrease in the ZP is observed for all samples over the time
- Colloidal stability is a combination of ND's concentration, time and surface charge associated with specific surface chemistry
- Overall colloidal stability of surface-modified samples is as follows: air Ox-NDs > annealed H-ND > plasma H-NDs > vacuum annealed NDs
- Surface terminations seem to have hydrophilic / hydrophobic nature typical for carbon nanostructures
- Nanobubbles are formed and stabilized on top of hydrophobic hydrogenated and vacuum annealed NDs samples after long term storage.

### 3.6 FTIR study

The spectra of as-received and surface-modified detonation NDs were presented and discussed in detail elsewhere (Chapter 2, section 3). Herein, a comparative analysis of the modified NDs (air oxidized, plasma and thermally hydrogenated, and vacuum annealed) dried from the suspension will be described and compared with either the initial powder or the NDs remaining in the pellet after centrifugation.

#### 3.6.1 Surface-modified nanodiamond powder

As a reminder from the previous chapter, below are the spectra obtained after air annealing (1 h 30 min, 550 °C), plasma hydrogenation (250 W, 12mbar, 20 min), hydrogen annealing (1 h, 550 °C), and vacuum annealing (1 h, 750 °C) taken after modification (Figure 3.49). KBr pellets with NDs were left to dry under nitrogen flow for 24 h (plasma H-NDs) and 48 h (air Ox-NDs, annealed H-NDs, and sp<sup>2</sup>-NDs) to minimize an adsorbed water content.

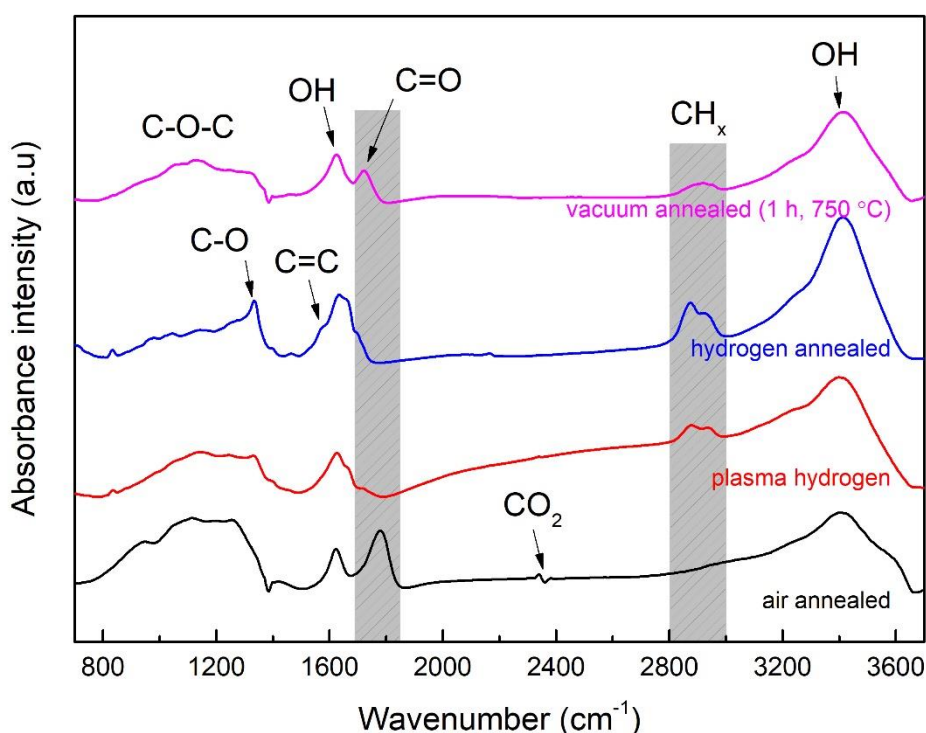


**Figure 3.49** – FTIR spectra of air Ox-NDs (black), plasma H-NDs (red), thermally H-NDs (blue), and vacuum annealed NDs (pink) dry powders. Grey fields indicate an area of interest used to analyze the surface modifications of the NDs (C=O and C-H<sub>x</sub> peak).

Briefly, C=O stretching (peak around 1730 - 1750 cm<sup>-1</sup>) associated with carbonyl-related groups is visible on both air Ox-NDs and vacuum annealed NDs with lower frequency shift in terms of the vacuum annealed powder. Thermal vacuum modification under 750 °C has already been shown to be insufficient to completely remove the carbonyl-related band observed also on as-received NDs. However, this frequency shift suggests the presence of

different structures in the oxygen-containing groups on the surface<sup>61</sup>. Bands at 2800 - 3000  $\text{cm}^{-1}$  associated with C-H vibrations are much more pronounced on plasma and thermally H-NDs compared to the vacuum annealed NDs. At the same time, some C-H content seen for vacuum annealed sample is also present on the native NDs, as shown in Chapter 2 (section 3)<sup>23</sup>.

### 3.6.2 Surface-modified nanodiamond pellet

The water addition and dispersion of the dry, surface-modified NDs powder involves a centrifugation step. After centrifugation, the supernatant containing NDs is separated from the remaining powder (non-dispersed). Such a powder comes in a form of pellet made of aggregated NDs. Here, the FTIR analysis was done on these NDs remaining in the pellet, after evaporation of the water over 24 - 48 h inside the oven (60 °C) (Figure 3.50).

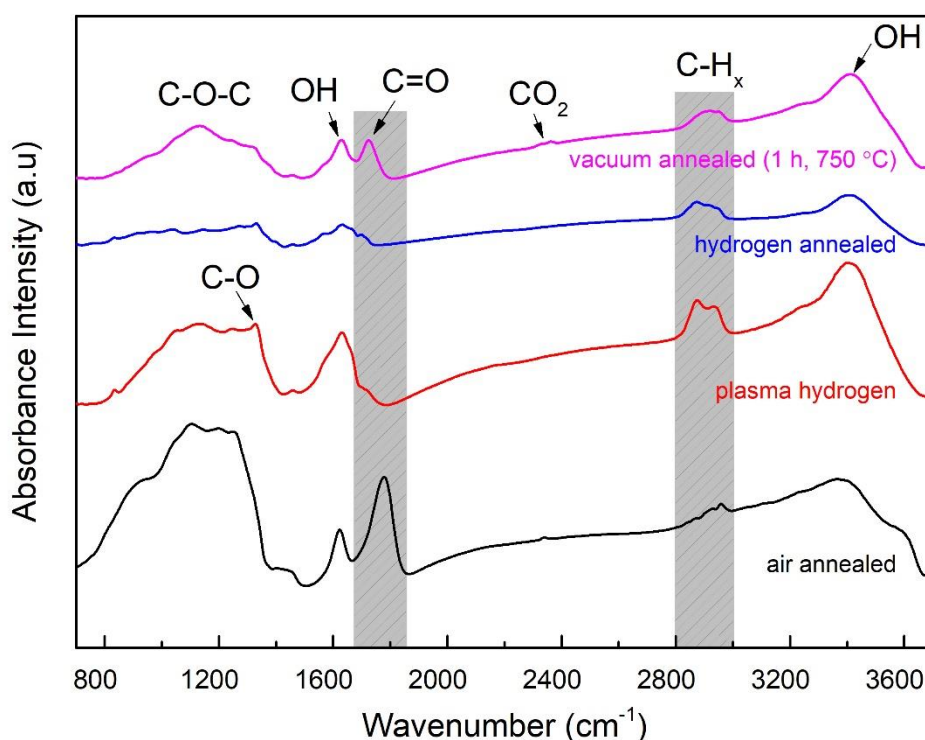


**Figure 3.50** – FTIR spectra of centrifugal pellets of air annealed (black), plasma hydrogenated (red), hydrogen annealed (blue), and vacuum annealed (pink) NDs. Grey fields indicate an area of interest used to analyze the surface modifications of the NDs (C=O and C-H<sub>x</sub> peak).

The FTIR spectra of the air annealed (1 h 30 min, 550 °C), plasma hydrogenated (12 mbar, 250 W, 20 min), hydrogen annealed (1 h, 550 °C) and vacuum annealed (1 h, 750 °C) pellets were taken. The FTIR samples made of NDs' pellets mixed with KBr (2 wt.%) were kept under nitrogen flow for 48 h (Ox-NDs, plasma H-NDs and vacuum annealed NDs) and 76 h (annealed H-NDs).

The FTIR spectra of centrifugal pellets are very similar to the one obtained on dried powders taken before water addition followed by sonication and centrifugation. The same spectral peaks, as described in the previous section (Figure 3.49), are present suggesting that NDs did not go any significant modifications after exposure to the aqueous environment and 1 h of sonication.

The vibrations of the diamond core and the surface chemistry (mainly C-O signatures) of all tested NDs gives a broad absorbance in the region 900 - 1500  $\text{cm}^{-1}$ . In addition to that, small features around 1300  $\text{cm}^{-1}$  can be related to C-O vibration coming from the oxidized groups or  $\text{CH}_2\text{OH}$ . These FTIR signatures are consistent with previously published works on Ox-NDs, plasma and thermally H-NDs as well the  $\text{sp}^2$ -NDs<sup>23,41,62,34</sup>. Note that despite extensive drying of NDs, peaks relative to water residues (OH at 1630  $\text{cm}^{-1}$  and 3500 - 3300  $\text{cm}^{-1}$ ) are always present in the FTIR spectra<sup>26,63</sup>. The  $\text{CO}_2$  seen on the spectrum of the air annealed NDs comes from the atmosphere.

It can be concluded that dry powder and pellet have the same chemical surface composition even after extensive exposure to water. Finally, curiosity-driven study led to the last part where FTIR analysis was performed on NDs successfully suspended in water.

### 3.6.3 Surface-modified nanodiamond suspension

The FTIR analysis can be also performed on NDs present in the supernatant (so-called NDs suspension) after complete evaporation of water content. The FTIR analysis preparation procedure includes drying of the 200  $\mu\text{l}$  of the NDs suspension inside the oven (60  $^\circ\text{C}$ ) for 24 h followed by addition of the KBr (2 wt.%) and another drying step under nitrogen flow for 48 h (air Ox-NDs, plasma H-NDs, and vacuum annealed NDs) and 78 h (annealed H-NDs).

To begin with, a clear modification of FTIR spectrum is observed on the surface-modified NDs successfully dispersed in water (Figure 3.51). In particular, the fingerprint region (wavenumber below 1500  $\text{cm}^{-1}$ ) representing bending vibrations characteristic for NDs has been clearly modified by the presence of water molecules. Successive drying did not restore the same shape as seen for the NDs powder and pellet samples. A large band with a maximum around 1050  $\text{cm}^{-1}$ , already present on the surface of the dried powders, appears as much larger, prominent easily distinguishable. The peak position can be attributed to C-O vibrations in alcohol groups (900 - 1200  $\text{cm}^{-1}$ ), previously reported for NDs-OH<sup>26</sup> and NDs-ethanol binding<sup>5</sup>. Another part of the spectra strongly affected by the suspension concerns the region ranging from 1100  $\text{cm}^{-1}$  to 1370  $\text{cm}^{-1}$  in which various oxygen-containing groups are present (ethers, acid anhydrides, lactones, and epoxy groups)<sup>64</sup>. Note that despite extensive drying of NDs, peaks relative to water residues (OH at 1630  $\text{cm}^{-1}$  and 3500 - 3300  $\text{cm}^{-1}$ ) are always present in the FTIR spectra<sup>26,63</sup>.

The hydrogen treatment aims to remove the carbonyl peak (C=O) at 1720 - 1730  $\text{cm}^{-1}$ . However, a band reappears immediately after water dispersion and stabilization whatever the surface termination. As this reappearance of C=O groups does not happen on pellet NDs, we can conclude that it does not come from the drying step in the oven, at only 60  $^\circ\text{C}$ . This suggests a possible surface oxidation, which may also take place spontaneously due to air

exposure<sup>65</sup>, but which seems to be specific to NDs which remains in suspension after centrifugation. Note that the presence of these C=O groups will help the hydrophilicity of NDs<sup>45</sup>. The same features are also observed in the spectra taken for NDs suspended in water for 50 days.

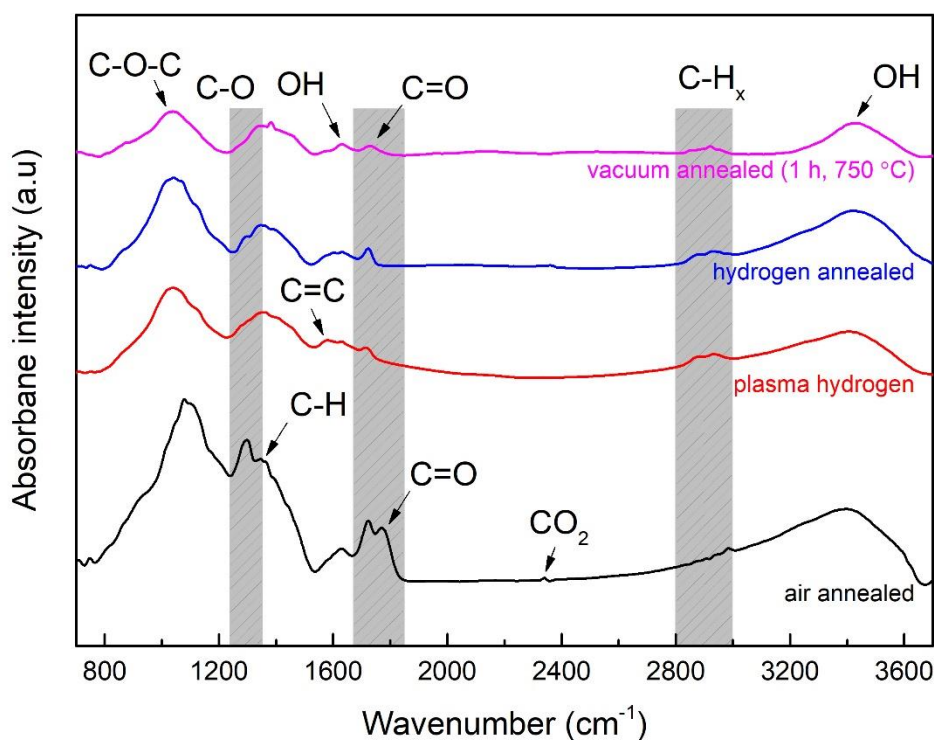


**Figure 3.51** – FTIR spectra of water-suspended air Ox-NDs (black), plasma (red) and thermally (blue) H-NDs and vacuum annealed NDs (pink). Grey fields indicate an area of interest used to analyze the surface modifications of the NDs.

### 3.6.4 Summary

To sum up, after centrifugation, NDs coming from the supernatant exhibit a slightly different FTIR spectrum than NDs coming from the pellet, which finally looks like the dried treated NDs. This FTIR study evidenced that H-NDs whatever the hydrogenation method is slightly re-oxidized (reappearance of C=O related group) and that water is strongly adsorbed on their surface, surprisingly as much as for carboxylated NDs which are really hydrophilic. This finding well emphasizes the high reactivity of hydrogenated NDs towards water molecules<sup>40</sup>. Peaks related to the formation of C-O groups (alcohol for instance) are also emphasized on NDs dried from the supernatant, which has already been signalled in the literature for hydrogenated NDs<sup>9</sup>. Note that long-term FTIR study of the different surface chemistries in suspension did not exhibit any major modification, which could have help on the understanding of the loss of colloidal stability.

## 3.7 Discussion about the colloidal properties of nanodiamonds according to their surface chemistries

In this work, we compared a large panel of surface chemistries (oxidation, hydrogenation, surface graphitisation), often reported in the literature, but performed on the same source of NDs and characterized using the same methods. Furthermore, all these NDs were put in suspension using the same protocol and analyzed by DLS with the same optimized procedure (Part 3). This offers a unique opportunity to really compare the behavior of these different modified NDs. The idea here is not to discuss in detail the origin of the zeta potential for each type of surface chemistries, there are several studies in the literature reporting different mechanisms. Our aim is to focus on their stability and how this parameter is affected. Indeed, in the literature, this parameter is almost never investigated, while it governs the use of the anionic or cationic NDs for further applications.

### 3.7.1 Air annealed nanodiamonds

First of all, among all surface terminations, an air oxidised NDs appear as the most stable colloidal suspension in water. This was expected according to the stability of the carboxylic groups in water which ensure a negative ZP<sup>12</sup> with a high absolute value (60 mV after 24h) in the range of neutral pH. Despite a significant decrease of ZP after 40 days (40 mV), the aggregation state measured by DLS seems to be unaffected (Part 5.2).

### 3.7.2 Hydrogenated nanodiamonds

Hydrogenated NDs produced by two different methods (plasma and thermal annealing) were also used in this Ph.D. work. Colloidal suspensions prepared just after hydrogenation exhibit similar properties with a positive ZP (55 mV and 64 mV, respectively) and a comparable aggregation state (Parts 4.2 and 4.3). The FTIR study of NDs from supernatant (Part 6) well supports a slight surface oxidation mechanism occurring during the preparation of colloidal suspensions in water. Indeed, according to FTIR spectra, carbonyl peaks (C=O) at 1720 - 1730  $\text{cm}^{-1}$ , which were efficiently removed after hydrogenation were again detected after water dispersion. Surface oxidation may also take place spontaneously due to air exposure of H-NDs<sup>40,65</sup>. According to the comparative FTIR investigation, this behavior is specific to NDs which remain in suspension after centrifugation. These C=O groups may favour the hydrophilicity of NDs<sup>45</sup> while they keep a positive ZP.

After 24 h, a significant decrease of ZP (20 % - plasma and 30 % - thermal) was observed whatever the hydrogenation method (Part 5.1). A slight agglomeration is noticed for plasma hydrogenated NDs. Let's discuss about the origin of this phenomena. This evolution can be either linked to modifications of the surface chemistry of NDs but also to an evolution of the interface between NDs and water. In the first case, spontaneous oxidation cannot be excluded as shown by FTIR characterization of water-suspended NDs. Oxygen-related FTIR features

seen on water-suspended NDs appears to be always present, whatever the age of the suspension. In addition to hydrogenated diamond surface, small graphitic reconstructions which could be present on the NDs are known to be very sensitive to oxidation<sup>44,66,59</sup>. The TEM investigations carried out on hydrogenated NDs from both methods reveal such sp<sup>2</sup>-C structures (Chapter 2, section 6). Concerning the evolution of the NDs / water interface, it has already been reported that the stabilization of hydrogenated NDs in water can involve adsorbates and/or water molecules re-organisation<sup>9,59</sup>. This may also explain the decrease of the ZP. Another option can reside in the presence of small particles, initially present in the suspension as a small size fraction, which start to surround bigger H-ND's aggregates. This would also explain slightly higher mean hydrodynamic diameter observed after 24 h. Presence of such ultra-small onion-like carbon (OLC), with diameter around 3 nm, has been also evidenced by the TEM study (Chapter 2) and other experiments described in the literature<sup>67,68</sup>.

After 50 days, a high degree of agglomeration of H-NDs is observed whatever the hydrogenation method (Part 5.2). However, this behavior is slower for hydrogen annealed NDs compared to plasma hydrogenated NDs. Bubbles have been observed on top of many H-NDs samples which agglomerate over time. Moreover, we observed that the effect increases when the sample is manually shaken or extensively exposed to ambient conditions during the experimental manipulation. Characterization of the gas has not been possible during this Ph.D. work but could be presumably O<sub>2</sub>, CO or CO<sub>2</sub>, or H<sub>2</sub><sup>69</sup>. In the literature, it has been shown that oxygen is required to stabilize the H-NDs<sup>12</sup>. Previous work of the team also revealed that stabilization of H-NDs in water is not efficient in degassed water and becomes possible when oxygen is re-dissolved in water<sup>70</sup>. Moreover, when the sample is degassed by bubbling with an inert gas (nitrogen or argon), NDs immediately agglomerate. As a consequence, we can expect that a modification of the gas content may result in a destabilization of the colloid. The colloidal properties of H-NDs can be only partially restored after repeated sonication and centrifugation steps leading to a lower hydrodynamic diameter but ZP cannot be fully recovered.

In the literature, the formation and the stability of oxygen nanobubbles induced by hydrophobic surface (inorganic clay surfaces modified with hexamethyldisilazane) has been reported by G. Pan and co-workers<sup>69</sup>. Authors have shown that the oxygen content of hydrophilic particles suspension is lower compared to the control sample whereas the hydrophobic suspension with higher oxygen content promotes the formation and the stabilization of a nanophase gas. Applying the same model of hydrophobic (H-NDs) and hydrophilic (Ox-NDs) surface properties, as suggested in 2016 by S. Stehlik et al.<sup>48</sup>, we can suggest that nanobubbles are created and stabilized by H-NDs. Until now, the origin of gas desorption is unexplored and requires further investigation.

The ageing of colloidal suspensions of H-NDs was also investigated for two concentrations (0.2 and 2 mg.ml<sup>-1</sup>). The drop of ZP occurs earlier and is larger for H-NDs suspended at lower concentration (Part 5.2). At the same time, a flocculation of H-NDs is measured by DLS. The same trend is observed for both hydrogenation techniques. According to the data, colloidal stability of NDs is a combination of several factors: the concentration, the time, and the

surface charge associated with the specific surface chemistry. In the literature, less attention is paid to the concentration of NDs. However, it is well-known that a low number of solvent-suspended particles may reduce its colloidal stability unless the stability is maintained by change in suspension's pH<sup>18,3,6</sup>.

### 3.7.3 Vacuum annealed nanodiamonds

Lastly, the colloidal behavior of NDs annealed under vacuum at different temperatures and different durations (750 °C and 850 °C; 1 h and 2 h) was investigated. Suspensions prepared after vacuum annealing exhibit very similar properties with a positive ZP included between 46 and 50 mV and a weighted mean size of 35 - 46 nm (Part 4.4). The origin of this positive ZP was previously studied by Gibson and al. and was attributed to pyrone-like structures present on the sp<sup>2</sup>/sp<sup>3</sup> NDs surface<sup>12</sup>. Our team also reported a few years ago on this positive ZP of vacuum annealed NDs being attributed to graphene patches present on the surface of NDs treated for 1 h at 750 °C<sup>43,41</sup>. Recently the same origin has been also reported by L. Gines et al. on hydrogenated HPHT NDs (thermal annealing method) with sp<sup>2</sup>-C on the surface<sup>44</sup>.

After 24 h, all vacuum annealed NDs start to agglomerate (Part 5.1). Among the different batches, the one annealed at 750 °C for 1 h exhibits the better colloidal stability. Contrary to H-NDs, no drop of ZP was measured. The early stages of graphitization performed at mild annealing conditions (1 h, 750 °C)<sup>43</sup> lead to colloidal properties comparable to oxidised or hydrogenated NDs, for ultra-fresh and 24 h aged states. This is not the case for NDs annealed under vacuum at higher temperature which are expected to be more graphitized for which the stability seems to be rapidly lost.

The colloidal stability of vacuum annealed NDs was then monitored up to 90 days (Part 5.2). In line with the trend observed after 24h, a high degree of agglomeration and flocculation occurs for these NDs except for mild annealing conditions (1 h, 750 °C). The later NDs still exhibit good colloidal properties with a positive ZP of 45 - 50 mV.

A first observation of these results reveals that finally only the stability over time of the suspension is affected by the different levels of annealing, while the colloidal properties of the ultra-fresh samples for the different treatments look very similar. The later observation would have let to think that whatever the annealing conditions, we finally sort one kind of modified NDs among the other after the sonication / centrifugation steps, presumably the less modified, and keep them in suspension. However, the different colloidal behaviors over the time do not support this hypothesis, and show that the various suspensions really differ.

An increasing ratio of the sp<sup>2</sup>/sp<sup>3</sup> carbon is of course expected while increasing the annealing conditions (but maximum vacuum annealing temperature was set to be below 900 °C in order to induce only surface graphitization)<sup>43</sup>. If we consider that this ratio is preserved in the particles in suspension, we may conclude from all our observations that the presence of more graphite on NDs only plays on the stability over time. It does not affect the phenomenon at the origin of the ZP, which allows to obtain good colloidal properties on all ultra-fresh suspensions. Note that even after agglomeration, ZP is not really affected, which means that

the phenomenon at the origin of the positive ZP seems to remain in a certain extent (the validity of high ZP for flocculating aggregates remains questionable). A modification of the surface chemistry (spontaneous oxidation) or an evolution of the interface (oxygen adsorbates) over the time can be proposed, but it would have most likely affect as well the ZP. An increase of the hydrophobicity<sup>71</sup> due to a larger presence of sp<sup>2</sup>-C phases can be suggested to explain this effect, but it would have also been affected the colloidal properties of ultra-fresh samples. One possible explanation would reside in the presence of these ultra-small graphitized particles in the sample (seen by TEM on non-suspended particles), with a proportion following the annealing level, which could progressively surround bigger NDs' agglomerates as proposed for plasma hydrogenated NDs. TEM characterization of the agglomerates formed in aged suspension would be useful to check this hypothesis.

### 3.7.4 General discussion on the colloidal behavior of cationic nanodiamonds

If we exclude the oxidized NDs, for which the origin of the charge and the stability is rather well understood, all our suspensions exhibit almost the same properties, with a hydrodynamic diameter ranging from 35 to 46 nm (weighted mean number values), a comparable polydispersity values (if we take into account the distribution given by the weighted mean intensity), and ZP ranging from + 47 to + 64 mV. All these suspensions were prepared with NDs from the same source, with the same protocol of preparation, and only the surface treatment differs. We can also notice that all these surface treatments include high temperature exposure in inert or reductive atmosphere, with temperature ranging from 550 °C for hydrogen annealing up to 850 °C for vacuum annealing. We can estimate the temperature during the hydrogen plasma treatment to be around 800 °C (given by a measurement with an optical fibre inserted in the quartz tube during a treatment). At these temperatures, a partial desorption of the oxygen happens (see FTIR of vacuum annealed NDs), which is amplified during the plasma by the presence of H radicals, and during the hydrogen annealing by some catalytic reaction at the surface<sup>60</sup>. Dangling bonds are thus created, which can be either saturated by a hetero atom if available (hydrogen for instance) or reconstructed with neighbour's carbon which promotes the formation of local graphitic reconstructions.

Concerning the saturation of the surface with hydrogen, parallel work conducted in the laboratory by Emilie Nehlig in collaboration with the tritium labelling laboratory from the CEA has shown that in our conditions of annealing or plasma, we can put 10 times more tritium at the surface (as well as in the core) of the tritium annealed NDs that on the tritium plasma treated NDs. If we consider that the same ratio is preserved with hydrogen, then we can conclude that the hydrogen coverage at the surface does not affect directly the value of the ZP. Maybe because of a saturation of the ZP value. However, if we look at the stability over the time, this difference may explain the quicker agglomeration of plasma hydrogenated NDs. It would support the idea of a weaker stabilization of oxygen adsorbates at their surface at the origin of the ZP.

Another general observation concerns the behavior of vacuum annealed NDs compared to the hydrogenated ones. We have seen that NDs annealed with the harshest conditions quickly

lose their colloidal stability and form agglomerates. One hypothesis would be the presence of ultra-small OLC particles strongly graphitized forming agglomerates. Our TEM investigations suggest their presence for the lowest annealing temperature. At the same time, we have seen that hydrogenation by plasma also brings weaker stability over time. This treatment is performed with harsher conditions than hydrogen annealing, the temperature being higher and some of the NDs directly exposed to high energy species of the plasma. A similar effect of graphitized ultra-small particles forming agglomerates can, therefore, be reasonably expected in plasma H-NDs to explain their stability. In that sense, hydrogen annealed and vacuum annealed (1 h, 750 °C) particles would be more similar.

---

## Bibliography

1. Krüger, A. *et al.* Unusually tight aggregation in detonation nanodiamond: Identification and disintegration. *Carbon* **43**, 1722–1730 (2005).
2. Mochalin, V. N., Shenderova, O., Ho, D. & Gogotsi, Y. The properties and applications of nanodiamonds. *Nat. Nanotechnol.* **7**, 11–23 (2012).
3. Mchedlov-Petrosyan, N. O., Kamneva, N. N., Marynin, A. I., Kryshal, A. P. & Ōsawa, E. Colloidal properties and behaviors of 3 nm primary particles of detonation nanodiamonds in aqueous media. *Phys. Chem. Chem. Phys.* **17**, 16186–16203 (2015).
4. Shakun, A., Vuorinen, J., Hoikkanen, M., Poikelispää, M. & Das, A. Hard nanodiamonds in soft rubbers: Past, present and future – A review. *Compos. Part A Appl. Sci. Manuf.* **64**, 49–69 (2014).
5. Inel, G. A., Ungureau, E.-M., Varley, T. S., Hirani, M. & Holt, K. B. Solvent–surface interactions between nanodiamond and ethanol studied with in situ infrared spectroscopy. *Diam. Relat. Mater.* **61**, 7–13 (2016).
6. Ozawa, M. *et al.* Preparation and Behavior of Brownish, Clear Nanodiamond Colloids. *Adv. Mater.* **19**, 1201–1206 (2007).
7. Nunn, N. & Shenderova, O. Toward a golden standard in single digit detonation nanodiamond. *Phys. Status Solidi A* **213**, 2138–2145 (2016).
8. Krüger, A. *et al.* Surface functionalisation of detonation diamond suitable for biological applications. *J. Mater. Chem.* **16**, 2322–2328 (2006).
9. Petit, T. *et al.* Unusual Water Hydrogen Bond Network around Hydrogenated Nanodiamonds. *J. Phys. Chem. C* **121**, 5185–5194 (2017).
10. Shenderova, O., Hens, S. & McGuire, G. Seeding slurries based on detonation nanodiamond in DMSO. *Diam. Relat. Mater.* **19**, 260–267 (2010).
11. Hackley, V. A. & Wiesner, M. R. Protocol for preparation of nanoparticle dispersions from powdered material using ultrasonic disruption. *CEINT, Natl. Inst. Standards Technol.* 1–10 (2010).
12. Gibson, N. *et al.* Colloidal stability of modified nanodiamond particles. *Diam. Relat. Mater.* **18**, 620–626 (2009).
13. Larionova, I. *et al.* Properties of individual fractions of detonation nanodiamond. *Diam. Relat. Mater.* **15**, 1804–1808 (2006).
14. Shenderova, O. Seeding slurries based on detonation nanodiamond in DMSO. *Diam. Relat. Mater.* **19**, (2010).
15. Kurzyp, M. *et al.* Hydroxyl Radicals Production Induced by Plasma Hydrogenated Nanodiamonds under X-ray Irradiation. *Chem. Commun.* **53**, 1237–1240 (2017).
16. Kozak, H. *et al.* Oxidation and reduction of nanodiamond particles in colloidal solutions by laser irradiation or radio-frequency plasma treatment. *Vib. Spectrosc.* **83**, 108–114 (2016).

17. Dideikin, A. T. *et al.* Rehybridization of carbon on facets of detonation diamond nanocrystals and forming hydrosols of individual particles. *Carbon* **122**, 737–745 (2017).
18. Kashyap, S., Mishra, S. & Behera, S. K. Aqueous Colloidal Stability of Graphene Oxide and Chemically Converted Graphene. *J. Nanoparticles* **2014**, 1–6 (2014).
19. Pichot, V., Comet, M., Fousson, E., Baras, C. & Spitzer, D. Dispersion of detonation nanodiamonds in a liquid medium. Retrieved from: [http://acs.omnibooksonline.com/data/papers/2007\\_B063.pdf](http://acs.omnibooksonline.com/data/papers/2007_B063.pdf) (Accessed: 10<sup>th</sup> September 2017)
20. Pentecost, A., Gour, S., Mochalin, V., Knoke, I. & Gogotsi, Y. Deaggregation of nanodiamond powders using salt- and sugar-assisted milling. *ACS Appl. Mater. Interfaces* **2**, 3289–3294 (2010).
21. Turcheniuk, K., Trecuzzi, C., Deeleepojananan, C. & Mochalin, V. N. Salt-Assisted Ultrasonic Deaggregation of Nanodiamond. *ACS Appl. Mater. Interfaces* **8**, 25461–25468 (2016).
22. Shenderova, O. *et al.* Modification of detonation nanodiamonds by heat treatment in air. *Diam. Relat. Mater.* **15**, 1799–1803 (2006).
23. Williams, O. A. *et al.* Size-dependent reactivity of diamond nanoparticles. *ACS Nano* **4**, 4824–4830 (2010).
24. Nesterenko, P. N., Mitev, D. & Paull, B. Elemental analysis of nanodiamonds by inductively coupled plasma hyphenated methods. In: Arnault, J.-C. (ed.) *Nanodiamonds. Advanced Material Analysis, Properties and Applications*, 109–130 (Elsevier, 2017).
25. Petit, T. Modifications de surface des nanodiamants : compréhension des mécanismes d'échanges électroniques et mise en évidence d'un effet thérapeutique. Thèse de doctorat de l'École Normale Supérieure de Cachan. Français (mars 2013).
26. Shenderova, O. *et al.* Hydroxylated Detonation Nanodiamond: FTIR, XPS, and NMR Studies. *J. Phys. Chem. C* **115**, 19005–19011 (2011).
27. Krueger, A. & Lang, D. Functionality is Key: Recent Progress in the Surface Modification of Nanodiamond. *Adv. Funct. Mater.* **22**, 890–906 (2012).
28. Paci, J. T., Man, H. B., Saha, B., Ho, D. & Schatz, G. C. Understanding the Surfaces of Nanodiamonds. *J. Phys. Chem. C* **117**, 17256–17267 (2013).
29. Mochalin, V. N. & Gogotsi, Y. Wet chemistry route to hydrophobic blue fluorescent nanodiamond. *J. Am. Chem. Soc.* **131**, 4594–4595 (2009).
30. Chakrapani, V. *et al.* Charge Transfer Equilibria Between Diamond and an Aqueous Oxygen Electrochemical Redox Couple. *Science* **318**, 1424–1430 (2007).
31. Dankerl, M. *et al.* Hydrophobic Interaction and Charge Accumulation at the Diamond-Electrolyte Interface. *Phys. Rev. Lett.* **106**, 196103 (2011).

32. Arnault, J.-C. *et al.* Surface chemical modifications and surface reactivity of nanodiamonds hydrogenated by CVD plasma. *Phys. Chem. Chem. Phys.* **13**, 11481–11487 (2011).
33. Korolkov, V. V., Kulakova, I. I., Tarasevich, B. N. & Lisichkin, G. V. Dual reaction capacity of hydrogenated nanodiamond. *Diam. Relat. Mater.* **16**, 2129–2132 (2007).
34. Girard, H. A. *et al.* Surface properties of hydrogenated nanodiamonds: a chemical investigation. *Phys. Chem. Chem. Phys.* **13**, 11517–11523 (2011).
35. Moche, H. *et al.* Carboxylated nanodiamonds can be used as negative reference in in vitro nanogenotoxicity studies. *J. Appl. Toxicol.* **37**, 954–961 (2017).
36. Landstrass, M. I. & Ravi, K. V. Hydrogen passivation of electrically active defects in diamond. *Appl. Phys. Lett.* **55**, 1391–1393 (1989).
37. Cui, J. B., Stammeler, M., Ristein, J. & Ley, L. Role of hydrogen on field emission from chemical vapor deposited diamond and nanocrystalline diamond powder. *J. Appl. Phys.* **88**, 3667–3673 (2000).
38. Yamaguchi, H. *et al.* Electron emission from conduction band of diamond with negative electron affinity. *Phys. Rev. B* **80**, 165321 (2009).
39. Zhang, L. & Hamers, R. J. Photocatalytic reduction of CO<sub>2</sub> to CO by diamond nanoparticles. *Diam. Relat. Mater.* **78**, 24–30 (2017).
40. Petit, T. *et al.* Surface transfer doping can mediate both colloidal stability and self-assembly of nanodiamonds. *Nanoscale* **5**, 8958–8962 (2013).
41. Petit, T. *et al.* Oxygen hole doping of nanodiamond. *Nanoscale* **4**, 6792–6799 (2012).
42. Dukovic, G. *et al.* Reversible Surface Oxidation and Efficient Luminescence Quenching in Semiconductor Single-Wall Carbon Nanotubes. *J. Am. Chem. Soc.* **126**, 15269–15276 (2004).
43. Petit, T., Arnault, J.-C., Girard, H. A., Sennour, M. & Bergonzo, P. Early stages of surface graphitization on nanodiamond probed by x-ray photoelectron spectroscopy. *Phys. Rev. B* **84**, 233407 (2011).
44. Gines, L. *et al.* Positive Zeta Potential of Nanodiamonds. *Nanoscale* **9**, 12549–12555 (2017).
45. Ji, S., Jiang, T., Xu, K. & Li, S. FTIR study of the adsorption of water on ultradispersed diamond powder surface. *Appl. Surf. Sci.* **133**, 231–238 (1998).
46. Korobov, M. V., Avramenko, N. V., Bogachev, A. G., Rozhkova, N. N. & Ōsawa, E. Nanophase of Water in Nano-Diamond Gel. *J. Phys. Chem. C* **111**, 7330–7334 (2007).
47. Petit, T. *et al.* Probing Interfacial Water on Nanodiamonds in Colloidal Dispersion. *J. Phys. Chem. Lett.* **6**, 2909–2912 (2015).
48. Stehlik, S. *et al.* Water interaction with hydrogenated and oxidized detonation nanodiamonds - Microscopic and spectroscopic analyses. *Diam. Relat. Mater.* **63**, 97–102 (2016).

49. Buzea, C., Pacheco, I. I. & Robbie, K. Nanomaterials and nanoparticles: sources and toxicity. *Biointerphases* **2**, MR17–MR71 (2007).
50. Volkov, D. S., Semenyuk, P. I., Korobov, M. V. & Proskurnin, M. A. Quantification of nanodiamonds in aqueous solutions by spectrophotometry and thermal lens spectrometry. *J. Anal. Chem.* **67**, 842–850 (2012).
51. Georges, J. Advantages and limitations of thermal lens spectrometry over conventional spectrophotometry for absorbance measurements. *Talanta* **48**, 501–509 (1999).
52. Sales, R. S. & Support, A. Dynamic Light Scattering training achieving reliable nano particle sizing. *ATA Scientific Instruments*. Retrieved from: <http://149.171.168.221/partcat/wp-content/uploads/Malvern-Zetasizer-LS.pdf> (Accessed: 19<sup>th</sup> August 2017)
53. Korobov, M. V *et al.* Improving the dispersity of detonation nanodiamond: differential scanning calorimetry as a new method of controlling the aggregation state of nanodiamond powders. *Nanoscale* **5**, 1529–1536 (2013).
54. Grall, R. *et al.* Impairing the radioresistance of cancer cells by hydrogenated nanodiamonds. *Biomaterials* **61**, 290–298 (2015).
55. Animal Resource Program. Administration by Injection. *The Pennsylvania State University* (2014). Retrieved from: <https://www.research.psu.edu/arp/experimental-guidelines/administration-by-injection.html>. (Accessed: 23<sup>rd</sup> August 2017)
56. Panich, A. M. & Aleksenskii, A. E. Deaggregation of diamond nanoparticles studied by NMR. *Diam. Relat. Mater.* **27–28**, 45–48 (2012).
57. Girard, H. A. *et al.* Hydrogenation of nanodiamonds using MPCVD: A new route toward organic functionalization. *Diam. Relat. Mater.* **19**, 1117–1123 (2010).
58. Stanishevsky, A. V., Walock, M. J. & Catledge, S. A. Surface modification and stability of detonation nanodiamonds in microwave gas discharge plasma. *Appl. Surf. Sci.* **357**, 1403–1409 (2015).
59. Arnault, J. C. & Girard, H. A. Hydrogenated nanodiamonds: Synthesis and surface properties. *Curr. Opin. Solid State Mater. Sci.* **21**, 10–16 (2016).
60. Ahmed, A.-I., Mandal, S., Gines, L., Williams, O. A. & Cheng, C.-L. Low temperature catalytic reactivity of nanodiamond in molecular hydrogen. *Carbon* **110**, 438–442 (2016).
61. Vinogradov, N. A. *et al.* Impact of Atomic Oxygen on the Structure of Graphene Formed on Ir(111) and Pt(111). *J. Phys. Chem. C* **115**, 9568–9577 (2011).
62. Gaebel, T., Bradac, C., Chen, J., Hemmer, P. & Rabeau, J. R. Size-reduction of nanodiamonds via air oxidation. *Diam. Relat. Mater.* **21**, 28–32 (2012).
63. Mochalin, V., Osswald, S. & Gogotsi, Y. Contribution of Functional Groups to the Raman Spectrum of Nanodiamond Powders. *Chem. Mater.* **21**, 273–279 (2009).

64. Schrand, A. M., Ciftan Hens, S. A., & Shenderova, O. Nanodiamond Particles: Properties and Perspectives for Bioapplications. In: Goddard, W. A., Brenner, D. W., Lyshevski, S. E. & Iafrate, G. J. (eds.) Handbook of nanoscience, engineering, and technology. Third Edition. 789-866 (CRC Press, 2012).
65. Nebel, C. E. Photocatalysis: a source of energetic electrons. *Nat. Mater.* **12**, 780–781 (2013).
66. Osswald, S., Yushin, G., Mochalin, V., Kucheyev, S. O. & Gogotsi, Y. Control of sp<sup>2</sup>/sp<sup>3</sup> carbon ratio and surface chemistry of nanodiamond powders by selective oxidation in air. *J. Am. Chem. Soc.* **128**, 11635–11642 (2006).
67. Gu, W., Peters, N. & Yushin, G. Functionalized carbon onions, detonation nanodiamond and mesoporous carbon as cathodes in Li-ion electrochemical energy storage devices. *Carbon* **53**, 292–301 (2013).
68. Sano, N. *et al.* Properties of carbon onions produced by an arc discharge in water. *J. Appl. Phys.* **92**, 2783–2788 (2002).
69. Pan, G. & Yang, B. Effect of surface hydrophobicity on the formation and stability of oxygen nanobubbles. *ChemPhysChem* **13**, 2205–2212 (2012).
70. Ruffinatto, S. *et al.* Spontaneous (bio)functionalization of hydrogenated nanodiamonds. In: Aharonovich, I. & Pauzauskie, P. (Chairs), Symposium conducted at the *MRS Spring Meeting. Phoenix, USA* (2016).
71. Lee, S.-C., Tai, F.-C. & Wei, C.-H. Correlation between sp<sup>2</sup>/sp<sup>3</sup> Ratio or Hydrogen Content and Water Contact Angle in Hydrogenated DLC Film. *Mater. Trans.* **48**, 2534–2538 (2007).





# Chapter 4

## Irradiation of nanodiamonds

### Summary

---

<b>4.1 Introduction.....</b>	<b>125</b>
<b>4.2 Bibliography review .....</b>	<b>125</b>
4.2.1 Water radiolysis .....	126
4.2.2 Fluorescence probes for HO <sup>•</sup> detection.....	126
4.2.3 Emission of electrons from detonation nanodiamond particles .....	128
4.2.4 Radiosensitization with nanoparticles .....	130
<b>4.3 Establishment of the irradiation protocol.....</b>	<b>132</b>
4.3.1 Properties of coumarin .....	132
4.3.2 Properties of 7-hydroxycoumarin .....	133
4.3.2.1 UV-Visible absorbance .....	134
4.3.2.2 Fluorescence emission .....	135
4.3.2.3 Stability of 7-hydroxycoumarin fluorescence .....	135
4.3.3 Fluorescence properties of nanodiamonds alone .....	136
4.3.4 Colloidal stability of nanodiamonds in coumarin / 7-hydroxycoumarin .....	137
4.3.5 Fluorescence properties of 7-hydroxycoumarin in the presence of nanodiamonds ....	138
4.3.5.1 Quenching effect.....	138
4.3.5.2 Removal of the quenching effect: nanodiamonds and sodium chloride.....	139
4.3.5.3 Removal of the quenching effect: 7-hydroxycoumarin and sodium chloride .....	140
4.3.5.4 Removal of the quenching effect: sodium chloride and centrifugation .....	141
4.3.6 Summary .....	142
<b>4.4 Measurements of HO<sup>•</sup> radicals .....</b>	<b>142</b>
4.4.1 Air annealed nanodiamonds.....	143
4.4.2 Plasma hydrogenated nanodiamonds .....	145
4.4.2.1 Effect of H- NDs from PlasmaChem on HO <sup>•</sup> production .....	145
4.4.2.2 Effect of the source of detonation nanodiamonds.....	147
4.4.3 Hydrogen annealed nanodiamonds.....	148

---

4.4.3.1 Effect of the source of detonation nanodiamonds.....	149
4.4.4 Vacuum annealed nanodiamonds .....	150
4.4.5 Summary .....	151
4.4.6 Aging effect vs. measurements of HO <sup>•</sup> radicals .....	152
4.4.6.1 Air annealed nanodiamonds .....	152
4.4.6.2 Plasma hydrogenated nanodiamonds .....	153
4.4.6.3 Hydrogen annealed nanodiamonds.....	154
4.4.6.4 Summary .....	156
<b>4.5 Gamma irradiation .....</b>	<b>157</b>
<b>4.6 Detection and quantification of solvated electrons via HO<sup>•</sup> and N<sub>2</sub>O / O<sub>2</sub>.....</b>	<b>158</b>
4.6.1 Principle of the method .....	158
4.6.2 X-rays irradiation.....	158
4.6.3 Gamma irradiation .....	160
4.6.4 Summary .....	162
<b>4.7 Discussion about the behavior of nanodiamonds under irradiation .....</b>	<b>163</b>
4.7.1 Discussion on the origin of the phenomenon.....	164
4.7.1.1 Effect of a metallic contamination.....	164
4.7.1.2 Surface effect .....	164
4.7.1.3 Colloidal stability effect.....	166
4.7.1.4 Effect of the core.....	166
4.7.1.5 Origin of the effect coming from water interface.....	168
<b>Bibliography .....</b>	<b>171</b>

---

## 4.1 Introduction

The radiosensitizing effect of H-NDs, previously demonstrated *in vitro*, is linked to two important physical phenomena: interaction of NDs with water and with ionizing radiation. As a consequence, the enhancement in reactive-oxygen species (ROS) production observed in bio-media, is also associated with the water radiolysis mechanism. Knowledge about colloidal properties and stability of NDs, presented in Chapter 3, was required to study interaction and behavior of detonation NDs under irradiation in water.

In the following chapter, an experimental protocol for detection of ROS under illumination of water-dispersed NDs is presented and discussed. In particular, coumarin (Cou) model, which was initially developed for gold nanoparticles (GNPs), has been adapted and used for NDs based on *in situ* experiments. Among many types of ROS produced, hydroxyl radical ( $\text{HO}^\bullet$ ) and solvated electron ( $e_{\text{aq}}$ ) have been chosen due to their high production yield and their importance in chemical damage to cells.

Surface-modified NDs dispersed in ultra-pure water were exposed to high ( $\gamma$ -Rays,  $E = 1.17$  MeV) and low (X-Rays,  $E = 17.5$  keV) energies which also corresponds to the radiotherapeutic range. Detection and quantification of  $\text{HO}^\bullet / e_{\text{aq}}$  production in the presence of NDs have been performed with respect to different surface chemistries (oxidized, hydrogenated, surface graphitized).

Interaction and behavior of surface-modified NDs with ionizing radiation according to the dose and energy are presented and discussed with respect to the literature. The concentration-dependent effect of  $\text{HO}^\bullet / e_{\text{aq}}$  overproduction, observed for specific source and surface modification of ND, is shown for the first time.

Finally, the main focus of this chapter is to clarify the chemical origin of the radiosensitizing effect by taking into account the specific surface chemistry and colloidal properties of detonation NDs' suspensions. The link between results obtained for carbon-based ND particles and metallic GNPs is made.

## 4.2 Bibliography review

The behavior of detonation NDs under illumination in aqueous media remains rather unexplored, except for UV wavelengths<sup>1,2</sup>. To study such a phenomena, the mechanism of water radiolysis<sup>3</sup> as well as the interaction of NDs with water molecules and irradiation<sup>4</sup>, needs to be understood. Up-to-date only few studies have dealt with the radiosensitizing effect of H-NDs<sup>5,6</sup>, however, other types of radiosensitizing nanoparticles (NPs) have already been explored<sup>7</sup>. In the following part, the essential knowledge about the interaction of light with water, matter represented by detonation NDs, as well as the current-state-of art of the radiotherapy with active NPs is presented.

### 4.2.1 Water radiolysis

Interaction of ionizing radiation with water molecules results in its decomposition and production of highly-reactive oxygen species (ROS). Up-to-date the mechanism behind the ROS production and the framework in which the water radiolysis occurs is well understood due to extensive studies in the past<sup>8,9</sup>.

Irradiation-induced water decomposition lead to generation of various species such as: solvated electron ( $e_{aq}$ ), hydroxyl radical ( $HO^\bullet$ ), superoxide ( $^{\bullet}O_2^-$ ), atomic hydrogen ( $H^\bullet$ ), hydroxyl ion ( $OH^-$ ), hydrogen peroxide ( $H_2O_2$ ), dioxide ( $H_2O$ ), dihydrogen ( $H_2$ ), and negligible  $HO_2^\bullet$  radical<sup>3</sup>.

The water radiolysis is nothing but a transfer of energy which takes place under different types of ionizing radiation (e.g. X-ray,  $\alpha$ ,  $\beta$ , and  $\gamma$ ) within a time scale in the order of  $10^{-6} - 10^{15}$  s.<sup>3</sup> The direct detection of ROS is limited by their high instability, short lifetime (ns range), and the speed of their interaction / recombination<sup>3</sup>.

The actual concentration of ROS produced after water illumination is defined by their radiolytic yield (*G-value*: number of species produced per 100 eV) as a function of the energy and pH given in  $\mu\text{mol}\cdot\text{J}^{-1}$ . Referring back to the energy transfer, the ROS are highly reactive and can further ionize the matter causing damage to biological systems (e.g. human cells)<sup>10</sup>.

Apart from the devastating effect, radiolysis can be widely used on a daily basis in e.g. radiosterilization<sup>11</sup>, sewage treatment<sup>12</sup> or even food conservation<sup>13</sup>. However, the main utilization of water radiolysis mechanism has been in radiotherapy to treat various types of cancer cells<sup>14,15</sup>.

Following that, the main impact and the highest radiolytic yield is assigned to  $HO^\bullet$ ,  $e_{aq}$ , and  $H^\bullet$  which are considered to be responsible for major radiation-induced damage to biological systems. Due to the high importance of these radicals, many studies have been devoted to their detection and quantification<sup>16,17,18</sup>.

### 4.2.2 Fluorescence probes for $HO^\bullet$ detection

In the literature related to radiotherapy treatment, it is reported that 50 - 70 % of biological damage to the cell is caused by  $HO^\bullet$  under X-rays<sup>18,19</sup>. The importance of  $HO^\bullet$  has been also experimentally demonstrated by Hall in 2000 who used specific scavengers for individual ROS species. The results obtained clearly indicated that  $HO^\bullet$  radical is mostly responsible for the radiation impairment<sup>20</sup>.

Based on these findings in radiochemistry domain, the importance of  $HO^\bullet$  resulted in many models trying to accurately detect and quantify the  $HO^\bullet$  production in aqueous media<sup>21</sup>. The direct detection is, however, limited by the experimental conditions<sup>22</sup>, their short lifetime and high reactivity toward recombination with other species<sup>23,24</sup>. Thus, mostly indirect methods based on fluorescence detection have been used for this purpose<sup>21</sup>.

The HO• stabilization problem has been overcome by designing so-called spin traps to trap the radicals by forming more stable and detectable species<sup>25</sup>. A chemically synthesized molecule (1,1,3-trimethylisindole *N*-oxide - TIMO) has been used to detect various ROS species (primary and secondary) which after interaction with TIMO could be characterized by Electron Paramagnetic Resonance (EPR). Similar approaches with entrapping HO• molecules have also been proposed by many others<sup>26,27,28</sup>. However, the main drawback of the trapping method comes from lack of selectivity toward HO• resulting in non-effective and limited precision in global quantification<sup>29</sup>.

The most popular methods to detect and quantify HO• are based on hydroxylation of aromatic rings and fluorescence measurements<sup>21,16</sup>. Attachment of HO• into aromatic ring of molecules (e.g. benzene, coumarin, phenoxazine) acting like a specific assay resulting in the formation of OH-related products which exhibit fluorescence properties<sup>30</sup>. Following the same trend, in 2005 A. Gomes et al. published a large-scale review with fluorescence probes used for detection of various ROS<sup>31</sup>. The authors listed sodium terephthalate as another type of hydroxylation-based probe for HO• detection forming fluorescent sodium 2-hydroxyterephthalate molecule<sup>31</sup>. However, the method was only effective in the optimum pH range (6.80 – 7.90) as shown initially by Tai C. et al. in 2009<sup>32</sup>. Another example also included the non-fluorescent 1,3-cyclohexanedione (CHD) which can be converted via multiple-step into a fluorescent compound in DMSO. In this case, the hydroxylated compound has to be heated up to 95 °C which may cause a problem with data interpretation<sup>32</sup>.

The main drawback of using aromatic molecules has been associated with their low solubility (for instance phenoxazine is insoluble) in water and high affinity toward spontaneous oxidation by other species than HO•<sup>33</sup>. Nevertheless, this method has been the most reproducible and highly selective toward HO• so far.

Apart from many aromatic rings considered as rather unsuitable for detection of HO• in water, coumarin appears to be the most promising one. Relatively good solubility (0.17 g / 100 ml) in water and hydroxylation of Cou-ring produces fluorescent compounds (e.g. 7-hydroxycoumarin) with high fluorescence yield.

In 2008, the same Cou method has been shown to be highly effective for HO• detection in the presence of TiO<sub>2</sub> particles<sup>16</sup>. The most recent Cou model was developed in 2014 for examination of HO• production enhancement induced by gold NPs (GNPs)<sup>18</sup>. Intensive development of radiosensitizing NPs resulted in many research studies allowing to quantify the effect based on water-radiolysis mechanism. The study conducted by C. Sicard-Roselli et al. examined hydroxylation mechanism of Cou toward detection of 7-hydroxycoumarin (7-OH Cou) which exhibits the strongest fluorescence properties. The detection efficacy was examined for various doses and concentrations of GNPs via fluorometer.

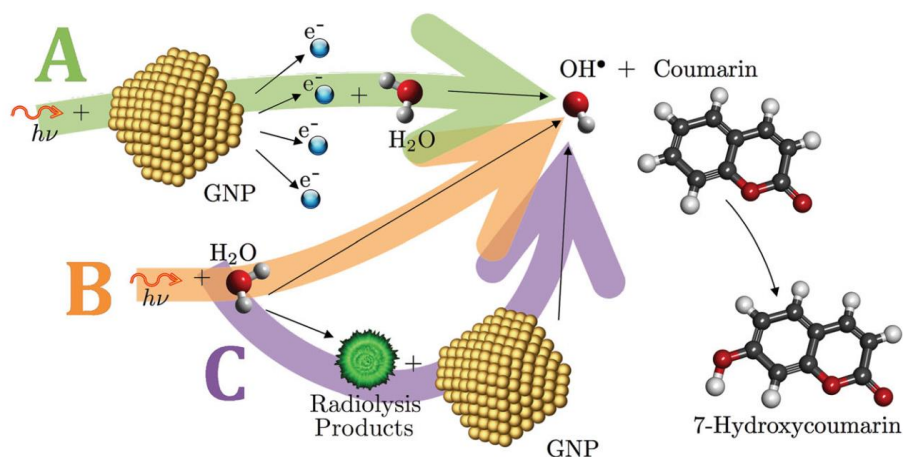


**Figure 4.1** – A schematic diagram of the pathways to form and determine the yield of the hydroxyl radical  $HO^\bullet$  in an irradiated solution containing gold nanoparticles<sup>18</sup>.

Finally, the same Cou model proposed by C. Sicard-Roselli, has been chosen for the experiments with detonation NDs based on its simplicity and high detection specificity toward  $HO^\bullet$ .

#### 4.2.3 Emission of electrons from detonation nanodiamond particles

High-energy irradiation (keV, MeV) of detonation NDs has been poorly explored. In contrast to the high-Z type of NPs, electron emission from NDs in water is a surface effect associated with active functionalities (see Chapter 1) and electronic properties of the diamond material (e.g. SC and NEA)<sup>34</sup>. Development of the surface treatments, dedicated to functionalization of detonation NDs<sup>35</sup>, allowed to expand the studies toward emission of electrons and radiosensitizing effect of non-metallic NDs<sup>5</sup>. The proof of concept started when T. Petit et al. demonstrated accumulation of electrons near the nanodiamond / water interface<sup>36</sup> suggesting potential electron emission from H-terminated NDs (H-NDs). At the same time, the same idea was also validated by Bolker and co-workers who probed NEA of isolated plasma hydrogenated detonation NDs by STS and KFM techniques<sup>37</sup>. The authors demonstrated that appropriately long hydrogen treatment (20 min) may give similar NEA property of detonation ND, as for planar diamond structure. Moreover, the NEA property seemed to be size- and surface-dependent leading to even lower band bending for smaller NDs. At the same time, the authors showed a dependency of the NEA to the length of the treatment, which we can connect to the hydrogenation level of the surface. The results of electron affinity versus ND size are presented below:

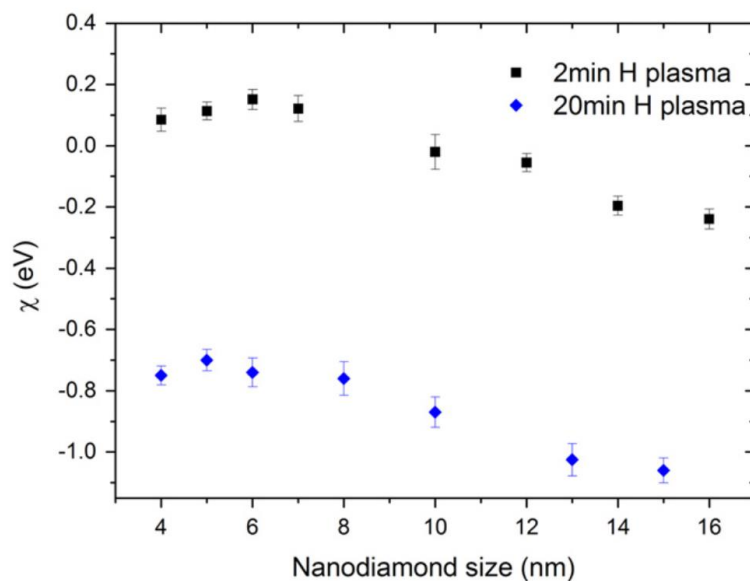


**Figure 4.2** – Electron affinity as a function of the ND size. Values for sample 1 (2 min in H-plasma) are marked with black squares, and those for sample 2 (20 min in H-plasma) are marked with blue diamonds<sup>37</sup>.

The most recent studies published by L. Zhang and R. Hamers in 2017, revealed electron emission ability of natural H-diamond NPs with high-quality crystallographic structure (median diameter of 125 nm) under UV illumination<sup>2</sup>. Moreover, the comparison with smaller, non-defect free detonation NDs, annealed under hydrogen flow according to the procedure presented elsewhere, has been reported<sup>38</sup>. The authors measured the photochemical reduction of CO<sub>2</sub> to CO in aqueous solution using H-NDs as an electron donor proving the concept of using ND particles instead of a planar diamond. More importantly, the same experimental conditions resulted in unsuccessful outcome in terms of detonation NDs (median diameter of 6 nm). Several reasons for the lack of detonation H-ND activity under UV have been highlighted, including a significant level of structural defects and fast surface-oxidation masking any possible effect.

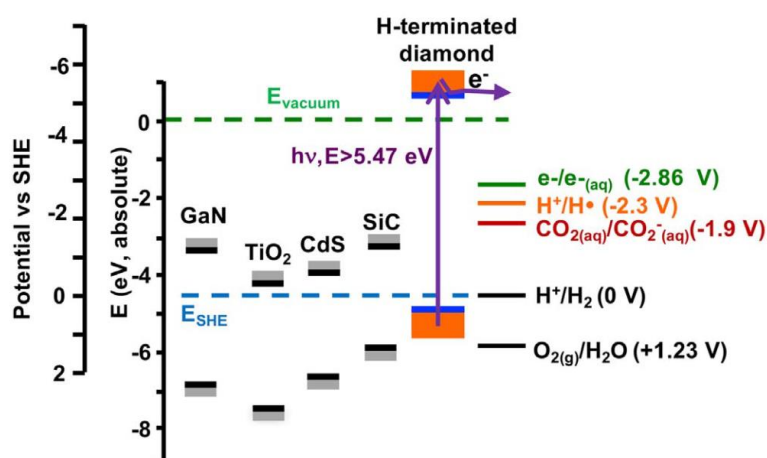


**Figure 4.3** – Energy band diagram of H-terminated diamond and some other semiconductors, together with related redox reactions of interest<sup>2</sup>.

Up-to-date the interaction of high-energy radiation (X-ray, gamma) with detonation NDs remains unexplored. The explanation arrives from classical physics of irradiation which says that the absorption of the light in carbon is lower than in metallic NPs, and hence, the NDs are considered to be less effective as photoemitters in the therapeutic range of energies.

#### 4.2.4 Radiosensitization with nanoparticles

The main problem of radiotherapy treatment is radioresistance and variety of cancer cells which requires aggressive therapy with a high dose of irradiation<sup>39</sup>. Reduction of the therapeutic dose can be achieved via a radiosensitizing agent (e.g. NPs) which enhances the effect of radiation<sup>7</sup>. This concept has been known for several decades<sup>40</sup> and has mostly been based on utilization of metal-based particles (e.g. silver, gold)<sup>41</sup>.

Nevertheless, the radiosensitizing NPs must meet specific requirements including bio-compatibility (no cyto- and gen-toxicity) and small size. In terms of design, specific shape, type of coating, mechanism of action, cell localization and energy activation also need to meet the medical expectations<sup>7,39</sup>. The radiosensitizing NPs can be divided into 3 main groups based on their atomic number and design:

- Metal-based NPs (e.g. Gold - Au, Silver - Ag, Platinum – Pt, Gadolinium – Gd)<sup>41</sup>
- Non-metallic NPs (e.g. Germanium – Ge, Bismut – Bi)<sup>42,43</sup>

The effect of NPs in dose enhancement is estimated by the SER (sensitization enhancement ration) factor, which is dose, concentration, and energy dependent<sup>41</sup>. In 2010 Chitrani reported that under X-ray irradiation (200 keV) gold nanoparticles (AuNPs) with a size of 50 nm, 14 nm, and 70 nm the SER effect was 1.43, 1.20 and 1.25, respectively<sup>44</sup>. More recently, the 32 nm AuNPs has been reported to give SER equal to more than 2<sup>18</sup>.

Among verity NPs, the main candidates for radiotherapy enhancement are silver (Z = 47) and gold (Z = 79). In the literature, many experiments can be found related to their *in vitro*<sup>45,46</sup>, and *in vivo*<sup>47,48</sup> effect. In particular, AuNPs have been used for radiotherapy enhancement since 2004<sup>49</sup>. Pioneering *in vivo* experiments in mice conducted by Hainfeld and co-workers showed that AuNPs in combination with X-ray (E = 250 keV) increased the survival rate from 0 % and 20 % up to 80 % with respect to gold and irradiation alone, respectively. In addition to that, the AuNPs were non-toxic whereas the therapeutic effect increased along with the concentration. The results of Hainfeld opened perspectives in the search of effective radiosensitizers.

In terms of silver nanoparticles (AgNPs), the study of Xu et al. showed the size-effect of 20, 50 and 100 nm particles on various cell lines (e.g. rat C6 glioma cells, human U251, and SHG-44). According to the results, the radiation (X-ray) efficiency was inversely related to the size of GNPs with the highest effect as follows:

$$20 \text{ nm} > 50 \text{ nm} > 100 \text{ nm}$$

Another complementary experiment performed *in vivo* on rats by Liu et al. (2013) showed that AgNPs induce apoptosis and activates the oxidative stress inside cells<sup>47</sup>. The experiments were performed under high-energy irradiation (X-ray, 6 MeV) with a dose of 10 Gy and a concentration of 10 and 20  $\mu\text{g}\cdot\text{ml}^{-1}$  injected intercellularly. Moreover, the authors suggested that the AgNPs produce  $\text{Ag}^+$  inside the cell which may catch released  $\text{e}^-$  and thus function as an oxidative agent for ROS production.

In the literature, many studies have been conducted toward the radiosensitizing effect of AuNPs<sup>50</sup> with several the theoretical studies revealing the enhancement effect is dose and energy dependent. However, the expected outcome is less promising than initially expected due to lack of standardization and selectivity of AuNPs leading to massive quantities required to observe an effect. A higher degree of complexity with respect to synthesis and experimental protocol<sup>51</sup> started to be observed resulting in contractionary results<sup>52</sup>. As a consequence, the research moved toward targeting and functionalization of AuNPs with a coating (e.g. PEG) to expand other possible bioapplications<sup>53,54</sup>.

The photoemission effect from NPs depends on the energy used to activate the emission. In other words, the incoming radiation transfer energy into an electron which can be ejected from its orbital with an energy equal to the initial one reduced by the binding energy.

The emission of the electron from the high-Z materials is associated with several incidents known from the basic physics namely: fluorescence scattering, Compton scattering, Auger electron, pair production (positron + electron), and Rayleigh scattering. The most important one in terms of cancer therapy includes Compton effect, photoelectric effect, and Auger-emission<sup>7</sup> (Figure 4.4).

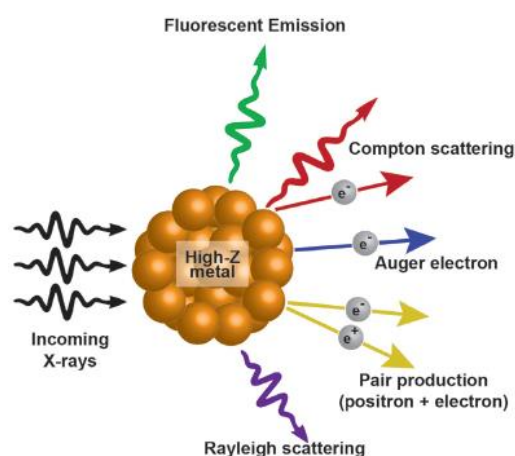


**Figure 4.4** – Interaction of X-ray with high-Z material nanoparticles<sup>7</sup>.

In terms of NPs, the main effect of irradiation takes place on the interface between water and solid material<sup>55</sup> and the recent studies have confirmed that organization of water molecules around NPs varies depending on the surface terminations and external environment<sup>56</sup>.

Up-to-date, the Au and Ag NPs did not reach the clinical step for radiosensitization. Only hafnium dioxide ( $\text{HfO}_2$ ) NPs have been tested in human with advanced tissue sarcoma in 2016. Clinical activity toward tumor reduction was observed with a mean value of 40 %. The  $\text{HfO}_2$  is already a commercial product (called NBTX) of Nanobiotix company<sup>57</sup>.

### 4.3 Establishment of the irradiation protocol

The ionizing radiation causes substantial damage to living organisms via direct and indirect interaction. Apart from the direct effects of irradiation, the indirect damage is caused by the production of highly-reactive but unstable oxygen species (e.g. peroxide –  $\bullet\text{O}_2^{-2}$ , superoxide –  $\bullet\text{O}_2^-$ , hydroxyl radical –  $\text{HO}\bullet$ , and singlet oxygen –  $^1\text{O}_2$ , hydrogen peroxide –  $\text{H}_2\text{O}_2$ ) via water radiolysis mechanism. The main damage to biological systems (e.g. DNA) is caused by  $\text{HO}\bullet$  and because of its importance, several methods have been developed to detect and quantify the  $\text{HO}\bullet$  radicals. The main limitation of its direct detection comes from the relatively short lifetime (nanosecond range)<sup>58</sup> and the lack of stability of  $\text{HO}\bullet$  in cellular conditions whereas the indirect method requires a highly selective and sensitive probe.

One characteristic feature of  $\text{HO}\bullet$  radicals is the chemical hydroxylation of aromatic rings (e.g. coumarin - Cou, benzene, or a phenoxazinone)<sup>21</sup>. At least one of the hydroxylated products possesses fluorescence properties which can be easily measured via fluorometer. Particularly interesting is the reaction of  $\text{HO}\bullet$  radicals with Cou which is highly selective allowing for its ease detection and quantification via 7-OH Cou.

Basic information about coumarin and one of its hydroxylated forms, the 7-hydroxycoumarin (7-OH Cou), including the structure, and the optical properties (absorption and emission spectra) are presented and discussed in this part. The solution preparation, handling, and irradiation protocol will be also detailed here.

#### 4.3.1 Properties of coumarin

Cou is an organic compound naturally occurred in plants which can be chemically synthesized in the laboratory conditions<sup>59</sup>. In the present experiments, the commercially produced Cou analog was purchased from Sigma-Aldrich in a form of colorless white crystal powder with a vanilla-like odor. The structure of Cou made of aromatic rings is presented below.

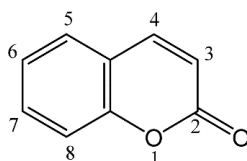


**Figure 4.5** – The Coumarin structure. Numbers indicate nomenclature of benzene atoms.

The Cou solution (targeted concentration of  $2.5 \times 10^{-3} \text{ mol.L}^{-1}$ ) was prepared by addition of ultra-pure water followed by a constant mixing over 8 h (1000 rpm) at room temperature. A mixing step is required due to the poor water solubility of Cou (maximum solubility of  $0.17 \text{ g.100 ml}^{-1}$ ). The concentration of the as-prepared mother Cou solution was then measured via the absorbance method, assuming that concentration is directly proportional to its absorbance obeying the Beer's law:

$$\text{Absorbance} = \varepsilon \times L \times C$$

#### Equation 4.1

Where  $\varepsilon$  is the Cou molar absorptivity constant (or molar extinction coefficient) and is equal to  $11\,600\text{ L mol}^{-1}\cdot\text{cm}^{-1}$ ,  $L$  is the path length of the cell holder (1 cm) and  $C$  is the concentration given in  $\text{mol}\cdot\text{L}^{-1}$ . The maximum value of the absorbance ( $A_{max}$ ) taken at 277 nm was measured and corrected with the baseline (absorbance at 400 nm -  $A_{400nm}$ ). An example of the Cou absorbance spectrum for one of the solutions taken by UV-Visible Spectrophotometer (brand: Thermo Electron Corporation, model: evolution 500) with the calculation of Cou concentration is presented below (Figure 4.6).

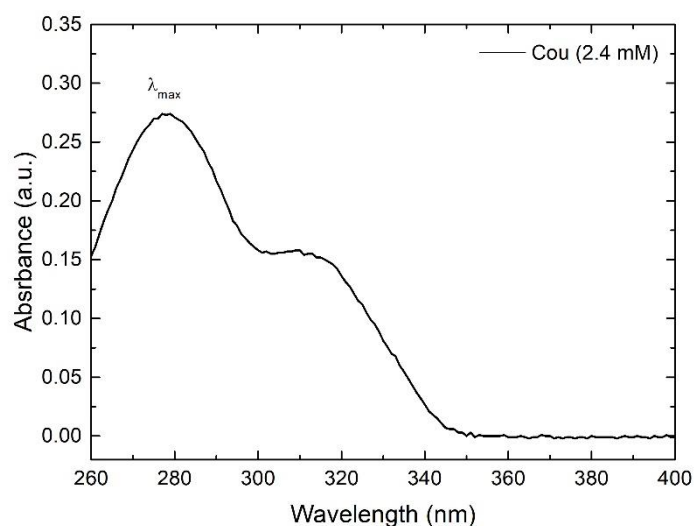


**Figure 4.6** – Coumarin (2.4 mM) absorbance spectrum taken at room temperature. The maximum absorbance ( $\lambda_{max}$ ) was measured at 277 nm with the background baseline taken at 400 nm.

By re-arranging the Beer's law and including the baseline correction ( $\lambda_{400nm}$ ), the Cou concentration calculation is as follows:

$$C = \frac{A_{max} - A_{400nm}}{\varepsilon L} \times 100 = \frac{0.277 + 0.002}{11\,600 \times 1} \times 100 = 2.4 \pm 0.1\text{ mM}$$

#### Equation 4.2

The Cou solutions were usually stored in the fridge and taken out prior the experiments.

### 4.3.2 Properties of 7-hydroxycoumarin

The hydroxylation of Cou results in the formation of isomers such as 3-OH, 4-OH, 5-OH, 6-OH, 7-OH, and 8-OH Cou which are the direct indicators of the oxidation reaction. Particularly interesting is the 7-hydroxycoumarin (7-OH Cou also called an umbelliferone) even though, the major product of Cou hydroxylation is 5-OH Cou. Only the 7-OH Cou is responsible for fluorescence properties in the visible region (maximum emission around 452 nm)<sup>60</sup> whereas emission from other derivatives can be neglected due to small radiation chemical yield.

Moreover, the good selectivity of Cou toward HO• radicals allows for detection of  $30 \times 10^{-9}$  mol.L<sup>-1</sup> of HO• with a relatively low concentration of Cou ( $10^{-5}$  mol.L<sup>-1</sup>)<sup>60,31</sup>.

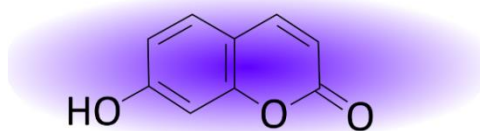


**Figure 4.7** – The 7-hydroxycoumarin structure. The violet shade indicates fluorescence emission around 452 nm which corresponds to violet / blue color.

#### 4.3.2.1 UV-Visible absorbance

Similarly to Cou, the synthetic 7-OH Cou powder was purchased from Sigma-Aldrich and stored at room temperature. A solution of 7-OH Cou (targeted concentration of  $1 \times 10^{-3}$  M) was prepared by mixing the powder with ultra-pure water over the night (magnetic mixer, 1000 rpm). Compared to Cou, 7-OH Cou has a lower solubility (maximum solubility of 0.3 g.L<sup>-1</sup>) at room temperature whereas it is highly reactive with light which requires the solution to be wrapped in an aluminum foil to limit the light exposure. The final concentration of 7-OH Cou was determined via absorbance measurement (Equation 4.2) for the 7-OH Cou molar absorptivity constant ( $\epsilon$ ) equal to 15 000 L.mol<sup>-1</sup>.cm<sup>-1</sup>. The absorbance spectrum (Figure 4.8) was recorded between 260 and 400 nm using UV-Visible Spectrophotometer (brand: Thermo Electron Corporation, model: evolution 500).

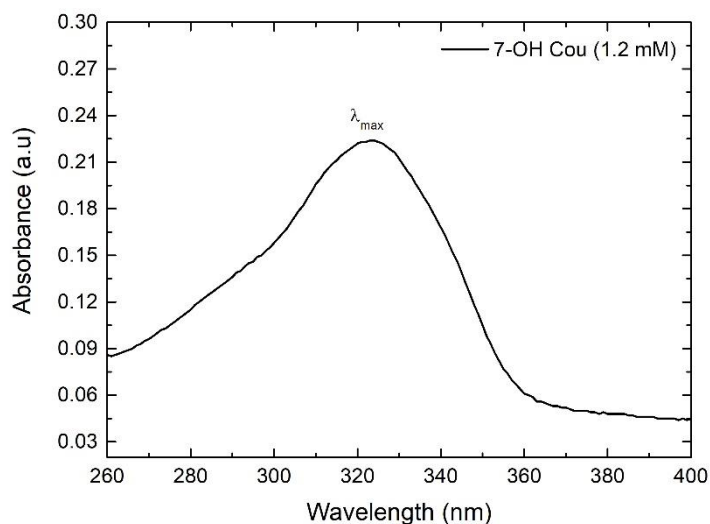


**Figure 4.8** – Absorbance spectrum of 7-OH Cou (1.2 mM) with a maximum of  $\lambda_{max} = 323$  nm. The 7-OH Cou peak intensity requires a background correction via subtraction of absorbance value measured at 400 nm.

#### 4.3.2.2 Fluorescence emission

The excitation of the 7-OH Cou molecule at a wavelength of 326 nm results in strong fluorescence emission with a maximum around  $\sim 452$  nm (Figure 4.9). The fluorescence reading was performed with a SpectraMax microplate reader (brand: Molecular Device) at 25 °C and the emission spectrum was recorded between 400 – 600 nm.

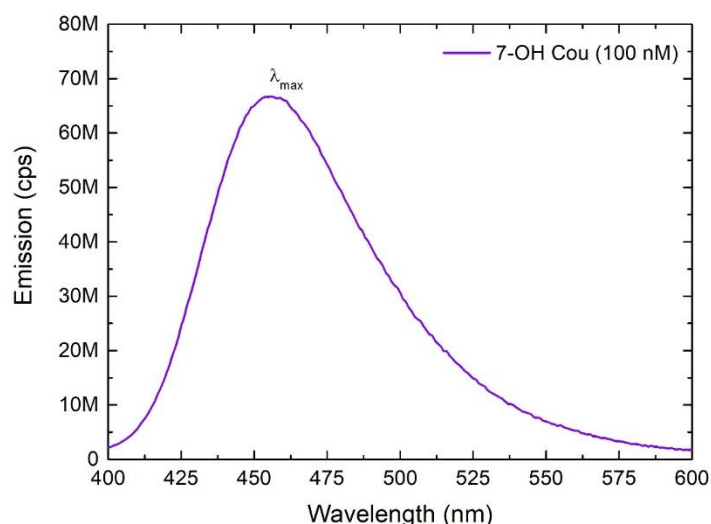


**Figure 4.9** – Fluorescence emission spectrum of 7-OH Cou (100 nM) with a local maximum of  $\lambda_{max} = 452$  nm for an excitation wavelength of 326 nm.

In the following experiments, the 7-OH Cou is produced after irradiation of Cou molecules in the presence or absence (water radiolysis mechanism) of NDs. The synthetic 7-OH Cou is only used to prepare calibration curve allowing to transform the fluorescence intensity signal into a 7-OH Cou concentration allowing to quantify the production of HO<sup>•</sup> radicals after irradiation.

#### 4.3.2.3 Stability of 7-hydroxycoumarin fluorescence

The irradiation protocol is based on the measurement of 7-OH Cou fluorescence signal hence its reproducibility is crucial to avoid any misleading results. The stability and the reproducibility of the 7-OH Cou signal were tested for seven different samples prepared using the same mother solution (Figure 4.10). The spectral acquisition was done at room temperature between 400 nm and 600 nm. The maximum value of the intensity was detected at 452 nm and plotted including the standard deviation between the measurements.

According to the results, the 7-OH Cou possesses very stable fluorescence properties with only one sample (number 4) exhibiting lower signal, probably due to dilution error. Most importantly, the dilution of 7-OH Cou solution does not introduce any significant error whereas the standard deviation between the measurements is within the range of  $\pm 4$  %.

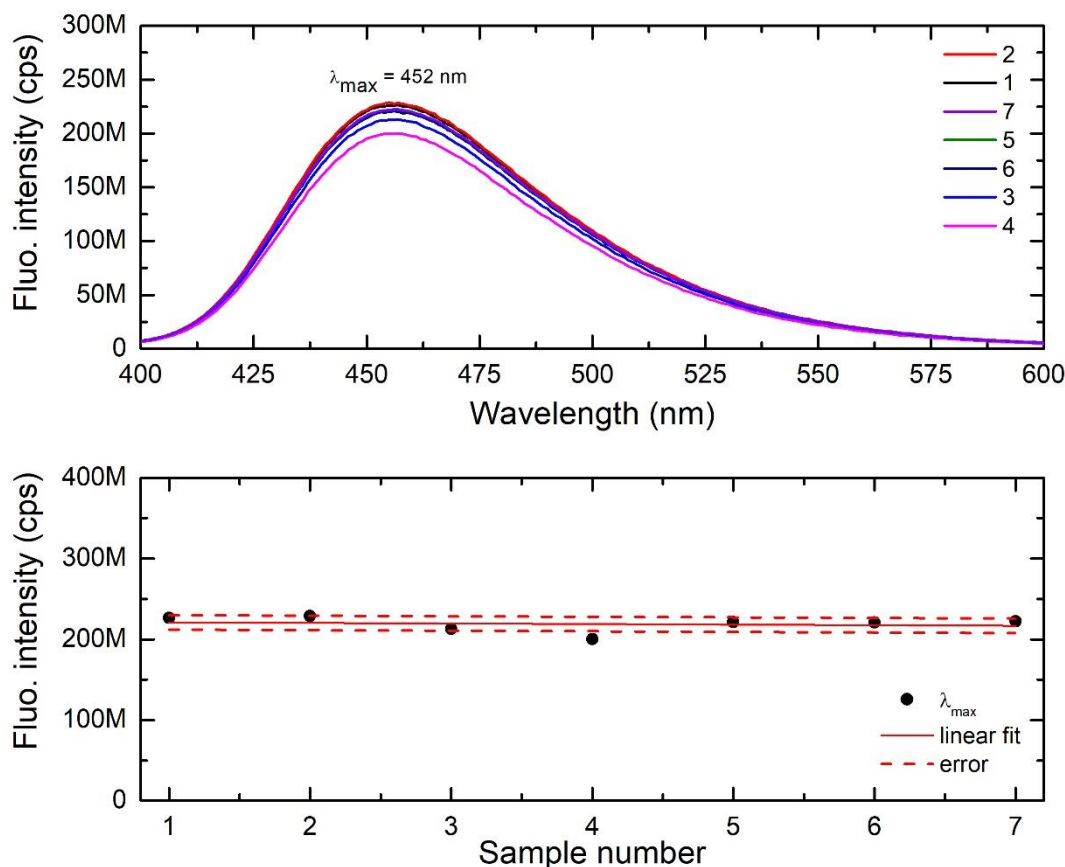


**Figure 4.10** – Stability of the 7-OH Cou signal measured for seven samples prepared at the concentration of 100 nM (top curve). The maximum fluorescence values (bottom curve) were plotted and linearly fitted (solid red line) including the uncertainty (dashed red line).

### 4.3.3 Fluorescence properties of nanodiamonds alone

NDs are known to exhibit some embedded fluorescence properties<sup>61</sup>, coming from known colored centers such as Nitrogen-Vacancy based centers<sup>61</sup> or from defective sites present in the detonation NDs<sup>62</sup>. Even if this fluorescence remains rather weak<sup>63</sup>, it may interfere with the reading of the 7-OH Cou signal. This requires testing optical properties of surface-modified NDs alone under conditions normally used to detect the Cou counterpart. As-received, air annealed (1 h 30 min, 550 °C), plasma hydrogenated (250 W, 12 mbar, 20 min) and vacuum annealed (1 h, 750 °C) detonation NDs (100  $\mu\text{g}\cdot\text{ml}^{-1}$ ) from PlasmaChem company were excited at the wavelength of 326 nm (the same as for 7-OH Cou) and emission spectra were recorded between 400 and 600 nm.

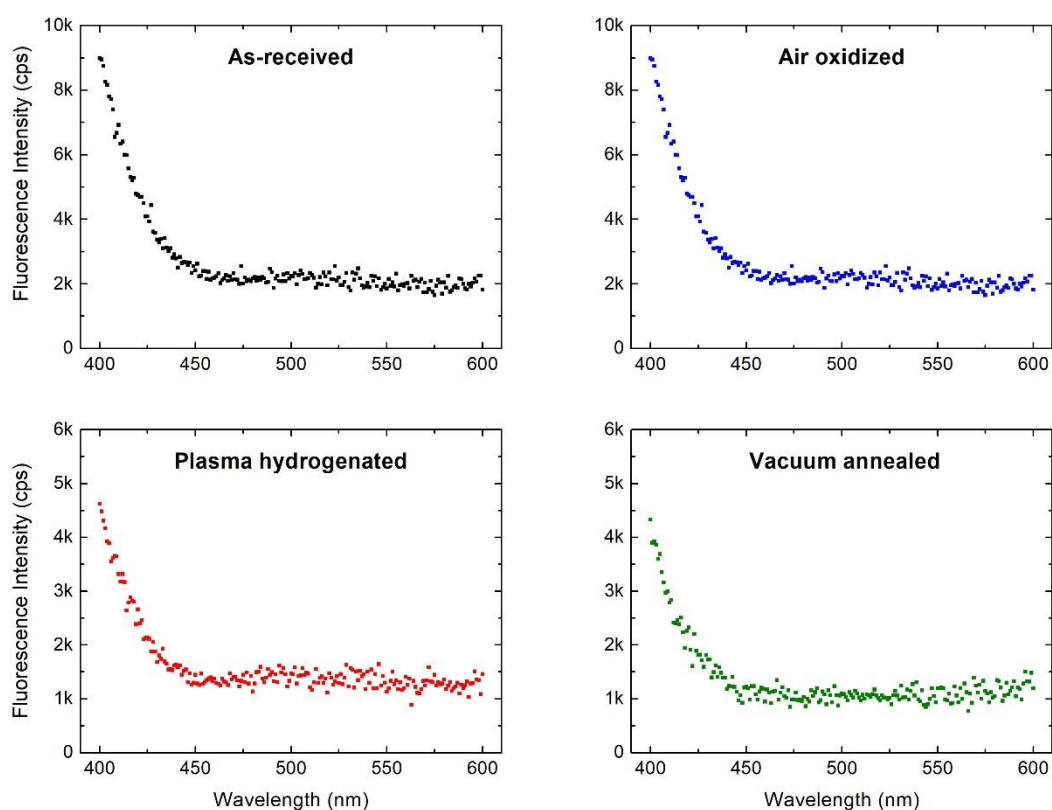


**Figure 4.11** – Emission spectra of PlasmaChem as-received (black), air annealed (blue), plasma hydrogenated (red), and vacuum annealed (green) measured at NDs' concentration of  $100 \mu\text{g.ml}^{-1}$  for an excitation wavelength of 326 nm.

Detonation NDs, when excited with the same wavelength as 7-OH Cou (326 nm), do not exhibit fluorescence properties (Figure 4.11) with no emission at 452 nm - only background noise is observed ( $\leq 1\%$  intensity compared to 7-OH Cou fluorescence signal). The small activity seen below 450 nm comes from the poor filtration of the excitation wavelength. The fluorescence signal of H-NDs at 452 nm compared to pure 7-OH Cou signal is within the background noise, and so will not affect our measurements.

#### 4.3.4 Colloidal stability of nanodiamonds in coumarin / 7-hydroxycoumarin

In Chapter 3, the colloidal stability of NDs has been discussed in water suspension as an important asset to perform irradiation experiments. However, the presence of Cou and 7-OH Cou molecules may also affect the colloidal stability of NDs due to some potential adsorption on the surface of NDs.

Colloidal properties of plasma H-NDs ( $100 \mu\text{g.ml}^{-1}$ ) in the presence of Cou alone and 7-OH Cou in Cou were measured via DLS.

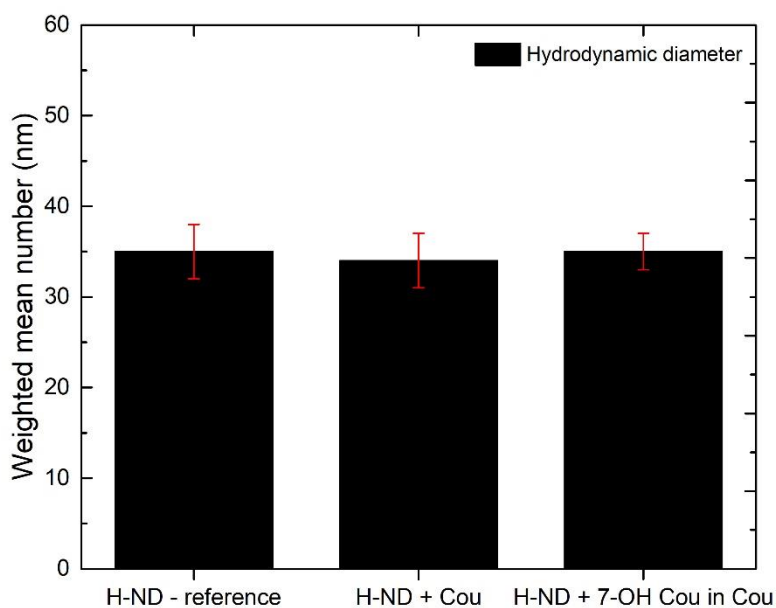


**Figure 4.12** – Colloidal properties of plasma H-NDs alone (reference), in the presence of Cou and 7-OH Cou in Cou water solution. DLS measurements were performed on freshly-prepared H-NDs suspension.

At the first glance, the hydrodynamic diameter is not affected by the presence of 7-OH Cou / Cou molecules with the mean measured size of NDs around 35 nm (Figure 4.12). No agglomeration of NDs is observed immediately after Cou / 7-OH Cou addition.

#### 4.3.5 Fluorescence properties of 7-hydroxycoumarin in the presence of nanodiamonds

In the literature, fluorescence properties of 7-OH Cou have been reported to be disturbed by the presence of NPs, notably metallic ones (e.g. GNPs)<sup>64,18</sup>. This effect is known as a ‘quenching’ and leads to a fluorescence diminution (little to no fluorescence signal) in the presence of a quencher material<sup>30,65</sup>. The level of the fluorescence ‘quenching’ has been associated with many factors. Specifically, with the primary size / concentration of NPs<sup>66</sup>, with the distance between NPs and dye molecules<sup>67</sup> but also with possible adsorption of the fluorescence probe at the surface of the NPs<sup>30,68,69</sup>. Here will be evaluated if the quenching effect occurs when mixing NDs with 7-OH Cou.

##### 4.3.5.1 Quenching effect

Plasma H-NDs and air Ox-NDs were mixed with synthetic 7-OH Cou (100 nM) in the presence of 0.5 mM Cou in water. Solutions with an increasing ND’s concentration (up to 100  $\mu\text{g}\cdot\text{ml}^{-1}$ )

were prepared to mimic the sample post-irradiation and check whether the ‘quenching’ effect of 7-OH Cou dye signal takes place. The 7-OH Cou emission spectra were recorded between 380 – 600 nm. The maximum fluorescence intensity at 452 nm was measured and plotted according to the concentration of NDs.

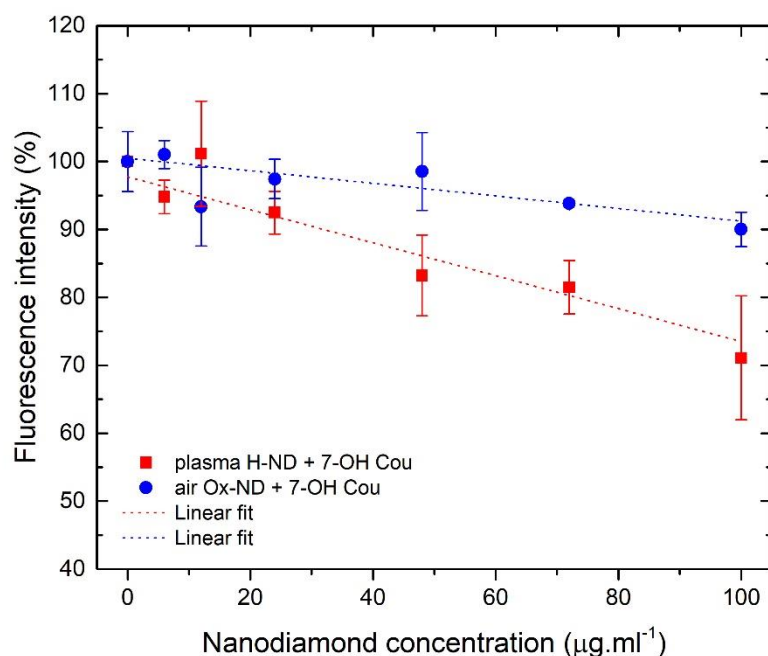


**Figure 4.13** – Evolution of the fluorescence intensity (maximum at 452 nm) of 7-OH Cou (100 nM) in Cou (0.5 mM) observed versus the concentration of plasma H-NDs (red) and air Ox-NDs (blue). The graph represents an average of four samples with data points fitted linearly (dotted lines).

The experimental data show a linear decrease of the 7-OH Cou fluorescence intensity in the presence of an increasing number of NDs *in situ*. The maximum concentration of plasma H-NDs results in the reduction of the fluorescence signal by ~30 % whereas for Ox-NDs it is lowered by ~10 %. Such a decrease proves directly that the presence of NDs disturbs the 7-OH Cou signal. Elimination of the ‘quenching’ mechanism is required to accurately measure a concentration of 7-OH Cou molecules produced after irradiation of surface-modified NDs in Cou solution.

#### 4.3.5.2 Removal of the quenching effect: nanodiamonds and sodium chloride

The addition of salt (KCl or NaCl) in combination with centrifugal force has been proposed in the literature as an efficient solution overcoming the quenching problem<sup>70,54</sup>. The agglomeration of NPs is induced by the high ionic strength which screens the surface charge of the particles resulting in a complete destabilization of the colloidal suspension. In addition, the centrifugation helps to remove particles from the experimental solution allowing to

release the fluorescence properties of dye molecules. Although, in some cases, the use of low concentration of KCl ( $1.0 \times 10^{-7} \text{ mol.L}^{-1}$  in DI water) has been reported to stabilize the NDs colloidal suspension<sup>71</sup>. Following these results, the minimum concentration of salt, necessary to destabilize the suspension, needs to be established. A progressive addition of NaCl solution into plasma H-NDs suspension was performed in parallel with DLS measurements of the hydrodynamic diameter and Zeta Potential.

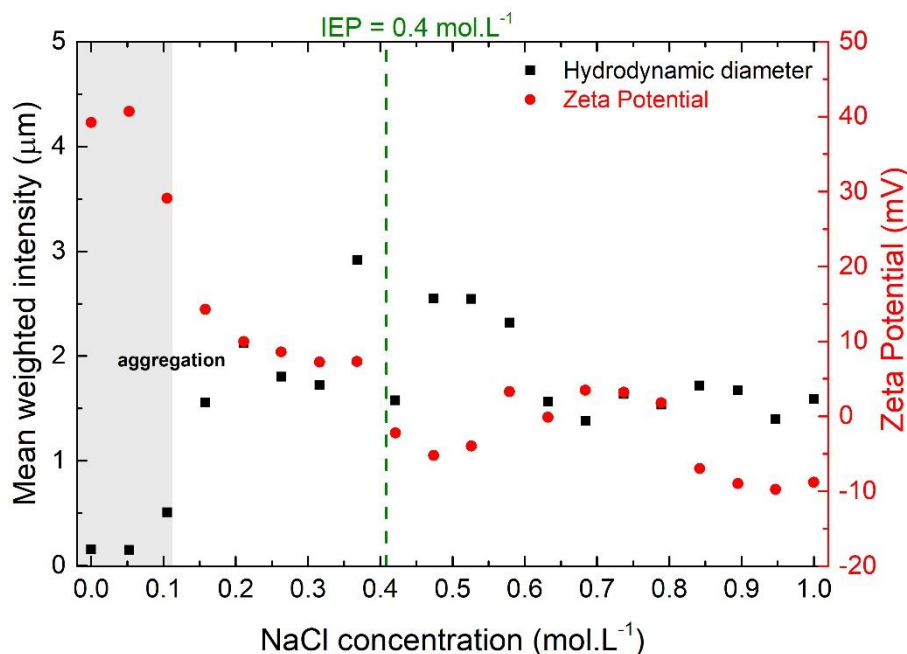


**Figure 4.14** – Titration of NaCl ( $0 - 1 \text{ mol.L}^{-1}$ ) into plasma H-NDs suspension ( $100 \mu\text{g.ml}^{-1}$ ) followed by a consecutive measurement of the hydrodynamic diameter (black) and Zeta Potential (red). The vertical green line indicates the isoelectronic point (IEP) at which ZP is equal to 0 mV.

A small addition of NaCl ( $< 0.1 \text{ mol.L}^{-1}$ ) already results in a rapid destabilization of H-NDs colloidal suspension (Figure 4.14). The hydrodynamic diameter increases c.a. 2-fold at NaCl concentration of  $0.1 \text{ mol.L}^{-1}$  whereas above this value, the size of NDs is close to the DLS detection limit hence the size value is only an estimation. The NaCl concentration of  $\sim 0.4 \text{ mol.L}^{-1}$  gives the ZP equal to 0 mV (IEP) which indicates a complete agglomeration and sedimentation of NDs.

In conclusion, the addition of NaCl (concentration  $> 0.1 \text{ mol.L}^{-1}$ ) induces a rapid destabilization and agglomeration of NDs in water suspension.

#### 4.3.5.3 Removal of the quenching effect: 7-hydroxycoumarin and sodium chloride

The NaCl titration experiment (concentration up to  $0.46 \text{ mol.L}^{-1}$ ) was also repeated for the synthetic 7-OH Cou solution ( $100 \text{ nM}$ ). The fluorescence intensity of 7-OH Cou was measured at 452 nm for six representative concentrations of NaCl. Data were normalized and plotted according to the concentration of NaCl.

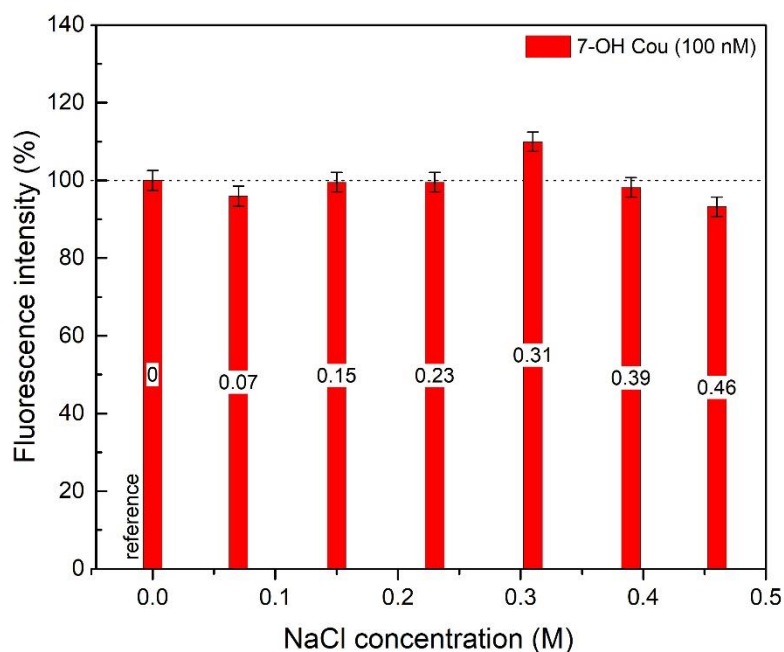


**Figure 4.15** – Effect of NaCl concentration on the 7-OH Cou fluorescence signal. Fluorescence intensity measured at 452 nm of six different samples was normalized with respect to the reference sample.

The NaCl concentration below 0.5 M does not seem to modify fluorescence properties of 7-OH Cou (Figure 4.15). The concentration of 0.15 M (10 %, w/v) has been chosen for the experimental protocol.

#### 4.3.5.4 Removal of the quenching effect: sodium chloride and centrifugation

The last experiment involves a combination of NaCl addition ( $0.15 \text{ mol.L}^{-1}$ ) and centrifugation and its effect on ‘quenching’ problem. Two types of surface-modified NDs were tested: plasma H-NDs and air Ox-NDs. The NDs (concentration up to  $100 \mu\text{g.ml}^{-1}$ ) were mixed with 7-OH Cou (100 nM) in the presence of 0.5 mM Cou in water to mimic the samples post-irradiation. The fluorescence signal at 452 nm was measured before and after NaCl / centrifugation treatment.

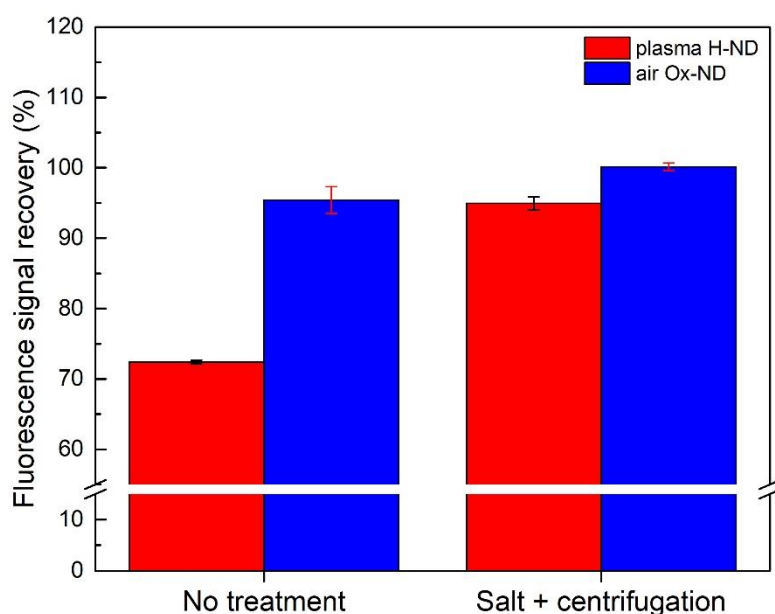


**Figure 4.16** – Percentage of the fluorescence signal measured without treatment (no treatment), after addition of sodium chloride (salt,  $0.15 \text{ mol.L}^{-1}$ ), and for a combined treatment (salt + centrifugation) for air Ox-NDs (blue) and plasma H-NDs (red).

Without any treatment, only ca. 70 % of expected fluorescence was measured for plasma H-NDs whereas for Ox-NDs ca. 95 % can be detected (Figure 4.16). When the NaCl solution was added followed by the centrifugation (18 000 g, 5 min) and the supernatant separation, 95 % and 100 % of the fluorescence was recovered for plasma H-NDs and Ox-NDs, respectively.

#### 4.3.6 Summary

- In all irradiation experiments, samples will be treated by addition of salt (10 %, w/v) and centrifugation (18 000 g, 5 min) whereas only supernatants (100  $\mu\text{L}$ ) will be deposited into microplates for fluorescence reading.

## 4.4 Measurements of HO• radicals

In the following part, the production of hydroxyl radicals (HO•) induced by X-rays and  $\gamma$ -rays by the surface-modified NDs (air annealed, plasma and thermally hydrogenated, and vacuum annealed) is presented. The effects of surface chemistry, activation energy, and source of detonation NDs are shown with respect to the HO• production efficiency. Irradiation experiments were performed for increasing doses and concentrations of various NDs suspensions.

#### 4.4.1 Air annealed nanodiamonds

First, the behavior of detonation PlasmaChem NDs after air annealing (1 h 30 min, 550 °C) was studied. The water-suspended NDs were exposed to X-rays (17.5 keV, dose rate of 20 Gy.min<sup>-1</sup>) in the presence of Cou solution. The raw fluorescence spectra obtained for the air Ox-NDs are presented below.

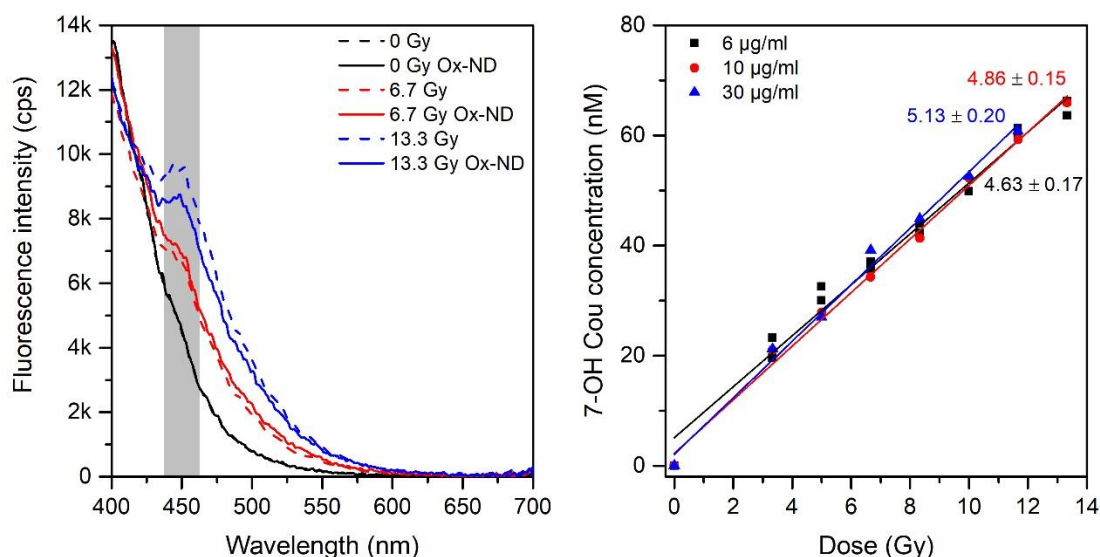


**Figure 4.17** – Representative data of fluorescence spectra for coumarin (dash line) and coumarin with 30 µg.ml<sup>-1</sup> of Ox-NDs (solid line). Data collected for both non-irradiated (black) and irradiated samples of two representative doses of X-rays irradiation (6.7 Gy – red and 13.3 Gy – blue). The highlighted grey area indicates part of the spectrum with the highest 7-OH Cou fluorescence intensity, the maximum was recorded at 452 nm. The graph on the right depicts the 7-OH Cou concentration in nM according to the dose (Gy) for selected concentrations of Ox-NDs (6, 10, and 30 µg.ml<sup>-1</sup>).

It is noticeable that before irradiation of air Ox-NDs (Figure 4.17 - left), almost no fluorescence signal is detected around 450 nm. After irradiation of Cou without Ox-NDs, a small peak can be seen at 452 nm, which intensity depends on the dose. However, in presence of Ox-NDs (30 µg.ml<sup>-1</sup>), it remains nearly the same or even lower for doses of 6.7 and 13.3 Gy, respectively.

Here, a calibration curve (measurement of the fluorescence intensity of synthetic 7-OH Cou at different concentrations) was used to transform fluorescence intensities into 7-OH Cou concentration, reported on the right graph of the Figure 4.17. Without NDs, the linear increase of 7-OH Cou concentration according to the X-rays dose depicts the standard radiolysis phenomenon<sup>18</sup>. In the presence of Ox-NDs, the linear increase is preserved and stay relatively stable with only some small fluctuations within an error bar thus no effect of additional HO• overproduction is observed (Figure 4.17 – right).

Taking into account slopes obtained for each concentration of Ox-NDs (indicated on Figure 4.17 - right) and dividing them by the slope of coumarin only (water radiolysis), the graph representing HO• overproduction effect vs. ND concentration can be plotted (Figure 4.18).

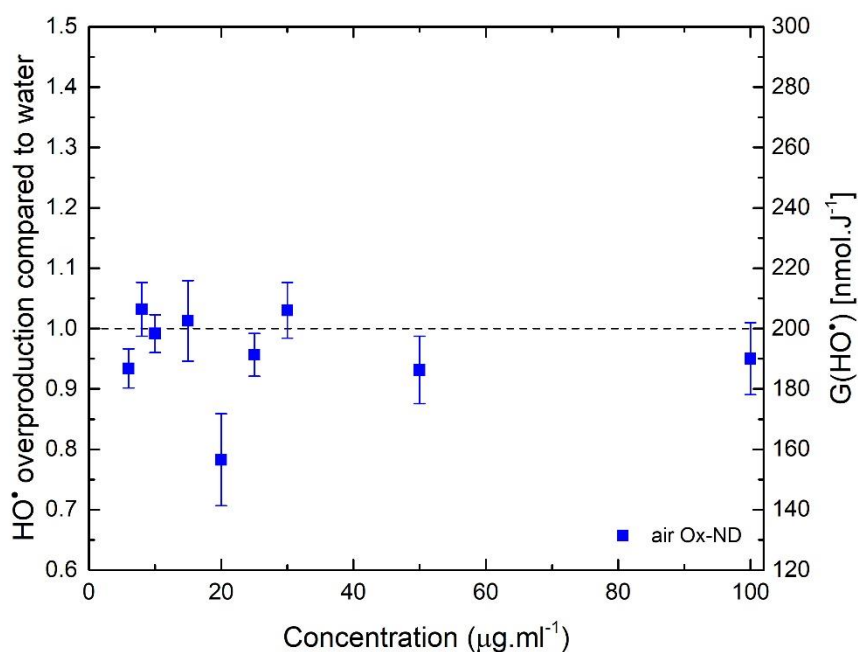


**Figure 4.18** – HO• overproduction as a function of ND concentration for Ox-NDs. The left Y-axis shows normalization to a production of HO• in water due to water radiolysis (horizontal dashed line). The right Y-axis shows the corresponding G-values in  $\text{nmol.J}^{-1}$  for HO• radicals.

For each Ox-NDs concentration, at least 2 independent experiments with 8 different doses were taken into account. Without NDs, at a concentration of  $0 \mu\text{g.ml}^{-1}$ , the value of 1 for HO• production depicts the yield of 7-OH Cou occurring during the water radiolysis, which corresponds to a known value of HO• equal to  $200 \text{ nmol.J}^{-1}$  in these conditions of irradiation (horizontal dashed line). The experiments with Ox-NDs and coumarin shows no significant HO• overproduction over the entire range of concentrations tested ( $0 - 100 \mu\text{g.ml}^{-1}$ ). The carboxylated surface of Ox-NDs appears to be non-photoactive under X-rays irradiation.

## 4.4.2 Plasma hydrogenated nanodiamonds

### 4.4.2.1 Effect of H- NDs from PlasmaChem on HO<sup>•</sup> production

The same experimental procedure was repeated for PlasmaChem NDs hydrogenated by microwave plasma.

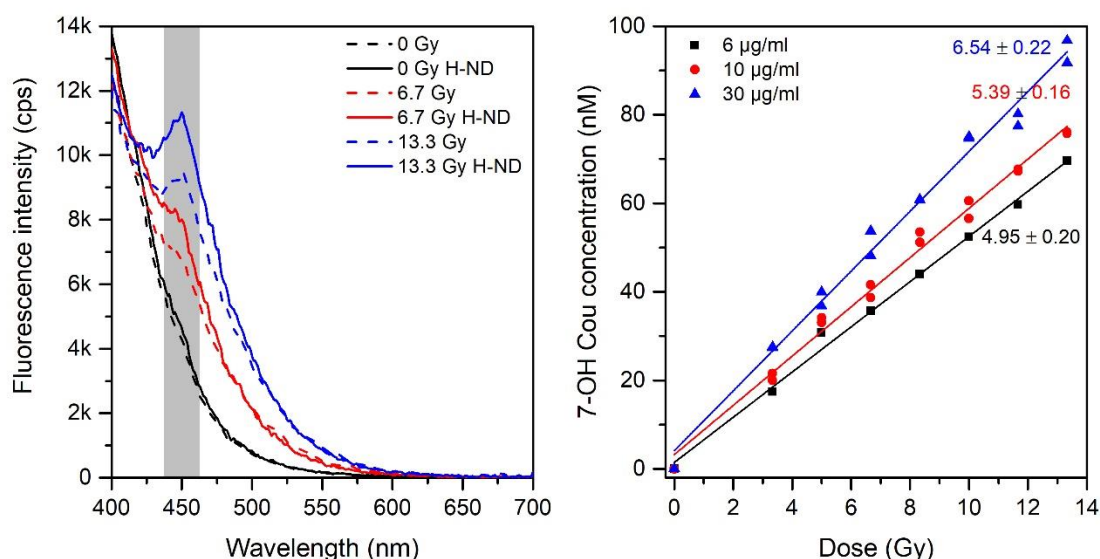


**Figure 4.19** – (Left) Representative data of fluorescence spectra for Cou (dashed line) and Cou with 30 µg.ml<sup>-1</sup> of H-NDs (solid line). Data collected for both non-irradiated (black) and irradiated samples of two representative doses of X-rays irradiation (6.7 Gy – red and 13.3 Gy – blue). The highlighted grey area indicates part of the spectrum with the highest 7-OH Cou fluorescence intensity and the maximum recorded at 452 nm. (Right) The graph depicts the 7-OH Cou concentration in nM according to the dose (Gy) for selected concentrations of H-NDs (6, 10, and 30 µg.ml<sup>-1</sup>).

In contrast to air Ox-NDs, in the presence of plasma H-NDs (30 µg.ml<sup>-1</sup>), the 7-OH Cou fluorescence signal is exalted depending on the dose of irradiation showing a first clear effect of HO<sup>•</sup> overproduction (Figure 4.19 – right). The fluorescence value at 452 nm was then measured for various concentrations of Ox- and H-NDs with respect to the dose. Results were treated and normalized according to the protocol discussed above. The same procedure was applied for all tested surface-modified samples.

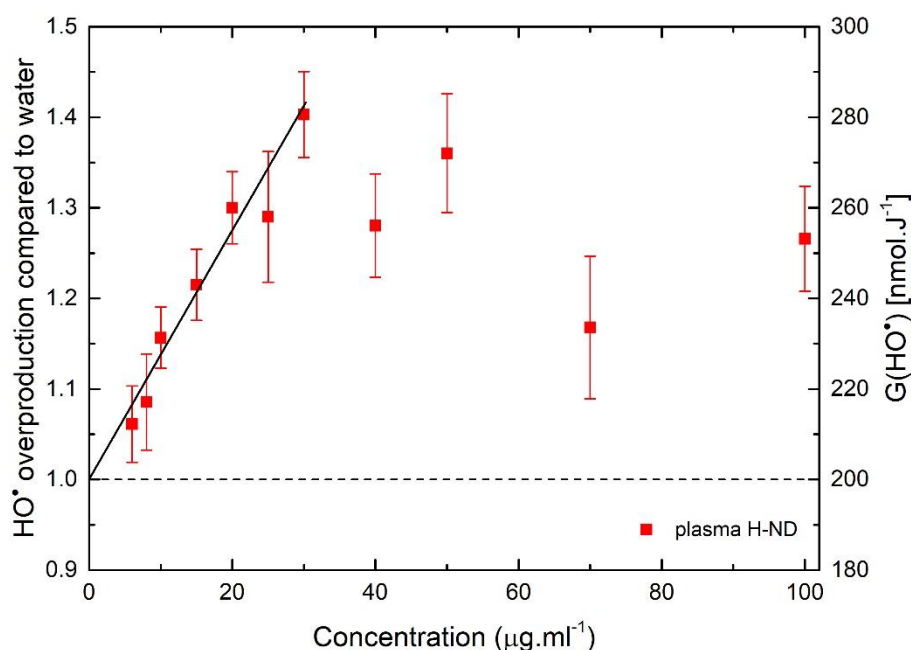


**Figure 4.20** – HO• overproduction as a function of concentration for plasma H-NDs. The left Y-axis shows normalization to the production of HO• by water radiolysis. The right Y-axis shows the corresponding G-values in nmol.J<sup>-1</sup> for HO• radicals. The horizontal dashed line represents production in water equal to 1.

The presence of plasma H-NDs in water induces an increase in concentration of HO• produced, with a concentration dependent phenomenon (Figure 4.20). Up to 30 µg.ml<sup>-1</sup>, this production of HO• is linear with the concentration of H-NDs resulting in an overproduction of 40 ± 5 % compared to water radiolysis. Above 30 µg.ml<sup>-1</sup>, the G(HO•) values seem to saturate or decrease. This decrease cannot be associated with the quenching effect because the combination of NaCl and centrifugation allows to recover 95 % of the fluorescence signal (see section 4.3.5.4). Consequently, the decline in the G(HO•) overproduction seems to be directly related to specific surface properties of H-NDs and faster recombination of the HO• species which limits hydroxylation of Cou probe leading to a saturation effect.

These results obtained for air Ox-NDs and plasma H-NDs were published at the beginning of 2017 in *Chemical Communication*, journal of the Chemical Society<sup>6</sup>.

## 4.4.2.2 Effect of the source of detonation nanodiamonds

The same microwave plasma treatment (250 W, 12 mbar, 20 min) was used to hydrogenate other sources of detonation NDs: Adamas Nanotechnologies and NanoCarbon Research Institute in order to check if the effect is not only specific to PlasmaChem NDs. The characterizations of plasma H-NDs (FTIR) from different sources are provided in Chapter 2. Plasma H-NDs from Adamas and Nanocarbon were dispersed in Cou solution and irradiated with X-rays in the same experimental conditions.

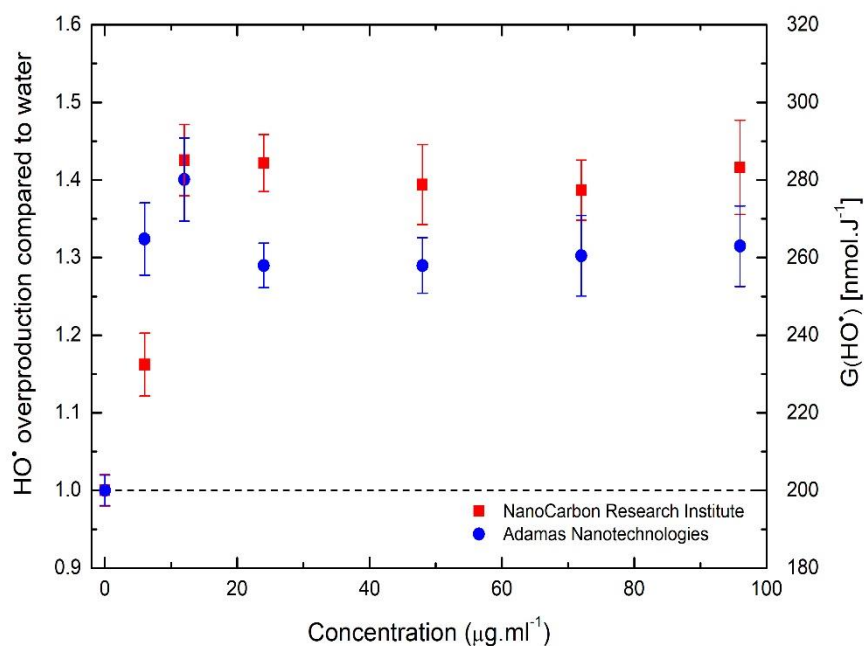


**Figure 4.21** –  $\text{HO}^\bullet$  overproduction as a function of concentration for two given sources of NDs: Adamas Nanotechnologies – blue and NanoCarbon Research Institute – red. The left Y-axis shows normalization to production of  $\text{HO}^\bullet$  by water radiolysis. The right Y-axis shows the corresponding G-values in  $\text{nmol.J}^{-1}$  for  $\text{HO}^\bullet$  radicals. The horizontal line represents production in water equal to 1. Data represent only one tested sample with two sets of data per source.

Looking at the data, it can be seen that microwave plasma treatment activated production of  $\text{HO}^\bullet$  radicals in the water medium, whatever the initial source of detonation NDs (Figure 4.21). The shape and the  $\text{HO}^\bullet$  overproduction efficiency is comparable for all plasma H-NDs samples. NanoCarbon Research Institute and Adamas Nanotechnologies H-NDs possess the same  $\text{HO}^\bullet$  overproduction profile with a maximum effect observed at NDs concentration of  $12 \mu\text{g.ml}^{-1}$ . Moreover, after the maximum effect is achieved ( $> 12 \mu\text{g.ml}^{-1}$ ), the  $\text{HO}^\bullet$  concentration saturates for both samples and no additional effect can be observed. According to error bars, the behavior above a concentration of  $12 \mu\text{g.ml}^{-1}$  corresponds to a plateau for  $\text{HO}^\bullet$  production. This is a difference with plasma H-NDs from PlasmaChem for which a decrease of  $\text{HO}^\bullet$  production has been measured for this concentration range.

To sum up, hydrogenation via microwave plasma treatment produces H-NDs which are photoactive independently of the source of detonation NDs. The maximum HO• overproduction efficiency is similar for all tested sources (increase by 40 - 50 % for a given concentration of NDs included between 12 - 30  $\mu\text{g}\cdot\text{ml}^{-1}$ ).

#### 4.4.3 Hydrogen annealed nanodiamonds

Complementary to plasma treatment, hydrogen termination of PlasmaChem NDs was obtained via thermal annealing under hydrogen gas (1 h, 550 °C). Water-dispersed thermally H-NDs were examined toward HO• production under X-rays.

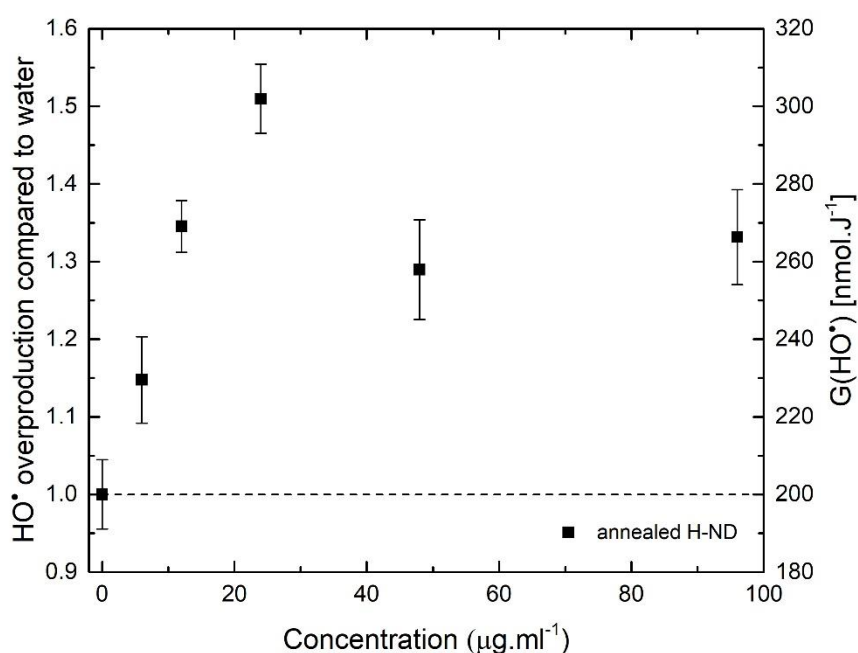


**Figure 4.22** – HO• overproduction as a function of NDs concentration for thermally annealed H-NDs. The left Y-axis shows normalization to the production of HO• by water radiolysis and the right Y-axis corresponds to  $G(\text{HO}^\bullet)$  value in  $\text{nmol}\cdot\text{J}^{-1}$ . The horizontal line represents production in water equal to 1. Data were reproduced for more than one H-NDs sample.

Equally to plasma hydrogenation, thermally annealed H-NDs are active under X-ray illumination (Figure 4.22). The HO• overproduction in water is observed with linear up to a concentration of 24  $\mu\text{g}\cdot\text{ml}^{-1}$  followed by a decrease and a saturation. The two data points representing the highest concentrations (48  $\mu\text{g}\cdot\text{ml}^{-1}$  and 96  $\mu\text{g}\cdot\text{ml}^{-1}$ ) of annealed H-NDs suggest the stabilization of HO• overproduction. Similarly to plasma H-NDs, the characteristic shape of the curve is also preserved for the thermally annealed sample.

In conclusion, the overall HO• overproduction profile (increase – decrease – plateau) is also maintained for thermally annealed H-NDs. The H-termination via thermal annealing results in

a better HO• production efficiency compared to microwave plasma treatment: 50 % instead of 40 %.

#### 4.4.3.1 Effect of the source of detonation nanodiamonds

Likewise, the PlasmaChem source of NDs, particles produced by Adamas Nanotechnologies were H-terminated via thermal annealing (1 h at 550 °C) followed by X-rays experiment with Cou.

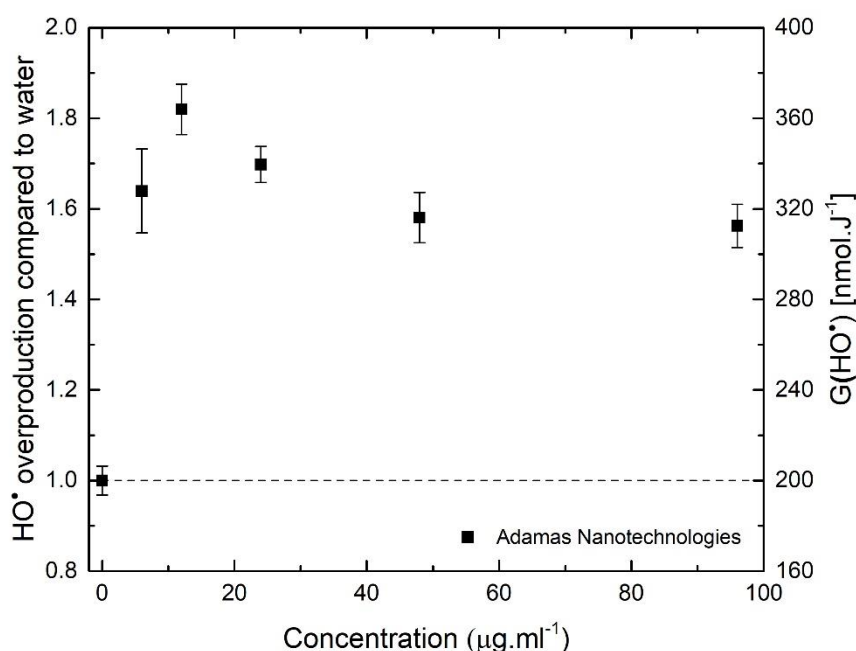


**Figure 4.23** – HO• overproduction as a function of concentrations for annealed H-NDs (Adamas Nanotechnologies). The left Y-axis shows normalization to the production of HO• by water radiolysis and the right Y-axis corresponds to G(HO•) value in nmol.J<sup>-1</sup>. The horizontal line represents production in water equal to 1. The data were obtained only for one H-NDs sample.

Hydrogen annealed Adamas NDs are active toward the production of HO• in water with the maximum effect obtained so far for all the samples (increase by + 82 ± 6 % at 12 µg.ml<sup>-1</sup>) (Figure 4.23). The HO• production increases linearly up to 12 µg.ml<sup>-1</sup> followed by the decline down to 58 ± 6 % for the maximum concentration (96 µg.ml<sup>-1</sup>). Nevertheless, the thermally annealed Adamas NDs show a higher efficiency compared to thermally hydrogenated PlasmaChem (the effect is higher while it is also observed for lower concentration).

On the whole, thermal annealing under hydrogen leads to larger discrepancies in HO• production efficiency compared to hydrogenation via plasma treatment. H-NDs from Adamas Nanotechnologies seem to be more effective compared to PlasmaChem. However, the data presented only represent one sample with two sets of data. Similar results were not

reproduced for other Adamas Nanotechnologies suspensions while PlasmaChem NDs were tested multiple time resulting in high reproducibility.

#### 4.4.4 Vacuum annealed nanodiamonds

In the final part, PlasmaChem NDs were vacuum annealed (1 h / 750 °C and 1 h / 850 °C, under pressure of  $1 \times 10^{-6}$  mbar), dispersed in water and exposed to X-rays. The HO• overproduction was measured for an increasing concentration of NDs.

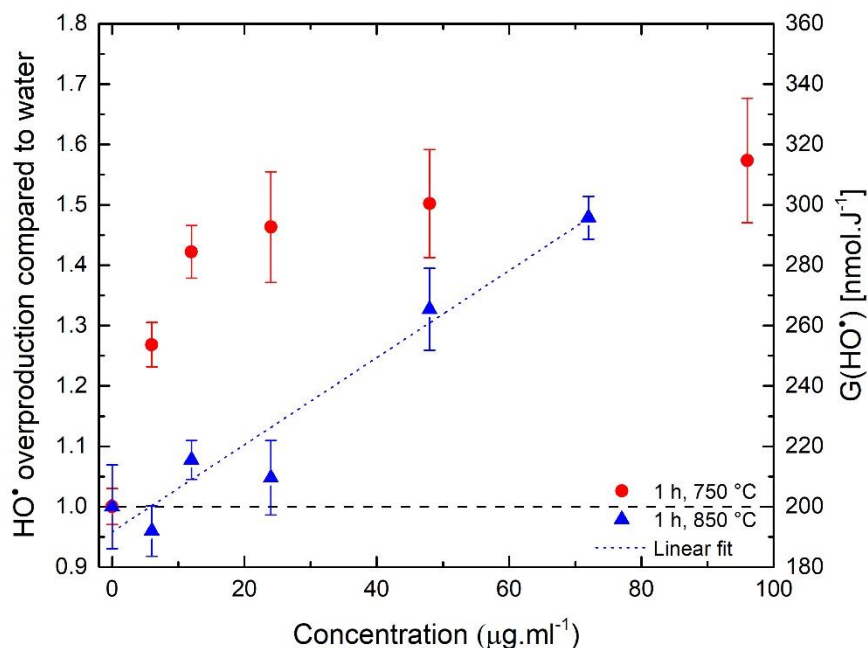


**Figure 4.24** – HO• overproduction as a function of NDs concentration for vacuum annealed (1 h / 750 °C in red and 1 h / 850 °C in blue) NDs. The left Y-axis shows normalization to the production of HO• by water radiolysis and the right Y-axis corresponds to  $G(\text{HO}^\bullet)$  value in  $\text{nmol}\cdot\text{J}^{-1}$ . The horizontal line represents production in water equal to 1. X-rays irradiation experiments were performed within 48 h after suspension preparation to reduce an influence of the aging effect.

In the same way as H-terminated NDs, surface modifications induced by vacuum annealing activate the surface toward HO• production with a specific profile depending on the treatment conditions used (Figure 4.24). For both samples, the maximum effect is observed for the highest concentration tested ( $+ 57 \pm 10 \%$  for  $96 \text{ g}\cdot\text{ml}^{-1}$  and  $+ 48 \pm 4 \%$  for  $70 \text{ }\mu\text{g}\cdot\text{ml}^{-1}$ ). The only difference between the samples is the profile of HO• overproduction versus concentration. For the lower annealing temperature (1 h, 750 °C), an increase of HO• production followed by a plateau is evidenced with the concentration of NDs whereas the higher annealing temperature (850 °C) gives a rather linear behavior. In contrast to plasma and thermally hydrogenated NDs (different sources), the decrease in HO• concentration is not observed at any concentration tested whereas the production seems to continue for higher concentrations. The data obtained for the NDs annealed under vacuum for 1 h at 750 °C were

reproduced for two different batches whereas sample treated for 1 h at 850 °C was tested only once.

Detonation NDs treated under vacuum also induce an overproduction of HO• in water environment under X-rays irradiation with the same increase and plateau (1 h, 750 °C). NDs annealed at 850 °C appears to be less effective than H-NDs in terms of HO• production, a higher concentration of these NDs is required to reach the same level of HO•.

#### 4.4.5 Summary

- Air oxidized NDs do not exhibit any photoactivity under X-rays irradiation (lack of HO• overproduction) and can be used as a negative control
- Hydrogenation (microwave plasma or thermal annealing) and vacuum treatment (1 h, 750 °C and 1 h, 850 °C) activate the overproduction of HO• species
- Overproduction of HO• is source-independent as shown for plasma H-NDs
- Higher HO• overproduction efficiency is observed for thermally modified NDs
- HO• production profile seen for H-terminated NDs indicates increase and plateau/decrease after the HO• overproduction is maximised
- Vacuum annealed NDs shows increase and plateau for 1 h, 750 °C and slower increase for 1 h, 850 °C.

#### 4.4.6 Aging effect vs. measurements of HO• radicals

In Chapter 3, the aging effects of surface-modified NDs have been discussed with results showing time-induced modifications of colloidal properties for the different surface chemistries. In the following part, the aging effect and its impact on HO• production are presented for PlasmaChem NDs. These NDs have been modified by air annealing, plasma, and thermal hydrogenation. The colloidal properties of these surface-modified NDs are shown prior the irradiation experiments performed with the X-ray source ( $E = 17.5$  keV).

##### 4.4.6.1 Air annealed nanodiamonds

To begin with, air annealed NDs (1 h 30, 550 °C) were suspended in water and kept in a closed glass vial at room temperature. The colloidal properties (weighted mean intensity and number, ZP) were measured via DLS technique one day before the irradiation experiment (see Table 4.1). X-ray irradiation of air Ox-NDs was performed for ND concentrations up to 50  $\mu\text{g}\cdot\text{ml}^{-1}$ .

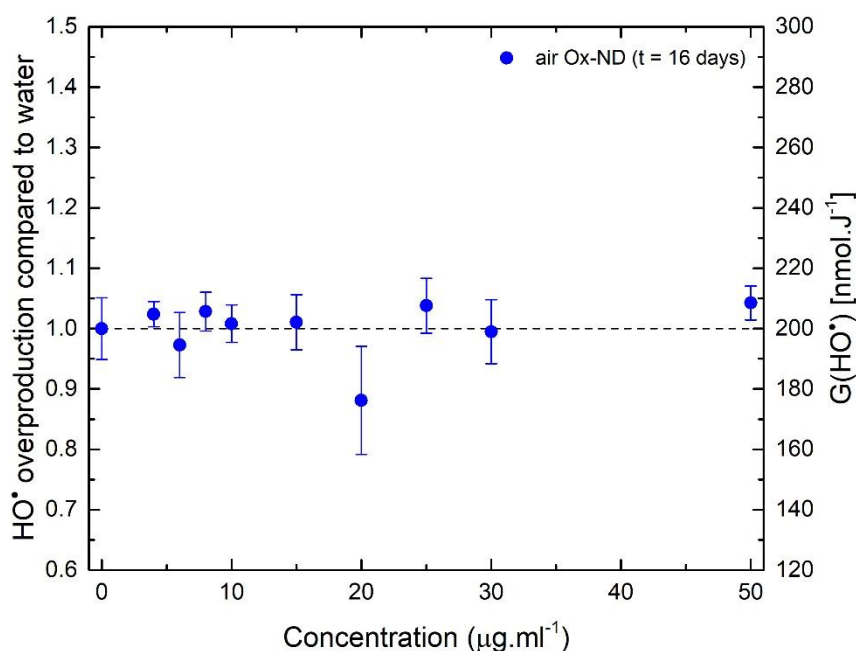


**Figure 4.25** – HO• overproduction as a function of concentration for air Ox-NDs measured after 16 days. The Y-axis includes G-value of HO• production compared to water radiolysis given in  $\text{nmol}\cdot\text{J}^{-1}$  assuming the production of HO• in water equal to 1 (horizontal dashed line).

The X-ray irradiation of Ox-NDs suspended in water for 16 days revealed a lack of HO• production over the entire range of concentrations tested (Figure 4.25). The normalized values of HO• remain around 1 which corresponds to the water radiolysis effect. The same results were also observed for freshly-prepared Ox-NDs suspension discussed in the previous part of this chapter (section 4.4.1).

In terms of colloidal properties measured on the day of sample preparation (< 24 h) and after 15 days, the only modification observed is an increase in hydrodynamic diameter (c.a. 1.3-fold by weighted mean intensity and number) and a decrease of the ZP (-5 mV). These changes are due to stabilization effect, previously shown in Chapter 3, whereas a good long-term colloidal stability of Ox-NDs has been presented.

Colloidal properties of air Ox-NDs	Weighted mean intensity (nm)	Weighted mean number (nm)	Zeta Potential (mV)
Fresh suspension	113 ± 2	45 ± 11	-60 ± 1
After 15 days	145 ± 1	57 ± 6	-55 ± 1

**Table 4.1** – Colloidal properties of air Ox-NDs freshly-prepared (< 24 h) and after 15 days.

To conclude, after 16 days, the air Ox-NDs remain unresponsive to X-ray stimulation. Besides that, the air Ox-NDs suspensions of different ages were tested many times thus the results obtained in this study were reproduced also for other batches.

#### 4.4.6.2 Plasma hydrogenated nanodiamonds

Secondly, plasma H-NDs (250 W, 12 mbar, 20 min) suspension was prepared and kept in a closed vial for 30 and 49 days. H-NDs were characterized via DLS and X-ray irradiated (17.5 keV). Data provided below correlate the colloidal properties of H-NDs with the HO• efficiency observed in water medium.

Colloidal properties of plasma H-NDs	Weighted mean intensity (nm)	Weighted mean number (nm)	Zeta Potential (mV)
Fresh suspension	121 ± 1	58 ± 6	56 ± 5
After 29 days	288 ± 23	101 ± 33	32 ± 1
After 48 days	439 ± 25	207 ± 54	26 ± 4

**Table 4.2** – Colloidal properties of plasma H-NDs suspension measured for freshly-prepared (< 24 h) and one-day prior the X-ray exposure (days 29 and 48).

The plasma H-NDs lose the photoemission activity (Figure 4.26) and shows a very weak HO• overproduction after 30 and 49 days (< 10 %). This lack of HO• overproduction can be related to the modifications of colloidal properties. The hydrodynamic diameter (weighted mean intensity) after 29 and 48 days is c.a. 2.4 and 3.6-fold higher, respectively, compared to the initial size (121 ± 1 nm). The colloidal instability of the suspension is also reflected in the value of the ZP which decreases by 24 mV (day 29) and 30 mV (day 48) with respect to the as-prepared sample (56 ± 5 mV). Such progressive agglomeration of plasma H-NDs is also in agreement with the results presented in Chapter 3 dealing with colloidal stability of H-terminated particles via plasma treatment.

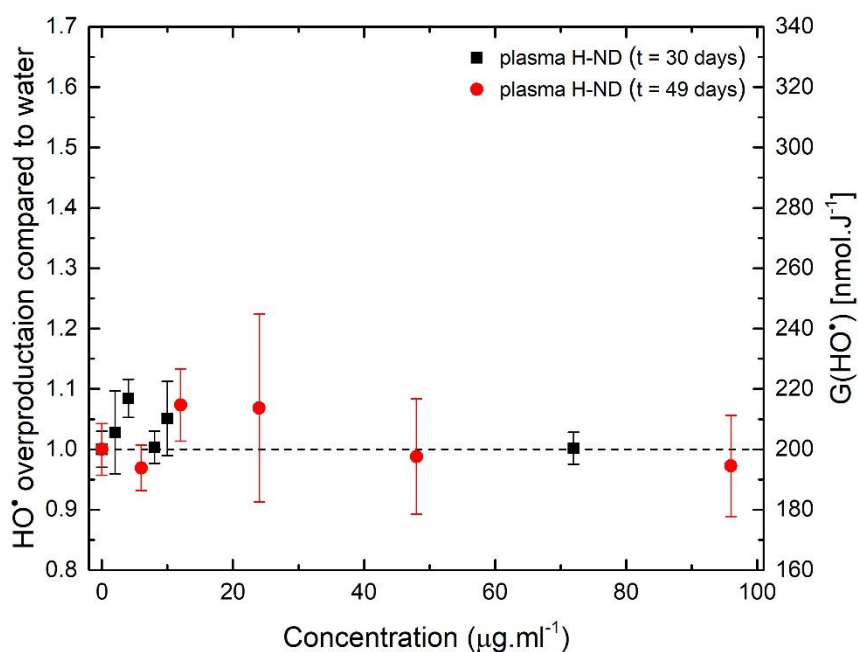


**Figure 4.26** – HO• overproduction as a function of concentration for plasma H-NDs measured on aqueous suspensions for 30 and 49 days. The Y-axis includes G-value of HO• production compared to water radiolysis given in nmol.J<sup>-1</sup> assuming the production of HO• in water equal to 1 (horizontal dashed line).

To sum up, lack of colloidal stability of plasma H-NDs in water results in an almost complete suppression of the HO• overproduction observed under X-rays.

#### 4.4.6.3 Hydrogen annealed nanodiamonds

The last tested suspension includes thermally annealed H-NDs (1 h, 550° C) prepared and stored at ambient temperature. X-ray irradiation (17.5 keV) of the sample was repeated after 32 and 64 days, respectively, including the DLS measurements before the experiment.

Unlike the plasma H-NDs suspension, thermally annealed H-NDs remain active toward HO• production after 32 and 64 days with a maximum effect observed for concentrations of 24 µg.ml<sup>-1</sup> and 12 µg.ml<sup>-1</sup>, respectively (Figure 4.27).

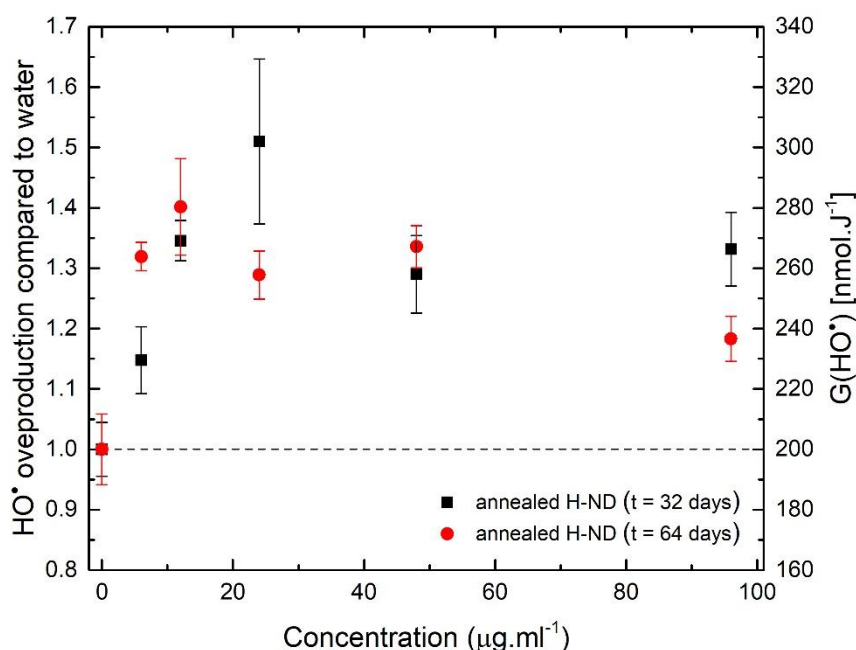


**Figure 4.27** – HO• overproduction as a function of concentration (left) for thermally annealed H-NDs after 32 (black) and 64 (red) days in water suspension. The Y-axis includes G(HO•) production compared to water radiolysis given in nmol.J<sup>-1</sup> assuming the production of HO• in water equal to one (horizontal dashed line).

Colloidal properties of annealed H-NDs (Table 4.3) evolve with an increase of the hydrodynamic diameter, as measured by weighted mean intensity, by a factor of 1.4 (day 31) and 5 (day 63). At the same time, the value coming from the weighted mean number reveal that a major population of NDs, with an average hydrodynamic diameter < 50 nm, still remain in water suspension, which is not the case for plasma treated samples (hydrodynamic diameter up to 200 nm). In accordance, the ZP of these H-NDs remains positive (~40 mV) even after 63 days in water media.

Colloidal properties of annealed H-NDs	Weighted mean Intensity (nm)	Weighted mean number (nm)	Zeta Potential (mV)
Fresh suspension	118 ± 1	34 ± 23	67 ± 3
After 31 days	162 ± 58	26 ± 14	65 ± 3
After 63 days	593 ± 101	49 ± 7	41 ± 1

**Table 4.3** - Colloidal properties of annealed H-NDs suspension defined for a freshly-prepared (< 24 h) sample and one-day prior the X-ray exposure (days 31 and 63).

In conclusion, the activity of annealed H-NDs toward photoemission seems to be preserved here thanks to the presence of the main population of NDs remaining below 50 nm (weighted mean number) after 64 days. At the same time, the ZP remains also high.

#### 4.4.6.4 Summary

- Air oxidized NDs continue to be non-responsive to external stimulation whatever the age of the suspension, as shown after 16 days in water
- Lack of colloidal stability (increase in the hydrodynamic diameter and decrease of the ZP) results in lowering (annealed H-NDs) or almost complete suppression (plasma H-NDs) of the HO• overproduction effect as compared to the freshly-prepared samples
- If the colloidal stability is not affected after a long period of time (hydrogen annealed samples) while keeping relatively small hydrodynamic diameters and high ZP, then the HO• overproduction effect is preserved.

## 4.5 Gamma irradiation

To investigate the effect of energy on HO<sup>•</sup> production efficiency, the same experiment as for X-rays (E = 17.5 keV) was performed with gamma rays (E = 1.17 MeV, dose rate 15.5 Gy.min<sup>-1</sup>) emitted by cobalt source. Air annealed and plasma hydrogenated NDs were mixed with coumarin (0.5 mM) and exposed to  $\gamma$ -irradiation. The dose of  $\gamma$ -irradiation was similar to the dose used for X-rays experiments.

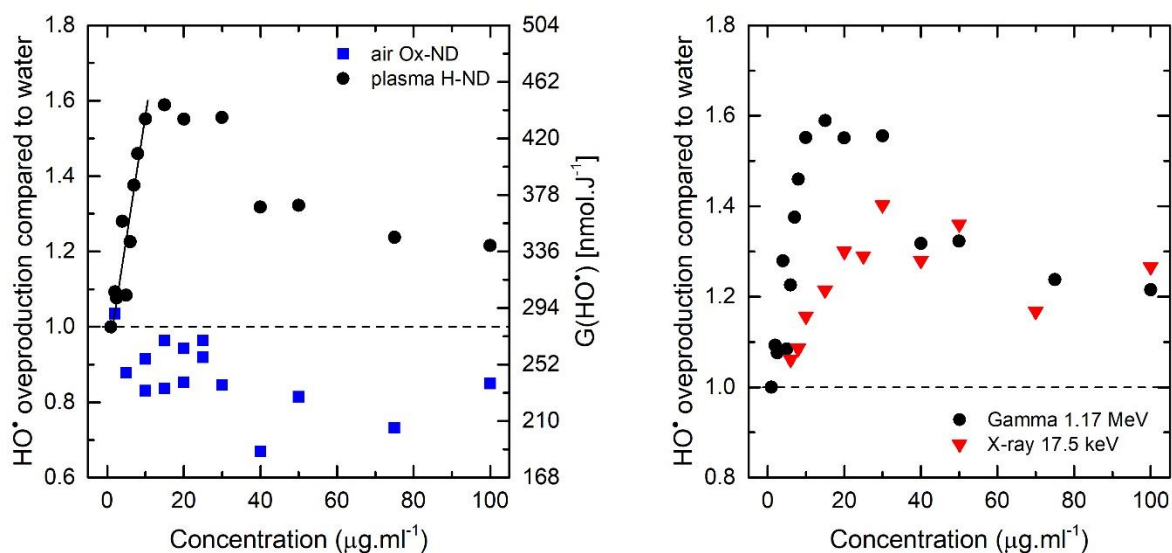


**Figure 4.28** – (Left) HO<sup>•</sup> overproduction as a function of NDs concentration measured for air Ox-NDs (blue) and plasma H-NDs (black) under gamma (1.17 MeV) irradiation. (Right) Comparison between HO<sup>•</sup> overproduction from plasma H-NDs exposed to gamma (black) and X-ray (red). The horizontal dashed line assumes the production of HO<sup>•</sup> in water equal to 1.

Similarly to X-rays experiments, an effect of HO<sup>•</sup> overproduction induced by plasma H-NDs can be also observed for  $\gamma$ -energy (Figure 4.28). The maximum HO<sup>•</sup> concentration is + 59 % higher compared to water radiolysis whereas the effect is c.a. + 20 % higher compared to X-rays. More importantly, the maximum effect under  $\gamma$ -illumination is observed for lower concentration of H-NDs (15  $\mu\text{g.ml}^{-1}$ ) compared to X-rays (30  $\mu\text{g.ml}^{-1}$ ).

The overall trend is similar for both gamma and X-rays energies with a linear increase up to a certain concentration (X-ray: 30  $\mu\text{g.ml}^{-1}$  and gamma: 15  $\mu\text{g.ml}^{-1}$ ) followed by a plateau and a decrease (HO<sup>•</sup> overproduction around 24 % at 100  $\mu\text{g.ml}^{-1}$  for X-rays / gamma). No HO<sup>•</sup> overproduction is obtained for air Ox-NDs whatever the source of energy. However, the data points for the Ox-NDs are rather scattered with no specific visual trend to be extracted.

In conclusion, it has been evidenced that plasma H-NDs are equally active under gamma irradiation (1.17 MeV) with + 20 % higher HO<sup>•</sup> production efficiency compared to X-rays (17.5 keV). The lack of photoemission from the air Ox-NDs has been also confirmed for  $\gamma$ -activation.

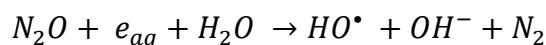
## 4.6 Detection and quantification of solvated electrons via HO• and N<sub>2</sub>O / O<sub>2</sub>

The illumination of a hydrogen-terminated surface of bulk diamond has been already shown to result in an electron emission<sup>72,34</sup>. Such electrons, when emitted in liquid water, can be captured by water molecules through bipolar interactions and become solvated (so-called solvated or hydrated electrons – e<sub>aq</sub>)<sup>55</sup>.

Since H-NDs have been shown to possess similar ability as the bulk diamond surface in terms of electronic configuration, production of e<sub>aq</sub> in an aqueous medium can be also expected<sup>72,2</sup>. However, detection of e<sub>aq</sub> has not been experimentally demonstrated for detonation NDs with a primary diameter of around 5 nm but only for 125 nm diamond NDs with a high-quality crystallographic structure<sup>55,2</sup>.

### 4.6.1 Principle of the method

The detection of e<sub>aq</sub> via HO• and Cou can be done by replacing the air atmosphere of the solution with gaseous mixture of nitrous oxide (N<sub>2</sub>O – 79 %) and oxygen (O<sub>2</sub> - 21 %). Both gases can act as e<sub>aq</sub> scavengers. However, only N<sub>2</sub>O can selectively react and convert e<sub>aq</sub> into HO• which can further hydroxylate the Cou probe. The interaction of e<sub>aq</sub> with O<sub>2</sub> gas creates O<sub>2</sub>• radicals which do not react with Cou that is why it is important to keep the ratio between N<sub>2</sub>O/O<sub>2</sub> constant.



#### Equation 4.3

As a consequence, the total radiolytic yield obtained under N<sub>2</sub>O atmosphere is a sum of two radiolytic yields: G(HO•) and G(e<sub>aq</sub>) seen for an experiment performed under air atmosphere:

$$G(HO^\bullet)_{N_2O / O_2} = G(HO^\bullet)_{air} + G(e_{aq})_{air}$$

#### Equation 4.4

In the following parts, the experimental detection of e<sub>aq</sub> via HO• and Cou was performed under air and N<sub>2</sub>O/O<sub>2</sub> atmospheres. Suspensions of plasma H-NDs and Ox-NDs (negative control) were irradiated with X-rays (17.5 keV) and γ-rays (1.17 MeV).

### 4.6.2 X-rays irradiation

PlasmaChem NDs were hydrogenated via microwave plasma and dispersed in ultra-pure water. Hydrosol was prepared in accordance with the protocol detailed in Chapter 3 and characterized via DLS and FTIR spectroscopy to ensure successful surface's modification. The X-rays irradiation experiment was performed under air and N<sub>2</sub>O/O<sub>2</sub> atmospheres (air was

replaced by  $N_2O/O_2$  after 40 min of suspension bubbling with the gaseous mixture). These experiments were performed by C. Sicard and E. Brun from the LCP laboratory.

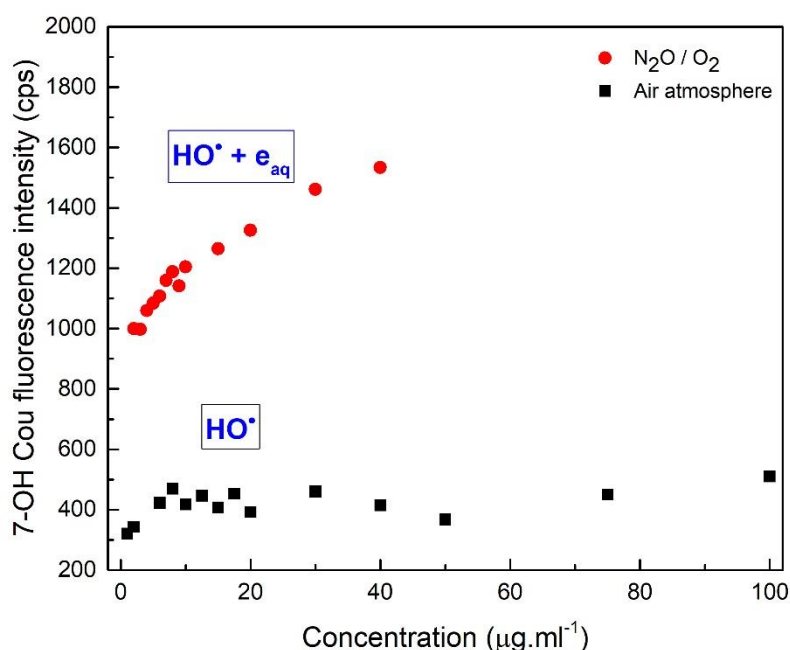


**Figure 4.29** – Fluorescence intensity of 7-OH Cou detected after X-rays irradiation ( $E = 17.5$  keV) of plasma H-NDs under air (black) and  $N_2O/O_2$  (red) atmospheres as a function of NDs concentration. Irradiation of colloids and fluorescence reading was performed on the same day to ensure the same experimental conditions.

The fluorescence intensity of 7-OH Cou increases in the presence of plasma H-NDs, both in air and in  $N_2O/O_2$  atmosphere proving photo illuminated activity of the surface (Figure 4.29). Under air atmosphere, a gradual increase in 7-OH Cou is observed until the maximum concentration of  $100 \mu\text{g.ml}^{-1}$  with an effect equal to + 59 % as compared to a reference signal (at  $0 \mu\text{g.ml}^{-1}$ ). For  $N_2O/O_2$  atmosphere, the 7-OH Cou fluorescence signal is 53 % higher with respect to Cou alone at the maximum concentration tested ( $40 \mu\text{g.ml}^{-1}$ ). Recent experiments performed by C. Sicard and E. Brun confirmed these curves showing that after  $40 \mu\text{g.ml}^{-1}$  fluorescence signal reaches a plateau for the measurements under  $N_2O/O_2$  atmosphere.

In order to detect production of solvated electrons, the 7-OH Cou fluorescence intensity obtained under air atmosphere needs to be subtracted from the fluorescence data obtained under  $N_2O/O_2$ . A simple subtraction eliminates the influence of the  $HO^\bullet$  radiolytic yield allowing to evidence the radiolytic yield of  $e_{aq}$  according to the Equation 4.4. Final fluorescence intensity data are then normalized to show the additional effect of  $HO^\bullet$  production induced by the presence of  $e_{aq}$  as a relative increase in the 7-OH Cou signal.

The same experimental procedure has been also applied for the air annealed (1 h 30 min,  $550^\circ\text{C}$ ) NDs, used as a negative probe. Under the air atmosphere, the Ox-NDs does not induce an additional  $e_{aq}$  production. Its behavior is compared to H-NDs in the following figure.

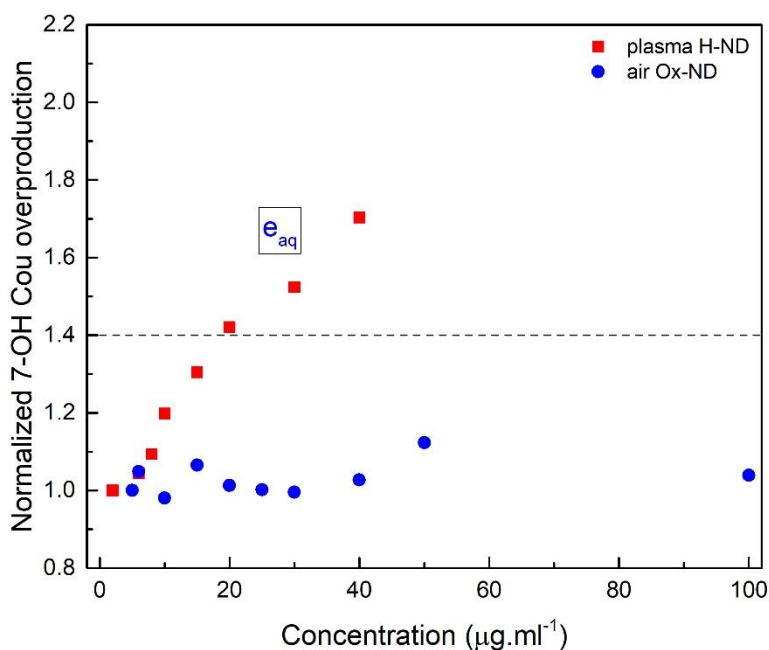


**Figure 4.30** – Normalized 7-OH Cou overproduction obtained after subtraction of the fluorescence intensity for plasma H-NDs (black) and Ox-NDs (blue) as a function of concentration. Blue, dashed line represents an average 7-OH Cou overproduction obtained in the presence of Ox-NDs.

Normalized values of 7-OH Cou fluorescence intensity show that the production of  $e_{aq}$  increases progressively with the concentration of plasma H-NDs while no significant effect is detected for the Ox-NDs (Figure 4.30). A maximum increase of + 70 % is observed at a H-NDs concentration of 40  $\mu\text{g.ml}^{-1}$  whereas for the Ox-NDs, the average 7-OH Cou signal does not exceed + 4 %. Data obtained for the Ox-NDs are in agreement with the previous experiments performed under air atmosphere. H-NDs are photoactive and the production of solvated electrons can be observed and quantified.

Bringing it all together, the introduction of scavenging N<sub>2</sub>O/O<sub>2</sub> gas into experimental suspensions allowed to detect the production of  $e_{aq}$  as a result of photoemission from the H-NDs surface. The concentration of detected  $e_{aq}$  increases progressively along with the concentration of H-NDs up to 40  $\mu\text{g.ml}^{-1}$ . No photoemission activity and hence no  $e_{aq}$  production is observed for the air Ox-NDs under X-rays.

### 4.6.3 Gamma irradiation

The same experimental procedure was repeated using plasma H-NDs (concentration range: 0 – 100  $\mu\text{g.ml}^{-1}$ ) exposed to  $\gamma$ -rays ( $E = 1.17 \text{ MeV}$ ).

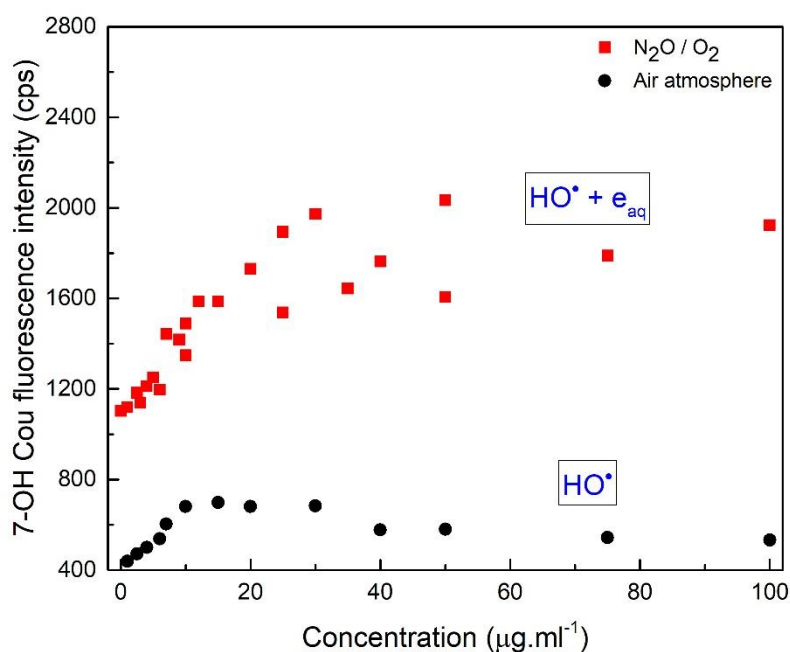


**Figure 4.31** – Fluorescence intensity of 7-OH Cou detected after  $\gamma$ -rays irradiation of plasma H-NDs under air (black) and  $N_2O/O_2$  (red, 2 independent measurements) atmospheres as a function of ND's concentration. Irradiation of colloids and fluorescence reading was performed on the same day to ensure the same experimental conditions.

After  $\gamma$ -irradiation (Figure 4.31), the production of  $HO^\bullet$  in air atmosphere has a similar profile to the one seen previously for the lower energy range (17.5 keV). A linear increase up to ND's concentration of  $10 \mu\text{g.ml}^{-1}$  followed by a plateau ( $10 - 30 \mu\text{g.ml}^{-1}$ ) and a gradual decrease until the end of concentration range is observed. The maximum effect of + 59 % is noted at the concentration of  $30 \mu\text{g.ml}^{-1}$  whereas for the highest concentration of H-NDs ( $100 \mu\text{g.ml}^{-1}$ ), the  $HO^\bullet$  overproduction effect goes down to + 22 %. When the air atmosphere is replaced by the  $N_2O/O_2$  gas, the production of 7-OH Cou rises along with the concentration of the NDs to reach a plateau above  $30 \mu\text{g.ml}^{-1}$  with a maximum effect of + 84 %.

However, the real influence in 7-OH Cou fluorescence increase caused by the presence of solvated electrons requires subtracting the curve obtained under air atmosphere from the  $N_2O/O_2$  characteristics. Normalized data shows the only  $e_{aq}$  which are converted into  $HO^\bullet$  radicals.

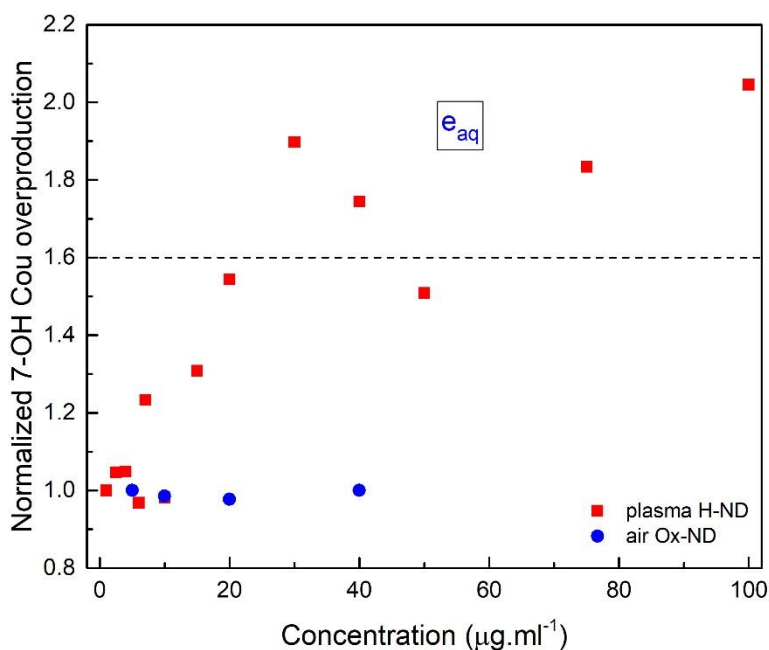


**Figure 4.32** – Normalized 7-OH Cou overproduction obtained after subtraction of the fluorescence intensity for plasma H-NDs (black) and Ox-NDs (blue) as a function of concentration.

The 7-OH Cou fluorescence data after subtraction were normalized for both plasma H-NDs and air Ox-NDs and plotted on the same graph (Figure 4.32). Air oxidized ND shows no increase in the HO• production under air and N<sub>2</sub>O/O<sub>2</sub> atmosphere which provided an experimental proof of lack of the e<sub>aq</sub>. The production of e<sub>aq</sub> continually increases with the concentration of the plasma H-NDs reaching a twice higher number with respect to water radiolysis (increase by a factor of 2 for the maximum concentration). The concentration of e<sub>aq</sub> is nearly the same as for H-NDs irradiated with X-ray. Plateau is also observed.

#### 4.6.4 Summary

- For the first time, production of e<sub>aq</sub> has been experimentally confirmed for detonation H-NDs
- No photoactivity toward HO• and e<sub>aq</sub> has been observed for Ox-NDs
- Production of HO• and e<sub>aq</sub> is c.a. 3.2 and 2.9 times higher under N<sub>2</sub>O/O<sub>2</sub> than under air atmosphere as seen for X-ray and γ-energy, respectively
- Production of e<sub>aq</sub> is higher compared to HO• for the same concentration of plasma H-NDs and does not decrease above 30 µg.ml<sup>-1</sup>. A plateau is observed for much higher concentration of H-NDs under N<sub>2</sub>O/O<sub>2</sub> compared to air atmosphere
- For the same concentration of plasma H-NDs (30 µg.ml<sup>-1</sup>), emission of e<sub>aq</sub> is c.a. 25 % times higher under γ-rays than X-rays.

## 4.7 Discussion about the behavior of nanodiamonds under irradiation

In this chapter, the HO<sup>•</sup> radicals and electrons production by colloidal suspensions of detonation nanodiamonds during radiolysis under X-rays (17.5 keV) and  $\gamma$ -rays (Co<sup>60</sup>, 1.17 MeV) were studied. Starting from the same source of NDs, different surface chemistries were (oxidized, hydrogenated, surface graphitized). The work presented has been undertaken following the finding a few years ago by our laboratory and colleagues from the life science division of CEA of a radiosensitization effect in tumoral cells of hydrogenated NDs<sup>25</sup>. The overall concept of this Ph.D. work was to clarify the chemical origin of this effect by taking into account the colloidal stability of NDs suspensions.

Let's start with a short summary of the behavior under illumination for each surface chemistry.

- First, nanodiamonds oxidized by air annealing do not exhibit any overproduction of HO<sup>•</sup> radicals or electrons when illuminated with X- or  $\gamma$ -rays in water. Whatever the concentration, no additional effect to water radiolysis was revealed by our experiments. Air annealed NDs, exhibiting a very good colloidal stability on long term and a negative zeta potential, seem to act as spectators during water radiolysis without interfering.
- On the contrary, plasma hydrogenated nanodiamonds exhibited a particular reactivity under X- and  $\gamma$ -rays illuminations, with an additional production of HO<sup>•</sup> compared to radiolysis alone of + 40 % and + 60 %, respectively. According to our experiments, this behavior is not source dependent as it was reproduced on two other sources of detonation NDs. Solvated electron overproduction was also evidenced with an overproduction compared to water radiolysis alone of + 80 % under X-rays and + 100 % under  $\gamma$ -rays. These measurements were carried out on fresh suspensions.

For hydrogen annealed samples, only irradiation under X-Rays was studied, with an HO<sup>•</sup> overproduction of +50 %. In addition to this moderate higher level of radicals' overproduction, hydrogen annealed samples exhibited a better efficiency over time. Their behavior after 64 days still led to an overproduction of + 40 % while for plasma hydrogenated NDs, the HO<sup>•</sup> overproduction drops from 40 % to less than 10 %. The link between the HO<sup>•</sup> overproduction and the colloidal stability of NDs will be further discussed.

- Surprisingly, vacuum annealed samples at 750 °C also revealed HO<sup>•</sup> overproduction abilities at least under X-rays illumination. However, the effect seems to decrease according to the temperature of annealing. For NDs annealed at 850 °C, a three-fold higher concentration is needed to reach the same overproduction level at + 50 %. It is also important to note that a different trend versus concentration is observed for these NDs annealed under vacuum compared to hydrogenated NDs.
- For both types of hydrogenated NDs and at least for vacuum annealed at the lowest temperature, a saturation of the overproduction effect has been observed when the

concentration of nanodiamonds exceeds  $20 \mu\text{g}\cdot\text{ml}^{-1}$ . This saturation is often followed by a decrease of the  $\text{HO}^\bullet$  overproduction at higher concentration. The role of a possible quenching effect has been ruled out by our experiments. Indeed, almost the whole fluorescence from 7-OH Cou is recovered by salt addition and centrifugation as shown previously in this chapter. The saturation effect can be related either to a recombination of  $\text{HO}^\bullet$  radicals produced,  $\text{HO}^\bullet$  scavenging by Cou being competed by  $\text{HO}^\bullet / \text{HO}^\bullet$  recombination when  $\text{HO}^\bullet$  concentration increases, or to an interaction of  $\text{HO}^\bullet$  radicals with NDs.

#### 4.7.1 Discussion on the origin of the phenomenon

In the following part, we will thus discuss what we can conclude from this Ph.D. work concerning the origin of the effect of  $\text{HO}^\bullet$  and solvated electrons overproduction during radiolysis in presence of hydrogenated or vacuum annealed NDs.

##### 4.7.1.1 Effect of a metallic contamination

If high Z materials are present in the suspension, they could absorb more energy than water and then would provide the overproduction effect seen. However, the reproducibility of the effect on different sources of NDs which exhibit very different levels of metallic impurities (elemental analysis performed by ICP-MS on the different sources of NDs - Chapter 2) invalidates the hypothesis of a phenomenon coming from these impurities. Furthermore, hydrogen or vacuum annealing treatments were not shown to bring metallic contamination (ICP-MS - Chapter 2). Metallic contamination could also have been provided by the ultrasonic treatment realized with a titanium horn. However, as oxidized NDs did not show any overproduction effect while they were sonicated the same way than hydrogenated NDs, we can also exclude this origin of the phenomenon.

Here, the effect of radical overproduction seems to come from the presence of nanodiamonds in the aqueous solution during the radiolysis, with the adequate surface chemistry and the adequate concentration.

##### 4.7.1.2 Surface effect

Excluding an effect of a metallic contamination, we could now focus on the effect of the surface chemistry, which has been shown to partially drive the phenomenon, at least for oxidized vs hydrogenated / vacuum annealed NDs.

For bulk diamond, hydrogenation has been shown to be a key parameter for the production of solvated electrons<sup>72</sup>. Here as well, we evidenced the effect on hydrogenated NDs, however, taking into account all our experiments, the following points appeared:

- **No correlation between the hydrogen covering of the NDs surface and the overproduction effect.** As explained previously, parallel works conducted by Emilie

Nehlig from the Tritium Laboratory of CEA have shown that hydrogen annealed NDs possess 10 times more hydrogen on their surface than plasma treated NDs. This result was deduced from tritium labeling of NDs from the same source (Plasma Chem) using both methods (plasma and annealing) which allows an accurate quantification of tritium amount by liquid scintillation. A simple calculation has shown that with plasma treatment, 1 carbon atom over 20 was effectively bonded with a tritium atom<sup>73</sup>, which rises up to 1 over 2 for annealed treated NDs. We can expect that such a difference would affect the energetic diagram of the particle and therefore its electron affinity<sup>74</sup>. However, no direct connection between the hydrogen covering of the NDs and the efficiency of radical production is seen despite a slightly higher HO• overproduction (50 % instead of 40 % for the same concentration). Only a saturation effect of the OH• overproduction whatever the negative electron affinity value would also explain this situation.

- **H terminations are preserved during ageing when the effect is almost lost** (see FTIR in Chapter 3). HO• overproduction has been shown to vanish according to the ageing of the suspension, with a more pronounced effect for plasma treated samples. However, for hydrogenated NDs, we have no real evidence of a significant loss of the hydrogenated terminations over time. FTIR done on suspended NDs, even for a long time, did not show real vanishing of the C-H related peaks or important increase of the oxygen-related groups. Only a weak re-oxidation with C=O related groups has been observed, but already present on ultra-fresh particles for which HO• overproduction is at its higher level.
- **Vacuum annealed samples also evidenced an overproduction effect.** The phenomenon is observed with almost the same efficiency on vacuum annealed NDs with the smoothest conditions (1 h / 750 °C). Here, there was no intentional addition of hydrogen at the surface of the nanodiamond during the treatment, performed under dynamic secondary vacuum (pressure lower than 10<sup>-6</sup> mbar all along the treatment). Even if hydrogen terminations were already present at the surface of the as-received material, as shown by FTIR, we cannot expect having increased the amount of C-H on the treated sample with the same efficiency than with plasma or annealing under 12 or 200 mbar of H<sub>2</sub>, respectively. Furthermore, FTIR evidenced that C=O groups already present at the surface of the raw material were preserved after this treatment (Chapter 2). The surface can be therefore considered as still partially oxidized.

A common point between hydrogen treated samples and vacuum annealed ones concerns the presence of graphitic reconstructions on their surface. Except for air annealed samples, our TEM observations reported such structures on all treated NDs (Chapter 2). One would therefore attribute the overproduction of HO• radicals to the presence of such sp<sup>2</sup> reconstructions. However, NEA has never been reported in the literature for graphitized diamond (and partly oxidized here). Furthermore, TEM also showed that they are more pronounced on vacuum annealed sample, while the effect of overproduction is not accentuated. The effect even decreases on vacuum annealed samples treated with harsher conditions, for which we expect higher amount of sp<sup>2</sup> carbon at their surface. This statement is also corroborated by several

tests done with plasma treated samples with also harsh conditions, for which Raman reports an important graphitization, and which exhibited no HO<sup>•</sup> overproduction (results not shown in this manuscript).

#### 4.7.1.3 Colloidal stability effect

For sure, **aggregation / agglomeration** plays a role. The effect tends to decrease when NDs tends to aggregate / agglomerate. Indeed, the study conducted all over the Chapter 3 on the stability over few hours to few tens of days came from the observation of strong discrepancies between the overproduction results at the beginning of this Ph.D. work, that we quickly attributed to the freshness of the suspension. As soon as the suspension starts to badly evolve, even slightly, the efficiency of overproduction is affected. This observation is also correlated by the different behaviors of plasma and annealed hydrogenated NDs in terms OH<sup>•</sup> overproduction and hydrodynamic diameter evolution over time (Chapter 4).

If the origin of the overproduction effect was only related to the position of the conduction band lying above the vacuum level as for bulk diamond, we would expect that this electronic configuration would be preserved even in small aggregates. As discussed previously, the colloidal evolution of the treated NDs can come of course from a moderate modification of their surface chemistry, but we believe more in an evolution of the interface between water molecules and NDs due to a modification of the dissolved species in suspension, a modification of the local pH, gas adsorption / desorption.

As a preliminary conclusion, we can therefore propose that **hydrogenation of the surface of our NDs and the related negative electron affinity is not the key parameter solely driving the overproduction of OH<sup>•</sup> and solvated electrons** during radiolysis.

This assessment is important as hydrogenated bulk diamond has been reported since few years to be an efficient solid source of solvated electrons under UV illumination<sup>34</sup>. Here, with nanodiamonds, hydrogen termination does not seem to explain alone the phenomenon observed, even if overproduction of not only HO<sup>•</sup> but also solvated electrons has been evidenced. However, we cannot affirm that these over-quantity of electrons during the water radiolysis comes from the nanodiamond, it can also result from exalted water radiolysis in presence of the nanodiamonds.

#### 4.7.1.4 Effect of the core

The effect of the diamond core has also to be discussed here. First, if we look at the energy absorption of water and carbon (Figure 4.33, top two), we can notice that there is no supplementary energy absorbed when NDs are in solution compared to water either with X or gamma rays.

In addition, experiments were realized with two irradiation energies: X-Rays (17.5 keV) and  $\gamma$ -Rays (1.17 MeV). Looking at the absorption curves of Figure 4.33-right, carbon is expected to absorb less for  $\gamma$ -Rays than for X-Rays. However, we recorded more HO<sup>•</sup> and solvated

electrons overproduction under  $\gamma$ -Rays than with X-Rays. This observation seems to invalidate an effect directly linked to a mechanism involving photon absorption by the core leading to the photoemission of an electron and its solvation, thanks to the NEA of the hydrogenated diamond surface.

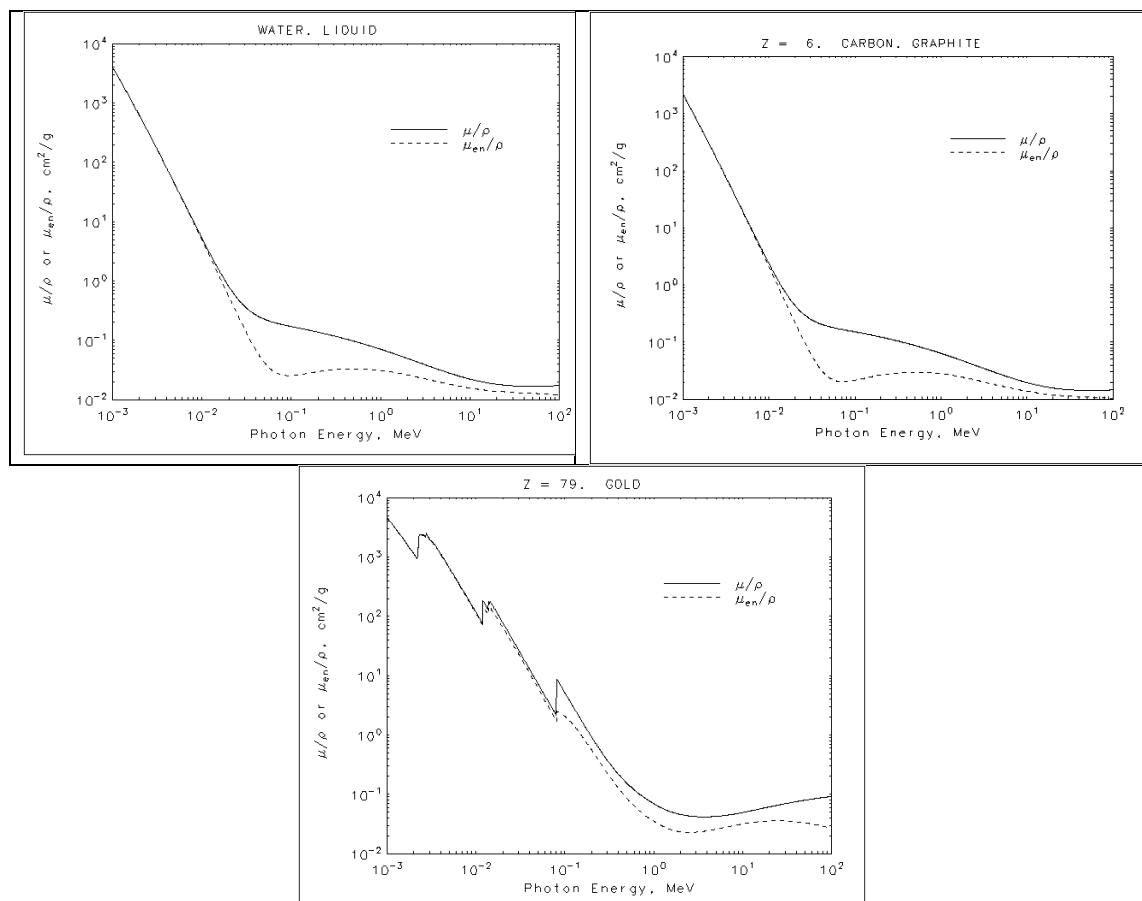


**Figure 4.33** – Absorption of photons in water, carbon, and gold according to their energy.

Indeed, if we consider the values reached at the plateau for  $\text{HO}^\bullet$  overproduction under X-Rays (400 fluorescence cnts, Figure 4.29) and  $\gamma$ -Rays (600 cnts, Figure 4.31), their ratio gives 1.5, which is close to the ratio of  $G(\text{HO}^\bullet)$  during water radiolysis for these two energies (1.4). This also pleads for a diamond core not providing electrons, the effect according to the energy appearing to be driven only by the radiolytic yield of  $\text{HO}^\bullet$ . Indeed, the same behavior of  $\text{HO}^\bullet$  overproduction according to the energy not dependent on the chemical nature of the nanoparticle core has already been observed with gold nanoparticles (GNPs).

These GNPs are usually considered as a model system for radiosensitization. In parallel to this Ph.D. work, we can, therefore, estimate the  $\text{HO}^\bullet$  overproduction for 6 nm gold NPs, using the same irradiation conditions and data analysis than for NDs. Results have been compared to the overproduction recorded for plasma H-NDs, as plotted in the Figure 4.34. It is surprising to observe a common shape between NDs and GNPs with a constant raise until  $\approx 30 \mu\text{g}\cdot\text{ml}^{-1}$  and then a plateau effect, and only a 3-fold factor of  $\text{HO}^\bullet$  overproduction between metallic

( $Z = 79$ ) and a carbon-based ( $Z = 6$ ) NPs with very different absorption at 17.5 keV (Figure 4.33). Here as well, the real **influence of the core toward  $\text{HO}^\bullet$  overproduction is questioned.**

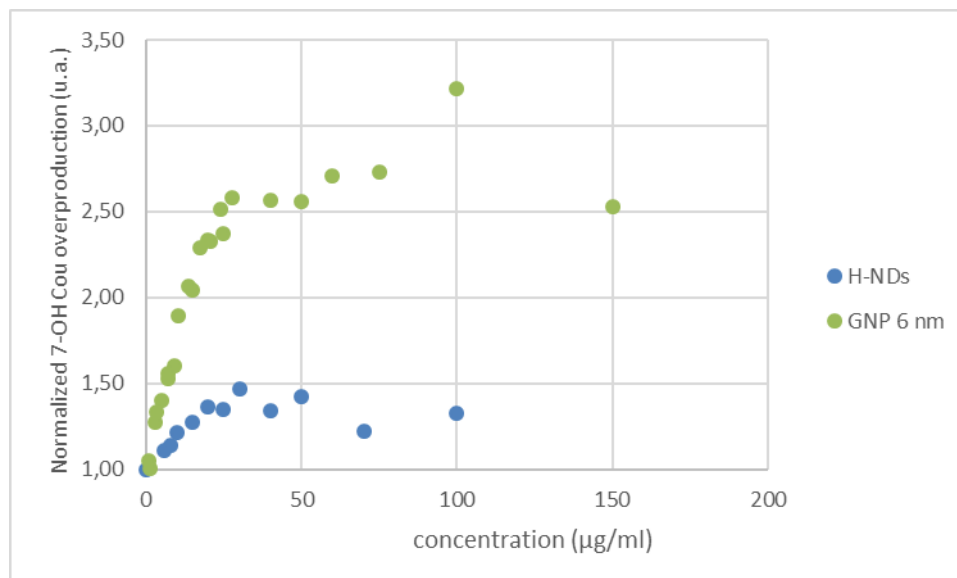


**Figure 4.34** – Normalized  $\text{HO}^\bullet$  overproduction according to the concentration of H-NDs and GNPs 6 nm suspended in water. X-ray irradiation at 17.5 keV.

As a side note, we also suggest using volume or surface area rather than concentration for any future comparison of  $\text{HO}^\bullet$  overproduction phenomena between AuNPs and H-NDs.

#### 4.7.1.5 Origin of the effect coming from water interface

In addition to the role of the NEA brought by H-terminations, these additional observations also raise an interrogation about the role of the nature of particle core. It would support the hypothesis that the overproduction observed here is not directly linked to electrons coming from the NDs and helped by the NEA, but more likely due to a **specific phenomenon in the water surrounding NDs which may promote locally the radiolysis**. It must be highlighted here that the effect has been observed for positively-charged NDs exclusively. Even more, a curve can be plotted with the maximum effect of  $\text{OH}^\bullet$  overproduction according to the Zeta potential of the suspension used (Figure 4.35), on which a dependency seems to appear. Such curve must be carefully handled as the value of the ZP also reflect somehow the aggregation / agglomeration state of the suspension. Nevertheless, a **link between positive ZP and  $\text{HO}^\bullet$  overproduction can be proposed.**

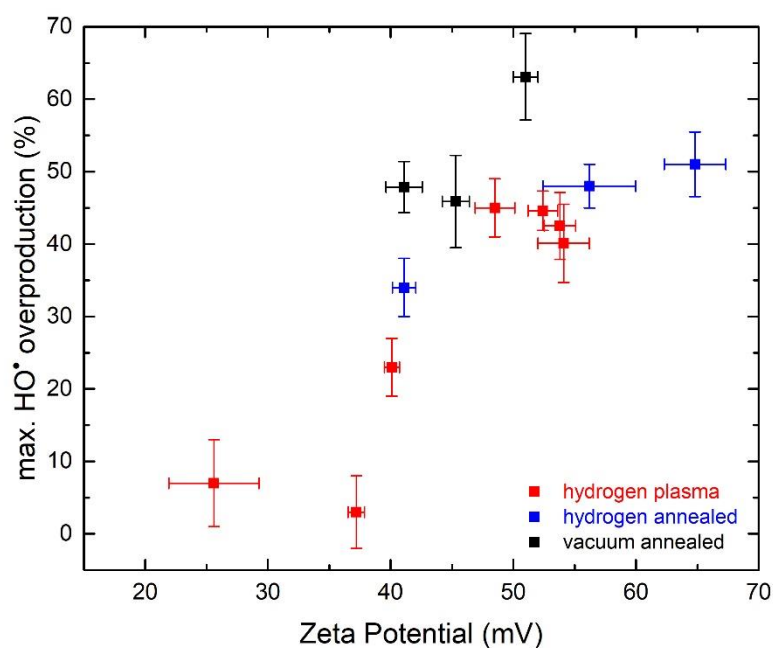


**Figure 4.35** – Maximum HO• overproduction according to the Zeta Potential of hydrogenated and vacuum annealed NDs suspension.

This hypothesis needs to be linked to the recent findings of several teams concerning the hydration of NDs, especially for hydrogenated or slightly  $sp^2$  reconstructed nanodiamonds<sup>75,76</sup>. In particular, Petit et al. reported a specific structure for water molecules surrounding plasma H-NDs and polyfunctional NDs using infrared, Raman and X-ray spectroscopies<sup>56</sup>. No direct bonding between water and the hydrogenated surface was detected due to the hydrophobic character of the hydrogenated diamond surface while a perturbation of water structure at long range was evidenced (see Figure below).

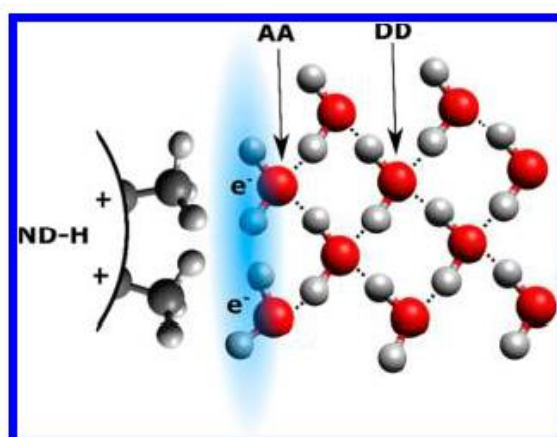


**Figure 4.36** – View of the water structure around hydrogenated NDs<sup>56</sup>.

Our results and hypothesis have to be put in context with the recent publication of Hamer's team, who reported on the lack of reduction of CO<sub>2</sub> in presence of detonation hydrogenated ND. Authors attributed the lack of reactivity of detonation NDs mainly to the high level of defects in the core as well as a spontaneous oxidation of the surface under UV. In our opinion, these results are not contradictory to our findings. In our work, such possible oxidation under X-Rays has been quickly investigated, and after 2000 Gy of irradiation at 17.5 keV, no modification of the colloidal properties or FTIR signature of oxidation was evidenced. Due to the different range of energy used, it seems that we avoid this oxidation effect. Furthermore, we can expect very different reactivities and mechanisms switching from UV to X- or  $\gamma$ -rays. We, therefore, propose the hypothesis that radical overproduction saw for hydrogenated and smoothly vacuum annealed NDs would be linked to their positive ZP and related specific interactions with water molecules. This hypothesis would more likely support a **local enhancement of the radiolysis around NDs** rather than a true photoemission of electrons from the ND core **to explain the overproduction of HO<sup>•</sup> radicals** and solvated electrons in presence of NDs.

## Bibliography

1. Girard, H. A. *et al.* Surface properties of hydrogenated nanodiamonds: a chemical investigation. *Phys. Chem. Chem. Phys.* **13**, 11517–11523 (2011).
2. Zhang, L. & Hamers, R. J. Photocatalytic reduction of CO<sub>2</sub> to CO by diamond nanoparticles. *Diam. Relat. Mater.* **78**, 24–30 (2017).
3. Le Caër, S. Water Radiolysis: Influence of Oxide Surfaces on H<sub>2</sub> Production under Ionizing Radiation. *Water* **3**, 235–253 (2011).
4. Mchedlov-Petrosyan, N. O., Kamneva, N. N., Marynin, A. I., Kryshchal, A. P. & Ōsawa, E. Colloidal properties and behaviors of 3 nm primary particles of detonation nanodiamonds in aqueous media. *Phys. Chem. Chem. Phys.* **17**, 16186–16203 (2015).
5. Grall, R. *et al.* Impairing the radioresistance of cancer cells by hydrogenated nanodiamonds. *Biomaterials* **61**, 290–298 (2015).
6. Kurzyp, M. *et al.* Hydroxyl radical production induced by plasma hydrogenated nanodiamonds under X-ray irradiation. *Chem. Commun.* **53**, 1237–1240 (2017).
7. Kwatra, D., Venugopal, A. & Anant, S. Nanoparticles in radiation therapy : a summary of various approaches to enhance radiosensitization in cancer. *Transl. Cancer Res.* **2**, 330–342 (2013).
8. Spinks, J.W.T. & Woods, R. J. Water and Inorganic Aqueous Systems. In: An introduction to radiation chemistry. Third edition, 243–313 (*Wiley-Interscience*, 1990).
9. Sunaryo, G. R., Katsumura, Y., Shirai, I., Hiroishi, D. & Ishigure, K. Radiolysis of water at elevated temperatures-I. Irradiation with gamma-rays and fast neutrons at room temperature. *Radial. Php. Chem.* **44**, 273–280 (1994).
10. Ferradini, C. & Jay-Gerin, J.-P. The effect of pH on water radiolysis: A still open question — A minireview. *Res. Chem. Intermed.* **26**, 549–565 (2000).
11. Basly, J. P., Basly, I. & Bernard, M. Radiosterilization dosimetry of vitamins: an ESR study. *Int. J. Radiat. Biol.* **74**, 521–528 (1998).
12. Guo, F. & Shen, H. Study of gamma irradiation-induced effects on organic pollutants and suspended solids in coking wastewater. *Desalin. Water Treat.* **52**, 1850–1854 (2014).
13. Gutiérrez, D. R., Char, C., Escalona, V. H., Chaves, A. R. & Rodríguez, S. del C. Application of UV-C Radiation in the Conservation of Minimally Processed Rocket ( *Eruca sativa* Mill.). *J. Food Process. Preserv.* **39**, 3117–3127 (2015).
14. Shi, J., Kantoff, P. W., Wooster, R. & Farokhzad, O. C. Cancer nanomedicine: progress, challenges and opportunities. *Nat. Rev. Cancer* **17**, 20–37 (2016).
15. Schmid, T. E. *et al.* Relative biological effectiveness of pulsed and continuous 20MeV protons for micronucleus induction in 3D human reconstructed skin tissue. *Radiotherapy Oncol.* **95**, 66–72 (2010).

16. Czili, H. & Horváth, A. Applicability of coumarin for detecting and measuring hydroxyl radicals generated by photoexcitation of TiO<sub>2</sub> nanoparticles. *Appl. Catal. B Environ.* **81**, 295–302 (2008).
17. Nakken, K. F. & Pihl, A. On the ability of nitrous oxide to convert hydrated electrons into hydroxyl radical. *Radiat. Res.* **26**, 519–526 (1965).
18. Sicard-Roselli, C. *et al.* A New Mechanism for Hydroxyl Radical Production in Irradiated Nanoparticle Solutions. *Small* **10**, 3338–3346 (2014).
19. Von Sonntag, C. Formation of Reactive Free Radicals in an Aqueous Environment. In: Free-Radical-Induced DNA Damage and Its Repair, 7–46 (*Springer*, 2006).
20. Coderre, J. Principles of Radiation Interactions. *Radiat. Chem.* 1–17 (2004). Retrieved from: [https://ocw.mit.edu/courses/nuclear-engineering/22-55j-principles-of-radiation-interactions-fall-2004/lecture-notes/raditn\\_chemistry.pdf](https://ocw.mit.edu/courses/nuclear-engineering/22-55j-principles-of-radiation-interactions-fall-2004/lecture-notes/raditn_chemistry.pdf) (Accessed: 16<sup>th</sup> August 2017)
21. Newton, G. L. & Milligan, J. R. Fluorescence detection of hydroxyl radicals. *Radiat. Phys. Chem.* **75**, 473–478 (2006).
22. Gutteridge, J. M. & Halliwell, B. Free radicals and antioxidants in the year 2000. A historical look to the future. *Ann. N. Y. Acad. Sci.* **899**, 136–147 (2000).
23. Janik, I., Bartels, D. M. & Jonah, C. D. Hydroxyl Radical Self-Recombination Reaction and Absorption Spectrum in Water Up to 350 °C. *J. Phys. Chem. A* **111**, 1835–1843 (2007).
24. Gligorovski, S., Streckowski, R., Barbati, S. & Vione, D. Environmental Implications of Hydroxyl Radicals. *Chem. Rev.* **115**, 13051–13092 (2015).
25. Gruber, N., Orelli, L. R., Cipolletti, R. & Stipa, P. Amidinoquinoxaline N-oxides: spin trapping of O- and C-centered radicals. *Org. Biomol. Chem.* **15**, 7685–7695 (2017).
26. Finkelstein, E., Gerald, M. R. & Rauckman, E. J. Spin trapping of superoxide and hydroxyl radical: Practical aspects. *Arch. Biochem. Biophys.* **200**, 1–16 (1980).
27. Nobuaki, S., Koji, M., Emino, S. & Toshihiko, I. A ratiometric fluorescent probe for imaging hydroxyl radicals in living cells. *Chem. Commun.* **0**, 496–497 (2004).
28. Li, B., Gutierrez, P. L. & Blough, N. V. Trace Determination of Hydroxyl Radical in Biological Systems. *Anal. Chem.* **69**, 4295–4302 (1997).
29. Pou, S., Hassett, D. J., Britigan, B. E., Cohen, M. S. & Rosen, G. M. Problems associated with spin trapping oxygen-centered free radicals in biological systems. *Anal. Biochem.* **177**, 1–6 (1989).
30. Ghosh, D., Nandi, N. & Chattopadhyay, N. Differential Förster Resonance Energy Transfer from the Excimers of Poly(*N*-vinylcarbazole) to Coumarin 153. *J. Phys. Chem. B* **116**, 4693–4701 (2012).
31. Gomes, A., Fernandes, E. & Lima, J. L. Fluorescence probes used for detection of reactive oxygen species. *J. Biochem. Biophys. Methods* **65**, 45–80 (2005).

32. Tai, C., Gu, X., Zou, H. & Guo, Q. A new simple and sensitive fluorometric method for the determination of hydroxyl radical and its application. *Talanta* **58**, 661–667 (2002).
33. Villegas, M. L., Bertolotti, S. G., Previtali, C. M. & Encinas, M. V. Reactions of excited states of phenoxazin-3-one dyes with amino acids. *Photochem. Photobiol.* **81**, 884–890 (2005).
34. Zhu, D., Zhang, L., Ruther, R. E. & Hamers, R. J. Photo-illuminated diamond as a solid-state source of solvated electrons in water for nitrogen reduction. *Nat. Mater.* **12**, 836–841 (2013).
35. Girard, H. A. *et al.* Hydrogenation of nanodiamonds using MPCVD: A new route toward organic functionalization. *Diam. Relat. Mater.* **19**, 1117–1123 (2010).
36. Petit, T. *et al.* Surface transfer doping can mediate both colloidal stability and self-assembly of nanodiamonds. *Nanoscale* **5**, 8958–8962 (2013).
37. Bolker, A., Saguy, C. & Kalish, R. Transfer doping of single isolated nanodiamonds, studied by scanning probe microscopy techniques. *Nanotechnology* **25**, 385702 (2014).
38. Ahmed, A.-I., Mandal, S., Gines, L., Williams, O. A. & Cheng, C.-L. Low temperature catalytic reactivity of nanodiamond in molecular hydrogen. *Carbon* **110**, 438–442 (2016).
39. Retif, P. *et al.* Nanoparticles for radiation therapy enhancement: The key parameters. *Theranostics* **5**, 1030–1044 (2015).
40. Mitsunaga, M., Nakajima, T., Sano, K., Choyke, P. L. & Kobayashi, H. Near-infrared theranostic photoimmunotherapy (PIT): repeated exposure of light enhances the effect of immunoconjugate. *Bioconjug. Chem.* **23**, 604–609 (2012).
41. Su, X.-Y., Liu, P.-D., Wu, H. & Gu, N. Enhancement of radiosensitization by metal-based nanoparticles in cancer radiation therapy. *Cancer Biol. Med.* **11**, 86–91 (2014).
42. Hossain, M. & Su, M. Nanoparticle Location and Material-Dependent Dose Enhancement in X-ray Radiation Therapy. *J. Phys. Chem. C* **116**, 23047–23052 (2012).
43. Chiu, S.-J., Lee, M.-Y., Chou, W.-G. & Lin, L.-Y. Germanium Oxide Enhances the Radiosensitivity of Cells. *Radiat. Res.* **159**, 391–400 (2003).
44. Chithrani, D. B. *et al.* Gold Nanoparticles as Radiation Sensitizers in Cancer Therapy. *Radiat. Res.* **173**, 719–728 (2010).
45. Huang, P. *et al.* Protein-directed one-pot synthesis of Ag microspheres with good biocompatibility and enhancement of radiation effects on gastric cancer cells. *Nanoscale* **3**, 3623–3626 (2011).
46. Lu, R., Yang, D., Cui, D., Wang, Z. & Guo, L. Egg white-mediated green synthesis of silver nanoparticles with excellent biocompatibility and enhanced radiation effects on cancer cells. *Int. J. Nanomedicine* **7**, 2101–2107 (2012).
47. Liu, P. *et al.* Silver nanoparticles: a novel radiation sensitizer for glioma? *Nanoscale* **5**, 11829–11836 (2013).

48. Babaei, M. & Ganjalikhani, M. The potential effectiveness of nanoparticles as radio sensitizers for radiotherapy. *BiolImpacts* **4**, 15–20 (2014).
49. Hainfeld, J. F., Slatkin, D. N. & Smilowitz, H. M. The use of gold nanoparticles to enhance radiotherapy in mice. *Phys. Med. Biol.* **49**, 309–315 (2004).
50. Mesbahi, A. A review on gold nanoparticles radiosensitization effect in radiation therapy of cancer. *Reports Pract. Oncol. Radiother.* **15**, 176–180 (2010).
51. Manimegalai, S., Grumezescu, A. M. & Rajeswari, V. D. Recent trends and methodologies in gold nanoparticle synthesis – A prospective review on drug delivery aspect. *OpenNano* **2**, 37–46 (2017).
52. Haume, K. *et al.* Gold nanoparticles for cancer radiotherapy: a review. *Cancer Nanotechnol.* **7**, 1–20 (2016).
53. Zhang, X.-D. *et al.* Size-dependent radiosensitization of PEG-coated gold nanoparticles for cancer radiation therapy. *Biomaterials* **33**, 6408–6419 (2012).
54. Gilles, M., Brun, E. & Sicard-Roselli, C. Gold nanoparticles functionalization notably decreases radiosensitization through hydroxyl radical production under ionizing radiation. *Colloids Surfaces B Biointerfaces* **123**, 770–777 (2014).
55. Hamers, R. J., Bandy, J. N. A., Zhu, D. Di, Zhang, L. & Zhu, D. Di. Photoemission from diamond films and substrates into water: Dynamics of solvated electrons and implications for diamond photoelectrochemistry. *Faraday Discuss.* **172**, 397–411 (2014).
56. Petit, T. *et al.* Unusual Water Hydrogen Bond Network around Hydrogenated Nanodiamonds. *J. Phys. Chem. C* **121**, 5185–5194 (2017).
57. Maggiorella, L. *et al.* Nanoscale radiotherapy with hafnium oxide nanoparticles. *Res. Artic. Futur. Oncol.* **8**, 1167–1181 (2012).
58. Fulford, J., Nikjoo, H., Goodhead, D. T. & O'Neill, P. Yields of SSB and DSB induced in DNA by Al(K) ultrasoft X-rays and alpha-particles: comparison of experimental and simulated yields. *Int. J. Radiat. Biol.* **77**, 1053–1066 (2001).
59. Maheswara, M., Siddaiah, V., Damu, G. L. V., Rao, Y. K. & Rao, C. V. A solvent-free synthesis of coumarins via Pechmann condensation using heterogeneous catalyst. *J. Mol. Catal. A Chem.* **255**, 49–52 (2006).
60. Louit, G. *et al.* The reaction of coumarin with the OH radical revisited : hydroxylation product analysis determined by fluorescence and chromatography. *Radiat. Phys. Chem.* **72**, 119–124 (2005).
61. Petit, T. *et al.* Nanodiamond as a multimodal platform for drug delivery and radiosensitization of tumor cells. *Proc. IEEE Conf. Nanotechnol.* 174–178 (2013).
62. Vervald, A. M. *et al.* Relationship Between Fluorescent and Vibronic Properties of Detonation Nanodiamonds and Strength of Hydrogen Bonds in Suspensions. *J. Phys. Chem. C* **120**, 19375–19383 (2016).

63. Slegerova, J. *et al.* Nanodiamonds as Intracellular Probes for Imaging in Biology and Medicine. In: Prokop, A., Iwasaki, Y. & Harada, A. (eds.) *Intracellular Delivery II*, vol. 7. Netherlands, Dordrecht, 363–401 (*Springer*, 2014).
64. Mayilo, S. *et al.* Long-Range Fluorescence Quenching by Gold Nanoparticles in a Sandwich Immunoassay for Cardiac Troponin T. *Nano Lett.* **9**, 4558–4563 (2009).
65. Kang, K. A., Wang, J., Jasinski, J. B. & Achilefu, S. Fluorescence manipulation by gold nanoparticles: from complete quenching to extensive enhancement. *J. Nanobiotechnology* **9**, 1–13 (2011).
66. Dulkeith, E. *et al.* Fluorescence Quenching of Dye Molecules near Gold Nanoparticles: Radiative and Nonradiative Effects. *Phys. Rev. Lett.* **89**, 203002 (2002).
67. Reipa, V., Purdum, G. & Choi, J. Measurement of nanoparticle concentration using quartz crystal microgravimetry. *J. Phys. Chem. B* **114**, 16112–16117 (2010).
68. Dong, L. Optical Properties of Nanoparticles in Composite Materials. Doctoral Thesis in Microelectronics and Applied Physics. Stockholm, Sweden (September 2012).
69. Kavitha, S. R., Umadevi, M., Janani, S. R., Balakrishnan, T. & Ramanibai, R. Fluorescence quenching and photocatalytic degradation of textile dyeing waste water by silver nanoparticles. *Spectrochim. Acta - Part A Mol. Biomol. Spectrosc.* **127**, 115–121 (2014).
70. Dukovic, G. *et al.* Reversible Surface Oxidation and Efficient Luminescence Quenching in Semiconductor Single-Wall Carbon Nanotubes. *J. Am. Chem. Soc.* **126**, 15269–15276 (2004).
71. Yoshikawa, T. *et al.* Appropriate Salt Concentration of Nanodiamond Colloids for Electrostatic Self-Assembly Seeding of Monosized Individual Diamond Nanoparticles on Silicon Dioxide Surfaces. *Langmuir* **31**, 5319–5325 (2015).
72. Hamers, R. J. & Bandy, J. Atmospheric-pressure photoelectron emission from H-terminated and amino-terminated diamond. *Phys. Status Solidi A* **213**, 2069–2074 (2016).
73. Girard, H. A. *et al.* Tritium labelling of detonation nanodiamonds. *Chem. Commun.* **50**, 2916–2918 (2014).
74. Ristein, J. Diamond surfaces: familiar and amazing. *Appl. Phys. A* **82**, 377–384 (2006).
75. Stehlik, S. *et al.* Water interaction with hydrogenated and oxidized detonation nanodiamonds - Microscopic and spectroscopic analyses. *Diam. Relat. Mater.* **63**, 97–102 (2016).
76. Petit, T., Arnault, J.-C., Girard, H. A., Sennour, M. & Bergonzo, P. Early stages of surface graphitization on nanodiamond probed by x-ray photoelectron spectroscopy. *Phys. Rev. B* **84**, 233407 (2011).



# Chapter 5

## General conclusions and perspectives

Depending on their surface chemistry, detonation NDs can act as an active nanomaterial with radiosensitizing properties that enhances the effect of radiotherapy treatment. These properties were demonstrated before this Ph.D. work for plasma H-terminated NDs (H-NDs) in collaboration with biologists from the Experimental Cancerology Laboratory (CEA-DSV-iR2CM). Radioresistant cancer cell lines were turned into senescence with a stopping of cell proliferation. An approach like this, based on carbon-based material, is a new alternative to metal-based NPs which have not reached yet the clinical trial (e.g. gold). NDs possess superior assets such as biocompatibility, versatile surface chemistry, and a low atomic number which can be further explored toward other related bioapplications (e.g. drug delivery).

However, mechanisms explaining the radiosensitizing effect of NDs has remained unknown, with only few suppositions published, which related it to the overproduction of reactive oxygen species in presence of H-NDs. This Ph.D. work aimed to better understand the relevant physical and chemical effects of the radiosensitization of detonation NDs in aqueous media. For this purpose, the photochemical activity of NDs with different surface chemistries was investigated. Hydroxyl radical ( $\text{HO}^\bullet$ ) and solvated electrons ( $e_{\text{aq}}$ ) produced under X-ray (17.5 keV) and gamma (1.17 MeV) energy were measured using surface-modified NDs in colloidal aqueous suspensions. Note that all along this Ph.D. work, the radiosensitizing effect for the different surface chemistries we produced (including hydrogen annealed NDs) were checked by *in-vitro* experiments performed by our colleagues from the CEA-DSV-iR2CM.

The present Ph.D. was mainly conducted with a single source of NDs to keep consistency and ensure comparability. Detonation NDs provided by the PlasmaChem GmbH company were chosen due to the purest grade currently available on the market and the relatively low-cost. At the same time, other non-commercial sources of NDs were also tested and compared with PlasmaChem detonation NDs showing that surface modification methods are rather universal and source-independent.

As-received detonation NDs have a polyfunctional and scattered surface chemistry which limits the possibility to control and study their interaction with ionizing radiation in water. To get control of the surface chemistry, native NDs were modified via physical methods toward homogeneous surface-terminations allowing to better understand their properties. Hydrogen-termination of NDs surfaces was achieved using two different methods: a hydrogen microwave plasma and a thermal treatment. The cleaning and formation of oxygen-containing functional groups were induced via annealing under air whereas annealing in vacuum was used to initialize  $\text{sp}^2$ -like reconstructions on NDs surface.

Following the production of the different surface modified NDs, several characterization techniques were used to study the crystallographic structure and the chemical composition with respect to the native material. In addition to that, quality assessment of NDs toward metallic and non-metallic impurities was performed by the ICP-MS analysis. The complementary techniques were applied to better understand the properties and the interaction of NDs in air atmosphere and water.

To study the photochemical activity toward ROS production in aqueous media, colloidal properties, and stability of surface-modified NDs as a function of time were established in neutral pH. Surface treatment led to the production of negatively (air annealed) and positively (plasma and thermal hydrogenation, vacuum annealing) charged NDs as measured in colloidal suspension. The stability of NDs in stabilizer-free suspension was investigated with respect to their surface chemistry and their preparation protocol on the same source. Attention was paid to optimization of the experimental procedure allowing to compare results from various sources and surface functionalities revealing the surface-specific reactivity toward water molecules.

Investigation of the colloidal properties of NDs revealed that the stability is a combination of several factors: the concentration, the time and the surface charge associated with the specific surface chemistry. This study revealed that freshness of the suspension, even few hours, is an essential factor to consider when looking at colloidal properties of NDs. These are all parameters which are often left out when ND stability is reported in the literature. We also suggest that more attention should be paid to the concentration of NDs to maintain NDs' properties in water and increase the lifetime of the suspension. The lower colloidal stability of specific NDs in suspension was related to the presence of nano-onions and  $sp^2$ -C on the surface of native and surface-modified NDs as confirmed by TEM, as well as a modification of the NDs / water interface (adsorbed species).

The key part of this Ph.D. work focused on the behavior under irradiation of surface-modified NDs with oxygen, hydrogen, and reconstructed  $sp^2$ -C terminations. The production of  $HO^\bullet$  radicals and  $e_{aq}$  was measured under X-rays and Gamma-rays with respect to the specific surface chemistry (oxidized, hydrogenated, and  $sp^2$ -C terminated) of NDs. Photoemission activity was investigated under air atmosphere whereas the presence of  $e_{aq}$  was probed by the mean of a gaseous mixture –  $N_2O/O_2$  acting as electron scavenger. For the first time, the detection of  $e_{aq}$  was successfully demonstrated for plasma hydrogenated detonation NDs under activation with a therapeutic energy range (keV / MeV).

Negatively charged Ox-NDs were demonstrated to be non-active when exposed to X-rays and gamma rays. The opposite effect was observed for plasma and thermally H-NDs which appeared to be equally responsive to X-ray and gamma rays (tested only on plasma treated samples). In both cases, the effect observed was both concentration- (until  $30 \mu\text{g}\cdot\text{ml}^{-1}$ ) and energy-dependent with an overproduction for optimized ND concentrations as high as 40 % - 100 % depending on the surface treatment, the experimental atmosphere, and the type of species detected ( $HO^\bullet$  or  $e_{aq}$ ). The results also showed that smoothly vacuum annealed NDs also enhance production of  $HO^\bullet$  radicals as hydrogenated NDs, but the effect seems to be limited by the graphitization stage.

These results become even more interesting when the comparison with H-terminated bulk diamond is made. In planar diamond structure, the effect is only observed in the presence of hydrogen while for NDs the surface chemistry appears to be less relevant (except for oxidized NDs). Furthermore, playing on the energy range, it appeared that the absorption of photons by the diamond core is not really driving the effect. Similar behavior was also reported for gold NPs.

We, therefore, proposed the hypothesis that radical overproduction seen for hydrogenated and smoothly vacuum annealed NDs is linked to their positive ZP and related specific interactions with water molecules. This hypothesis would more likely support an enhancement of the radiolysis of water surrounding NDs rather than a true photoemission of electrons from the nanodiamond core to explain the overproduction of HO<sup>•</sup> radicals and solvated electrons in the presence of NDs.

## Perspectives

- Colloidal stability of NDs

The main drawback of surface-modified NDs colloids (plasma and thermally hydrogenated, and vacuum annealed) is their limited stability. The lifetime and quality of NDs suspensions could potentially be improved via surface pre-treatment, e.g. air annealing before surface modification treatment. In addition to that, an increase in the concentration of NDs can also limit its agglomeration in colloidal suspension.

- Gas ‘bubbles’

Modification of colloidal properties of NDs along with gas desorbing from the water have been observed. In parallel, the bubbles occurring on the surface have been associated with loss of colloidal stability. Investigating the nature of the gas desorbing from NDs suspension could explain the role of gasses (e.g. oxygen) in colloidal stability and agglomeration of NDs.

- X-ray irradiation of NPs

We have observed a similar trend in HO<sup>•</sup> production for GNPs and NDs which indicate an influence from the surrounding water structure. Further investigation of the water structure around GNPs and NDs is required to understand the link between electron emission efficiency and the physical nature of NPs.

- OLC-NDs

The origin of photoemission activity from vacuum annealed NDs could be established by irradiation of fully graphitized NDs with OLC-like carbon structure. The reduction of HO<sup>•</sup> production activity has been observed for an increasing time/temperature of vacuum treatment hence no HO<sup>•</sup> production is expected from OLC-NDs. Such an experiment could potentially explain the influence of surface functional groups (e.g. hydrogen), which has been mostly associated with SC and NEA of detonation NDs. Since the various surface

functionalities (e.g. oxygen, hydrogen) are still present after vacuum annealing at 850 °C for 1 h the final conclusion cannot be made.

- Electron emission in water

According to the last publication of R. Hamers<sup>1</sup>, fast surface oxidation of detonation NDs takes place under UV illumination. However, the same effect has not been successfully demonstrated under a high dose of X-rays (no surface modification). More experiments should be conducted to characterize the surface of NDs before and after irradiation for various doses and energies of irradiation. These can be done via FTIR characterization of NDs suspended in water. In addition to that, the same experiments with detonation NDs should be performed under UV light to confirm the effect observed by R. Hamers and co-workers. Lastly, the X-ray and gamma experiments should be repeated for larger detonation ND particles which have better diamond quality and more homogeneous crystallographic structure.

## Bibliography

1. Zhang, L. & Hamers, R. J. Photocatalytic reduction of CO<sub>2</sub> to CO by diamond nanoparticles. *Diam. Relat. Mater.* **78**, 24–30 (2017).



# Scientific communication

## Publications

- Yoshikawa, T. *et al.*, 'Electrostatic Self-Assembly of Diamond Nanoparticles onto Al- and N-Polar Sputtered Aluminum Nitride Surfaces', *Nanomaterials*, 2016, 6(11), 217 (co-author)
- **Kurzyp, M.** *et al.*, 'Hydroxyl radical production induced by plasma hydrogenated nanodiamonds under X-ray irradiation', *Chem. Commun.*, 2017, 53(7), 1237-1240 (author)
- Petit, T. *et al.*, 'Unusual Water Hydrogen Bond Network around Hydrogenated Nanodiamonds', *J. Phys. Chem. C*, 2017, 121(9), 5185–5194 (co-author)

## Oral Presentations

- 'Physical chemistry investigation of ROS production from plasma hydrogenated nanodiamond', Hasselt Diamond Workshop SBDD XXI, 09<sup>th</sup> - 11<sup>th</sup> of March 2016, Hasselt, Belgium
- 'Plasma Hydrogenated Nanodiamond Enhanced X-ray Therapy', European Materials Research Society, 03<sup>th</sup> - 05<sup>th</sup> of May 2016, Lille, France
- 'Plasma hydrogenated nanodiamond as a promising material for radiosensitization: chemical investigation of the reactive oxygen species production', MRS Spring Meeting, March 28<sup>th</sup> – April 1<sup>st</sup> 2016, Phoenix, USA (*presented by Jean-Charles Arnault*)
- 'Surface modifications of detonation nanodiamond particles towards radiation-induced hydrated electrons and hydroxyl radical production', 28th ICDCM, 3<sup>rd</sup> – 7<sup>th</sup> of September 2017, Gothenburg, Sweden
- 'Hydroxyl radical and hydrated electron production from surface-modified detonation nanodiamonds', MRS Fall Meeting, November 26<sup>th</sup> – December 1<sup>st</sup> 2017, Boston, USA

## Posters

- 'Advances in nanoparticulate carriers', 19<sup>th</sup>-20<sup>th</sup> of October 2015, Institute Pasteur, Paris, France
- ESONN'2016 International Summer School, August – September 2016, Grenoble, France



# Appendix

## Summary

---

A.1 PlasmaChem GmbH commercial nanodiamonds powder: quality data sheet .....	186
A.2 Submicron latex beads as a spherical nanoparticles standard for DLS .....	187
A.3 Effect of centrifugal force and speed .....	188
A.4 Colloidal properties of as-received PlasmaChem nanodiamonds .....	188
A.5 Stability over 50 days .....	189
A.6 Fourier Transform Infrared Spectroscopy.....	189

---

# A.1 PlasmaChem GmbH commercial nanodiamonds powder: quality data sheet

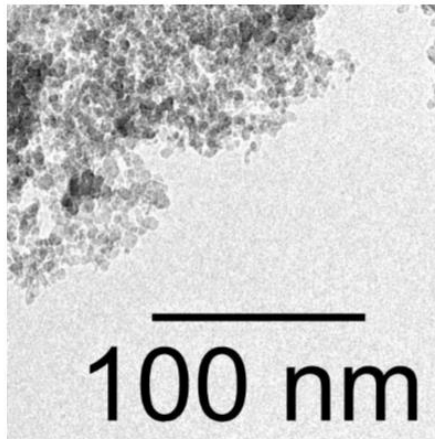


Plasmachem GmbH, Rudower Chaussee 29, 12489 Berlin

## Additional Product Information

Product Name: Nanodiamonds Powder, extra-pure  
Catalogue Number: PL-D-G02  
Average particle size: 4-6 nm  
SSA (BET): > 350 m<sup>2</sup>  
Form: dry powder  
Nondiamond carbon content: traces  
Controlled admixtures, %: Fe < 0.05; sum of other metals < 0.01  
Ash content: < 0,1%  
Picnometric density: ca. 3.18 g/cm<sup>3</sup>

TEM micrograph



Plasmachem GmbH Rudower Chaussee 29, D-12489 Berlin, Germany  
Betriebsnummer 0844771 Steuernummer 37/482/20830  
Phone: +49-30-63926313 Fax: +49-30-63926314 HRB 99010 B, UST ID-No. DE 157830095  
Account No. 2400422, Commerzbank Mainz BLZ 55040022, SWIFT COBADEFF550 IBAN: DE02550400220240042200  
Account No. 7241133006 Berliner Volksbank BLZ 10090000, SWIFT BEVODEBB IBAN: DE25100900007241133006

**Zollnummer 5479908**

### ***Production of nanodiamonds by detonation technique***

Diamond phase is formed during explosion conversion of carbon-containing explosives. The detonation of explosive processing in closed container results in the lack of oxygen and the incomplete combustion. In this case, the synthesis of diamond occurs under pressures above 230 kbar at temperatures above 2 300 K, which corresponds to the region of thermodynamic stability on the carbon phase diagram. A distinct feature of the process is that the time of synthesis in the explosion zone does not exceed 0.2 - 0.5 ps. The NDs size is limited by the synthesis time and is 5 nm approximately. The primary NDs are covered by graphitic material as the soot formation continues even after the pressure dropped. Therefore, a thorough purification is needed to obtain graphite-free diamond. Usually oxidizing mineral acids are used. The purified detonation soot contains up to 98 % carbon, with residual hydrogen, oxygen, and nitrogen.

## **A.2 Submicron latex beads as a spherical nanoparticles standard for DLS**

Latex beads based on polystyrene are spherically-shaped particles with a narrow size distribution used as a reference standard to test the accuracy and precision of the DLS equipment. The size of the beads obtained during the experiment depends on the dispersive surfactant as well as the sample temperature. Herein, the nominal sphere size of  $200 \pm 6$  nm was measured in well-controlled room temperature. The recommended procedure involves analysis performed on latex beads dispersed both in ultra-pure water and in 10 mmol.L<sup>-1</sup> of sodium chloride (NaCl). Addition of NaCl provides better stabilisation of the particles due to presence of Na<sup>+</sup> and Cl<sup>-</sup> ions reducing the Brownian motion of the particles. Results are presented in the Table A.1.

<b>Dispersant</b>	<b>Weighted mean intensity (nm)</b>
NaCl (10 mmol.L <sup>-1</sup> )	204 ± 3
Water	216 ± 3

**Table A.1** – Results of the size distribution measurement for NP commercial standard obtained in ultra-pure water and sodium chloride solution.

The size measured in water and sodium chloride is 8 % and 2 % respectively higher compared to the reference value. This difference of 6 % be simply explained by higher ionic strength of NaCl compare to ultra-pure water. Presence of ions reduce to natural movement of the particles resulting in lower dispersion of the scattered light and hence the smaller average size of the polystyrene particles. To sum up, results obtained in NaCl are within standard deviation of  $\pm 10$  nm given by the producer (Sigma ALDRICH - MFCD00243243) proving a high accuracy of our equipment.

## A.3 Effect of centrifugal force and speed

### *Air annealed nanodiamond*

The effect of centrifugation parameters (G-force, rotation speed) on final concentration and colloidal properties of Ox-NDs suspension is presented. The sonication parameters were kept constant (time = 60 min, amplitude = 80 %, pulse repetition frequency – PRF = 0.5 cycle per second, titanium ultra-sound probe H3, sample volume = 4 ml).

Initial concentration (mg.ml <sup>-1</sup> )	Centrifugation			Final concentration (mg.ml <sup>-1</sup> )	Weighted mean intensity (nm)	Weighted mean number (nm)
	time (min)	force (g)	speed (rpm)			
5.9	40	2400	3861	5.1	112 ± 2	54 ± 3
5.6	40	3260	4500	3.5	103 ± 2	37 ± 17

**Table A.2** – Relation between centrifugal force / speed and final concentration of the air annealed NDs suspension. The DLS characterization (weighted mean intensity and number of three measurements) was performed at sample concentration of 0.1 mg.ml<sup>-1</sup> within 1 h after suspension preparation.

## A.4 Colloidal properties of as-received PlasmaChem nanodiamonds

The PlasmaChem detonation NDs were dispersed in the ultra-pure water (18.2 MΩ) and characterized via DLS technique (Zeta Potential measurement).

Source of NDs	Mean Zeta Potential (mV)
PlasmaChem	33 ± 1

**Table A.3** – ZP of as-received PlasmaChem NDs dispersed (concentration of 0.1 mg.ml<sup>-1</sup>) in ultra-pure water. Value in the table represents average of 3 independent measurements obtained on the same day after suspension preparation (referred as fresh suspension). The sample was sonicated for 1 h prior the measurement to reduce agglomeration of the native particles.

## A.5 Stability over 50 days

### *Hydrogen annealed nanodiamonds*

Colloidal properties of Adamas Nanotechnologies NDs thermally annealed under hydrogen (1 h at 550 °C) were studied over 50 days. ND suspensions were prepared and stored at room temperature at a concentration of  $\sim 2 \text{ mg}\cdot\text{ml}^{-1}$ .

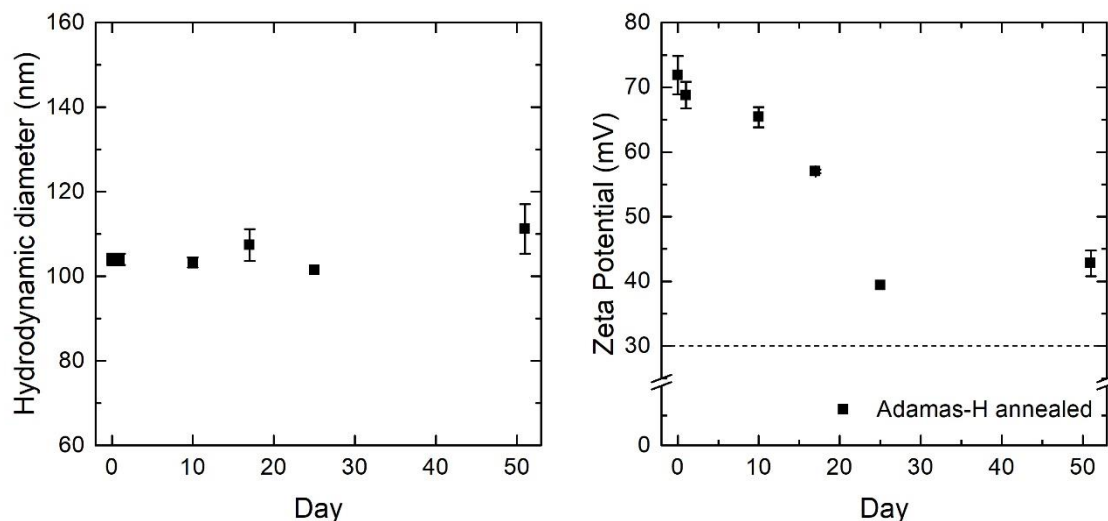


**Figure A.1** – Colloidal properties of thermally hydrogenated NDs (Adamas Nanotechnologies) monitored over 50 days. Black dashed line indicates instability region in which DLS measurement have low data quality due to aggregation and flocculation of ND particles during the analysis. Note the Y-axis breaks.

## A.6 Fourier Transform Infrared Spectroscopy

Fourier Transform Infrared Spectroscopy (FTIR) allows the analysis of photon absorption in the infrared range ( $700 - 3500 \text{ cm}^{-1}$  in our case) in a transmission sample. Unlike conventional absorption spectroscopy, consisting of exposing the sample to be analyzed to a monochromatic beam and measuring the absorption for each wavelength, the FTIR is based on an interferometry method from a beam polychromatic. Thanks to a Michelson interferometer, the sample is only exposed to a few wavelengths, which vary according to the position of the moving mirror of the interferometer. After transmission in the sample, an interferogram according to the displacement of the mirror is measured by a detector.

From this interferogram, a Fourier transform will make it possible to go back to the absorption spectrum of the analyzed sample. The advantages of going through a Fourier transform include the fact of not needing a monochromator for the infrared source and to be able to obtain a spectrum quite quickly. The FTIR schematic diagram is shown in Figure A.2.

The advantage of using infrared wavelength range, the vibrations of the molecules can be excited. The wavelengths absorbed will thus correspond to the chemical bonds present in the molecules being probed. For the same chemical bond, several vibratory modes can be excited, at different wavelengths since each mode requires a different energy. By correlating the absorption bands to different modes, it is possible to precisely determine the chemical bonds present on the probed sample.

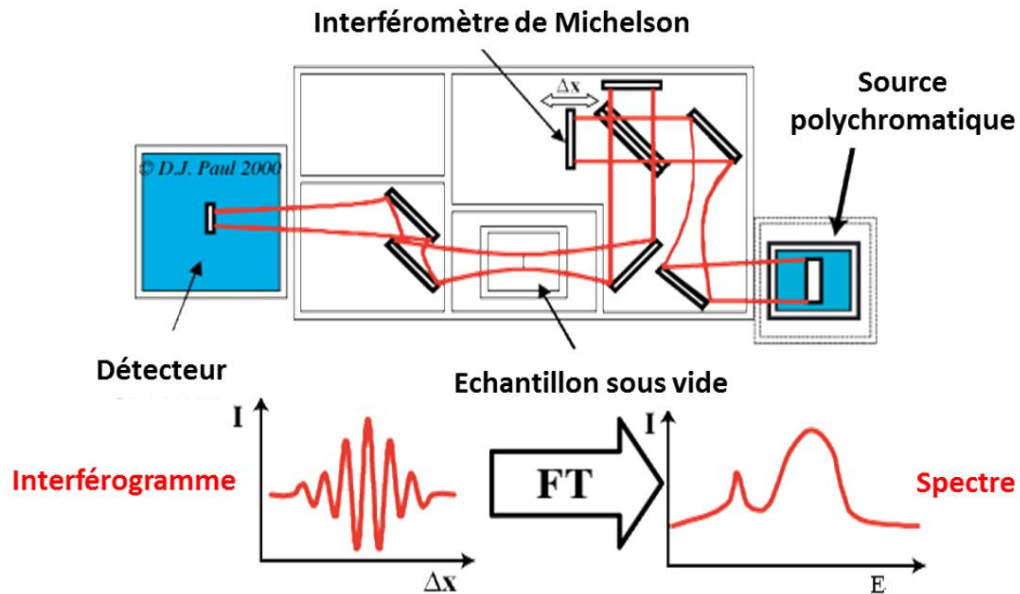


**Figure A.2** – Principle of FTIR operation.



**Titre :** Le nanodiamant hydrogéné comme radiosensibilisant : investigations chimiques et physiques des mécanismes impliqués

**Mots clés :** nanodiamants, modification de surface, colloïdes, radicaux hydroxyles, électrons solvatés, radiosensibilisation

**Résumé :** Parmi tous les nanomatériaux carbonés, les nanodiamants de détonation (NDs) possèdent des propriétés physico-chimiques exceptionnelles faisant d'eux un matériau idéal pour les applications en biologie. Aujourd'hui, la production industrielle permet de synthétiser des NDs ayant une taille de 5 nm comportant un cœur diamant et une enveloppe de surface possédant différentes terminaisons. La chimie de surface des NDs peut être modifiée par recuit ou par plasma donnant des NDs négativement ou positivement chargés en suspension dans l'eau. Notre équipe a récemment démontré des propriétés radiosensibilisantes des NDs hydrogénés par plasma (H-NDs) sur des lignées cellulaires cancéreuses radiorésistantes. Ces résultats prouvent leur aptitude thérapeutique comme agents radiosensibilisants. Cependant, les mécanismes impliqués dans cet effet ne sont pas bien compris. L'objectif principal de ce travail de thèse est d'étudier le comportement des NDs en suspension dans l'eau sous irradiation (rayons X et gamma) et de mesurer la production d'espèces réactives de l'oxygène (ROS) en particulier les radicaux hydroxyles HO<sup>\*</sup>. Des expériences complémentaires ont permis de détecter la production d'électrons solvatés (e<sub>aq</sub><sup>-</sup>). La détection des radicaux HO<sup>\*</sup> et des électrons solvatés (e<sub>aq</sub><sup>-</sup>) a été réalisée en utilisant une sonde fluorescence, la 7-OH coumarine, dans des atmosphères différentes (air and N<sub>2</sub>O/O<sub>2</sub>). Différentes chimies de surface ont été comparées (oxydée, hydrogénée, graphitisée en surface) préparées à partir de la même source de NDs. En parallèle, les propriétés colloïdales et la stabilité de ces NDs dans l'eau ont été étudiées à court et à long terme en fonction de leur chimie de surface. Une surproduction de radicaux HO<sup>\*</sup> a été mesurée pour les H-NDs hydrogénés par les deux méthodes et pour les NDs recuites sous vide à 750 °C. De plus, une surproduction d'électrons solvatés a été mise en évidence pour les H-NDs. Ces résultats sont discutés en fonction de la chimie de surface, la stabilité colloïdale et les interactions spécifiques des molécules d'eau avec les NDs.

**Title :** Hydrogenated nanodiamond as radiosensitizer: chemical and physical investigations of the involved mechanisms

**Keywords :** nanodiamonds, surface modification, colloids, hydroxyl radicals, solvated electrons, radiosensitization

**Abstract :** Among all nanocarbons, detonation nanodiamonds (NDs) possess outstanding chemical and physical properties suitable for bioapplications. Well-controlled mass production provides NDs with a primary size of 5 nm made of a diamond-core and a shell-coating containing various surface terminations. Surface chemistry of NDs can be tuned via thermal or plasma treatments providing either positively or negatively charged NDs in water suspension. Our group recently showed that plasma hydrogenated NDs (H-NDs) induce a radiosensitizing effect on radioresistant cancer cell lines providing potential therapeutic abilities as radiosensitizing agents. Nevertheless, the mechanisms involved behind this effect are not currently well understood. The main goal of this Ph.D. is to study the behavior of NDs suspended in water under ionizing radiations (X-ray and gamma) and to investigate the production of reactive oxygen species (ROS), in particular hydroxyl radicals (HO<sup>\*</sup>). Additional experiments allow to detect also produced solvated electrons (e<sub>aq</sub><sup>-</sup>). The detection of HO<sup>\*</sup> radicals and solvated electrons was realized in the presence of a fluorescence probe, the 7-OH coumarin, under various atmospheres (air and N<sub>2</sub>O/O<sub>2</sub>). Starting from the same source of NDs, different surface chemistries were compared (oxidized, hydrogenated, and surface graphitized). In parallel, colloidal properties and stability of these modified NDs in water with respect to their surface chemistry were investigated in a short and long-term period of time. An overproduction of HO<sup>\*</sup> was observed for H-NDs for both hydrogenation methods and vacuum annealed NDs at 750 °C. In addition, the production of solvated electrons was confirmed for H-NDs. These results were discussed taking into account the surface chemistry, the colloidal stability, and the specific interactions of water molecules with NDs.

